Preparation and Spectroscopic Investigations of Rare Earth Ions Doped Tungstate-Tellurite Glasses for Photonic Applications

A Thesis Submitted
In Partial Fulfillment of the Requirements
for the Degree of

DOCTOR OF PHILOSOPHY

in

PHYSICS

By

VIKAS

(Reg. No.: 2K19/Ph.D./AP/02)

Under the Joint-Supervision of

Dr. M. Jayasimhadri	**Dr. D. Haranath**
Associate Professor	Professor
Department of Applied Physics	Department of Physics
Delhi Technological University	National Institute of Technology
Delhi-110 042	Warangal-506 004

Department of Applied Physics

DELHI TECHNOLOGICAL UNIVERSITY
(Formerly Delhi College of Engineering)
Shahbad Daulatpur, Bawana Road, Delhi-110042. India

July 2024

DEDICATED TO….

MY FAMILY

DELHI TECHNOLOGICAL UNIVERSITY
Formerly Delhi College of Engineering
(Under Delhi Act 6 of 2009, Govt. of NCT of Delhi
Shahbad Daulatpur, Bawana Road, Delhi-110 042

CANDIDATE’S DECLARATION

I ***Mr. Vikas*** **(*Reg. No.: 2K19/Ph.D./AP/02*)** hereby certify that the work which is being presented in the thesis entitled *“**Preparation and Spectroscopic Investigations of Rare Earth Doped Tungstate-Tellurite Glasses for Photonic Applications**”* in partial fulfillment of the requirements for the award of the Degree of Doctor of Philosophy in the discipline of ***Physics,*** submitted in the Department of ***Applied Physics***, Delhi Technological University (Formerly Delhi College of Engineering), Delhi is an authentic record of my own work carried out during the period from August 2019 to July 2024 under the joint supervision of ***Dr. M. Jayasimhadri,*** Department of Applied Physics, Delhi Technological University, Delhi and ***Dr. D. Haranath***, Department of Physics, National Institute of Technology, Warangal.

The matter presented in the thesis has not been submitted by me for the award of any degree of this or any other Institute.

Vikas
(Reg. No.: 2K19/Ph.D./AP/02)

This is to certify that the candidate has incorporated all the corrections suggested by the examiners in the thesis and the statement made by the candidate is correct to the best of our knowledge.

Dr. M. Jayasimhadri
Supervisor & Associate Professor
Department of Applied Physics
Delhi Technological University
Delhi-110 042, India

Dr. D. Haranath
Joint-supervisor & Professor
Department of Physics
National Institute of Technology
Warangal- 506 004, India

Signature of the External Examiner

DELHI TECHNOLOGICAL UNIVERSITY

Formerly Delhi College of Engineering
(Under Delhi Act 6 of 2009, Govt. of NCT of Delhi
Shahbad Daulatpur, Bawana Road, Delhi-110 042

CERTIFICATE BY THE SUPERVISOR(s)

Certified that ***Mr. Vikas (Reg. No.: 2K19/Ph.D./AP/02)*** has carried out their research work presented in this thesis entitled ***"Preparation and Spectroscopic Investigations of Rare Earth Doped Tungstate-Tellurite Glasses for Photonic Applications"*** for the award of ***Doctor of Philosophy*** from Department of Applied Physics, Delhi Technological University, Delhi, under our joint-supervision. The thesis embodies results of original work, and studies are carried out by the candidate himself and the contents of the thesis do not form the basis for the award of any other degree to the candidate or to anybody else from this or any other University/Institution.

Dr. M. Jayssimhadri
Superiveror & Associate Professor
Department of Applied Physics
Delhi Technological University
Delhi-110 042, India

Dr. D. Haranath
Joint-supervisor & Professor
Department of Physics
National Institute of Technology
Warangal-506 004, India

Prof. A. S. Rao
Head, Department of Applied Physics
Delhi Technological University
Delhi-110 042

ACKNOWLEDGMENTS

This thesis represents not only my work at the keyboard, it is a milestone in more than four years of work at Delhi Technological University and specifically within the Luminescent Material Research Laboratory (LMRL). The Journey of my research is accomplished with the valuable support of many people. It is a pleasant aspect that I have now the opportunity to express my gratitude for all of them. First and foremost, I must acknowledge and express thanks to the ***Almighty****, for his blessing, protection and guiding me throughout this period.*

At the outset, I would like to my profound sense of gratitude, indebtedness and reverence to my supervisor, ***Dr. M. Jayasimhadri****, Department of Applied Physics, Delhi Technological University (DTU), Delhi and my joint supervisor,* ***Dr. D. Haranath****, Department of Physics, National Institute of Technology, Warangal, who nurtured my research capabilities for a successful scientific career. It has been an honour to work under excellent, enthusiastic and distinguished supervisors. Their unremitting encouragement, constant help, meticulous supervision and constructive criticism throughout my study for carving another milestone in my academic journey. Their massive knowledge of the subject, systematic gaze, farsightedness and perseverance were a constant source of inspiration during this thesis work. I feel privileged to have worked under such great supervision.*

I further stand ovate to ***Prof. A. S. Rao****, Head and DRC Chairman, Department of Applied Physics, DTU, for his timely advice, valuable help, suggestions and support. My heartfelt recognition for* ***Prof. Suresh C. Sharma****, former Dean (Academic PG) DTU,* ***Prof. Rinku. Sharma****, Dean (Academic PG) DTU and my SRC and DRC committee members for their enduring support. I express my sincere gratitude to* ***Dr. Mukhtiyar Singh****, Department of Applied Physics, DTU and* ***Dr. J. Suresh Kumar****, University of Aveiro, Portugal, for his timely advice and support.*

It is my pleasure to express my sincere thanks to all the **faculty** *members of the Department of Applied Physics for their continuous encouragement and help during my research work. I am also grateful to the* **Advanced Instrumentation Centre (AIC)**, *especially* **Mr. Sandeep Mishra** *and other* ***technical*** *and* ***non-technical staff*** *for their timely support and cooperation whenever required.*

Now it's time to sincerely thank my dear former and present lab mates whose support helped in accomplished my work. It is my pleasure to thank ***Dr. Amit K. Vishwakarma, Dr. Kaushal Jha, Dr. Mukesh K. Sahu, Dr. Harprret Kaur, Dr. Sumandeep Kaur, Dr. Shankar Subhramanian, Dr. Deepali*** *and present lab mates* ***Mr. Indrajeet Maurya, Ms. Vertika Siwach, Mr. Anupam Yadav, Mr. Vishvendra Singh*** *for their support. I would like to thank* ***Dr. Nisha Deopa, Dr. Aman Prasad, Dr. Kanika, Dr. Arti Yadav, Dr. Mohit Tyagi, Dr. Ravita Pilania, Mr. Rajat Bajaj, Dr. Pooja Rohilla, Ms. Anu Mor, Ms. Sheetal, Mr. Videsh*** *and present other lab members of MASR lab. I am especially thankful to my dear friends and fellow researchers* ***Ms. Vertika Siwach, Dr. Rajesh Kumar, Mr. Ramesh Kumar, Dr. Mrityunjay Kumar, Mr. Harender Mor, Ms. Komal Verma, Ms. Shilpa Rana, Mr. Kulwinder Kumar*** *for their help during my entire research tenure. I wish to acknowledge the enjoyable company and suitable help rendered by my dear friends,* ***Dr. Meenu Grewal, Mr. Sonu Grewal, Mr. Nakul Grewal, Mr. Monu Rao, Mr. Lakshay Grasha, Mr. Akshay Grasha, Dr. Anshul Baloda, Mr. Pardeep Sheoran, Mr. Saurabh Sangwan, Mr. Gaurav Sangwan, Mr. Sahil Sangwan*** *for their help and support during this tenure.*

Finally, I thank my family for their support and motivation, at every moment of my research period. With heartful gratitude and love, I express my gratefulness to my father ***Shri Vedpal Sangwan****, and mother* ***Smt. Sarla Devi*** *and younger brother* ***Er. Amit Sangwan*** *for their continual love and encouragement over the entire course of my life. I am thankful to my sweet wife* ***Dr. Anita***

***Sheoran** for the valuable suggestions, endless support and faith in me throughout my existence. My heartfelt acknowledgement to my loving children **Mr. Anvik Sangwan** and **Ms. Anaya Sangwan** who always make me smile before going to work.*

*I gratefully acknowledge the **Delhi Technological University (DTU**), Delhi for extending all the necessary facilities and also for providing financial assistance in the form of a **Junior Research Fellowship (JRF)** and **Senior Research Fellowship (SRF)** during the period of my research. I extend my gratitude to the DTU and staff in Administration, Accounts, Store & purchase, Central Library and Computer Centre for all the necessary facilities help and services.*

Writing this thanking note was more like a walk through my life where many faces came in and out. I thanks to one and all for your timely presence in my life.

Thank You all!!!!!

(Vikas)
(Reg. No. 2K19/Ph.D./AP/02

LIST OF RESEARCH PUBLICATIONS INCLUDED IN THESIS

1. **Vikas,** M. Jayasimhadri, D. Haranath, "Spectroscopic investigations of Dy^{3+} doped tungstate tellurite glasses for solid-state lighting applications" ***International Journal of Applied Glass Science,*** 13 (2022) 645-654. ***(I.F.: 2.10)***
2. **Vikas,** M. Jayasimhadri, D. Haranath, "Optical and luminescent characteristics of thermally stable new Eu^{3+} doped potassium tungstate tellurite glasses for epoxy-free luminescent devices" ***Current Applied Physics,*** 58 (2024) 11-20. ***(I.F.: 2.40)***
3. **Vikas Sangwan,** M. Jayasimhadri, D. Haranath, "Colour-tunable features of the thermally stable Tb^{3+}/Eu^{3+} co-doped telluro tungstate glasses for photonic applications" ***Journal of Physics D: Applied Physics,*** 57 (2024) 195301. ***(I.F.: 3.10)***
4. **Vikas Sangwan,** M. Jayasimhadri, D. Haranath, "Colour-tunable and warm white light emitting thermally stable Dy^{3+}/Sm^{3+} co-activated tungstate tellurite glasses for photonic applications" ***Journal of Luminescence,*** 266 (2024) 120276. ***(I.F.: 3.30)***
5. **Vikas Sangwan,** M. Jayasimhadri, D. Haranath, "Thermally stable white light emission and energy transfer analysis of tungstate-tellurite glasses co-activated with Dy^{3+}/Eu^{3+} for optoelectronic applications" **Journal of Molecular Structure,** 1322 (2025) 140577 ***(I.F.: 4.00)***
6. **Vikas Sangwan,** M. Jayasimhadri, D. Haranath, "Spectroscopic characteristics of red-emitting $Ca_3Bi(PO_4)_3$: Eu^{3+} phosphor in tungstate-tellurite glass (PiG) for photonic applications" communicated to **Optical Materials.** ***(I.F.: 3.80)***

LIST OF RESEARCH PUBLICATIONS NOT INCLUDED IN THESIS

1. **Vikas**, M. Jayasimhadri, **“**Thermally stable red luminescence from Eu^{3+} activated telluro zinc phosphate glass under near ultraviolet light excitation for photonic applications” ***Luminescence*** 37 (2022) 2059-2066. ***(I.F.: 3.20)***

2. **Vikas Sangwan,** Vertika Siwach, Mukesh K Sahu, Indrajeet Maurya, M. Jayasimhadri, D. Haranath, “Influence of Dy^{3+} ions on spectroscopic studies of thermally stable telluro zinc phosphate glasses for white light emitting devices” ***Material Today: Proceeding*** 2024.

3. Vedika Dubey, Tannavi, **Vikas Sangwan,** Indrajeet Maurya, M. Jayasimhadri, “Investigation of structural and luminescent aspects of Sm^{3+} activated yttrium niobium titanate phosphor for optoelectronic applications” communicated to **Journal of Electronic Materials.** ***(I.F.: 2.20)***

RESEARCH WORK PRESENTED AT CONFERENCES

INTERNATIONAL CONFERENCES:

1. **Vikas Sangwan,** Vertika Siwach, Indrajeet Maurya, M. Jayasimhadri, D. Haranath ***"Multicolour emission and energy transfer features in Dy^{3+}/Eu^{3+} bi-activated tungstate-tellurite glasses for w-LED applications"*** presented in 2nd International Conference on Spectroscopy in Material Science-2024 **(ICOSIMS-2024)** at University of Aveiro, Portugal, during 5-7th June 2024.
2. **Vikas Sangwan,** Vertika Siwach, M. Jayasimhadri, D. Haranath "***Tunable Luminescence and energy transfer mechanism in Dy^{3+}/Eu^{3+} co-activated potassium tungstate tellurite glasses for optoelectronic applications"*** presented in International Conference on Atomic, Molecular, Material, Nano and Optical Physics with Applications **(ICAMNOP-2023)** at Delhi Technological University, Delhi, during 22-24th December 2023.
3. **Vikas Sangwan,** Vertika Siwach, Mukesh K. Sahu, M. Jayasimhadri, D. Haranath "***Multicolor emission and energy transfer mechanism in Tb^{3+}/Eu^{3+} co-activated potassium tellurite glasses for photonic applications"*** presented in International Conference on Luminescence and its Applications **(ICLA-2023)** at CSIR-Indian Institute of Chemical Technology (CSIR-IICT), Hyderabad, during 3-6th July, 2023.
4. **Vikas Sangwan,** Vertika Siwach, Mukesh K Sahu, Indrajeet Maurya, M. Jayasimhadri, D. Haranath, ***"Influence of Dy^{3+} ions on spectroscopic studies of thermally stable telluro zinc phosphate glasses for white light emitting devices"*** presented in 1st International Conference on Spectroscopy in Material Science-2023 **(ICOSIMS-2023)** at University of Aveiro, Portugal, during 20-22nd June 2023.
5. **Vikas,** Deepali, Vertika Siwach, M. Jayasimhadri, D. Haranath, ***"Thermally stable green emitting luminescent behaviour of Tb^{3+} doped potassium tungstate tellurite glasses for***

optoelectronic device applications" presented at International Union of Materials Research Society- International Conference in Asia-2022 **(IUMRS-ICA 2022)** at Indian Institute of Technology, Jodhpur, during 19-23th December, 2022.

6. **Vikas Sangwan,** M. Jayasimhadri, D. Haranath, ***"Spectral investigations of thermally stable Eu^{3+} doped potassium tungstate tellurite glasses for epoxy-resin free red component of photonic device applications"*** presented at 5th International Conference on Nanomaterials Science and Mechanical Engineering **(ICNMSME)** at University of Aveiro, Portugal, during 5-8th July, 2022.

NATIONAL CONFERENCES:

7. **Vikas,** Mukesh K. Sahu, M. Jayasimhadri, ***"Structural and spectroscopic studies of Eu^{3+} activated red emitting sodium calcium niobate phosphor for WLEDs"*** presented at National Conference on Luminescence and its applications **(NCLA-2020)** at National Institute of Technology, Warangal, during 10-12th February, 2020.

ABSTRACT

Preparation and Spectroscopic Investigations of Rare Earth Ions Doped Tungstate-Tellurite Glasses for Photonic Applications

All over the universe, artificial illumination has significant adverse effects on human civilization, biotic communities, and eco-friendly environments. Since the emergence of human civilization, scientists and researchers have worked to develop efficient illumination technologies that are beneficial for illumination applications in a daily life. The development of the light-emitting diode was a crucial innovation in the 20th century. In the current years, bright illumination emitting sources, i.e., white light emitting diodes (w-LEDs) are considered to be the 4th generation solid-state lighting (SSL) devices because of their favorable characteristics, including higher reliability, low energy consumption, longer lifespan, eco-friendly and high luminous efficiency. At this time, w-LEDs available in the market consist of an inorganic phosphor and a n-UV/blue LED chip along with organic epoxy resin, which has negative features such as high correlated color temperature (CCT), low color rendering index (CRI) and low efficiency. Since the organic epoxy resin used to combine the inorganic phosphor has weak thermal stability thus suffering the lifespan and color quality of the w-LEDs. Hence, inorganic glasses and phosphor in glass (PiG) have the potential to alleviate these shortcomings of inorganic phosphor-based w-LEDs because they exhibit exceptional high thermal stability and can perform both as encapsulating materials and luminescence converters at the same time. They are considered to be superior to their crystalline equivalents and include exceptional applications such as optical fibre, optical data storage systems, optical thermometer sensors, lasers, w-LEDs, display and lighting devices, etc. Moreover, PiG has gained much attention because it has several advantages over single-crystal and transparent ceramics. The advantages are (i) luminescence can be controlled via mixing diverse phosphors and glass host compositions, (ii) simple method of preparation, and (iii)

reproducible consistently. Thus, PiG has been deemed as an appropriate luminescence converter for high-power w-LEDs as a result of its robustness, excellent thermal stability, minimal thermal expansion coefficient, and high temperature as well as humidity resistance.

Tellurite-based glasses have been considered the most admirable glass formers among the various glass-forming oxides owing to their numerous unique characteristics, including low melting temperature (≈ 850 ºC), wide transmission ranges from 0.4 to 5.0 μm, minimum phonon energy (≈ 800 cm^{-1}), maximum refractive index (≈ 1.9-2.5) and better solubility of REIs. As tellurite glasses possess low phonon energy, the light output shall be enhanced by reducing the non-radiative transition (NRT) between the higher and lower energy states of REIs. The addition of WO_3 in tellurite glasses can act as an excellent modifier helping to increase chemical stability, quantum efficiency and also to reduce non-radiative losses. Further, the introduction of alkali oxides such as Li_2O, Na_2CO_3 and K_2CO_3 in the tellurite-based glasses helps to decrease the non-radiative losses and enhances the strength of the host glass matrix. Moreover, the inclusion of heavy metal oxide such as bismuth trioxide (Bi_2O_3) serves as an unconventional network former in the glass host matrix. These characteristics of tungstate-tellurite glasses make them an appropriate choice for their applications in photonic devices. This thesis focuses on the optimization of rare earth doped glass system and a specific type of orthophosphate phosphor (Eu^{3+}-activated $Ca_3Bi(PO_4)_3$ phosphor) in undoped tungstate-tellurite glasses, also known as development of PiG development.

Chapter 1 starts with a brief introduction, the origin of the problem, the motivation of the research work, and an overview of the current literature. This chapter provides an introduction to different types of glass, the components involved in the glass formation, and their specific properties. Furthermore, the importance of the tungstate-tellurite glasses and phosphor in glass (PiG) have been discussed in detail. Thereafter, the chapter focuses on the principle of

photoluminescence, the energy transfer processes and the utility of rare earth-doped glass for illumination and display devices. The shortfalls and limitations of the existing white light technology and how to overcome those problems have been discussed. The motivation to carry out the present research work and the objectives of the thesis work are stated at the end of the chapter.

Chapter 2 describes the experimental technique to synthesize and characterize the tungstate-tellurite glasses and phosphor in the optimized tungstate-tellurite glass (i.e., development of PiG). The chapter describes the melt-quenching technique in detail to obtain the desired glass. Then the chapter follows the different analytical techniques that have been used to analyze the as-prepared glasses for their suitable applications. The thermal, structural, vibrational, morphological, and photoluminescent properties of the as-prepared samples have been investigated by thermogravimetric analysis (TGA)-differential scanning calorimetry (DSC), X-ray diffraction (XRD), Raman spectroscopy, Fourier Transform Infrared Spectroscopy (FT-IR), field emission scanning electron microscopy (FE-SEM), Spectrofluorophotometer. A brief introduction to the above-mentioned characterization techniques has been discussed in this chapter.

Chapter 3 explains the synthesis of transparent TeO_2 – Li_2O – WO_3 – ZnO – Bi_2O_3 (tungstate-tellurite) glasses doped with Dy^{3+} ions via employing a conventional melt quenching procedure. A broad hump in the X-ray diffraction profile confirmed the non-crystalline or amorphous nature of the prepared glasses. The absorption spectrum exhibits several bands between the 400-1800 nm range, which confirms that the transitions initiate from the lowest energy state ($^6H_{15/2}$) to the numerous excited states. The photoluminescence (PL) spectral profiles reveal three significant peaks centred at 481 (blue), 575 (yellow), and 664 nm (red) related to the Dy^{3+} ions under n-UV (388 nm) excitation. Furthermore, the chromaticity coordinates of the

prepared tungstate-tellurite glasses were situated in the white light region and nearest to the standard white light (0.33, 0.33). The decay profiles show the bi-exponential behaviour of the Dy^{3+} doped tungstate-tellurite (x = 0.1, 1.0, and 2.0 mol%) glasses. The energy transfer mechanism between the Dy^{3+}- Dy^{3+} ions has been determined to be a dipole-dipole in nature using the Inokuti-Hirayama (I-H) model to the decay profiles of the prepared tungstate-tellurite glasses. Moreover, temperature dependent PL spectra demonstrate the appreciable thermal constancy of the prepared glasses having a high value of activation energy. The above results indicate that the Dy^{3+} doped tungstate-tellurite glasses are potential luminescent materials to utilize in solid state lighting applications, especially for white LEDs. [Part of this work has been published in the ***International Journal of Applied Glass Science*** 13 (2022) 645-654] **(I.F.: 2.10)**

Chapter 4 presents the optimization and preparation of the alkali tungstate-tellurite glasses in molar composition: 49.0 TeO_2 – 20.0 R_2O – 15.0 WO_3 – 10.0 ZnO – 5.0 Bi_2O_3 – 1.0 Eu_2O_3 (R = Li, Na and K) using the melt quenching process. The luminescent characteristics of the prepared glasses have been examined in detail to reveal the optimization of the alkali ions in the prepared glasses. It is evident from the luminescent studies that the potassium tungstate-tellurite glasses exhibit comparatively stronger luminescence than the emission for the other two alkali-based tungstate-tellurite glasses, indicating the better quality of the potassium tungstate-tellurite glasses to proceed for further studies. Based on the above analysis, potassium tungstate-tellurite glass matrices with molar composition (50.0 – x) TeO_2 – 20.0 K_2O – 15.0 WO_3 – 10.0 ZnO – 5.0 Bi_2O_3 – x Eu_2O_3 (where x = 1.0, 3.0, 5.0 and 7.0 mol%) were synthesized to determine the optimal concentration of dopant (Eu_2O_3). Further, to estimate the aggregate weight loss, glass transition temperature (T_g) and thermal stability factor (ΔT) of the prepared host glass matrix, thermogravimetric analysis - differential scanning calorimetry (TGA – DSC) were utilized. Various functional groups were revealed via employing Fourier transform infrared (FT–IR)

spectroscopy. The optical bandgap (E_{Opt}) values for all the prepared Eu^{3+} doped potassium tungstate-tellurite glasses have been evaluated by employing the absorption spectra. Under n-UV and blue excitations, Eu^{3+} doped potassium tungstate-tellurite glasses are demonstrating reddish emission at 614 nm ascribed to the $^5D_0 \rightarrow {}^7F_2$ transition, in which the emission intensity is increasing continuously with Eu^{3+} ions content up to 5.0 mol%. The experimental lifetime profiles demonstrate the single exponential nature of the prepared glasses under n-UV excitation. Furthermore, temperature dependent photoluminescence (TDPL) spectra indicate excellent thermal stability of the prepared glasses with a high value of activation energy (ΔE). The prototype organic epoxy resin/binder-free device has been developed using the optimized glass matrix (i.e., 5.0 mol% Eu^{3+} doped potassium tungstate-tellurite glass) and n-UV LED chip. All the aforementioned findings validate that the optimized Eu^{3+} doped potassium tungstate-tellurite glass is an auspicious candidate for the red component to fabricate organic epoxy-free white LEDs. [Part of this work has been published in the ***Current Applied Physics*** 58 (2024) 11-20 **(I.F.: 2.40)]**

Chapter 5 explains the energy transfer and luminescent properties of Sm^{3+} doped, (Dy^{3+}/Sm^{3+}) and (Dy^{3+}/Eu^{3+}) co-doped potassium tungstate-tellurite transparent glasses, prepared via melt quenching technique. The optical characteristics of the prepared glass matrices were examined with the aid of the absorption spectra. Sm^{3+} doped potassium tungstate-tellurite glass matrices reveal a strong intense emission peak at ~600 nm associated with the orange-red region band ($^4G_{5/2} \rightarrow {}^6H_{7/2}$) transition. In Dy^{3+}/Sm^{3+} co-doped glasses, the emission intensity progressively upsurges with an increment in Sm^{3+} ion content (up to 1.5 mol%) confirming the energy transfer between Dy^{3+} and Sm^{3+} ions. Likewise, Dy^{3+}/Eu^{3+} dual-doped glasses demonstrate intense emission peaks in the blue, yellow, and red regions of the electromagnetic spectrum. Application of Dexter’s energy transfer formulation with Reisfeld’s approximation revealed that the energy transfer mechanism involves a non-radiative dipole-dipole (d-d) interaction between (Dy^{3+} and Sm^{3+}) and (Dy^{3+} and Eu^{3+}) ions. The average lifetime values for the $^4F_{9/2}$ level of the

Dy^{3+} ion in the above-mentioned glasses were measured and found that these values decreased with increasing activator (Sm^{3+} and Eu^{3+}) ion contents. The color coordinates (x, y) and the correlated color temperature (CCT) values of the prepared glasses were estimated. Based on the chromaticity coordinates and CCT values, it has been found that the desired colour of the prepared glass samples can be modulated from warm white light to orange-red light and warm white to red region by precisely adjusting the concentration of Sm^{3+} and Eu^{3+} ions and at specified n-UV/blue excitation wavelengths, respectively. Furthermore, the emission intensity observed at 373 K was 83.83% for TWKZBi: Dy^{3+}/Sm^{3+} glasses and 85.92% at 373 K for TWKZBi: Dy^{3+}/Eu^{3+} glasses compared to the emission intensity at the initial temperature, indicating the excellent thermal stability of the prepared glasses. Hence, the above results confirm that the prepared (Dy^{3+}/Sm^{3+}) and (Dy^{3+}/Eu^{3+}) co-doped potassium tungstate-tellurite transparent glasses can be a promising candidate for white light and other photonic devices. [Part of this work has been published in the ***Journal of Luminescence*** 266 (2024) 120276 **(I.F.: 3.30)** and part of this work has been communicated to the ***Journal of Molecular Structure*** **(I.F.: 4.00).]**

Chapter 6 presents the successful incorporation of Tb^{3+}/Eu^{3+} into the transparent tungstate-tellurite glass matrix prepared using the melt quenching approach. The existence of functional units corresponding to the different vibrations has been examined via Raman spectroscopy. Several emission peaks have been observed in the Tb^{3+} doped TWKZBi glasses under n-UV and blue excitations and the maximum luminescent intensity has been detected for 2.0 mol% of the Tb^{3+} doped TWKZBi glass sample. The color coordinates were obtained to be (0.303, 0.560) and (0.343, 0.646) under n-UV and blue excitations, which lies in the pure green region and suggests its utility as a green component for white LEDs and display devices. While Eu^{3+} doped TWKZBi glass revealed the strongest emission at 614 nm associated with the $^5D_0 \rightarrow {}^7F_2$ transition. The CIE coordinates (0.650, 0.348) lie in the red region indicating its potential application for fabrication in red component LEDs and display devices. The emission spectra of the co-doped Tb^{3+} and Eu^{3+}

ions in the TWKZBi glasses have been studied and the maximum energy transfer efficiency is found to be 32.82% under n-UV excitation. The energy transfer from sensitizer (Tb^{3+}) to activator (Eu^{3+}) ion happens through dipole-dipole interaction, as confirmed by Dexter's and Resisfeld's approximation. The emission colour of the prepared Tb^{3+}/Eu^{3+} co-activated potassium tungstate-tellurite glasses has been easily tunable from green to the reddish region in the CIE diagram by varying the Eu^{3+} ion concentration. Furthermore, the decay profiles for the $^5D_4$ level of the Tb^{3+} ions diminish with varying the concentration of Eu^{3+} ions, confirming the energy transfer from Tb^{3+} to Eu^{3+} ions. Moreover, temperature dependent photoluminescence studies indicate that the Tb^{3+}/Eu^{3+} co-activated potassium tungstate-tellurite glasses have good thermal stability. All the aforementioned results reveal the suitability of the Tb^{3+}/Eu^{3+} co-activated potassium tungstate-tellurite glasses for photonic applications. [Part of this work has been published in the ***Journal of Physics D: Applied Physics*** 57 (2024) 195301] **(I.F.: 3.10)**

Chapter 7 focused on the development of red-emitting phosphor in glass (PiG) with different concentrations with the help of the melt quenching method via the incorporation of the Eu^{3+}: CBP phosphor into the tungstate-tellurite glass. X-ray diffraction (XRD) and field emission scanning electron microscopy (FE-SEM) analysis validate the successful inclusion of the Eu^{3+}: CBP phosphor within the tungstate-tellurite glass. Rietveld refinement analysis of the PiG systems also confirms the crystal peaks indeed belong to the Eu^{3+}: CBP phosphor. When excited with the n-UV and blue lights, the emission profiles of the Eu^{3+}: CBP phosphor and PiG systems demonstrate the hypersensitive transition around 612 nm ($^5D_0 \rightarrow {}^7F_2$), which has been stronger than the other observed transitions. The emission intensity of the TWKZBi: CBPEu PiG system exhibits strong intensity in comparison to the Eu^{3+} doped CBP phosphor. CIE colour coordinates of the fabricated PiG systems under n-UV and blue excitations were situated in the red emission region and demonstrated excellent colour purity. Moreover, the thermal quenching behaviour was improved from 84.72 to 91.52% at 100 ºC in the temperature range from room temperature to

200 ^{o}C and activation energy increased from 0.1938 to 0.2698 eV due to the homogenous behavior and better network stability. Thus, the combination of the aforementioned findings ensures that the red-emitting PiG systems have the potential to be utilized in photonic applications. [Part of this work has been communicated to the ***Optical Materials***] **(I.F.: 3.80)**

Chapter 8 summarizes the relevant conclusions based on the results obtained in the previous chapters and outlines the future scope of the work.

LIST OF FIGURES

LIST OF TABLES

TABLE OF CONTENTS

Table of contents **Page number**

Chapter 1: Introduction and Motivation of the Research Work………..…………1

Chapter 2: Preparation and Characterization Techniques……………………35

Chapter 3: Spectroscopic Investigations of Dy^{3+} Doped Tungstate-Tellurite Glasses for Solid State Lighting Applications……..……………59

Chapter 4: Optical and Luminescent Characteristics of Eu^{3+} Doped Potassium Tungstate-Tellurite Glasses for Epoxy Free Luminescent Devices………………………………………………...….80

Chapter 5: Colour Tunable and Warm White Light Emitting Thermally Stable (Dy^{3+}/Sm^{3+}) and (Dy^{3+}/Eu^{3+}) Co-activated Tungstate-Tellurite Glasses For Solid State Lighting Applications…………………..104

Chapter 6: Multicolour Emitting Tb^{3+}/Eu^{3+} Co-doped Tungstate-Tellurite Glasses for Photonic Applications……..…………………...……141

Chapter 7: Luminescent Properties of Red emitting $Ca_3Bi(PO_4)_3$: Eu^{3+} Phosphor in Tungstate-tellurite Glasses for Photonic Applications……………………………………………………164

Chapter 8: Summary and Future Scope of the Research Work……………...185

Chapter – 01

Introduction and Motivation of the Research Work

The present chapter focuses on the motivation, literature survey, and systematic research work aimed in developing efficient visible light emitting rare earth doped glasses for photonic device applications. This chapter provides an introduction to multiple varieties of glass, the components needed in glass formation, and their specific properties. The chapter then describes about the several types of luminescence with a detailed emphasis of photoluminescence and some energy transfer mechanisms. A rare earth doped glass system and its applications for white light-emitting devices are being discussed. Further, a comprehensive explanation of the rare earth elements and their significance has also been provided. Finally, the importance of the tungstate-tellurite glasses and phosphor in glasses (PiGs), along with the objectives of the thesis work, are presented at the chapter's conclusion.

1.1. Introduction and Motivation

In recent times, the worldwide demand for energy and power consumption has been mounting exponentially with the ever-growing population and people yearning for a luxurious lifestyle. Undoubtedly, to meet this rising demand it has become essential to look for better renewable energy generation sources along with multiple conservation and mitigation steps. Since the year 2000, energy consumption has doubled and primary sources based on fossil fuels including oil, coal, and gas still provide 80% of the energy needed to meet demands [1-4]. The fossil fuel-based power/energy generation methods generate huge amounts of carbon dioxide (CO_2) and adversely affect the environment. The environment change has become a serious global concern that threatens the life of every human and wagered their fundamental needs including access to water, food production, use of land, and physical capital [5]. Hence, the green energy revolution and the deterioration of CO_2 emissions processes shall be adapted using all available technological options [5-8]. Thus, many researchers and scientists have been working on energy-efficient technologies, which can diminish dependence on fossil resources and decrease energy consumption.

The rapidly increasing demand for energy can be resolved by choosing powerful strategies, i.e., energy-saving approaches and retaining green renewable power generation techniques. There are three energy-saving techniques [9]:

- Energy saving by technology
- Energy saving by management
- Energy saving by policies or regulations

Advanced energy-saving technologies have tremendous potential to save an enormous amount of energy worldwide. One of the advanced energy-saving technologies is solid-state lighting (SSL) technology. SSL technologies are utilized in every area from industries to domestic fields. Lighting consumes 22% of electricity and 8% of all energy sources in the United States, and if the trend on SSL is appropriate, the technologies could minimize the electricity consumption for lighting by 33% in the upcoming decades [10-12]. Three types of traditional lighting sources are available: high-intensity discharge lamps, fluorescent lamps, and incandescent light. SSL works on mainly inorganic or organic light-emitting diodes (LEDs). In inorganic ones, the LED is a p-n junction, consisting of an InGaN alloy that emits wavelengths in the range of 360 to 470 nm depending on the Indium concentration. Devices utilizing SSL technology are anticipated to be pivotal in the forthcoming years. They present an opportunity to conserve significant quantities of electrical power and mitigate carbon emissions via an estimated 28 million metric tons annually on a global scale [13-15]. Despite their sufficient roles in reducing energy consumption and being eco-friendly, SSL-based devices including traffic signals, white LEDs (w-LEDs), full-color displays, liquid-crystal displays, cellular phone illumination, automotive displays, etc., offer crucial advantages over their predecessors, in terms of their performance, longer durability and cost-effectiveness. The diverse array of applications has inspired researchers to enhance SSL technology continuously, aiming for increasingly customizable and energy-efficient luminescence. The development of this technology has culminated in the prevalence of w-LEDs, which have advantages over traditional lighting sources. This happens owing to their compact dimension, shock resistance behavior, higher reliability, versatile design opportunities, higher transparency, and tremendously longer lifetime [16, 17].

Generally, there are two main methods of producing white LEDs. The first method is by utilizing an InGaN blue emitting LED chip and YAG: Ce^{3+} phosphor. This method of phosphor converted w-LEDs (pc-w-LEDs) has the benefits of being cost effective with higher illumination. Unfortunately, various drawbacks have been noticed, including, a low value of color rendering index (with Ra near 70-80), halo effect, and a high value of correlated color temperature (CCT) of approximately 7750 K [18-20]. Conversely, the other tactic of producing w-LEDs is by using red (R), green (G), and blue (B) (RGB) phosphors excited by near-ultraviolet (n-UV)/blue LED chips. This process has merits such as high CRI values but lacks luminescent efficiency because of the blue light re-absorption [20]. Also, in both the procedures, phosphor materials were encapsulated in an epoxy organic resin/binder that preserves the powder assembled in the w-LEDs module. Such epoxy resin has shortcomings, including the cracks or delamination of epoxy encapsulation and yellow stains of the epoxy, which have a significant impact on the hue produced by the w-LEDs. Later, silicone-based polymers with exceptional thermal stability have been employed to make epoxy. These polymers provide obstacles such as lower w-LEDs performance and divergence from the originally stated shape owing to thermal shrinkage [21, 22]. As a result, the making process becomes more complex, time-consuming and costly, reducing the commercial effectiveness of w-LEDs encapsulant.

Rare-earth doped glasses and phosphor-in glasses (PiGs) are used as alternatives for pc w-LEDs due to their simplicity of production, capacity to create any shape, improved thermal stability, cheaper production costs, and specifically epoxy resin-free manufacturing techniques. Tellurite based glass has been chosen as the suitable glass former due to its unique properties like low melting temperature, high dielectric constant, chemical durability and stability, low phonon energy, better solubility of rare earth ions, high refractive index, and broad optical transmission [23-25]. These unique properties suggest the impactful research to be carried out for the application of the glasses and PiGs in the field of photonic applications. The discussion about the tellurite glasses, PiGs, and their potential characteristics for use in photonic applications has been dealt with in the *section 1.8,* of the present chapter.

1.2. Classification of Solids

Solid materials are typically divided into two fundamental groups: non-crystalline/amorphous and crystalline. The atomic structure of solids can be studied using a technique called X-ray diffraction (XRD). The crystalline materials exhibit distinct geometric arrangements, characterized by atoms arranged in a regular order extending over a long range. Crystalline materials show the property of anisotropy. The XRD pattern for crystalline solids corresponds to the sharp peak, which is related to the different periodicity. While the non-crystalline/amorphous solids do not show any clear-cut geometric structure and are represented by broad humps in the XRD patterns. The amorphous materials have short-range order which means no regular prearrangement of the atoms, and also represent the property of the isotropy. Quartz, calcite, sugar crystals, etc are examples of crystalline solids, while amorphous solids include glass, plastic and rubber.

1.3. Glass or Vitreous System

Glass plays a significant role in our daily lives, serving as lighting fixtures, vehicle headlights, television and computer screens, mobile displays, and window panes. Glass is the best example of a non-crystalline material, which is fragile, rigid, and typically radiant with diverse colors. The word, glass was derived from the Latin word “glaseum” that refers to something that is translucent and possesses a shiny appearance. Research into new glass materials has received considerable attention in modern times due to their exceptional thermal and chemical stability. The scientific terminology of glass in accordance with the American Society of Testing Material (ASTM) is ‘*an inorganic product of the fusion which has been cooled to a rigid condition without crystallization”.* However, glasses can be prepared from the sol-gel method in which the above condition is not satisfied. So, the most important thing about glass is that it exhibits time-dependent glass transformation behavior. The best definition of a glass is "*Any material whether it is organic, metallic or inorganic synthesized by any method, which displays glass transformation behavior is called glass"* [26]. Some exclusive properties of glasses, which are given below make them vital solids for applications in science and technology [26]:

- Glasses are non-crystalline or amorphous materials having short-range order.
- Unlike crystals, glasses do not exhibit a specific melting point.
- Glasses are good thermal and electrical insulators at normal temperatures when the temperature increases, they convert to conducting nature.
- Glasses are isotropic, hard, and brittle.
- Glasses are made by countless techniques and soften before melting.
- The glass viscosity declines with rising temperature.
- Glass adheres to Hooke's Law until it reaches the point of fracture under sufficient stress.
- There are many properties ex:- density, elastic constant, specific heat, dielectric permittivity and luminescent properties.
- The internal energy is always greater for glass than the crystalline phase of the exact composition.

1.3.1. Glass Transition Behaviour

The nature of glass transition is labeled through the thermodynamic variables, namely either enthalpy or volume with changing temperature. In order to recognize this concept, let us consider a small volume of liquid/fluid kept at a temperature greater than that of the melting point/temperature. Now, when the fluid is cooled, one of these subsequent phenomena might occur:

(a) Alteration of the materials/substances into a crystalline state, resulting in the periodic structure and formation of long-range order at the melting point (T_m). When this occurs, the enthalpy drops abruptly to the value requisite to achieve the crystalline state.

(b) When the cooling of a fluid occurs at a rate slower than its melting temperature, yet it doesn't crystallize, which termed as a supercooled liquid. When the temperature decreases, the liquid's structure keeps on rearranging, but its enthalpy doesn't decrease rapidly due to the irregular reordering. With further cooling, viscosity increases. Eventually, viscosity rises to a point where atoms cannot rearrange themselves sufficiently within the experiment's timeframe to reach equilibrium. At this stage, the structure lags behind, causing the enthalpy to deviate from the equilibrium line, reducing the slope of the curve. Viscosity increases to a level where the liquid attains a fixed structure, becoming temperature-independent-a state known as a frozen liquid or glass. The temperature range within which the enthalpy of the solidified substance and the equilibrium fluid indicates the glass transformation area [26]. Such solidified fluid is then known as glass.

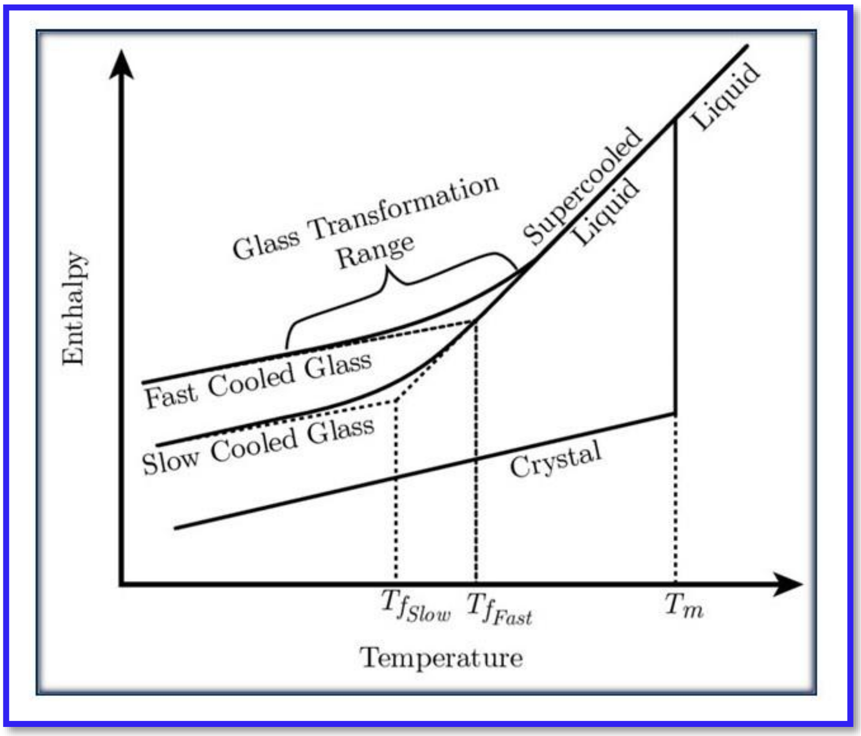

Fig. 1.01. *Enthalpy versus temperature plot for glass-forming substances.*

The effect of temperature on the enthalpy of glass formation is depicted in Fig. 1.01. If we extrapolate the glass and the super-cooled liquid lines, they intersect at a temperature known as the *fictive temperature.* The value of the glass transition (T_g) is affected by the heating rate utilized for drawing these curves. T_g cannot be measured as the genuine property of glass since it depends on both the experimental procedures employed in the measurement and the heating rate utilized for that measurement. However, T_g can serve as a valuable indicator of the predicted temperature at which the super-cooled fluid transforms into a solid on cooling [26, 27].

1.3.2. Components of Glass

The components required to prepare a specific glass can potentially be separated into several sections in accordance with their involvement in the manufacturing procedure, which are:

- Glass or network former
- Glass or network modifier
- Flux
- Fining agent
- Colorant

The critical component of any glass mixture is the glass former, which is always considered to be the most essential ingredient. Each glass contains one or more ingredients, which serve as the key components of the structure. Such components are usually referred to as *glass formers or network formers*. The main glass or network formers are boric oxide (B_2O_3), silica (SiO_2), and phosphoric oxide (P_2O_5), which are all readily available. Many more compounds are available, such as TeO_2, GeO_2, V_2O_5, Sb_2O_3, Ga_2O_3, etc., which may act as glass formers under certain conditions and are also known as conditional glass formers. To reduce the processing temperature of the glass batch, an additional oxide is added known as the *flux* for example sodium oxide (Na_2O) and lead oxide (PbO). Further, to improve the chemical durability of the glass, certain components are added known as the *glass modifier*, which includes alkaline earth and transition metals. Colorants are added to the glass batch to obtain the desired color of the final glass for example rare earth or transition metal oxides. The inclusion of the fining agents in the glass batch is for the removal of the bubbles for example antimony oxide (Sb_2O_3), sodium chloride (NaCl), and certain fluorides. To have a look at the representation of the glass batch, we have taken SiO_2 in both the crystalline and non-crystalline form as illustrated in Fig. 1.02 (a and b). In the crystalline form, the SiO_2 is a periodic arrangement of the tetrahedron such that the silicon atoms are at the center and the oxygen atoms are at the apex. The non-crystalline SiO_2 also has the same tetrahedron, but there is no regularity in the structure [26-28].

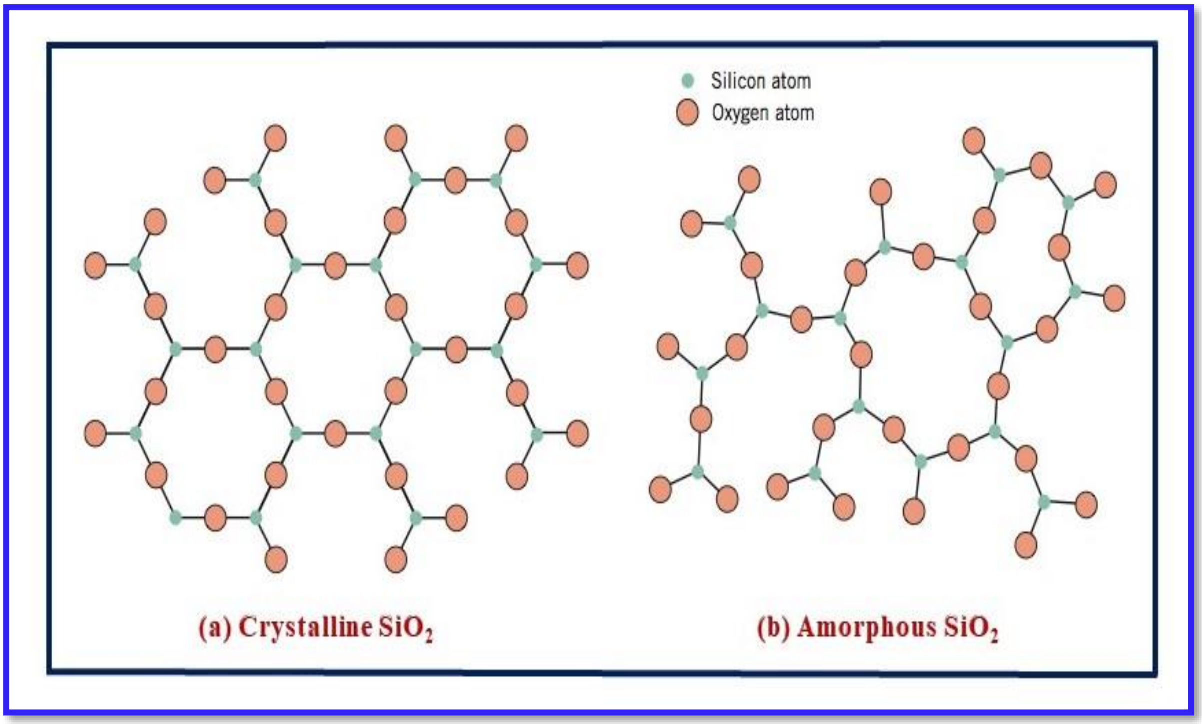

Fig. 1.02 (a & b). *Molecular arrangement in the crystalline and amorphous* SiO_2.

1.3.3. Classification of Glasses

Usually, glasses are categorized into two main groups: natural glass, which is formed by natural processes, and artificial glass, which is manufactured by humans in laboratories.

1.3.3.1. Natural Glasses

The formation of natural glasses occurs when molten lava cools rapidly upon reaching the earth's surface. Examples are pumice, pechsteins, obsidians, etc. Natural glasses are also formed via a sudden upsurge in the temperature following strong shock waves. Moreover, certain rare events can also result in the formation of glass through biological processes. Intense heat and energy from meteoritic impacts in the Libyan Desert lead to the establishment of rocks that are glassy in nature.

1.3.3.2. Artificial Glasses

The formation of artificial glasses can take place in a wide range of materials. However, we will just restrict ourselves to the context, which will be useful from the point of the present thesis work. The classification and brief explanation of these artificial glasses are as follows:

(i) Oxide Glasses

These classes are much more diverse and play a significant role in the composition of inorganic glasses. Among numerous oxides, the most studied glasses belong to the borate (B_2O_3), silicates (SiO_2), tellurites (TeO_2), phosphates (P_2O_5), tungstates (WO_3) and germinates (GeO_2). For the present thesis work, tungstate-tellurite glasses were considered which will be discussed more in detail in this Chapter (*section 1.8).*

(ii) Chalcogenide Glasses

These glasses, sometimes referred to as semiconductor glasses are made by combining the IV group (Ge, Pb, Si), V group (P, As, Bi, Sb) and VI group (Se, Te, S) constituents. The glasses that do not contain oxygen are suitable in modulators, infrared optical transmission, deflectors for infrared rays, and electrical switching.

(iii) Halide Glasses

Under halide glass, Beryllium fluoride (BeF_2) melt forms a very viscous liquid. The morphology of BeF_2 is similar to that of vitreous silica and is known as the weakened model of silica. Zinc chloride ($ZnCl_2$) also falls under this category. However, it is incapable of forming glasses as easily as BeF_2. These glasses are suitable candidates for high-power lasers, which find application in thermonuclear fusions-for example, fluoro-borates, fluoro-zirconates, fluoro phosphates, etc.

(iv) Metallic Glasses

In recent era, metallic glasses have gained much importance. There are two categories of metallic glasses: metal-metal alloys and metal-metalloids. They possess diverse characteristics, including zero magnetization, short magnetic loss, hardness and larger mechanical strength, as well as good chemical corrosion resistance. These glasses were exploited in application such as high-frequency power transformers.

1.3.4. Glass Preparation Procedures

The approach to prepare the non-crystalline or amorphous materials includes the following: -

- Melt quenching
- Chemical vapor deposition
- Reaction and Shear amorphization
- Sputtering
- Glow-discharge decomposition

- Irradiation
- Thermal evaporation
- Gel-desiccation
- Electrolytic deposition
- Shockwave transformation
- Chemical reaction

Among the methods discussed earlier, the melt quenching approach stands out as the most commonly utilized and commercially viable method, which will be discussed in *section 2.1, in Chapter 2.*

1.4. Luminescence

The term “luminescence” is derived from the Latin word “lumen”, which implies “light”. The concept of “luminescence” was introduced in 1888 by physicist Eilhardt Wiedemann [29]. Luminescence is the process by which a substance/material emits electromagnetic radiation. The luminescent substance can absorb particular invisible radiation or external energy and emits light, primarily in visible or near-infrared (NIR) regions. Luminescence is frequently referred to as cold body radiation when compared to the incandescence process, which produces hot light. One of the ubiquitous occurrences in daily life is luminescence, which can be seen in many things including fluorescent lights, televisions and displays, and many more. Various methods may be used to stimulate substances/materials, and these methods can be categorized into distinct classes based on the sources of excitation, as shown in Table 1.01.

Table 1.01: The type of luminescence, their mode of excitation and applications.

Types of Luminescence	**Mode of Excitation**	**Applications**
Photoluminescence (PL)	Photons	❖ Display devices ❖ Lighting sources ❖ Lasers ❖ Solar cells ❖ Thermal sensors
Thermoluminescence (TL)	Heat	❖ Dosimetry of ionizing radiation ❖ Geological dating ❖ Environmental monitoring
Electroluminescence (EL)	Electric field	❖ Laser diodes ❖ Light emitting diodes (LEDs) ❖ EL sensors ❖ EL displays
Chemiluminescence	Chemical reaction	❖ Chemical analysis
Bioluminescence	Biochemical reaction	❖ Analytical Chemistry
Cathodoluminescence	Electron beam	❖ TV screen ❖ Cathode ray oscilloscope ❖ Field emission display
Radioluminescence	X-rays	❖ X-ray scintillators ❖ X-ray display

Among above mentioned various types of luminescence, the main focus of the present thesis/research work is based on the photoluminescence (PL) mechanism.

1.4.1. Photoluminescence (PL)

The absorption of energy by the activator ions in terms of photons and then succeeding emission of light most likely in the visible area of the EM spectrum is generally acknowledged as photoluminescence. The activator ions possess abundant energy levels that allow them to become excited by absorbing photons, thereby functioning as centers for luminescence. In general, the PL occurs in the following sequences: -

(i) Absorption of energy (i.e., photons) via the activator and drives it to attain a higher/excited energy level.

(ii) The activator ion relaxes to its lowest energy level in the excited state (10^{-8} seconds).

(iii) Emission of a photon to the lower energy as the activator ions reach the ground state from the excited state (10^{-9} seconds).

Initially, incident photons are absorbed by the activator ions, prompting them to transit to higher energy levels. Subsequently, relaxation to the emitting state from these higher excited energy levels occurs through a non-radiative process, facilitated by photons (typically heat or lattice vibrations within the solid, referred to as phonons). The closely spaced energy levels above the emitting state prohibit radiative relaxation. Additionally, the states above the emitting one don’t last long enough to emit light. So, when activator ions deexcite from the emitting state to the ground state, they release light (radiative). Also, the emitting state is far from the next lower state, which terminates the possibility of non-radiative transition (NRT). This type of radiative emission is named as photoluminescence (PL). Fluorescence and phosphorescence are the two types of PL based on their immediate and delayed emission process, respectively [30, 31].

a. Fluorescence

In this class of PL, the emission occurs for short period (less than 10^{-8} seconds), when the source of the excitation is switched off. Emission of visible light in a very fast manner as the excited ions return to the lowest excited state and finally to the specific ground state.

b. Phosphorescence

In this PL process, delayed emission occurs after removing the source of the excitation and emission keeps on continuing for an extensive interval from milliseconds to ~10 seconds to several hours also known as afterglow luminescence [31]. The excited ions return to the ground state slowly as the phosphorescence materials glow for extended periods. In phosphorescence, material upon absorbing the excitation energy, ions reach up to the excited state having dissimilar spin and return after some time to the ground state and give the radiative emission.

1.4.2. PL Processes

(i) *Absorption:* When a particular radiation is incident on the materials/substances and part of the radiation is taken by the ions in a material/substance, it is known as absorption as presented in Fig. 1.03 (a). Absorption is a process by which ions soak up the part of radiation in the ground energy level/state to reach the higher/excited energy level/state. Owing to absorption, the incident radiation is attenuated after passing through a material [32].

(ii) *Excitation:* A part of radiation by ions can stimulate to move them from the ground energy level to the higher/excited energy levels is named as excitation, as presented in Fig. 1.03 (b). Thus, excitation is the addition of part of the energy to an ion, that results in its alteration, ordinarily from the ground state to one of the excited states [33].

*(iii) Non-radiative relaxatio*n: When a stimulated ion at a higher/excited energy state moves towards the lower excited states and releases a very trivial amount of energy through molecular vibration or atomic collisions, which is acknowledged as a non-radiative relaxation process, as depicted in Fig. 1.03 (c). Radiative, non-radiative, or a combination of the two processes may be used in the relaxation of ions to the ground state. A phonon (heat or lattice vibration) results from the non-radiative process [34]

(iv) Emission: When an electron is stimulated and moves from its lowest excited state to lower energy levels, it releases photons that have an energy equal to the difference between the involved energy levels. This process is known as emission or radiative transition, as shown in Fig. 1.03 (d). [30].

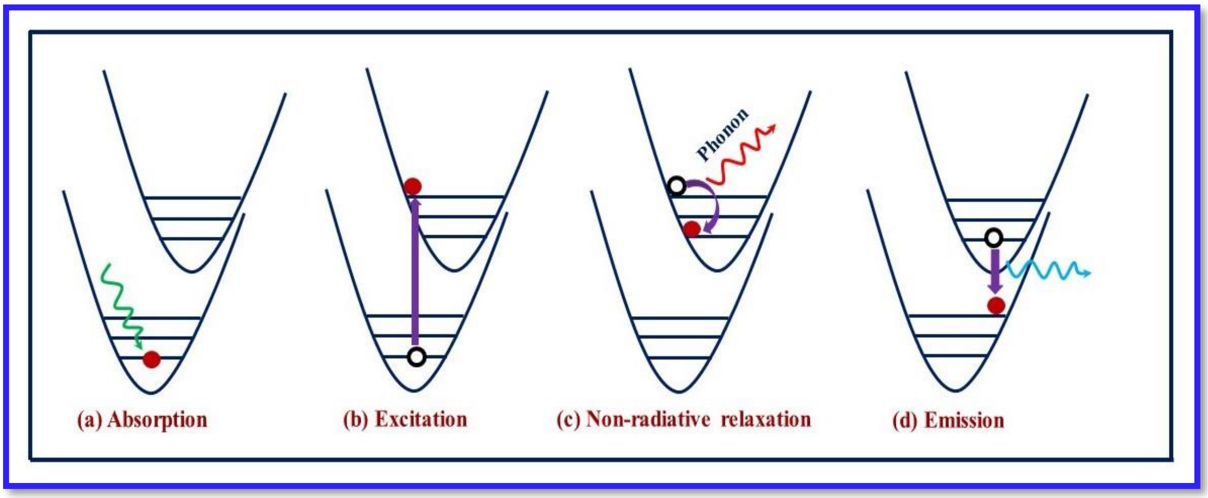

Fig. 1.03: *PL processes **(a)** Absorption, **(b)** Excitation, **(c)** Non-radiative relaxation and **(d)** Emission.*

1.4.3. Luminescent materials

Phosphors reveal the phenomenon of luminescence and are termed as luminescent materials. Phosphor is a material, which can convert the energy absorbed from external energy sources such as invisible UV, β, or X-rays into visible light. Phosphor consists of an inorganic host matrix in which some impurity ions are intentionally added called dopants (i.e., activator and sensitizer) [35-37].

(i) *Host Matrix/Lattice:* Generally, a host compound with a high optical bandgap can be used for any crystalline phosphor. The activator ions are strongly held by the inorganic host matrix, which sensitizes their luminescence characteristics. Sometimes, host matrix may efficiently absorb the high energy $(h\vartheta_1)$ photons and emits radiation in the visible region with less energy $(h\vartheta_2 < h\vartheta_1)$ as presented in Fig. 1.04 (a) referred to as self-luminescent materials. A portion of the absorbed energy is released as phonons owing to molecular vibrations or atomic collisions (see Fig. 1.04 (b)).

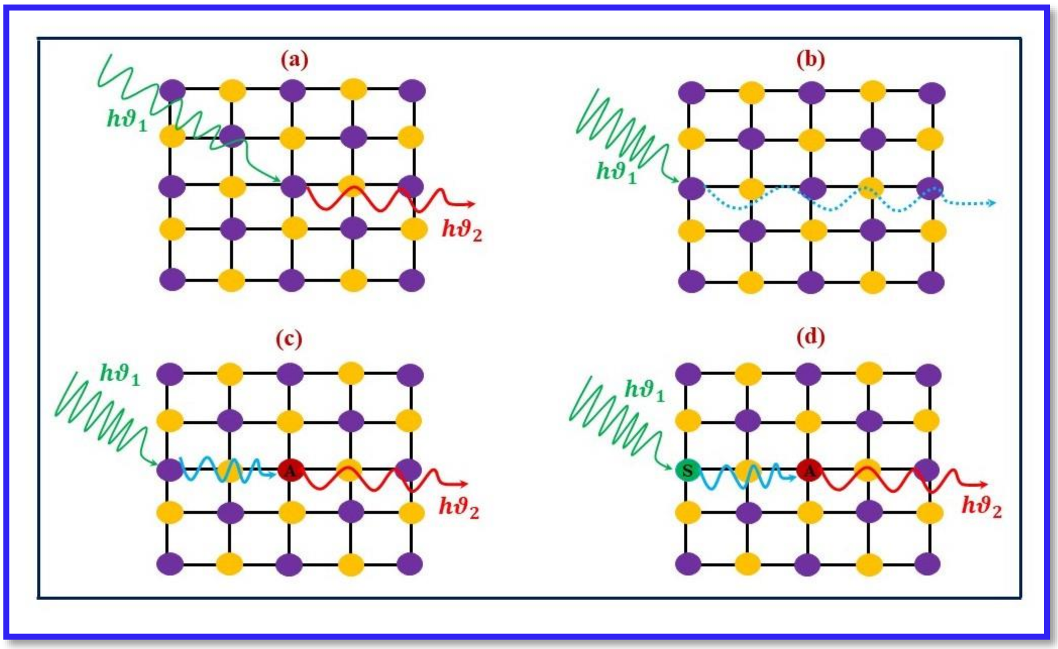

Fig. 1.04: *Luminescence mechanisms related to host lattice, sensitizer and activator.*

(ii) *Activator:* Inorganic phosphor hosts are typically activated with activators, which are minor quantities of impurities or additives. When an ion from an activator element leaps to the excited energy state upon absorbing the excitation energy and releases the energy as radiation while coming back to the ground state [30, 38]. As shown in Fig. 1.04 (c), the high energy $(h\vartheta_1)$ radiation is absorbed by the host matrix and, subsequently,

transfers the energy to activator ions and emission takes place from the activator ions. Activator ions exhibit varying responses in different host lattices, based on their electronic configuration, structure, and solubility in glass/phosphor matrices.

(iii) *Sensitizers:* If activator ions have very weak absorption, sensitizer ions can be added as another type of impurity. It enhances the absorption capacity and then transfers the received energy to activator ions. Fig. 1.04 (d) shows the luminescence mechanism involving the absorption of energy by a sensitizer and the transfer of a part of this energy to the activator ions. The behavior of the sensitizer ions differed in various host lattices because of characteristics including their electronic configuration, structure, and neighbouring atoms [30].

Typically, there is a certain threshold of activator ion concentration at which the emission intensity decreases owing to concentration quenching. This decrease can be caused by the transfer of energy between the closest ions, referred to as cross-relaxation [39]. In addition to the optimal concentration of activator ions, several other parameters influence the features of luminescence. The luminescent properties of the phosphor are influenced by multiple components, including the production technique, host material, surrounding conditions, activator and sensitizer ions.

1.4.4. Energy Transfer (ET) Mechanism

This section will provide a detailed discussion of the process involved in energy transfer (ET). To understand the ET, let us first understand the terms donors/sensitizers and acceptors/activators. A donor is some species that provides energy, electrons, protons, etc. whereas an acceptor is the one which accepts the energy, electron, proton, etc. In the present discussion, the donor absorbs the energy and transfers this energy to the acceptor ion. The ions or luminescent centers in the host matrix are called activators. Also, phosphors are commonly inorganic substances that are doped with a trivial number of impurities or quenchers known as dopants or activator centers. The ion/group that acts as a luminescent center in the phosphor is known as the activator of the matrix. The absorption of energy is done by the host matrix or activators. In numerous instances, emissions occur just at activator centers. Afterwards, a sensitizer was incorporated to enhance the absorption process. In an ET mechanism, a sensitizer triggers the activator before emitting the probable light emission. Undoubtedly, a process referred to as host sensitization can take place when the ion of the host matrix acts as a sensitizer, transferring the absorption energy to the activator ion [40, 41]. Nevertheless, a portion of the excitation energy will be transferred from one luminescent site to another site.

(i) As demonstrated in Fig. 1.05 (a), light (photons) is emitted directly after exciting the activator.

(ii) Light (photon) is emitted by direct excitation of the sensitizer and then activator via phonon emission or energy transfer, as presented in Fig. 1.05 (b).

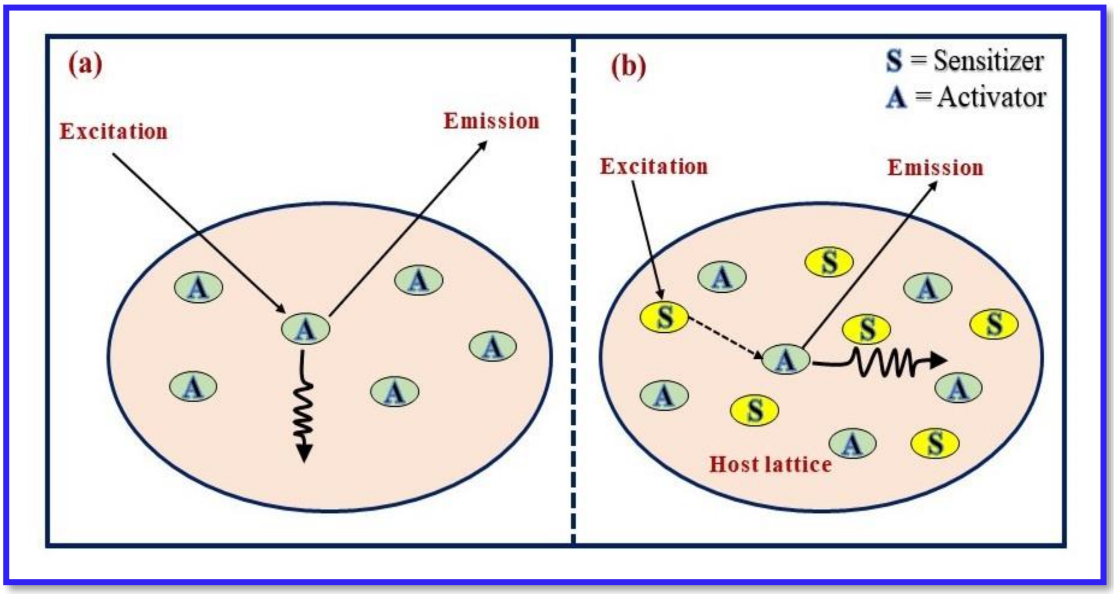

Fig. 1.05: *Schematic representation of* ***(a)*** *excitation and emission excitation;* ***(b)*** *excitation, energy transfer and emission in the host matrix.*

The luminescence in inorganic phosphors generally has the process of excitation, emission and energy transfer (ET), as illustrated in Fig. 1.05 (b). The emission from the luminescent center of the phosphor involves two primary processes. The first process, known as Stokes emission, occurs when the energy of the released photons is less than that of the incident photon energy. This loss in energy is caused by lattice relaxation, resulting from a change in the strength of the chemical bond. The Stokes shift refers to the distinction among the energy levels of absorption and emission. Conversely, there is a potential for the phosphor to absorb two or more photons simultaneously when excited by a longer wavelength light source, leading to the emission of a photon with higher energy than the incident one. The resulting process is termed as up-conversion, and the ensuing emission is referred to as anti-Stokes emission. In addition, the energy transfer (ET) process between ions is completed by four basic mechanisms:

(i) Resonant radiative energy transfer by the activator re-absorption and sensitizer emission.
(ii) Non-radiative transfer concerned with resonance among activator and sensitizer.
(iii) Multi-photon assisted energy transfer and
(iv) Cross-relaxation among two identical ions.

As illustrated in Fig. 1.06 (a), the effectiveness of radiative energy transfer depends on how efficiently the activator ion can be excited through the sensitizer emission. There needs to be a momentous overlapping between the sensitizer's emission spectrum and the activator's excitation spectrum. The lifetime of sensitizer fluorescence remains unaltered irrespective of the activator concentration, provided energy transfer occurs radiatively. Further, the increase in activator concentration causes a substantial reduction in the decay time of sensitizer fluorescence, indicating non-radiative energy transfer (NRET), as depicted in Fig. 1.06 (b). The efficient energy transfer (ET) mechanism occurs due to the equivalent energy gap amid the ground and excited states of the sensitizer and the activator. In phosphors, the ET process primarily relies on the competitive interaction and distinctive transitions of the sensitizer and activator, as well as the distance separating them. If these two ions have different excited states, phonon-assisted non-radiative transitions occur between the ions instead of radiative energy transfer, as shown in Fig. 1.06 (c). Fig. 1.06 (d) illustrates a straightforward energy level diagram, that includes cross-relaxation. Cross-relaxation takes place when an ion in the excited state transfers a part of its energy to other ions in the ground state, such that they both lie in an intermediate state which does not yield any radiative emission. Cross-relaxation terminology mentions types of down-conversion energy transfer that occur between the indistinguishable two nearby luminous ions or centers. This results in both ions simultaneously occupying some intermediate states within the energy range amid the two initial states. [42-44].

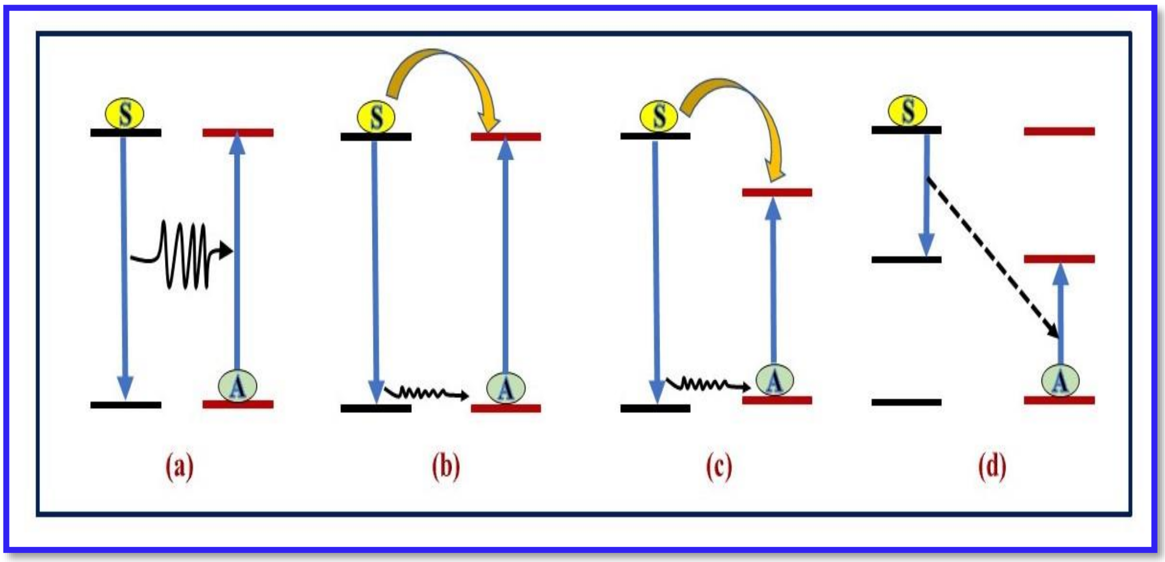

Fig. 1.06: A *schematic diagram to illustrate the ET process* ***(a)*** *resonant radiative transfer through emission of sensitizer (S) and re-absorption of activator (A);* ***(b)*** *non-radiative transfer with resonance between sensitizer and activator;* ***(c)*** *multiphonon-assisted ET; and* ***(d)*** *cross relaxation among the two identical ions.*

1.5. Rare Earth (RE) Elements

The RE name was given to the elements of lanthanides series in the periodic table preliminary from lanthanum ($^{139}_{57}La$) to Lutetium ($^{174}_{71}Lu$) also with Scandium ($^{44}_{21}Sc$) and

Yttrium ($^{88}_{39}Y$) [45]. Nevertheless, these elements are bountiful in the environment, disseminated, and not accessible as dense minerals. Yttrium and Scandium are also comprised in the category of RE reasoning for their existence in the similar ore and showing comparable characteristics as the lanthanides. While these substances have similar chemical conduct, they have unique physical parameters including color and luminescent behavior. As a result of their enthralling characteristics, RE substances are exploited in a variety of domains, including, material science, applied physics, and chemistry as well as fundamentally in the various fields of science and technology.

In RE elements, *4f* shells are progressively filled and the *5s* and *5p* orbitals are strongly shielded by these *4f* shells. The shielding effect reduces the significance of the *4f* orbital in chemical bonding, resulting in the modest perturbation and minimal effect on the neighboring ligand atoms. [46-48]. This shielding of *4f* is responsible for their unique optical properties. Mostly, the RE exists in RE_2O_3 oxide form having RE^{3+} state, but very few can exhibit RE^{2+} state also. The RE enters the crystal in either of two states (RE^{2+} or RE^{3+}) having the electronic configuration as $4f^{n-2}$ 5d $5s^2$ $5p^6$ or $4f^n$ $5s^2$ $5p^6$, respectively. The atomic number of RE elements, ionic radii, electronic configuration and ground state of the RE^{3+} ions are given in Table 1.02. Their electronic configuration enables them to be utilized in various fields such as optical, optoelectronic, pharmaceutical applications, etc. Promethium (Pm) is very special among these, as it exhibits a radioactive nature with a very minute half-life and is absent in nature. Pm was initially produced in the atomic reactor and discovered to be beneficial in CAT scans of the human circulatory analysis.

Table 1.02: Atomic number of rare earth (RE) elements, ionic radius (in Å), electronic configuration and ground state term of the RE^{3+} ions.

Atomic Number	Trivalent RE^{3+} Ions	Ionic Radius (RE^{3+}) (Å)	Electronic Configuration (RE^{3+})	Ground State Term
57	La^{3+}	1.032	$[Xe]4f^0$	$^1S_0$
58	Ce^{3+}	1.010	$[Xe]4f^1$	$^2F_{9/2}$
59	Pr^{3+}	0.990	$[Xe]4f^2$	$^3H_4$
60	Nd^{3+}	0.995	$[Xe]4f^3$	$^4I_{9/2}$
61	Pm^{3+}	0.983	$[Xe]4f^4$	$^5I_4$
62	Sm^{3+}	0.958	$[Xe]4f^5$	$^6H_{5/2}$
63	Eu^{3+}	0.947	$[Xe]4f^6$	$^7F_0$
64	Gd^{3+}	0.938	$[Xe]4f^7$	$^8S_{7/2}$
65	Tb^{3+}	0.923	$[Xe]4f^8$	$^7F_6$
66	Dy^{3+}	0.912	$[Xe]4f^9$	$^6H_{15/2}$
67	Ho^{3+}	0.901	$[Xe]4f^{10}$	$^5I_8$
68	Er^{3+}	0.890	$[Xe]4f^{11}$	$^4I_{15/2}$
69	Tm^{3+}	0.880	$[Xe]4f^{12}$	$^3H_6$
70	Yb^{3+}	0.868	$[Xe]4f^{13}$	$^2F_{7/2}$
71	Lu^{3+}	0.861	$[Xe]4f^{14}$	$^1S_0$

The RE ions activated luminescent materials exhibit various electronic transitions from $^{2S+1}L_J$ to free ion level or J-manifolds in *4f* subshell as illustrated in Dike's energy level diagram in Fig. 1.07 [49]. The RE ions exhibit stokes shift which is one of the criteria for developing any luminescent material. Due to the presence of a partially filled *4f* shell in RE-doped materials, photoluminescence (PL) is observed. This phenomenon can be attributed to charge transfer transitions, intra-configurational $4f^n$ transitions, or transitions between $4f^n$-$4f^n$-$5d^1$

states. The PL features of RE-activated glasses/phosphors are well understood based on their degenerate energy levels. Generally, the interactions among various levels are classified based on *f-f* transitions [50].

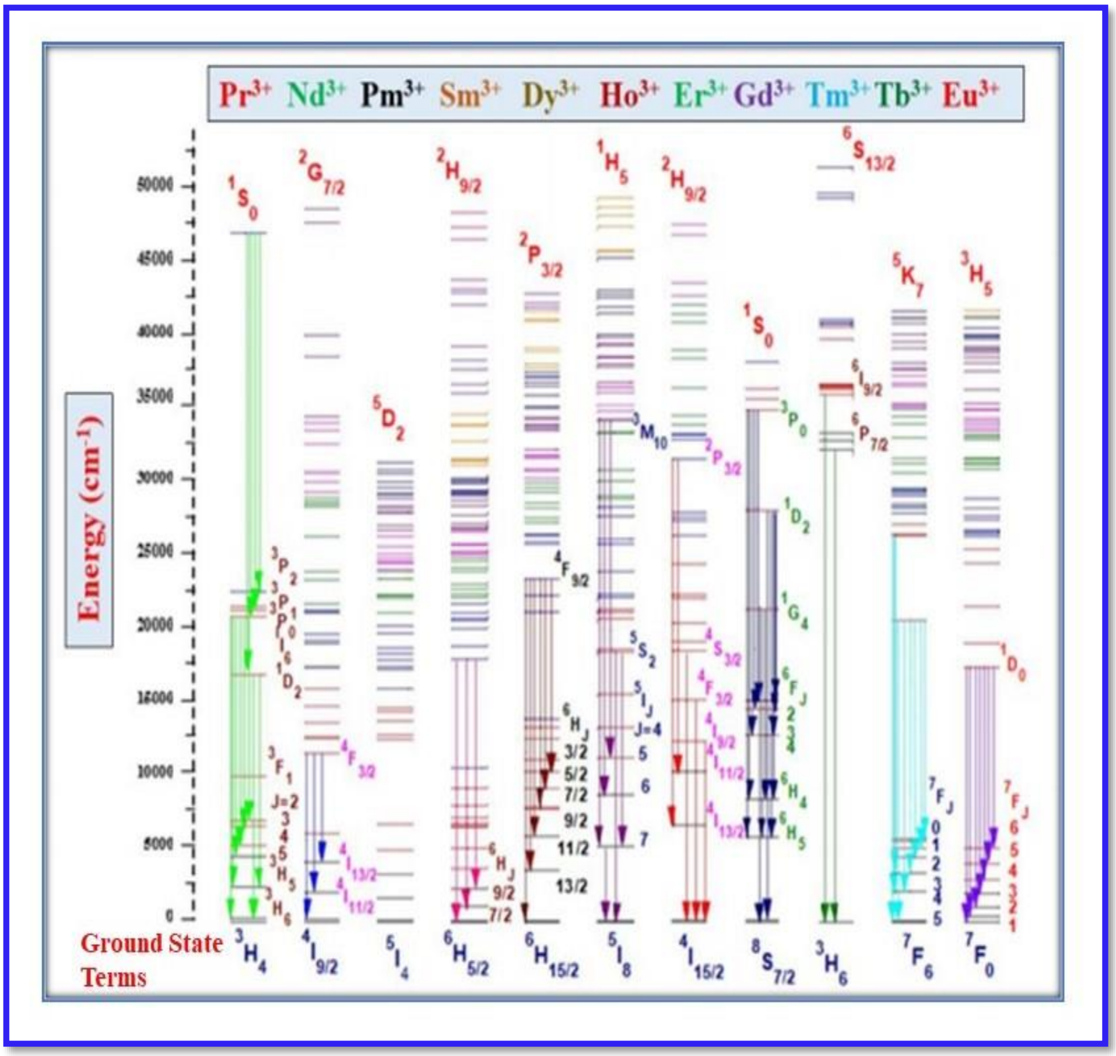

Fig. 1.07: *Energy levels and specific transitions of trivalent RE ions.*

1.5.1. Intra-Configurational $4f^n$-$4f^n$ Transitions

To recognize the natural frequencies of the lanthanide system, absorption and luminescence spectroscopy are the most significant approaches. Excitation and emission energies in the $4f^n$-$4f^n$ transitions remain unaffected by the host matrix into which the doping ions are introduced considering that they eventually get shielded from *5s* and *5p* electrons.

That's why the RE ions-induced spectra show narrow linewidth. The transitions inside *4f* shells are strictly forbidden since the parity remains unchanged in accordance with the Laporte's rule. When rare-earth (RE) ions interact with the crystal field or lattice vibrations, it can lead to a mixing of states with different parities into *4f* states. Sometimes, these transitions may not be allowed, but when spin-orbit interaction occurs, they become permitted and evident. The photoluminescence (PL) lifetime associated with *4f-4f* transitions typically falls within the range of milliseconds or microseconds due to the forbidden nature of the PL transition. Three categories of *4f-4f* transitions in the RE ions are as follows [34, 51]:

(i) Electric dipole/Induced electric dipole (ED) transition
(ii) Magnetic dipole (MD) transition
(iii) Electric quadrupole transition

(i) Electric Dipole/Induced Electric Dipole (ED) Transition

The ED transition occurs when a rare earth ion interacts with the electric field of incident electromagnetic radiation. The ED transition typically arises due to the linear movement of charges. The electric dipole moment has an odd parity and is forbidden as per the Laporte selection rule. However, electric dipole transitions between *4f* and *5d* are parity acceptable and therefore have oscillator strengths much more than that of *f-f* transitions having a magnitude of 10^{-1}-10^{-2}. The selection rules governing an induced electric dipole moment transition are $\Delta l \pm 1$; $\Delta\tau = 0$; $\Delta S = 0$; $|\Delta L| \leq 6$; $|\Delta J| = 2$, 4 or 6 if $J = 0$ (or) $J^{'} = 0$. The forbidden *f-f* electric dipole transitions come into the picture due to the admixing of $4f^{N}$ configuration with the excited configuration of the opposite parity for instance $4f^{N-1}5d$. The mixing of the electron states of the opposite parity is allowed due to the non-centrosymmetric interactions. These transitions are relatively much weaker than the ordinary electric dipole transitions with intensities of the order 10^{-6} and are called induced/forbidden ED transitions [34, 52].

(ii) Magnetic Dipole (MD) Transitions

When the magnetic field component of the approaching light interacts with the RE ions through a magnetic dipole, a strong transition appears, which is known as the magnetic dipole transition. The magnetic dipole occurs when charges are shifted rotationally while the direction of rotation endures constant under inversion via a point. The magnetic dipole transition undergoes uniform transformation under inversion and shows even parity, allowing transition among states with the same parity. Thus, a magnetic dipole is permitted via Laporte's selection criteria, such as $|\Delta L| \leq 0$; $\Delta S = 0$; $\Delta l = \pm 1$; $|\Delta J| = 0, \pm 1$ (but $J = 0 \leftrightarrow 0$ transition is forbidden) [53, 54].

(iii) Electric Quadrupole Transition

An electric quadrupole transition occurs when a charge has both, a zero-dipole moment and a quadrupole nature. Even-parity electric quadrupole transitions were shown to be much weaker than both magnetic dipole transitions and induced electric dipole transitions. There is little research evidence regarding the electric quadrupole transition of RE ions. Hypersensitive transitions are special definite transitions that may be identified using the quadrupole transition selection criterion. An electric quadrupole transition is classified as a hypersensitive transition and is also known as a pseudo-quadrupole transition. [34].

1.5.2. Inter-Configurational $4f^{n-1}5d$ Transitions

The *4f* and *5d* subshells have the ability to transfer electrons with parity. The $4f^{n-1}$-$5d$ transitions have a high sensitivity to the vicinity of rare earth ions, and their energy is substantial due to the enormous influence of the ligand field effect on the *d* orbital. Such ligand field results in the *5d* level being split into multiple levels due to shielding. The positions of the absorption bands related to the *4f-5d* transition in the spectrum also differ significantly depending on the host lattice due to the distinct variations in crystal field splitting. In contrast, the splitting of the *5d* orbitals and the de-excitation of the *4f-5d* electrons do not consistently influence the emission bands. The emission spectra from the near-ultraviolet (n-UV) to the red region, and is mostly dependent on the crystal lattice of the host material [38, 55].

1.5.3. Unique Properties of RE Ions

With regard to the distinctive interactions mentioned earlier, rare earth (RE) ions demonstrate unique properties that differentiate them from other optically active ions, as outlined below:

- These ions show narrow spectral lines and have longer emission lifetimes.
- Rare earth ions display luminescence in several wavelength ranges including, in visible and NIR regions of the electromagnetic spectrum
- Their *4f-4f* transitions (intra-configurational) in RE ions have minor homogenous line widths.
- They possess multiple energy levels that are suitable for optical pumping.
- There are well-developed theoretical models available, which can be used for the systematic analysis of energy levels, excited state dynamics, and transition intensities.

The aforementioned fascinating characteristics of these divalent (+2) and trivalent (+3) RE ions are in several applications, especially in solar cells, display devices, bio-medical treatments, indoor plant cultivation, fingerprint sensing, and solid-state lighting applications [56-59].

1.6. Excited State Dynamics of RE Ions

When sufficient energy is applied to excite a rare earth (RE) ion, the excitation process triggers de-excitation through intra-*4f* electronic transitions within the RE ion [60-62]. The mechanism of excitation and de-excitation is elucidated by the time-resolved intensity spectrum depicted in Fig. 1.08.

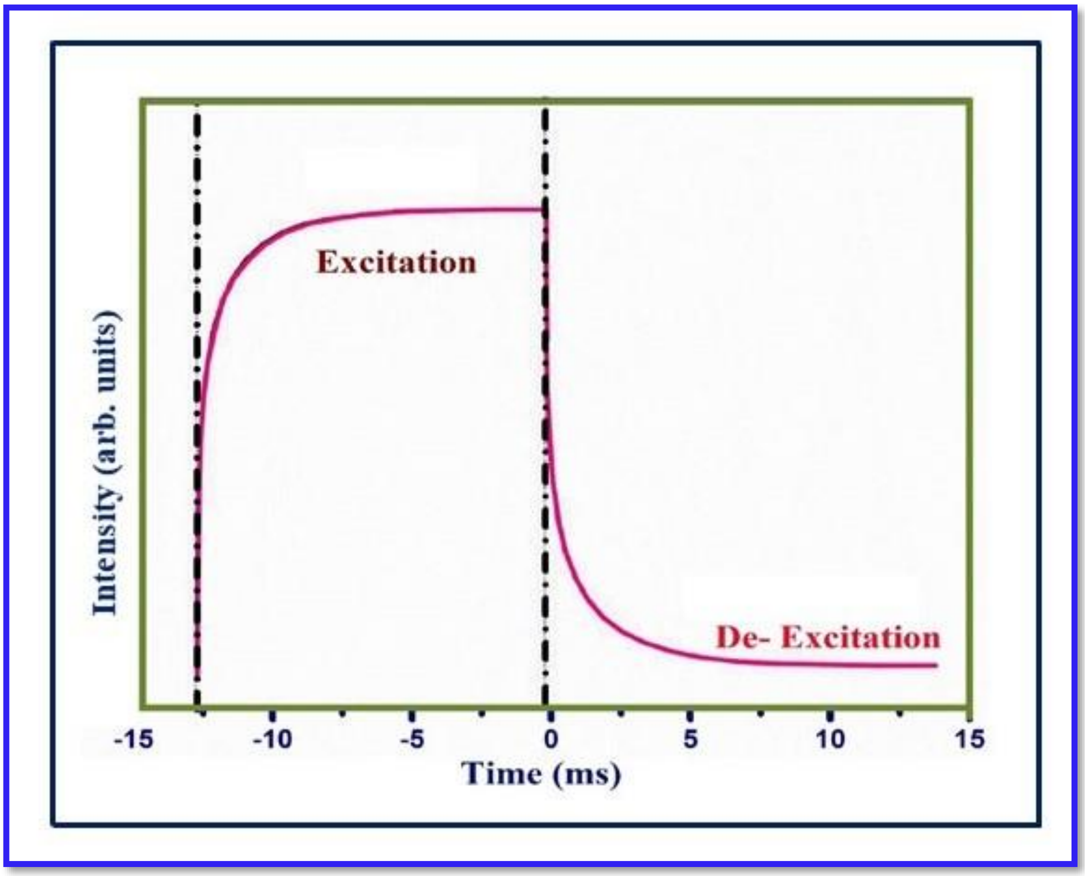

Fig. 1.08: *Excitation and de-excitation processes as a function of time for RE ions.*

The radiative transition among nearby RE ions or cross-relaxation (CR) channels can both de-excite the RE ions from the excited state to the ground state. At low concentrations of RE ions, interaction among them is minimal, allowing the photoluminescence (PL) decay profile to be accurately described by a single exponential equation. The PL intensity can be quantified with the help of the following expression:

$$I\,(t) = I_0 + A\,exp\left(-\frac{t}{\tau}\right) \tag{1.1}$$

In the above expression, the photoluminescence intensities at specific time t = 0 and t = t are denoted as I_0 and $I\,(t)$, respectively. A signifies the fitting constant value. The lifetime in the excited state of the RE ion is represented as τ and it can be evaluated using the intensity logarithmic plot with time. From Fig. 1.08, it can be noted that the intensity of the excited state decreases to 1/e after a time τ. In an excited state, the following equation can be used to determine the experimental lifespan of the RE ions:

$$\tau_{exp} = \frac{\int t\, I(t)dt}{\int I(t)dt} \tag{1.2}$$

In a few scenarios, these ion decay curves are well-fitted with the bi-exponential expression. The bi-exponential fit curves PL intensity can be shown using the expression

$$I = I_0 + A_1\, exp\left(-\frac{t}{\tau_1}\right) + A_2\, exp\left(-\frac{t}{\tau_2}\right) \tag{1.3}$$

where τ_1 and τ_2 represent the fast and slow components of lifetime. The A_1 and A_2 represent the fitting constants. By using τ_1 and τ_2, the average lifetime (τ_{Avg}) of the emitting level can be estimated using the formula given below [63]:

$$\tau_{Avg} = \frac{A_1\tau_1^2 + A_2\tau_2^2}{A_1\tau_1 + A_2\tau_2} \tag{1.4}$$

The fluorescence lifetime is influenced by the rates of both radiative and non-radiative relaxations. As the rates of non-radiative relaxations increase, often due to the presence of enlarged surface defects or quenching centers, the lifetime values of fluorescence decrease.

1.7. Colorimetry Characteristics

A prominent peak exhibiting a wide range of intensities can be observed in the emission spectra of inorganic materials (crystalline and amorphous) doped with rare-earth (RE) ions. The presence of these peaks is indicative of the susceptibility of human vision, which is a fundamental aspect of luminescence. The determination of the actual colour of the light emission is established through the analysis of its wavelength and the corresponding chromaticity coordinates. The colour coordinates of the Commission Internationale de I'Eclairage (CIE) are employed for the purpose of analyzing the actual hue of the emission spectrum of the luminescent substances. The analysis of the various colours within the visible region involves a comparison of the CIE coordinates derived from emission spectra and standard equal energy points. In order to determine the CIE color coordinates, the initial step involves assessing the tristimulus values (X, Y and Z) by utilizing the power spectral density in the way as follows [64]:

$$X = \int \bar{x}(\lambda)P(\lambda)d\lambda \tag{1.5}$$

$$Y = \int \bar{y}(\lambda)P(\lambda)d\lambda \tag{1.6}$$

$$Z = \int \bar{z}(\lambda)P(\lambda)d\lambda \tag{1.7}$$

In the above equations, $\bar{x}$, $\bar{y}$ and $\bar{z}$ signifies the matching functions in the CIE diagram as revealed in Fig. 1.09.

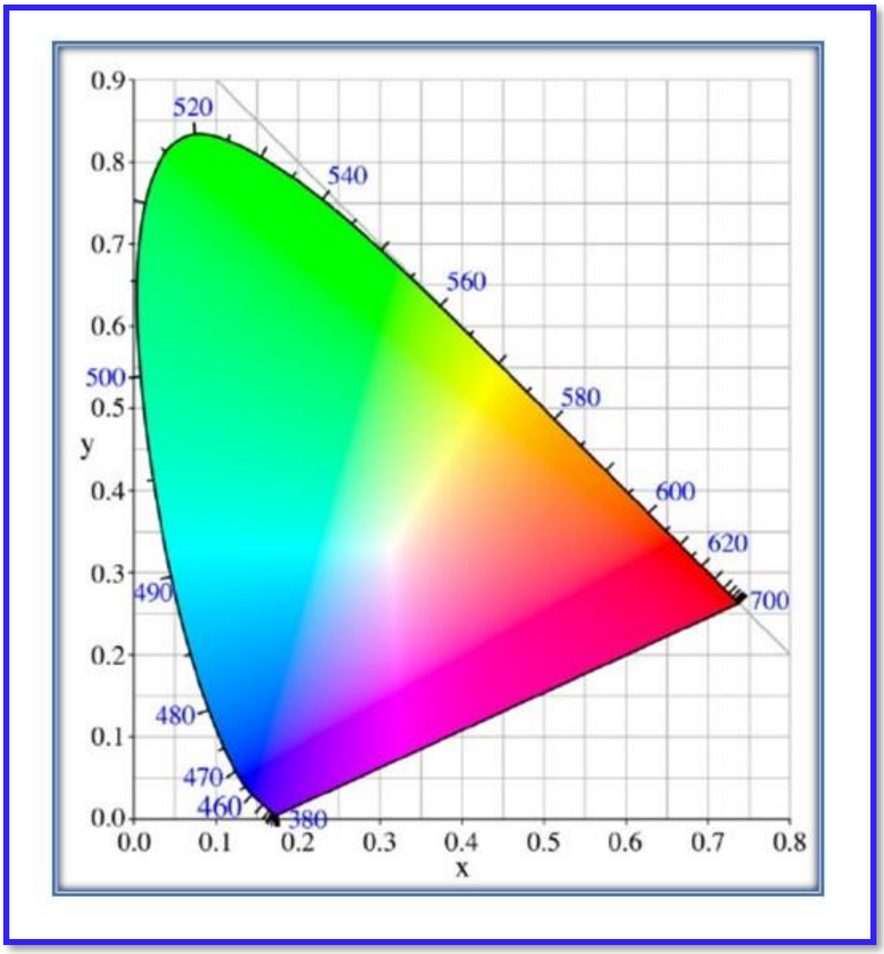

Fig. 1.09: *CIE chromaticity diagram.*

CIE color coordinates were computed with the help of calculated X, Y and Z values by employing the following expression:

$$x = \frac{X}{X+Y+Z} \tag{1.8}$$

$$y = \frac{Y}{X+Y+Z} \tag{1.9}$$

The temperature of the utmost analogous to a blackbody radiator is entitled as the correlated color temperature (CCT) of the light emitting source. A black body is a perfect physical substance that absorbs all inward radiation, regardless of incident angle or wavelength, and without any emission of radiation at 0 K. As a result, the CCT is defined as the absolute temperature of a black body with the chromaticity closest to the light source. The CCT is an important parameter for the identification of cool or warm white lighting devices. A lamp with a low value of CCT (< 5000 K) shows the warm appearance of emitted light. While the lighting devices with a high value of (> 5000 K) CCT signifies the cool nature of emitted light. In short, the CCT is the color of the light emitted from the lamp and the color appearance itself. The CCT can be assessed by the expression established by McCamy [65]:

$$CCT = -449.0\, n^3 + 3525.0\ n^2 - 6823.3\, n + 5520.3 \tag{1.10}$$

Here, $n = \frac{x-x_e}{y-y_e}$, x_e = 0.332, y_e = 0.186, which denotes the coordinates for the epicenters. The higher value of CCT, the better will be the visual acuity with higher brightness perception.

1.8. Present Glass and Phosphor in Glass (PiG) System

In order to strengthen the disadvantages of the organic epoxy resin, two distinct inorganic materials such as oxide glasses and phosphor in glass (PiG) have evolved as practical alternatives. According to the literature reports, heavy metal oxide glasses possess desirable properties for the development of various technologies including, non-linear optical devices, electro-optic switches, electro-optic modulators, solid-state laser materials, and IR technologies. This is due to their high density, refractive index, and low phonon energies. [66-69]. In general, the host glass matrix with relatively low phonon energies can give high quantum efficiency and is therefore useful for the designing of good photonic devices [23-25]. In the present thesis work, we have chosen tellurite-based oxide glasses as they carry low phonon energy (~ 750 cm^{-1}) and high refractive index (1.9-2.4), good dielectric constant, low melting temperature, and high rare earth ions solubility [23, 25]. Researchers are taking an interest in understanding tellurite glasses due to their spectral physical and chemical properties. Also, these glasses receive good attention as they are chemically stable, mechanically strong, and are transparent in the wavelength range from visible to NIR regions [24, 67, 68]. Based on the above-mentioned special characteristics, tellurite glasses are suitable candidates for potential applications including optical fibers, laser windows, IR domes, and modulators [24]. Tellurium oxide (TeO_2) is a conditional glass former, but it is difficult to get a single constituent of TeO_2 glass. The modifier improves the glass formation strength through the breaking chains of the structural units and increases the entropy. The addition of tungsten trioxide (WO_3) to a tellurite-based glass host prevents the formation of steady glass. The inclusion of WO_3 in the TeO_2 glass matrix serves as an excellent modifier that reduces the non-radiative loss and assists in increasing the quantum efficiency [23, 25]. Also, the presence of WO_3 in the TeO_2 glass augments its electrical, thermal and chemical properties to a greater extent. Further, WO_3 keeps electrochromic and photochromic properties and is beneficial in smart windows, display devices and sensors [25]. The presence of zinc oxide (ZnO) in the glass host plays a unique role as it acts as a network former and network modifier as well. In addition, ZnO-based glasses are thermally stable, and covalent in nature. Glasses containing ZnO are of significant interest owing to their low cost, intrinsic emitting properties, and non-toxic nature [23, 25]. Further, the introduction of alkali oxides such as Li_2O, Na_2CO_3 and K_2CO_3 in the tellurite-based glasses helps to decrease the non-radiative losses and enhances the strength of the host glass matrix. Also, alkali oxides eliminate the air bubbles from the molten glass and improve the glass transition temperature [70, 71]. Moreover, the inclusion of heavy metal oxide such as bismuth trioxide (Bi_2O_3) serves as an unconventional network former in the glass host matrix. The existence of conventional glass network forming cations may be produced from a glass-forming network comprising both the octahedral (BiO_6) and Pyramidal (BiO_3) units owing to the bismuth (Bi^{3+}) ion's small field strength and highly polarizability [71, 72]. For the present thesis work, we have considered three host batches based on the tungstate tellurite glasses for analysis (i) $TeO_2 – Li_2O – WO_3 – ZnO – Bi_2O_3$, (ii) $TeO_2 – M_2O – WO_3 – ZnO – Bi_2O_3$ (M = Li, Na and K) and (iii) $TeO_2 – WO_3 – K_2O – ZnO – Bi_2O_3$ glass batches. The first batch and its importance are discussed in *Chapter 3*, the second batch and its importance are covered in *Chapter 4*, and the third batch is addressed in *Chapters 5, 6, and 7*.

A more reasonable and practical solution for inorganic LED color converters has been achieved with phosphor in glass (PiG), as explained in *Chapter 7*. PiG has gained much attention because it has several advantages over single-crystal and transparent ceramics. The advantages are (i) luminescence can be controlled via mixing diverse phosphors and glass host compositions, (ii) simple method of preparation, and (iii) reproducible consistently. Thus, PiG has been deemed as an appropriate luminescence converter for high-power w-LEDs as a result of its robustness, excellent thermal conductivity, minimal thermal expansion coefficient, and high temperature as well as humidity resistance [73]. Consequently, phosphor in glass is expected to be a promising way to replace the organic epoxy resin with glass materials to encapsulate the required phosphor. The phosphor particles in PiGs can be strongly segregated via a thermally conductive glass matrix and the optical characteristics of the added phosphor remain intact even in adverse conditions, such as intense UV light radiation and high temperatures [73, 74]. Furthermore, the luminous characteristics of PiGs might be easily modified by adjusting the fraction of mixed phosphor. Thus, the PiGs can be an appropriate candidate to replace the organic epoxy resin with a glass matrix to encapsulate the essential phosphor.

1.9. Objectives of the Present Work

The research on RE-doped glasses and phosphor in glass for photonic applications has gained enormous attention in recent years because of its tremendous advantages. In the current thesis work, efforts have been made to synthesize rare earth doped tungstate-tellurite glasses and phosphor in tungstate-tellurite glasses with improved luminescent properties and finally to examine them for photonic applications. the short-term specific objectives of the thesis work are:

- To explore the preparation of suitable glasses via the melt quenching technique.
- To analyze the structural, physical, and optical characteristics of the prepared glasses using various characterization techniques.
- Identification of the appropriate activator ions and enhance the luminescent properties using effective sensitizer ions and optimizing the concertation of doping ions.
- To study in detail the optical, luminescent, and colorimetric properties of the optimized glass for advanced lighting applications.
- To extend research work by selecting an appropriate phosphor and incorporating this phosphor in the optimized glasses (i.e., development of PiG).
- Finally, analysis of the spectroscopic properties in detail to disclose the utility of the optimized glass/PiG in advanced lighting devices with enhanced colorimetric properties.

Chapter – 02

Preparation and Characterization Techniques

The development of high-quality amorphous or glassy materials necessitates a deep understanding of experimental methodologies. A detailed description of the melt-quenching process for synthesizing glassy phase materials is described in this chapter. The synthesized glassy materials were assessed for their thermal, physical, structural, optical, and photoluminescent features. The experimental techniques used to determine physical parameters, including densities, refractive index, and concentration of RE ions in these glassy materials were explained. The present chapter also discusses the usefulness of various sophisticated analytical tools, including Thermogravimetric analysis (TGA) – Differential Scanning Calorimetry (DSC), X-ray diffraction (XRD), Fourier Transform Infrared (FT-IR) and Raman spectroscopy, absorption spectroscopy, photoluminescent studies, etc. This chapter explains the fundamental principles and instrumentation used in various characterization techniques.

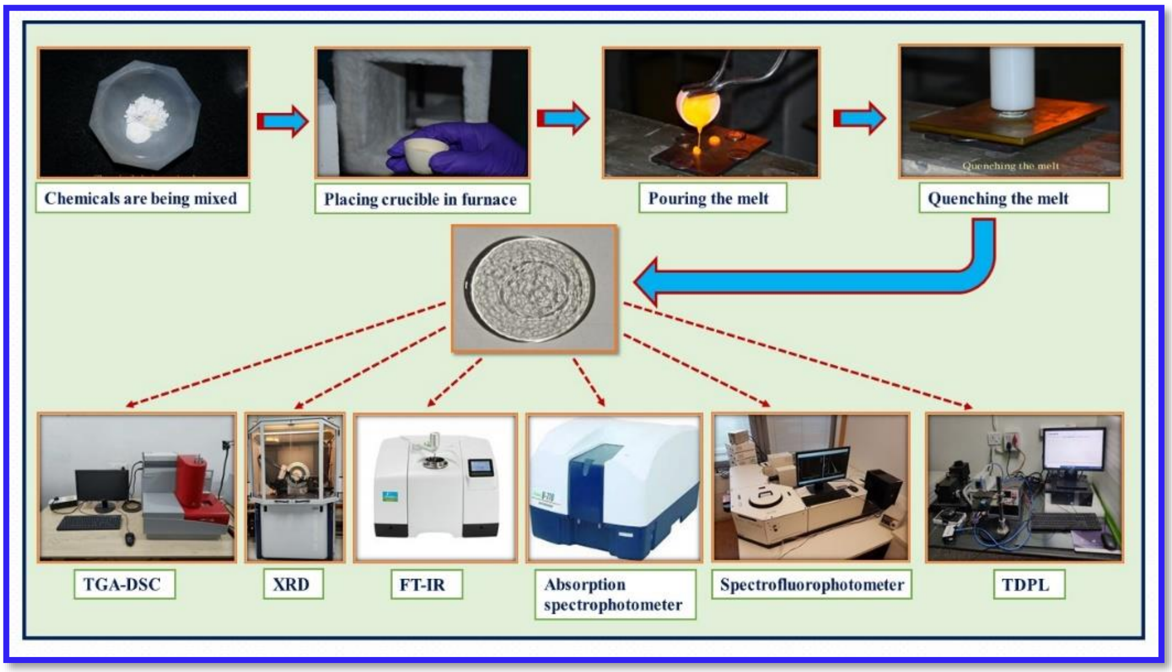

2.1. Glass Preparation

The foremost stage in the experimental study is preparation and the essential characterizations of the amorphous materials. As outlined in *Chapter 1*, there are various synthesis procedures for developing glassy materials. The established procedure is the traditional melt quenching process, in which the molten form is quickly cooled to obtain the amorphous solid materials. One of the distinctive features of the traditional melt quenching procedure for emerging non-crystalline/amorphous materials is that the amorphous solid is produced by the continual hardening (i.e., increase in the viscosity) of the melt. For my thesis research work, this process was utilized to synthesize the different glass host compositions along with various rare-earth ions (REIs) acting as singly/doubly dopants. The different glass host compositions (in mol%) are given below:

- $(50.0 - x)\ TeO_2 - 20.0\ Li_2O - 15.0\ WO_3 - 10.0\ ZnO - 5.0\ Bi_2O_3$ with varying concentration of Dy^{3+} ions as dopant.
- $(50.0 - x)\ TeO_2 - 20.0\ K_2O - 15.0\ WO_3 - 10.0\ ZnO - 5.0\ Bi_2O_3$ with varying concentration of Eu^{3+} ions as dopant.
- $(50.0 - x)\ TeO_2 - 20.0\ WO_3 - 15.0\ K_2O - 10.0\ ZnO - 5.0\ Bi_2O_3$ with varying concentrations of Tb^{3+}, Eu^{3+}, Dy^{3+} and Sm^{3+} ions as singly/doubly dopants as per the requirement.

The starting ingredients used for the synthesis process are tellurium oxide (TeO_2), lithium oxide (Li_2O), potassium oxide (K_2O), tungsten oxide (WO_3), zinc oxide (ZnO), and bismuth (III) oxide (Bi_2O_3), which possess the high purity ($\geq$ 99.0%). The RE ions dysprosium (III) oxide (Dy_2O_3), europium (III) oxide (Eu_2O_3), terbium (III) oxide (Tb_2O_3), and samarium (III) oxide (Sm_2O_3) certain high purity (99.99%). In the melt-quenching process, a precise amount of starting ingredients is weighed according to the stoichiometric ratio and mixed for an hour using an agate mortar. To achieve a homogeneous blend, acetone is used as a wetting medium.

Then, the homogenous mixture was transferred into an alumina crucible and kept inside the temperature-controlled programmable electric muffle furnace at the desired temperature for an hour. The mixture is melted for an hour in the temperature-controlled programmable muffle furnace, to obtain homogenous bubble-free melt. When the melting process is completed, the melt is poured onto a pre-heated brass plate (heated using another temperature-controlled programmable muffle furnace) and air-quenched by another brass metal plate. Furthermore, the quenched glassy materials were annealed at a desired temperature in another muffle furnace to eliminate the thermal and mechanical stress. After that, transparent, bubble-free glassy materials were obtained and used for further characterization. A flow diagram effectively illustrates several phases of the synthesis process, which are summarized in Fig. 2.01.

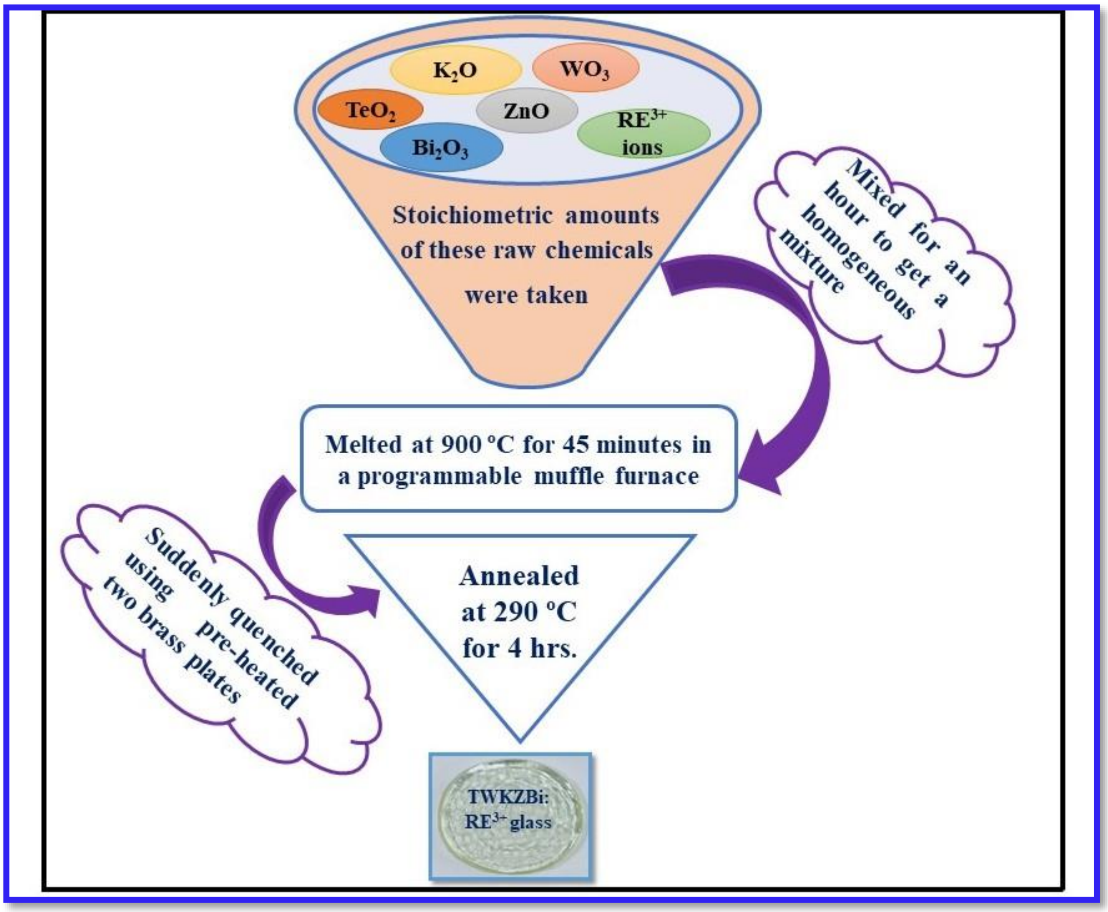

Fig. 2.01: *Schematic flow diagram of the melt quenching process used to prepare the TWKZBi: RE^{3+} glasses.*

2.2. Synthesis of Phosphor Materials

The synthesis of phosphor materials is a crucial step in the process of analyzing materials. Several synthesis procedures, including solid state reaction (SSR), molten salt, co-precipitation, combustion, sol-gel, hydrothermal and solvothermal were used to synthesize phosphor materials [75-77]. To produce various powder materials and phosphors, the SSR method is a simple and widely used technique. [78].

2.2.1. Solid-State Reaction (SSR) Route

One of the standard and common techniques for the synthesis of crystalline ceramic phosphor powder is the SSR route. The SSR route is commonly used in the development of cost-effective and high-volume production of phosphors for industrial purposes [79]. This method involves mixing of high-purity chemicals in a stoichiometric ratio and dissolving them in acetone. To ensure the precursors were crushed homogeneously, the ingredients were then grounded for a long duration. Due to their solid powder form, the ingredients need to be uniformly heated at high temperatures as they don't react at room temperature, even when maintained for hours. After grinding, the samples were placed in an alumina crucible and sintered at high temperatures in a programmable muffle furnace. The resulting phosphor is ground to ensure homogeneous sintering of the samples after allowing them to naturally cool to room temperature.

Eu^{3+} induced $Ca_3Bi(PO_4)_3$ phosphors were successfully synthesized via employing the SSR route. The phosphor was synthesized using highly pure calcium carbonates ($CaCO_3$), bismuth oxide (Bi_2O_3), ammonium dihydrogen phosphate ($NH_4H_2PO_4$) and europium (III) oxide (Eu_2O_3) as precursor materials. The stoichiometric ratio of these ingredient materials were weighted with the help of a digital weighing balance and then kept in an agate mortar for 1 hour of grinding. Acetone is commonly utilized as a dispersing medium in the process of grounding. Lastly, the mixture was placed in an alumina crucible and heated in a programmable electric furnace. The heating profile involved two stages: one at 700 ºC for an hour, followed by another at 1200 ºC for 4 hours in an air medium. After being prepared, the sample was allowed to cool to room temperature and then crushed again for further analysis.

2.3. Fabrication of Phosphor in Glass (PiG) Samples

The PiG samples have been synthesized using the two-step process. In the first step, precursor TWKZBi glass was obtained through the melt quenching method, as discussed *in section 2.1.* The obtained precursor glass frit has been crushed into fine powder. The second step is to introduce the synthesized Eu^{3+} induced $Ca_3Bi(PO_4)_3$ (CBP: Eu^{3+}) phosphor into the prepared precursor frit glass at a low sintering temperature. The CBP: Eu^{3+} phosphor was successfully synthesized using the SSR route as discussed *in section 2.2.1.* To be specific, CBP: Eu^{3+} phosphor and precursor TWKZBi glass have been mixed together with different concentrations of phosphor, respectively. Approximately 10 gm of the homogenous mixture was placed in an alumina crucible and kept in the temperature-controlled programmable electric furnace at 900 ºC for 30 minutes. The resulting melt was poured onto the pre-heated brass plate and thermally treated following the same parameters used in the preparation of the TWKZBi glass host matrix, as described *in section 2.1.*

2.4. Characterization Techniques

The effective usage of synthesized glassy materials in optoelectronic devices requires an understanding of several parameters that can be characterized using relevant characterization tools. The glassy materials were analyzed by employing the standard equipments to determine their thermal, structural, optical, and luminescent features. The following sections focused in detail the experimental techniques used to characterize the prepared glassy materials.

2.4.1. Thermal Analysis

The thermal characteristics of the raw material can be characterized using thermogravimetric analysis (TGA) and differential scanning calorimetry (DSC). The word “differential” designates the distinction in the behavior between the material being studied and an inserted reference material. In this way, the temperature where either heat is absorbed or released can be found. In this way, the temperature at which any event absorbs or releases heat may be determined. The thermal analysis provides insight into certain properties such as weight changes, enthalpy thermal capacity, phase transition, crystallization, melting and thermal stability. Nevertheless, in this thesis work, thermogravimetric analysis and differential scanning calorimetry (TGA-DSC) were used to determine the phase transition, crystallization and melting temperatures of the raw material.

TG Analysis: In TG analysis, the weight or mass loss of the raw material is continually tracked as a progressive increase in the temperature or time in a controlled environment. A thermal decomposition or thermogram curve is a graph that shows the weight percentage as a function of temperature or time. The following diagram displays information regarding oxidation, decomposition, desorption, and vaporization. The weight change in the TG analysis curve reflects the desorption or absorption of gases from the material under investigation. An augmentation in the mass signifies the process of absorption, while a reduction in the mass suggests desorption. Conversely, a minimal alternation in mass indicates the stability of the material.

Differential Scanning Calorimetry: DSC is a technique that measures the difference in the energy inputs between a material and a reference substance when the temperature changes. This measurement is accomplished via subjecting both the material and reference substance to a controlled temperature profile. The fundamental distinction between DTA and DSC lies in the fact that DSC is a calorimetric technique that quantifies the energy difference, while DTA records temperature variations. DSC is a technique used to quantify the heat absorbed or released during a physical or chemical change in the substance. DSC assists in the determination of endothermic and exothermic events in the sample, as well as the temperature variation. The crucial characteristic is the presence of two thermocouples linked to a voltmeter. One thermocouple is positioned inside an inserted material, such as Al_2O_3, and the other is positioned within the sample being investigated. As the temperature is increased, deflection in the voltmeter is observed, if the sample is undergoing a phase transition. The operating temperatures typically range from ambient temperature to around 1650 ºC. The current thesis investigates the thermal stability of glassy material utilizing the Sitaram EVO TGA-DSC instrument as represented in Fig. 2.02.

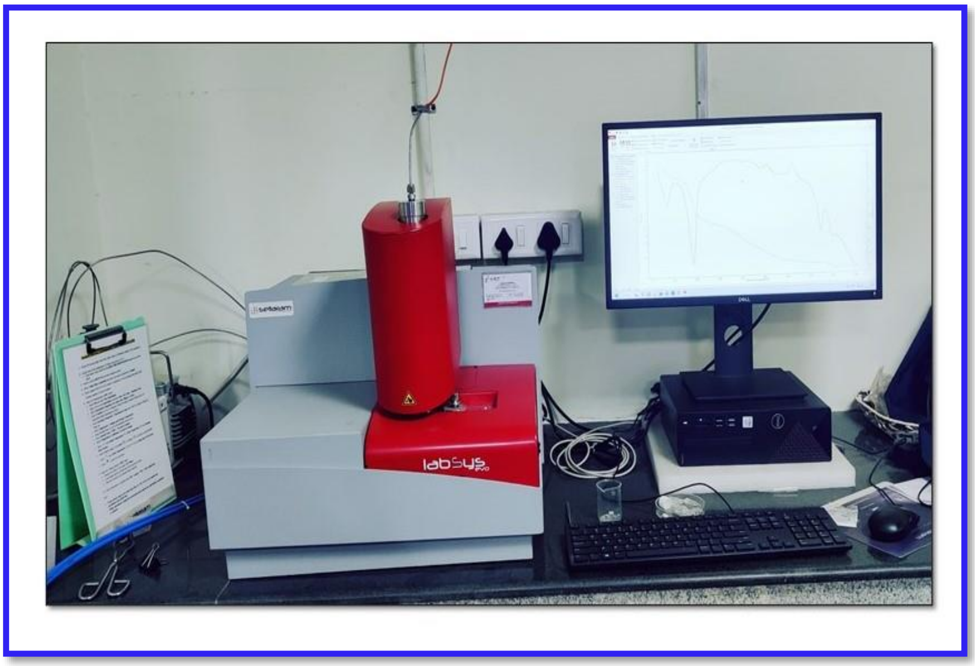

Fig. 2.02: *TGA-DSC instrument*

2.4.2. X-ray Diffraction (XRD)

XRD is the primary and most important non-destructive technique used to analyze the structural and phase characteristics of all the prepared crystalline or non-crystalline materials.

X-rays are a kind of electromagnetic (EM) radiation with very short wavelengths, typically ranging from a few angstroms to 0.1 angstroms. This implies that the energies typically lie in the range of 100 eV – 100 keV. The X-ray wavelength is equivalent to the size of the atoms, which makes it suitable to study the structural arrangement of atoms in materials. In crystalline materials, the periodic arrangement of atoms in the three-dimensional array that constitutes the crystal plane is referred to as lattices. A unit cell is the smallest constituent of the crystal structure. The translational vectors a, b, and c determine the atomic positions in a lattice, which also represent the length of the edges. The angles α, β, and γ refer to the measurements between these vectors. Crystalline solids may be categorized into 07 crystal systems, which are further sub-categorized into 14 Bravais lattices. Each crystalline substance has a unique diffraction profile and the XRD data accurately represents the lattice structure of an unknown substance, making it useful for identifying its phase. The X-ray diffraction method was invented in 1912 by Von Laue. In this experiment, a crystal made of CuS was subjected to a stream of X-rays, and the resulting patterns were captured on photographic plates. Mr. W. L. Bragg and his son elucidated the fundamental principle governing the rule of the diffraction pattern and successfully determined the initial crystal structure [80]. This technique is most effective for crystalline or partially crystalline substances; however, it is sometimes used to investigate non-crystalline substances.

Bragg's Law: A crystal is a solid structure consisting of atoms, ions, or molecules that are organized in regular patterns over three dimensions. When X-rays of a certain wavelength are incident on a crystal at specific angles, they get reflected from the surface of a crystal and the plane of atoms inside the crystal [81]. A group of atoms organized on a series of parallel planes with a distance of separation d, as shown in Fig. 2.03. Now, let us consider a beam of completely parallel monochromatic X-rays with a certain wavelength (λ) that is directed towards the crystal at an angle of (θ). The disparity in the length of paths traveled by wave 1 and wave 2 is

$$BC + CD = dSin\theta + dSin\theta \quad (2.1)$$

$$= 2dSin\theta \quad (2.2)$$

The scattered waves 1 and 2 will be in phase if the path difference is equal to the multiple of the whole number and wavelength of the x-ray. The condition for a diffraction to occur constructively is [82]:

$$n\lambda = 2dSin\theta \quad (2.3)$$

This relation is known as Bragg's law, after W.L. Bragg and it is one of the most important laws used for interpreting X-ray diffraction data.

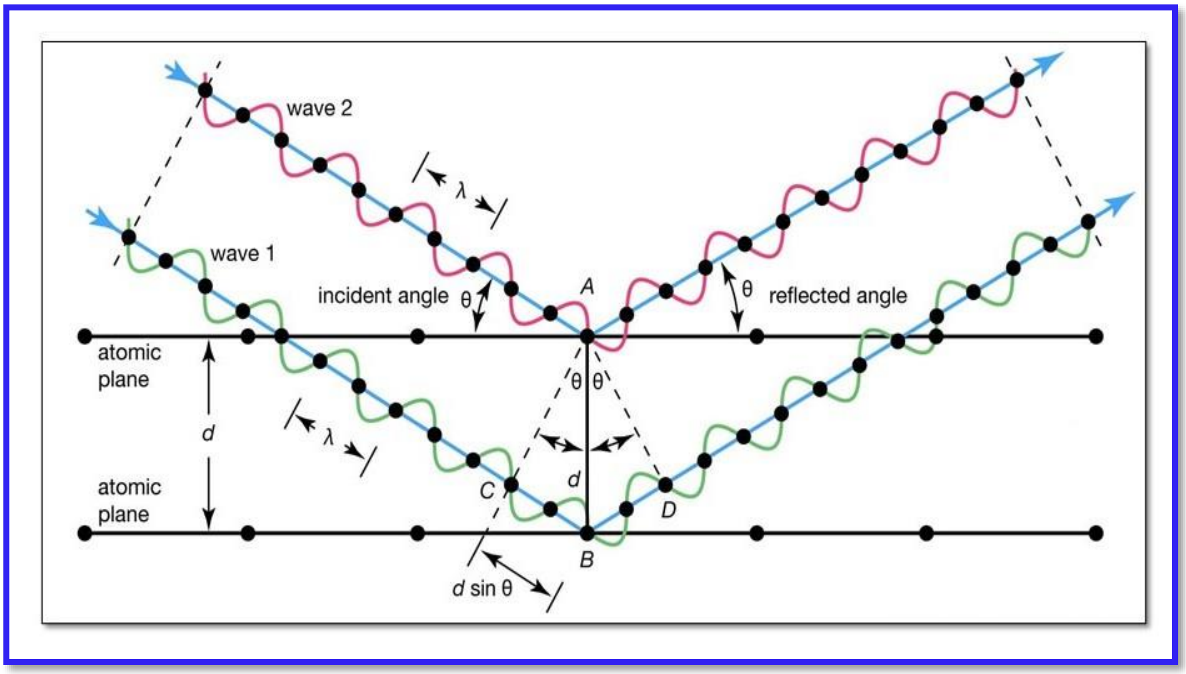

Fig. 2.03: *Schematic representation of Bragg's law.*

Calculation for Crystallite Size: The X-ray diffraction pattern is a plot between diffraction intensities and a scale of 2θ. The intensity and the position of diffracted peaks have several pieces of information associated with the crystal structure. The peak position indicates the different phases present in the material and its lattice structure.

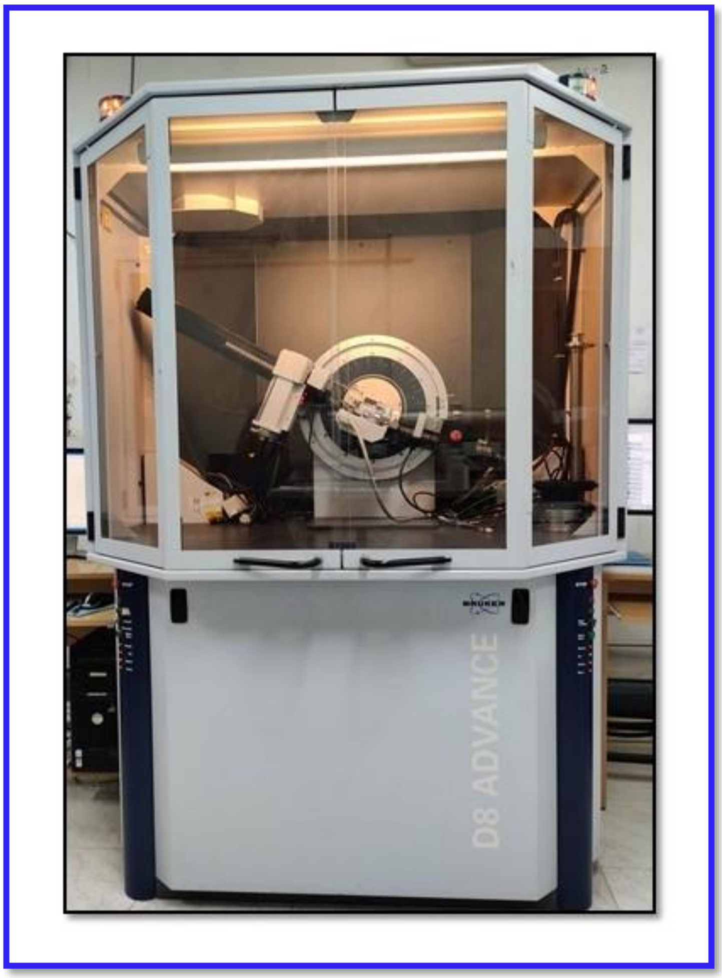

Fig. 2.04: *Bruker D8 advanced X-ray diffractometer setup.*

If there is any deviation from the ideal structure, the broadening of the diffraction peak or shift in the peak positions is observed. In 1918, P. Scherrer for the first time observed that the crystallite size less than 200 nm gives rise to peak broadening and gave a formula for relating the crystallite size to the peak width, known as Scherrer's formula [83]:

$$D = \frac{k\lambda}{\beta Cos\theta} \tag{2.4}$$

In the above formula, the mean crystallite size is denoted by *D*, the wavelength of the X-ray is represented by λ, *k* signifies the dimensionless shape factor and takes a typical value of 0.9, but the value varies with the actual shape of the crystallite, the line broadening at full-width half maximum (FWHM) is represented by β and the Bragg angle is denoted by θ, respectively. The Scherrer's formula is utilized to ascertain the crystallite size of the material. In the present work, Bruker D8 advanced x-ray diffractometer was used and is illustrated in Fig. 2.04.

2.4.3. Fourier Transform Infrared (FT-IR) Spectroscopy

Infrared (IR) spectroscopy is an extremely important non-destructive technique for the determination of various existing functional groups in crystalline or non-crystalline materials.

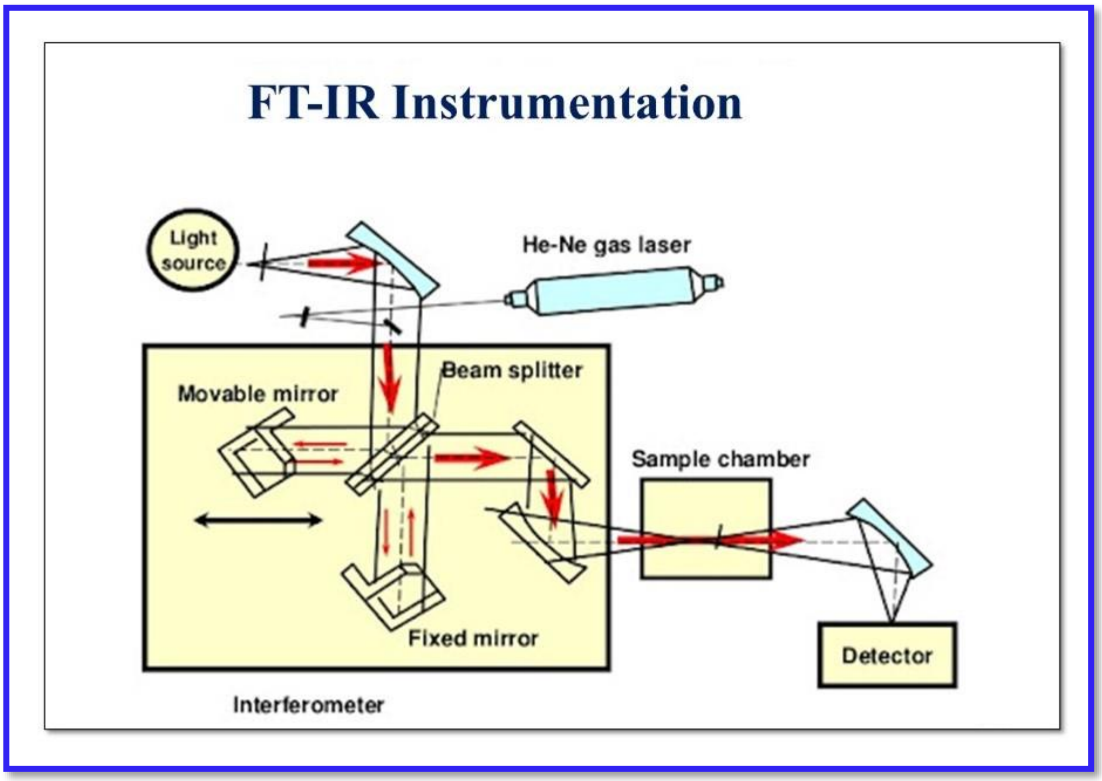

Fig. 2.05: *Schematic working diagram of FT-IR setup.*

In all substances, the molecular total energy is the summation of vibrational, electronic, and rotational energy levels. FT-IR spectroscopy deals with the interaction of infrared (IR) radiation (400–4000 cm^{-1}) with the molecules of the sample. The cm^{-1} unit is the wavenumber scale and is given by $1/\lambda_{cm}$. In general, there are two kinds of molecular vibration present; stretching and bending. The distance between two successive atoms varies during stretching, but the angle between them remains constant. However, in bending the position of the atom changes with respect to the bond axis. The amplitude of the vibration of a specific frequency increase in proportion to the amount of IR radiation that strikes the molecule. The amplitude of the vibration of a certain frequency has gone up correspondingly. As a result, IR spectroscopy provides a method for identifying the functional groups, including OH, C=O, NH_2, and NO_2 present them with the molecules [84]. FT-IR tool is commonly based on the Michelson Interferometer method. Fig. 2.05 shows a schematic diagram of the FT-IR instrument's working principle.

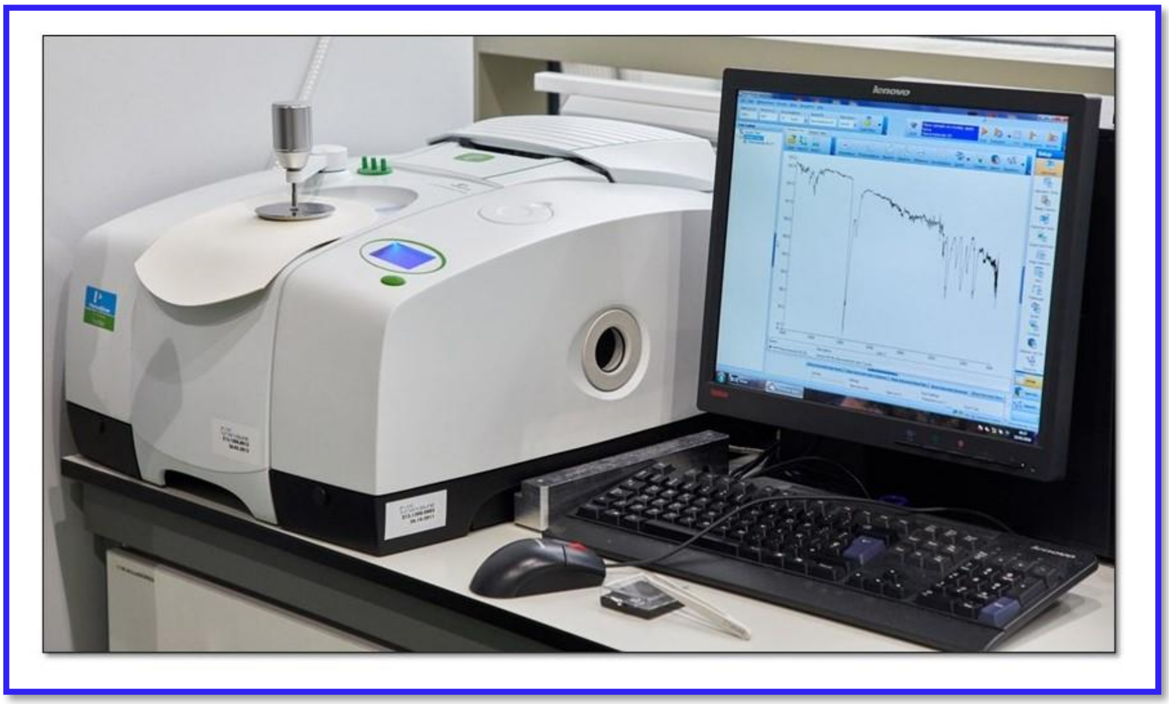

Fig. 2.06: *Frontier Perkin Elmer's FT-IR spectrometer setup.*

The interferometer method comprises two mirrors, which are placed at right angles to each other via a beam splitter. One of the mirrors moves a certain distance while the other remains constant, and the output beam is formed as a result of the interference of the reflected beams from both mirrors. When the beam passes through the sample/substance, it produces an interference pattern, which is then used to obtain the IR spectrum of the material using the

Fourier transform method. The FT-IR measurement was taken using Frontier Perkin Elmer's FT-IR spectrometer. The pellet has been made via combining TWKZBi glass matrix powder with KBr and compressing it mechanically at 1.5 tons. Fig. 2.06 illustrates the FT-IR spectrometer used for measurement.

2.4.4. Raman Spectroscopy

Raman spectroscopy is a highly effective method for characterizing materials, offering fast non-destructive analysis that can be applied in both the laboratory and mass production scales. It gives the structural information based on a molecule system vibration and rotational modes as well as electronic information.

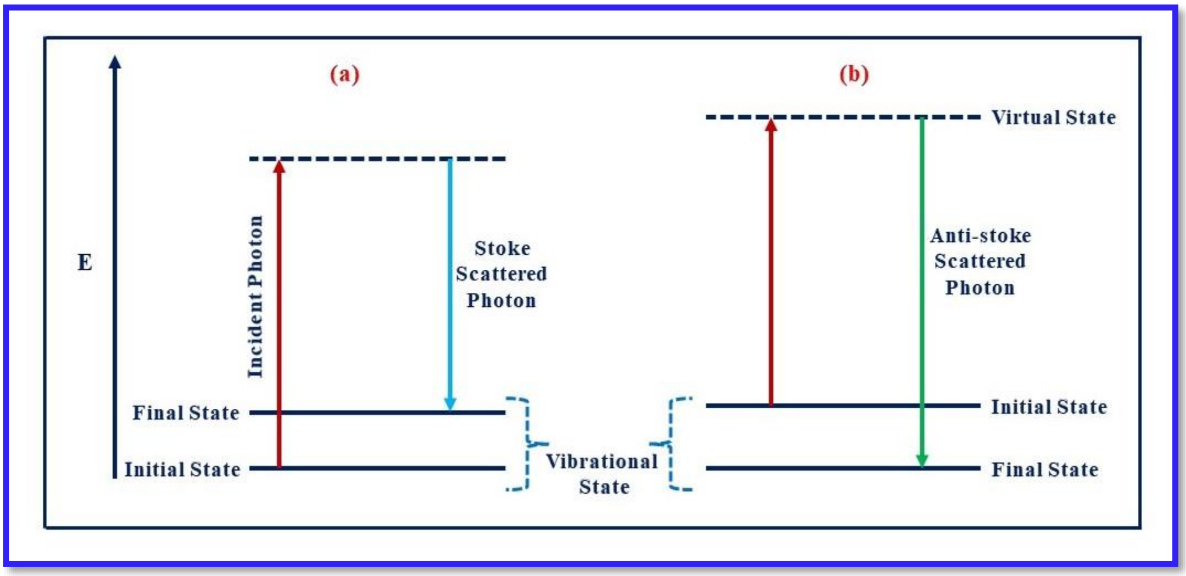

Fig. 2.07: *Schematic energy level diagram of Raman scattering* ***(a)*** *Stokes and* ***(b)*** *Anti-stokes scattering.*

The scattering of light from a molecule or crystal is either inelastic or elastic. Elastic scattering is when the scattered photon has the same energy or frequency as that of the incident photon, while in the case of inelastic scattering the scattered and the incident photon has different frequency or energy. The inelastic scattering process is called the Raman effect, while the elastic scattering is termed as Rayleigh scattering. The Raman effect was first discovered in

1928 by famous physicist C. V. Raman [85]. If the sample is being illuminated by a coherent monochromatic light source for example: a laser. The scattered light spectrum gives a string line termed as an exciting line of the same incident frequency and some weak lines are also generated on either side of the exciting line. If the frequency is less than the frequency of the exciting line it is designated as the stoke line as labeled in Fig. 2.07 (a). Whereas if the exciting line frequency is greater, then it is called an anti-stokes line as illustrated in Fig. 2.07 (b). The difference in energy among the incident and scattered photons is referred as the Raman shift in wavenumber (cm^{-1}).

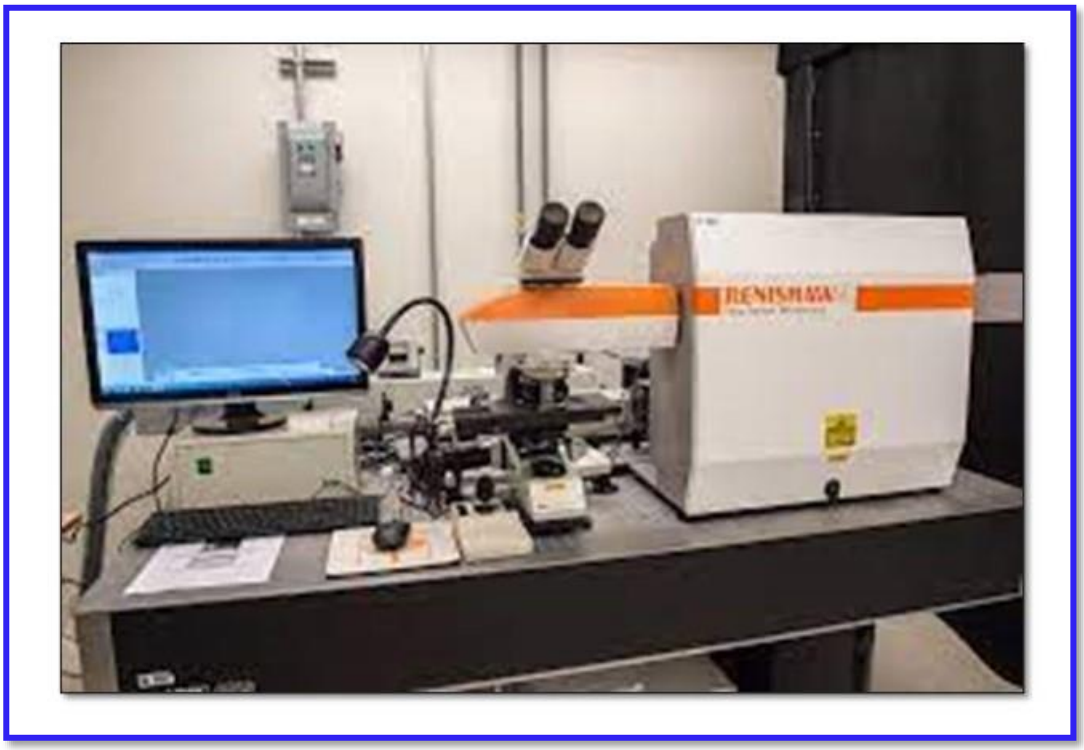

Fig. 2.08: *Renishaw micro-Raman spectrometer setup.*

Sometimes a few molecules are already in vibrationally excited states. The Raman scattering from vibrational states leaves the photon in its ground state. The scattered photon will possess more energy than the excited photon. In the present study, Renishaw 1000 B micro-Raman spectrometer is as shown in Fig. 2.08 with Argon ion laser having 448 nm wavelength was used for the glass sample characterization.

2.4.5. Optical Absorption Spectroscopy

When a light or beam of electromagnetic radiation strikes a material/object, three separate phenomena occur transmission, absorption, and scattering of the radiations. In absorption spectroscopy, a source of light stimulates the sample, and the transmitted light is collected at the opposite end of the sample. The light passing through a material/sample of finite thickness includes information about the material/sample since it becomes modified after the interaction with the material/sample. UV-VIS-NIR spectroscopy serves as a widely accessible non-destructive method for determining the optical characteristics of diverse inorganic and organic substances. Consider, I_0 as the incident light intensity; I is the transmitted light intensity. The transmittance, T can be expressed as $T = \frac{I}{I_0}$. When a monochromatic beam passes across a homogeneous sample, the intensity of the transmitted light is dependent on the thickness of the sample. From the transmittance spectra, the value of the absorbance (A) can be calculated with the help of the following equation [86]:

$$A = log_{10}\left(\frac{I}{I_0}\right) = log_{10}\left(\frac{1}{T}\right) \tag{2.5}$$

in the present study, the absorption coefficient $\alpha(h\vartheta)$ was determined from the absorption data using the relation given below [86]:

$$\alpha(h\vartheta) = \frac{1}{d} ln\left(\frac{I_0}{I_t}\right) \tag{2.6}$$

where the absorption coefficient is denoted by $\alpha(\vartheta)$, the thickness of the glass sample is represented by d and the intensities of the incident and transmitted radiation are signified by I_0 and I_t, respectively. The parameter $ln\left(\frac{I_0}{I_t}\right)$ represents the absorbance. In most non-crystalline materials, the fundamental absorption edge follows the Urbach rule, which describes the extent of the exponential tail. The absorption edges of a non-crystalline material can be associated with the inter-band transitions concerning the tails of the localized states where the density of states decreases dramatically [87]. The Urbach empirical equation can be expressed as:

$$\alpha(\vartheta) = Cexp\left(\frac{h\vartheta}{\Delta E}\right) \tag{2.7}$$

where the parameter C denotes the arbitrary constant, the Urbach energy (ΔE) represents the extent of the band tails of the localized state. Urbach energy can be determined via drawing a graph among $ln\big(\alpha(\vartheta)\big)$ and $h\vartheta$ and evaluating the inverse of the slope attained.

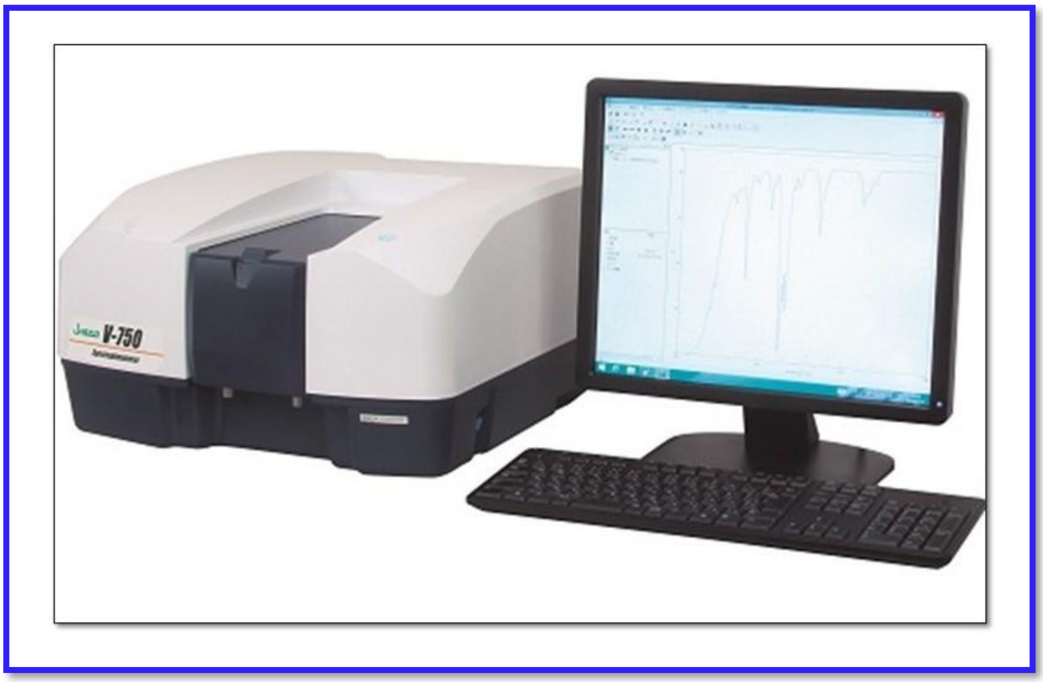

Fig. 2.09: *JASCO V750 UV-VIS-NIR spectrophotometer setup.*

In the present thesis, the optical absorption studies were performed at ambient temperature via applying a JASCO V750 UV-VIS-NIR spectrophotometer with a spectral resolution of 0.1 nm, as shown in Fig. 2.09. The instrument has a deuterium lamp for UV and a tungsten light for the visible to infrared. The wide source signal is dispersed into individual wavelengths using monochromators. To prevent the overlapping of various orders of diffraction lines, optical filters are used. The essential function of this instrument is based on a double-beam technique in which one beam passes through the sample.

2.4.6. Photoluminescence (PL) Spectroscopy

Any light-sensitive substances including, liquid, glass, powder, or thin film samples can have their photoexcitation and emission measured utilizing the non-destructive, versatile, and contact-free PL spectroscopy method.

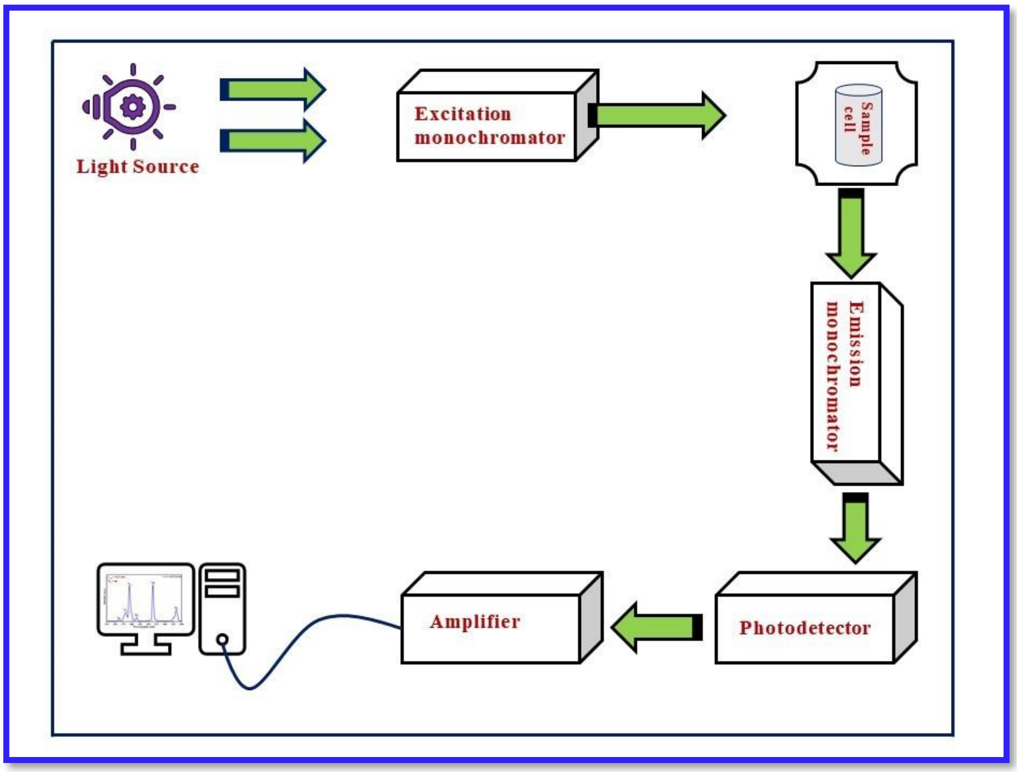

Fig. 2.10: *Schematic representation of the PL spectrofluorophotometer.*

PL investigations were recognized as one of the most sensitive and commonly used methods for examining the optical properties of the materials including, luminescence of impurities, band structures, absorption, and point defects with high accuracy. The sample is typically exposed to a range of light beams, some of which are absorbed, excited by the sample ions, and de-excited by emancipating radiative emission, ideally in the region of visible light as well as certain non-radiative relaxations [88, 89]. PL spectroscopy is an effective tool for investigating carrier ions transition and radiative/non-radiative recombination in light-influenced materials. PL spectroscopy can offer applicability in the fields of molecular electronics, environmental science, medical diagnostics, industries, day-to-day life devices and cell biology. The spectrofluorophotometer includes various components such as an excitation light source, monochromator, sample cell, lenses, photodetector, amplifiers and a computer for operating and recording the experimental spectrum, as depicted in Fig. 2.10. The excitation source used should provide a continuous spectrum in the specified wavelength range. Xenon (Xe) lamps can provide a moderately continuous light output and are used as a light source, which emits light in the 220 to 800 nm range. The emitted light beam is passing through the monochromator. The most widespread kind of monochromator uses a diffraction grating. A monochromator employs diffraction grating, which means that the collimated light illuminates a grating and leaves with a diffraction angle determined by the wavelength. The monochromator can be adjusted to transmit certain wavelengths. The excitation monochromator is to select the particular wavelength of light from the incident beam. A minimal amount of incoming light is absorbed by the sample and it subsequently radiates light in every possible direction. The light is emitted at a 90 ^{0} angle, with some passing of light via a monochromator to reach the detector. The emitted light is sensed by the PMT tube as a detector. The detector can be a single-channel (senses only one wavelength at a time) or multichannel (detects all emitted wavelengths). All the components were handled and commanded with the help of dedicated software in a computer system. Furthermore, the observed spectrum was amplified with the PMT tube, translated into signal form, and recorded by the computer for future examination. The computer screen illustrates the captured spectrum of intensity as a function of the wavelength of the emitted light. PL refers to the physical phenomenon in which light is emitted from a substance when it is excited by multiple wavelengths of light sources. The PL characteristics were recorded by a Shimadzu (Model: RF-5301 PC) spectrofluorophotometer equipped with a 150-watt Xe lamp used as an excitation source, as illustrated in Fig. 2.11. To record the PL characteristics, initially sample holder was filled with prepared samples (crystalline or non-crystalline), and placed at the appropriate position in the path of the incident source of the excitation beam.

Fig. 2.11: *Shimadzu (Model: RF-5301 PC) spectrofluorophotometer setup.*

The excitation and emission spectra were obtained by choosing the suitable excitation/emission wavelength, scanning at a medium scan rate, using a 0.1 nm slit width and a high voltage PMT system. The excitation profile can be established by scanning at a certain range of wavelengths while keeping track of specific and fixed emission wavelengths. The bands observed in the excitation spectrum will also be used to record the emission spectral profiles. Lastly, the software exhibits the spectrum with a plot of the wavelengths and the intensity of emitted light.

2.4.7. Time-Resolved PL (TRPL) Spectroscopy

TRPL is a commonly used tool for investigating the slow/fast electrical deactivation processes involved in the emission of photons from certain energy levels in the luminescent materials under particular excitation. This process is commonly referred to as PL decay time or lifespan. The PL decay time is an intrinsic characteristic of a luminescent material, offering valuable insights into the dynamics of its excited state. The PL decay time of luminescent materials can be affected by various factors, including the molecular environment. These factors may include the presence of dopant ions, solvent temperature, quenchers, and interactions with other molecules. Therefore, the disparities in PL decay time can provide insights into the specific surroundings of the materials.

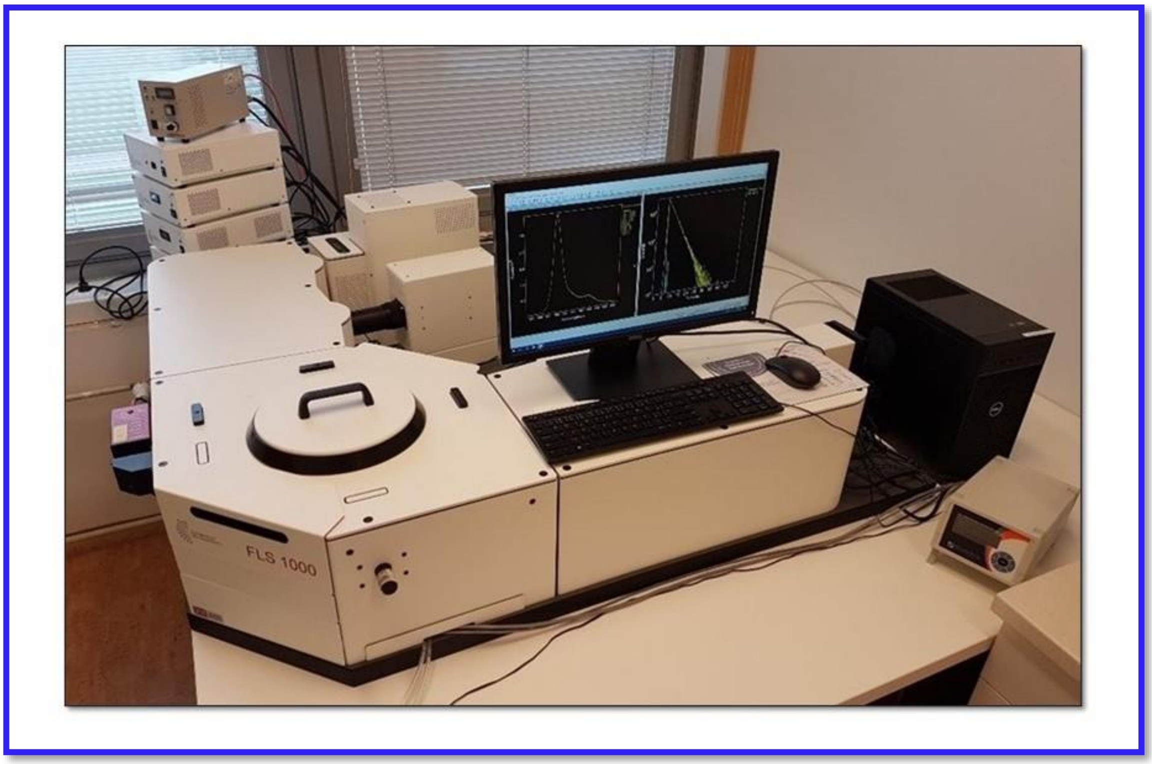

Fig. 2.12: *Edinburgh FLSP 920 spectrofluorophotometer setup.*

The significant components of TRPL are an excitation and emission monochromator, the pulsed light source (Xe flash lamp or pulsed laser), single-photon sensitive detector, controlled by a computer running specific software. A fast photodetector can be utilized to record the emission of a sample over time while it is being excited by a particular pulse light source. This approach can be employed to track material quality, identify spectrum emissions with distinct emissive states, and explore how energy is transferred from one component to another in mixed composites and samples. The observed PL decay time is an intrinsic feature of PL characteristics that can provide insight into excited state dynamics [90, 91]. The PL decay time profiles have been recorded at an ambient temperature using Edinburgh FLSP 920 spectrophotometer, as shown in Fig. 2.12. The apparatus was equipped with a microsecond Xe flash lamp source and a single photon count photomultiplier tube detector. The PL decay time profiles have been fitted using differential exponential functions.

The PL decay profiles were fitted using single or bi-exponentially with the following equation, as shown below [92, 93]:

$$I(t) = I_0 + A_1 exp\left(-\frac{t}{\tau_1}\right) \tag{2.8}$$

and

$$I(t) = I_0 + A_1 exp\left(-\frac{t}{\tau_1}\right) + A_2 exp\left(-\frac{t}{\tau_2}\right) \tag{2.9}$$

where the PL intensities at a certain time 0 and t are represented by I_0 and $I(t)$, respectively. The fitting constant parameters are denoted by A_1 and A_2. The slow and fast decay times for exponential mechanisms are signified by τ_2 and τ_2. The average value of the PL decay time for the samples was calculated from the given formula [94]:

$$\tau_{Avg} = \frac{A_1\tau_1^2 + A_2\tau_2^2}{A_1\tau_1 + A_2\tau_2} \tag{2.10}$$

The PL decay time for the RE ions doped luminescent (crystalline or non-crystalline) materials usually ranges from a few microseconds to milliseconds.

2.4.8. Temperature Dependent PL (TDPL) Spectroscopy

TDPL appears to be a highly effective, fundamental, and influential optical properties investigation tool, extensively utilized to investigate localized state, thermal stability, and carrier transport in semiconductor or luminescent substances.

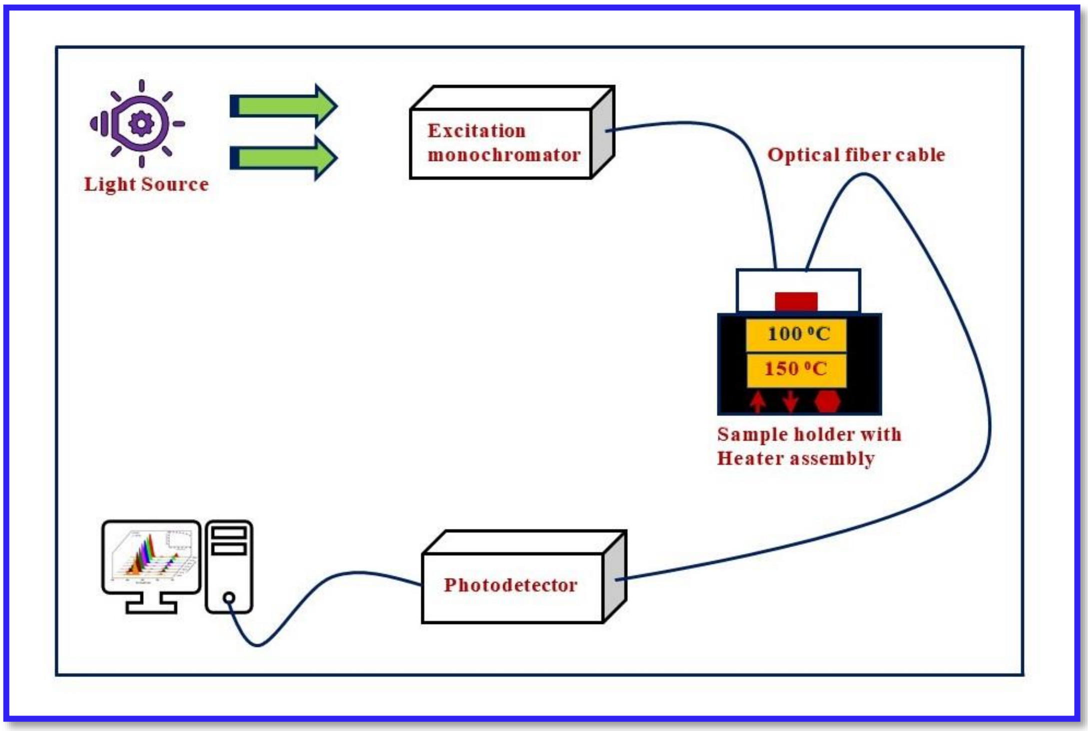

Fig. 2.13: *Schematic representation of the TDPL spectrofluorophotometer.*

In TDPL spectroscopy, PL spectra of the synthesized luminescent substances were measured at various temperatures and find out the change in PL characteristics with rise or fall in temperature. Based on the PL spectra recorded at various temperatures, a methodological framework has been developed to investigate the thermal stability, defect associated with the non-radiative transitions, and carrier transport dynamics. The fundamental parts of a TDPL spectrofluorophotometer are the light source (Xe lamp or laser), temperature-controlled sample holder, monochromator, photodetector, and computers along with specific software as depicted in Fig. 2.13. The Xe lamp is utilized as a light source, which emits light in the 200 to 800 nm range. The emitted beam of light passes through the monochromator, which can choose the required wavelength of light used for excitation. The selected wavelength incident on the temperature-controlled sample holder via optical fiber. A luminescent sample emits light under a particular excitation wavelength, which can be passed through another optical fiber and detected by the photodetector. Finally, the detected spectrum was recorded by the computer for further processing.

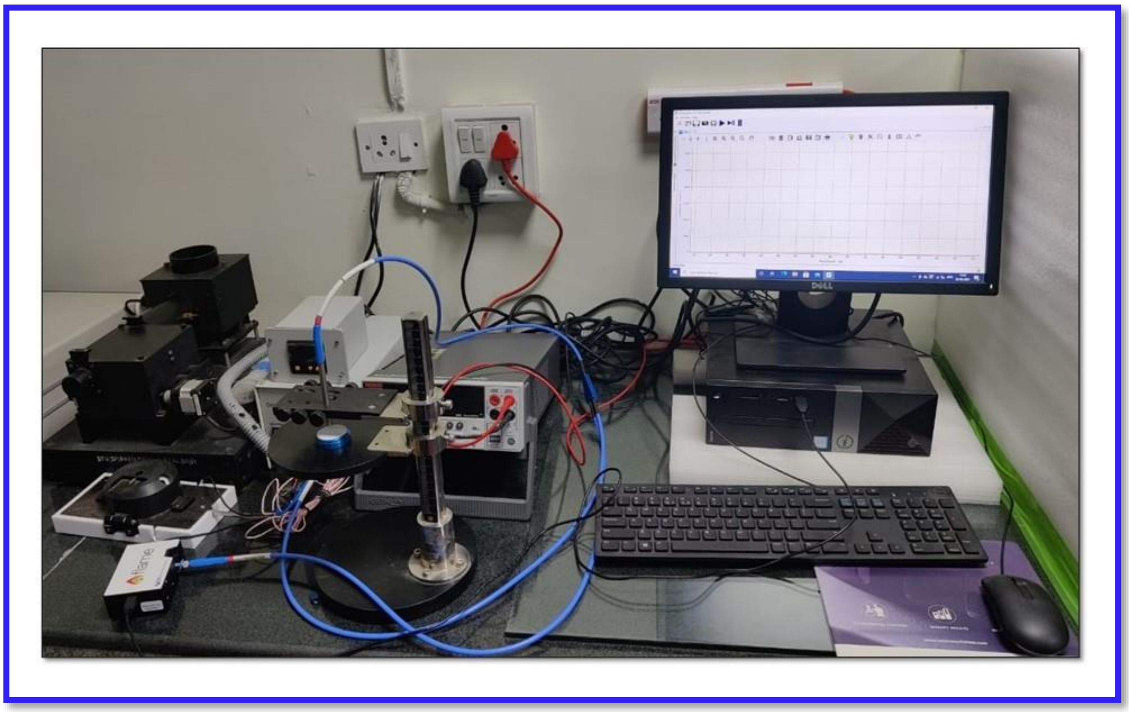

Fig. 2.14: *Ocean optics (Model: FLAME-S-XR1-ES) TDPL spectrofluorophotometer setup.*

In the present thesis, the TDPL features of the prepared samples (crystalline or non-crystalline) are captured using the Ocean Optics (Model: FLAME-S-XR1-ES) spectrofluorophotometer as illustrated in Fig. 2.14. In TDPL data, the emission intensity of the luminescent materials under certain sources of excitation wavelengths can be increased/decreased with higher temperatures. The influence of temperature on the PL characteristics of luminescent materials has become an important aspect of the applicability of phosphor in various photonic applications. The lighting device requires excellent thermal stability of the non-crystalline or crystalline substances to withstand at high temperatures of 120 to 150 ^{0}C, generated by n-UV/blue LED chips during operating times.

Based on TDPL spectral profiles measured at higher temperatures, a systematic framework for investigating the thermal stability of the luminescent materials has been developed. The activation energy (ΔE) has become a significant characteristic for the phosphor to determine the thermal stability of the luminescent materials. It has been calculated using the Arrhenius equation as shown below [95]:

$$I_T = \frac{I_0}{1+Cexp\left(-\frac{\Delta E}{K_B T}\right)} \tag{2.11}$$

Here, I_0 and I_T represents the PL intensity at initial and specific temperature T(K), respectively. An arbitrary constant and Boltzmann constant are signified by C and K_B, respectively. The activation energy (ΔE) has been computed with the help of the Arrhenius equation, based on the straight-line fitted slope between ln $\left[\left(\frac{I_0}{I_T}\right) - 1\right]$ and $\frac{1}{K_B T}$ [96, 97].

Chapter – 03

Spectroscopic Investigations of Dy^{3+} Doped Tungstate-Tellurite Glasses for Solid State Lighting Applications

A series of Dy^{3+}-activated lithium tungstate-tellurite (TLWZBiDy) glasses have been synthesized employing the conventional melt quenching procedure. The structural and luminescent features of TLWZBi glasses were examined in detail to reveal their feasibility in solid-state lighting (SSL) applications. Various physical parameters such as density, molar volume, and other parameters were evaluated. A broad hump showed in the X-ray diffraction (XRD) profile affirms the non-crystalline or amorphous behavior of the as-prepared TLWZBi glasses. The absorption spectrum exhibits several bands between the 400 and 1800 nm range, which confirms that the transitions initiate from the lowest energy state ($^6H_{15/2}$) to numerous excited states. Photoluminescence (PL) spectra reveal three significant peaks centered at 481 nm (blue), 575 nm (yellow), and 664 nm (red) related to Dy^{3+} ions under 388 nm excitation. The chromaticity coordinates of TLWZBiDy glasses were situated in the white light region and nearest to the standard white light (0.33, 0.33). The decay profile shows the bi-exponential behavior of the prepared TLWZBiDy$_x$ (x = 0.1, 1.0, and 2.0 mol%) glasses. Temperature-dependent PL spectra show appreciable thermal constancy of the prepared TLWZBiDy glasses having a high value of activation energy. The above results indicate that Dy^{3+} doped tungstate-tellurite glasses are potential luminescent materials to utilize in SSL applications, especially for white LEDs.

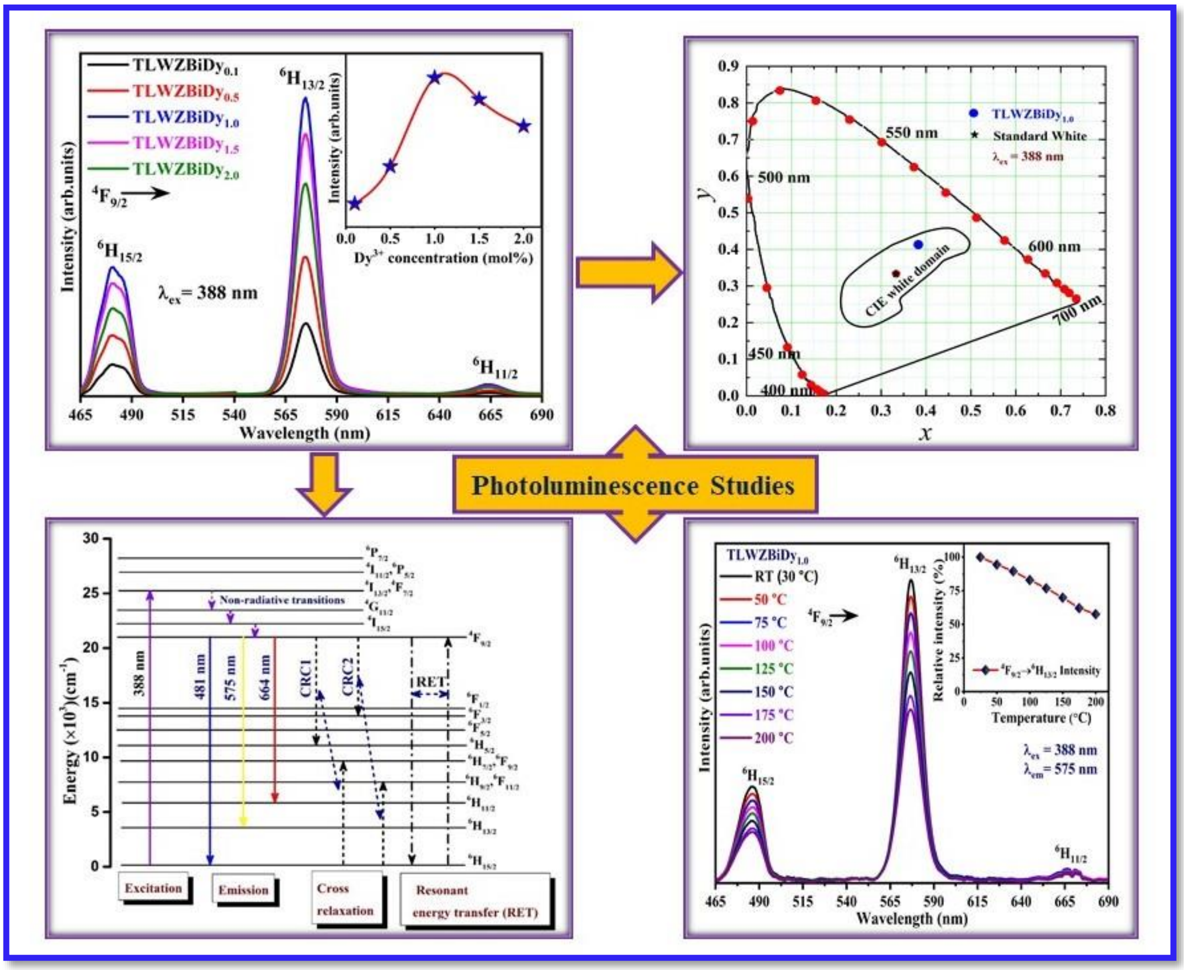

Part of this work has been published in: International Journal of Applied Glass Science 13 (2022) 645-654 (I.F.: 2.10)

3.1. Introduction

In recent times, searching for modern technologies has escalated to accomplish the demands in the areas of illumination and display devices due to the growing global consciousness of eco-friendly practices, the energy conversation, and sustainable evolution [98-100]. Solid state lighting (SSL) has become a vital and practicable alternative to traditional applications in the illumination industry. The SSL techniques can save a huge amount of electricity and diminish carbon emissions worldwide by some ten thousand metric tonnes yearly [4, 16, 12, 18, 101]. There are three distinct methods to produce white light based on SSL devices: (1) by combining the light of distinct primary colors (red, green, and blue) emitted by an individual chip known as multi-chip LEDs, (2) by using a near-ultraviolet (n-UV) LED chip to stimulate blue, green and red-emitting phosphors and (3) by combining the blue-emitting (InGaN) LED chip coated with yellow-emitting phosphor. The last two methods required phosphor, which can convert the near-ultraviolet/blue radiation into visible light. These phosphors coated white light-emitting diodes (w-LEDs) require epoxy resins, which are made up of organic material and deteriorate at high temperatures due to less thermal stability. The phosphor in w-LEDs can be replaced with luminescent glasses that have high thermal stability and lack of epoxy resins. [14, 102]. Luminescent glasses have many beneficial properties like low production cost, good transparency, simple manufacturing procedures, and better thermal stability. Also, the glasses can perform the role of an encapsulant as well as a wavelength converter, which provides an organic-free lighting assembly and prevents light scattering losses that occur due to the enormous difference in refractive index between organic resin and phosphor [103, 104]. Hence, luminescent glasses are the potential choice for SSL applications and are also useful for photovoltaics, solid-state lasers, color displays, optical amplifiers, etc. [103, 105, 106].

In the past few years, several scientists and researchers focused on the development of RE^{3+} doped glasses based on various glass-forming oxides such as borates, germanates, silicates, tellurites, phosphates, etc through the optical absorption and luminescent characteristics to explore their suitability for solid-state lighting applications [14, 102-106]. Tellurite based glass has attracted abundant attention owing to its admirable characteristics like high refractive index, chemical durability, high dielectric constant, low melting point, low phonon energy, and better solubility of rare earth ions [25, 107]. In a glass system, zinc oxide (ZnO) acts as both the glass modifier and glass former, which has considerable importance owing to the specific advantages such as wide-direct bandgap, low production cost, higher excitation binding energy, intrinsic emitting property, and also non-toxic and hygroscopic nature [70]. The addition of lithium oxide (Li_2O) has a good ability to reduce the melting temperature, viscosity, improve the physical properties, and enhance the stability or diminish the hygroscopic landscape of the glass former [72]. Bismuth oxide (Bi_2O_3) acts as an unconventional glass network former [108]. The addition of tungsten oxide (WO_3) increases the devitrification resistance and chemical stability, and it acts as an excellent modifier [24]. Hence, based on the literature, the glass host matrix for the current work has been chosen as $TeO_2 – Li_2O –WO_3 – ZnO – Bi_2O_3$ (TLWZBi). However, the luminescent performance of the glass can be appreciated by the proper dopant added to the glass host matrix. Amongst the trivalent rare earth (RE^{3+}) ions, dysprosium oxide (Dy_2O_3) with electronic configurations plays an essential role in white light generation [109, 110].

The white light generation by Dy^{3+} activated substances can be achieved by adjusting the intensity proportion of yellow (Y) and blue (B) color, which can be achieved by tuning the luminescence intensity to the appropriate Y/B ratio. Many investigators have examined Dy^{3+} ions doped boro-tellurite [111], aluminofluoro borophosphate [112], titanium tungstate tellurite [113], and borosilicate glasses [114]. In the current era, various rare earths Pr^{3+}, Ce^{3+}, Dy^{3+},

Dy^{3+}/Tb^{3+}, etc. doped white light-emitting glasses/ glass-ceramics have been prepared for lighting as well as lasing applications [115-116]. Soltys et al. explored the luminescence properties of Ce^{3+} ions doped in barium gallo-germanates glasses and also energy transfer studies from Tm^{3+} to Dy^{3+} to utilize for white LED applications [117]. K. Jha et al. reported the multicolor light-emitting properties of Dy^{3+}/Eu^{3+} co-doped ZPBT glasses under n-UV excitation and the appropriate combination of emission peaks gives the warm-white light. Also, these glasses may serve as both encapsulant materials and luminescent converters for the manufacturing of organic resin/binder-free white light-emitting diodes [118]. Moreover, to the best of the author's knowledge, no report has been published on the luminescence properties of Dy^{3+} doped TLWZBi glasses.

With the aim to explore the present host as both encapsulant material and luminescent convertors, Dy^{3+} doped TeO_2 – Li_2O – WO_3 – ZnO – Bi_2O_3 glass samples have been synthesized. The effect of Dy^{3+} ion concentration on the absorption and luminescent spectra of the as-synthesized glasses was studied and analyzed in detail. The CIE chromaticity coordinates, decay profile, and temperature-dependent PL properties ensure that the prepared thermally stable warm white light emitting Dy^{3+} doped TLWZBi glass is a probable candidate for SSL appliances.

3.2. Experimental Procedure and Characterization Tools

The Dy^{3+} activated TLWZBi glasses have been prepared with a melt quenching procedure as described in *section 2.2.1.* The molar chemical compositions are (50.0-x) TeO_2 - 20.0 Li_2O -15.0 WO_3 - 10.0 ZnO - 5.0 Bi_2O_3 - x Dy_2O_3 (where x = 0, 0.1, 0.5, 1.0, 1.5 and 2.0 mol% and named as TLWZBi, $TLWZBiDy_{0.1}$, $TLWZBiDy_{0.5}$, $TLWZBiDy_{1.0}$, $TLWZBiDy_{1.5}$, and $TLWZBiDy_{2.0}$, respectively). Finally, transparent, bubble-free, light yellowish glasses were obtained for further characterization.

3.2.1. Theory (Physical and Optical Properties)

The density (ρ) of TLWZBiDy glasses has been evaluated at RT using Archimedes' principle as given below [119]:

$$\rho = \frac{W_1}{(W_1 - W_2)} \times \rho_x \tag{3.1}$$

where, W_1 and W_2 signify the weight of glasses in air atmosphere and deionized (DI) water, respectively. ρ_x denotes the density of DI water (ρ_x = 0.9982 g/mL). The refractive index (n) of TLWZBiDy glasses was evaluated using the relation proposed by Dimitrov et al. from the optical bandgap [120]:

$$\frac{n^2-1}{n^2+2} = 1 - \sqrt{\frac{E_{opt}}{20}} \tag{3.2}$$

Furthermore, a few physical and optical parameters like molar volume (V_m), RE ion concentration (N), polaron radius (r_p), inter-ionic distance (r_i), field strength (F), reflection loss (R), molar refractivity (R_m), molar polarizability (α_m) and dielectric constant (ε) estimated for the prepared TLWZBiDy glasses with the help of standard formulas available in the literature [102, 120, 121].

3.3. Results and Discussion

3.3.1. Structural Analysis

The XRD profiles of TLWZBi and TLWZBiDy$_{1.0}$ glasses in the 2θ scale ($10^\circ < 2\theta < 70^\circ$) are presented in Fig. 3.01. The XRD patterns indicate a broad hump with a lack of any crystalline peaks revealing the prepared glasses possess amorphous features. Also, the doping of RE^{3+} in TLWZBi glasses does not change the amorphous feature. Hence, the diffraction pattern affirms the amorphous or non-crystalline behavior of TLWZBiDy glasses.

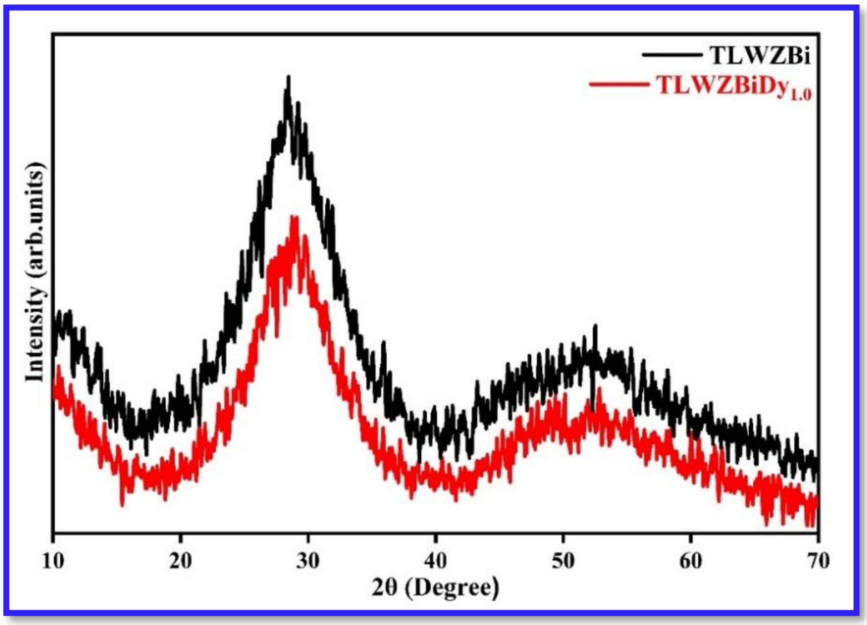

Fig. 3.01. *XRD patterns of TLWZBi and TLWZBiDy$_{1.0}$ glasses.*

3.3.2. Physical Properties

The physical parameters (ρ, V_m, N, r_i, r_p, and F) of TLWZBiDy glass samples are tabulated in Table 3.01. Density is the vital factor used to know the change in geometrical alignment, cross-link density, structural compactness or softening, dimension of interstitial spaces, and coordination number.

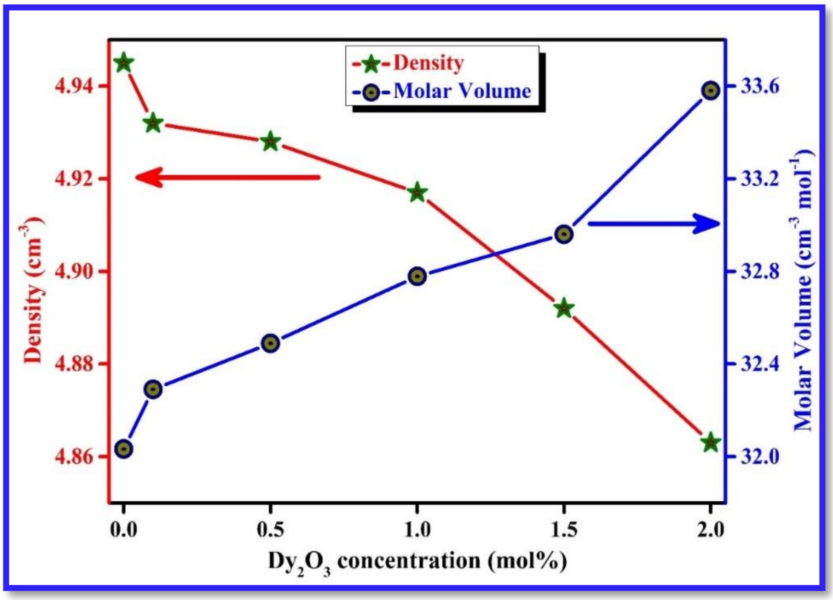

Fig. 3.02. *Density (ρ) and molar volume (V_m) of the TLWZBiDy glasses.*

The change in molar volume and density of TLWZBiDy glasses with increment in Dy_2O_3 doping content is presented in Fig. 3.02. The result shows that the ρ value decreases and V_m increases with a surge in Dy^{3+} ions content. The decrease in ρ with an increment in the Dy^{3+} ions concentration of TLWZBiDy glasses owing to the structural changes such as the formation of non-bridging oxygens (NBOs) [102]. The deliberation of RE ion concentration (N) in the glasses is a crucial parameter used to understand the additional physical parameters like field strength (F), Polaron radius (r_p), and inter-ionic distance (r_i). As the values of N increase, field strength (F) also increases which means when more Dy^{3+} ions are added to the glass matrix their inter-ionic distance (r_i) will be less, and field strength (F) is more.

Table 3.01. Physical parameters of Dy^{3+} doped TLWZBi glass.

Parameters	**TLWZ Bi**	**TLWZ BiDy$_{0.1}$**	**TLWZ BiDy$_{0.5}$**	**TLWZ BiDy$_{1.0}$**	**TLWZ BiDy$_{1.5}$**	**TLWZ BiDy$_{2.0}$**
Density (ρ, g cm^{-3})	4.945	4.932	4.928	4.917	4.892	4.863
Molar volume $(V_m, cm^3 mol^{-1})$	32.033	32.290	32.489	32.779	32.960	33.581
RE ion Concentration $(N \times 10^{22}, ions /cm^3)$	-	0.186	0.928	1.837	2.723	3.585
Inter-ionic distance $(r_i, Å)$	-	8.131	4.761	3.790	3.324	3.033
Polaron radius $(r_p, Å)$	-	3.276	1.919	1.527	1.339	1.222
Field strength $(F \times 10^{15}, cm^{-2})$	-	0.614	1.792	2.830	3.681	4.417

Polarons are quasi-particles so they are constituted owing to the amalgamation of the defect state or trapped electron that can move inside the system. Therefore, the value of N increased which led to a decrease in r_p [102].

3.3.3. Optical Absorption Spectroscopy

The optical absorption spectrum of TLWZBiDy$_{1.0}$ glass was recorded from the 400-1800 nm range and is presented in Fig. 3.03. The spectrum exhibits several absorption bands centered at 453, 474, 753, 807, 907, 1099, 1286 and 1682 nm initiating from lowest energy level ($^6H_{15/2}$) to different excited energy levels of $^4I_{15/2}$, $^4F_{9/2}$, $^4F_{3/2}$, $^6F_{5/2}$, $^6F_{7/2}$, $^6F_{9/2}$, $^6F_{11/2}$ + $^6H_{9/2}$, and $^6H_{11/2}$ belongs to $4f^9$ electronic configuration of Dy^{3+} ions, respectively [108].

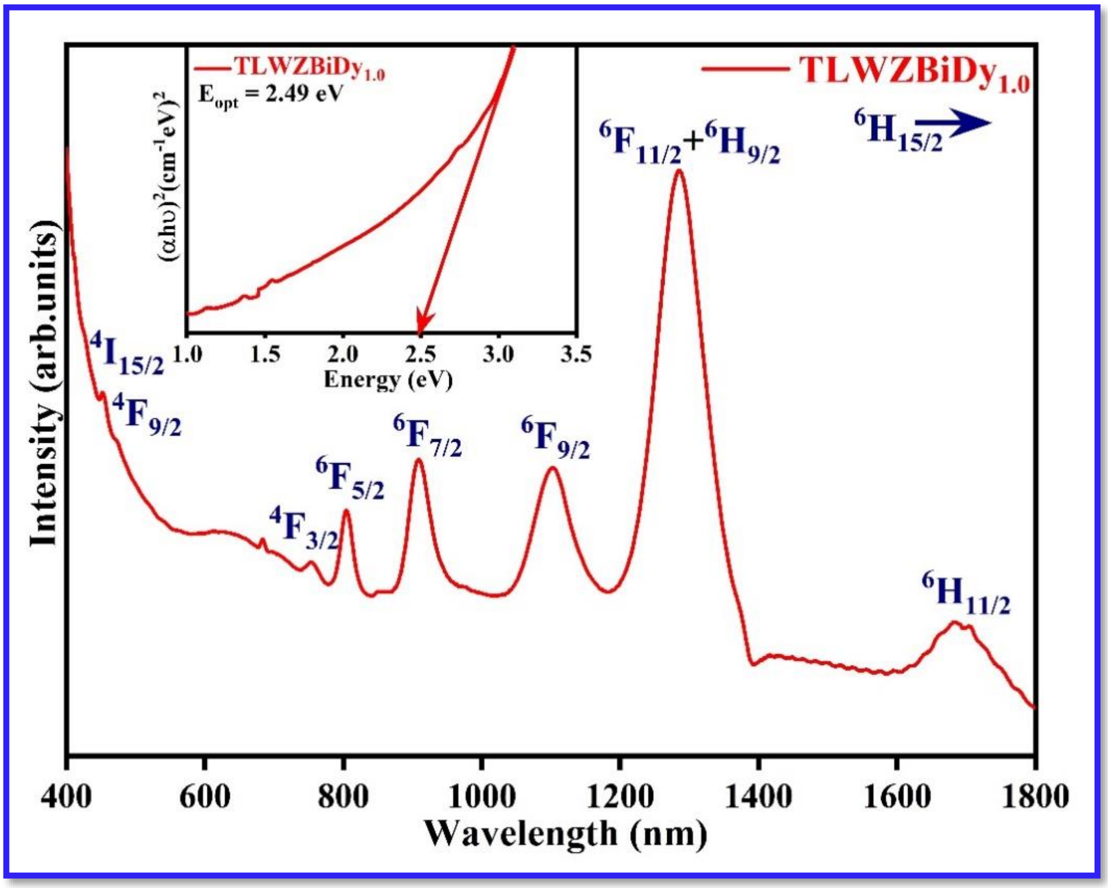

Fig. 3.03. *Absorption spectrum of TLWZBiDy$_{1.0}$ glass. The inset shows Tauc's plot for TLWZBiDy$_{1.0}$ glass.*

A specific transition of RE ions along with an acute sensitivity to ligands and their surrounding environment of the ions leads to a higher intensity of absorption. These transitions are referred to as hypersensitive transitions [109]. The weak absorption bands in the n-UV and visible region were owing to the spin forbidden rule and intense absorption bands in the NIR region because of the spin allowed rule (i.e., $\Delta S = 0$) as well as an orbital angular momentum selection rule (i.e., $\Delta L = 2$). Among all absorption bands, a strong intense absorption band is obtained in the NIR region (1286 nm) corresponding to the ($^6H_{15/2} \rightarrow {}^6F_{11/2} + {}^6H_{9/2}$) transition, which is hypersensitive and obeys the selection rule $|\Delta L| \leq 2, |\Delta S| = 0, |\Delta J| \leq 2$ [103, 109].

The optical bandgap (E_{opt}) energy values of TLWZBiDy glass samples were analyzed by absorption spectra using the Davis and Mott equation as given below [102]:

$$(\alpha h\vartheta) = A(h\vartheta - E_{opt})^r \tag{3.3}$$

where α denote the absorption coefficient, A represents the band tailing parameter, $h\vartheta$ represents the incident photon energy, and E_{opt} denotes the optical bandgap energy. The value of 'r' depends on the nature of transitions, which results in (r = 2) indirect allowed and (r =1/2) direct allowed. The direct allowed bandgap energy of TLWZBiDy glasses was evaluated using Tauc's plot by extrapolation of the linear region to $(\alpha h\vartheta)^2$ versus energy graph. The inset of Fig. 3.03 illustrates Tauc's plot of the $TLWZBiDy_{1.0}$ glass sample for direct allowed (r = 2) transition. The premeditated optical band gap (E_{opt}) values are tabulated in Table 3.02. The E_{opt} values manifested a decrement with an increment in the Dy_2O_3 ions concentration in the glasses owing to an increment in electron localization, which enhances the donor centers in the glasses [115]. The other optical parameters like refractive index (n), reflection loss (R), molar polarizability (α_m) and molar reflectivity (R_m) of TLWZBiDy glasses have been assessed and used with the help of standard formulas and are presented in Table 3.02.

Table 3.02. Optical properties of Dy^{3+} doped TLWZBi glasses.

Parameters	TLWZBi $Dy_{0.1}$	TLWZBi $Dy_{0.5}$	TLWZBi $Dy_{1.0}$	TLWZBi $Dy_{1.5}$	TLWZBi $Dy_{2.0}$
Direct optical band gap (eV)	2.63	2.57	2.49	2.44	2.41
Refractive index (n)	2.50	2.52	2.54	2.56	2.57
Reflection loss (R, %)	11.15	11.34	11.57	11.77	11.87
Molar reflectivity (R_m, cm^3)	22.59	22.73	23.13	23.59	23.94
Molar polarizability $(\alpha_m \times 10^{-24}, cm^3)$	8.96	9.02	9.18	9.36	9.50
Dielectric constant (Ɛ)	6.25	6.35	6.45	6.55	6.60

The values of *n* of TLWZBiDy glasses directly depend on the density and molar polarizability. The *n* of TLWZBiDy glasses progressively increased with an increment in doping concentration of Dy^{3+} ions leading to greater packing of the host matrix.The values of reflection loss (*R*), molar polarizability (α_m), and molar reflectivity (R_m) were increased with an increment in the Dy_2O_3 ions concentration in the glasses, which affirms the generation of higher NBOs [115].

3.3.4. Luminescent Properties

The photoluminescence excitation (PLE) spectrum of TLWZBiDy$_{1.0}$ glass has been examined in the range of 325 to 500 nm at an observing emission at 575 nm wavelength, as displayed in Fig. 3.04. Numerous excitation peaks were observed and assigned at 351 ($^6H_{15/2} \rightarrow {}^5P_{7/2}$), 366 ($^6H_{15/2} \rightarrow ({}^4I_{11/2},{}^6P_{5/2})$), 388 ($^6H_{15/2} \rightarrow ({}^4I_{13/2},{}^4F_{7/2})$), 426 ($^6H_{15/2} \rightarrow {}^4G_{11/2}$), 453 ($^6H_{15/2} \rightarrow {}^4I_{15/2}$) and 474 ($^6H_{15/2} \rightarrow {}^4F_{9/2}$) nm ascribing the Dy^{3+} ions [36, 122]. The intense excitation peak observed at n-UV (388 nm) was opted to record the photoluminescence (PL) spectra.

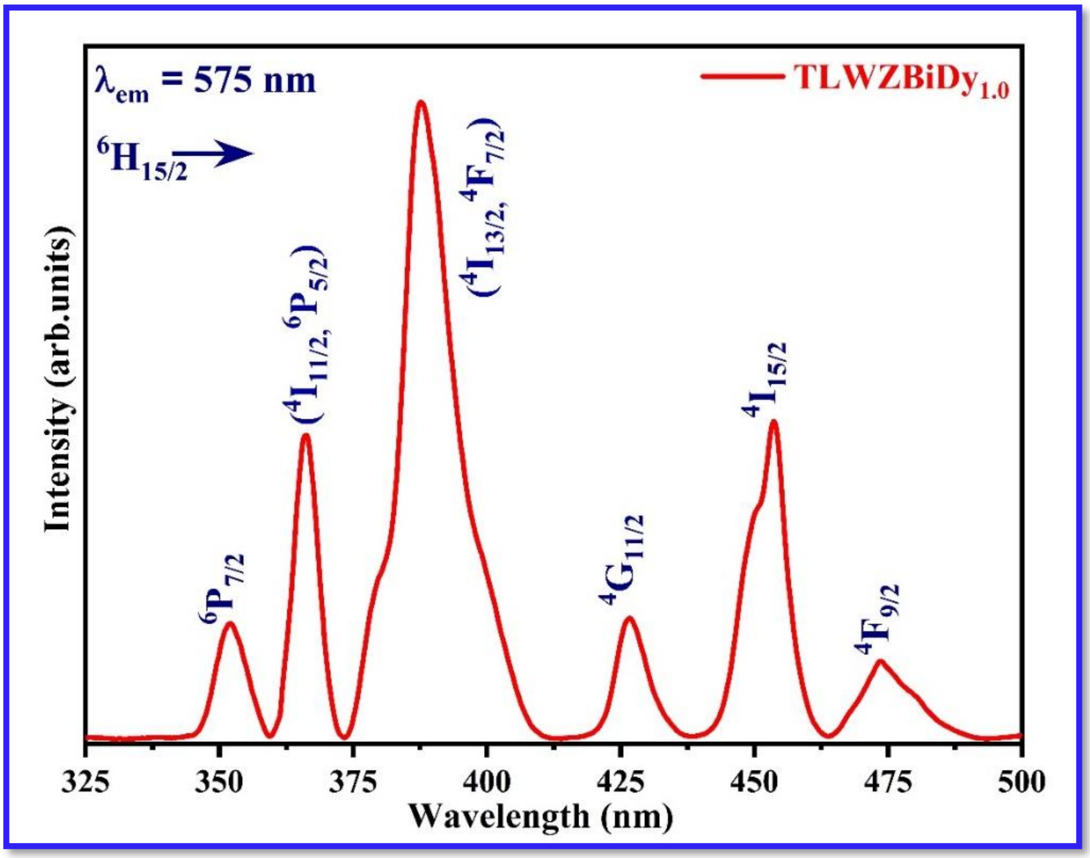

Fig. 3.04. *PLE spectrum of TLWZBiDy$_{1.0}$ glass by monitoring emission at* λ_{em} *= 575 nm.*

Fig. 3.05 illustrates the PL spectra of as-synthesized TLWZBiDy glasses. The PL spectra have been recorded at ambient temperature in the range from 465 to 690 nm via exciting at n-UV (388 nm) wavelength. The PL spectra exhibit three emission peaks centered at 481, 575, and 664 nm in the visible region. The orientation of peaks and their appearance do not show significant changes for the varying doping concentration of Dy^{3+} ions owing to the shielding behavior of *4f* electrons through the *5s* and *5p* outer electron shell. The first peak was observed at 481 nm corresponding to the $^4F_{9/2} \rightarrow {}^6H_{15/2}$ (blue) transition owing to the magnetic dipole (MD) transition and the second peak was observed at 575 nm related to the $^4F_{9/2} \rightarrow {}^6H_{13/2}$ (yellow) transition owing to the forced electric dipole (ED) transition. Furthermore, a third weak emission peak was also observed at 664 nm ascribed to the $^4F_{9/2} \rightarrow {}^6H_{11/2}$ (red) transition. The MD transition is not very sensitive to the crystal field strength of the glass host [107, 120].

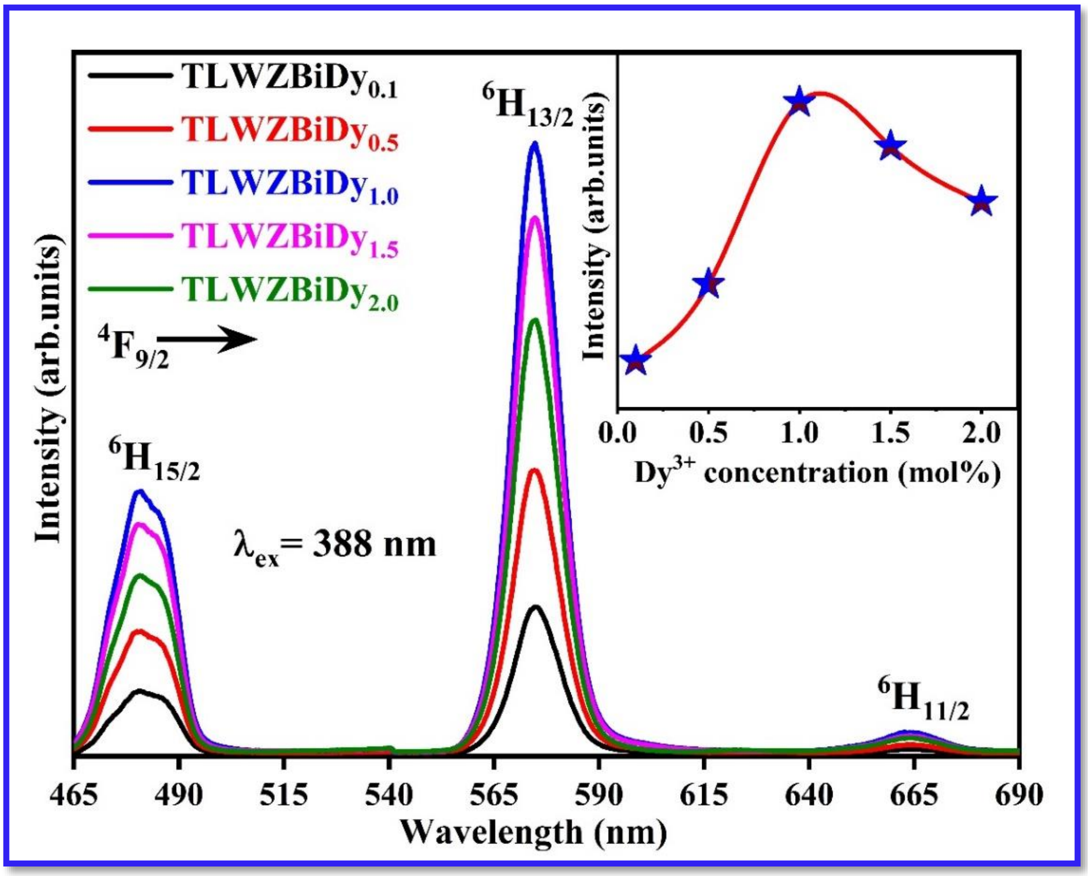

Fig. 3.05. *PL spectra of the as-prepared Dy^{3+} doped TLWZBi glasses at λ_{ex}= 388 nm. The inset plot shows the variation of PL intensity with different Dy^{3+} concentration ions in TLWZBiDy glasses.*

From Fig. 3.05, the PL intensity of the yellow peak is higher than the blue peak, which is due to locating (Dy^{3+}) ions at low symmetry sites and an environment lacking inversion centers in the glass host [116]. The increase in Dy^{3+} ions content in TLWZBiDy glass host composition leads to an increment in emission up to (x = 1.0 mol%). Beyond this content, the emission intensity diminishes owing to the quenching of PL intensity with concentration. The quenching that occurs may be because of resonance energy transfer (RET) among the neighboring Dy^{3+} ions and numerous cross relaxation channels (CRC). The intensity ratio of yellow to blue (Y/B) of TLWZBiDy glass samples was calculated at 388 nm excitation for various Dy^{3+} ions concentrations. The Y/B intensity ratio of TLWZBiDy glasses was estimated in the range of 1.96 to 2.06 by varying the doping concentration of Dy^{3+} ions. The Y/B ratio of TLWZBiDy glasses has been improved with an increment in Dy^{3+} ions content and exhibits a high degree of covalency for the Dy-O bond and asymmetrical ligand atmosphere for Dy ions [103].

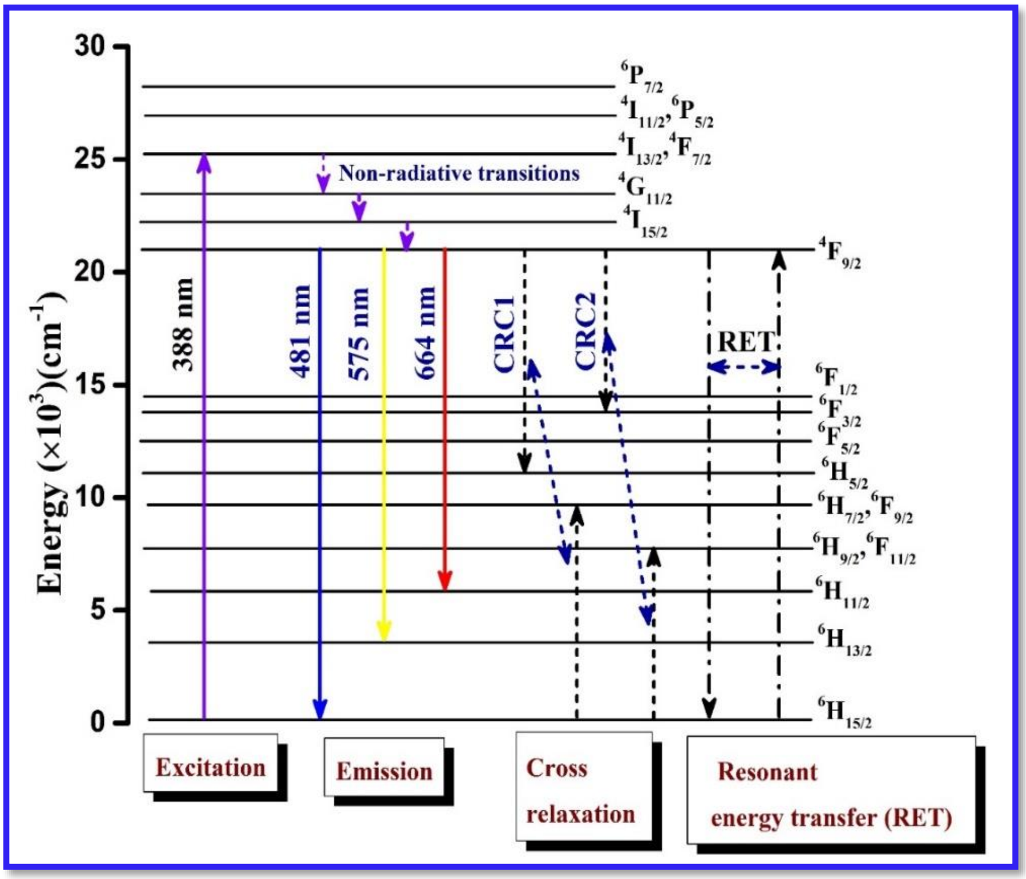

Fig. 3.06. *Partial energy level diagram of Dy^{3+} doped TLWZBi glasses.*

Fig. 3.06 illustrates the partial energy level scheme of as-prepared TLWZBiDy glasses, which contains the excitation, emissions as well as other possible non-radiative transitions (NRT) kind of the Dy^{3+} ions such as RET and CRC mechanisms. As illustrated in Fig. 3.06, the energy levels above $^4F_{9/2}$ are very closely distributed, and thus, Dy^{3+} ions relax predominantly via NRT to the $^4F_{9/2}$ level. On the other side, a larger energy gap between the excited energy level ($^4F_{9/2}$) and to lower energy level ($^6F_{1/2}$) diminishes the probable NRT resulting in radiative transitions (RT). The NRT and concentration quenching may occur because of RET and CRCs channels adjacent among Dy^{3+}- Dy^{3+} ions. The possible RET and CRC (CRC1 and CRC2) are designated as [122-124]:

$$\text{RET01: } ({}^4F_{9/2} + {}^6H_{15/2}) \rightarrow ({}^6H_{15/2} + {}^4F_{9/2})$$

$$\text{CRC1: } ({}^4F_{9/2} + {}^6H_{15/2}) \rightarrow {}^6H_{5/2} + ({}^6H_{7/2} + {}^6F_{9/2})$$

$$\text{CRC2: } ({}^4F_{9/2} + {}^6H_{15/2}) \rightarrow {}^6F_{3/2} + ({}^6H_{9/2} + {}^6F_{11/2})$$

The excitation wavelength (388 nm) excited the Dy^{3+} ions from the lower energy level (${}^6H_{15/2}$) to a higher excited energy level (${}^4I_{13/2}$, ${}^4F_{7/2}$), then decay NRT to ${}^4I_{15/2}$ and ${}^4F_{9/2}$ levels before carrying out the downward radiative transitions (${}^4F_{9/2} \rightarrow {}^6H_{15/2}$), (${}^4F_{9/2} \rightarrow {}^6H_{13/2}$) and (${}^4F_{9/2} \rightarrow {}^6H_{11/2}$) of LTTD glasses [124].

3.3.5. Colorimetric Properties

The luminescent color of TLWZBiDy glasses has been evaluated with the PL intensity at 388 nm excitation wavelength and shown in the CIE 1931 (Commission International de I’Eclairange) plot [124].

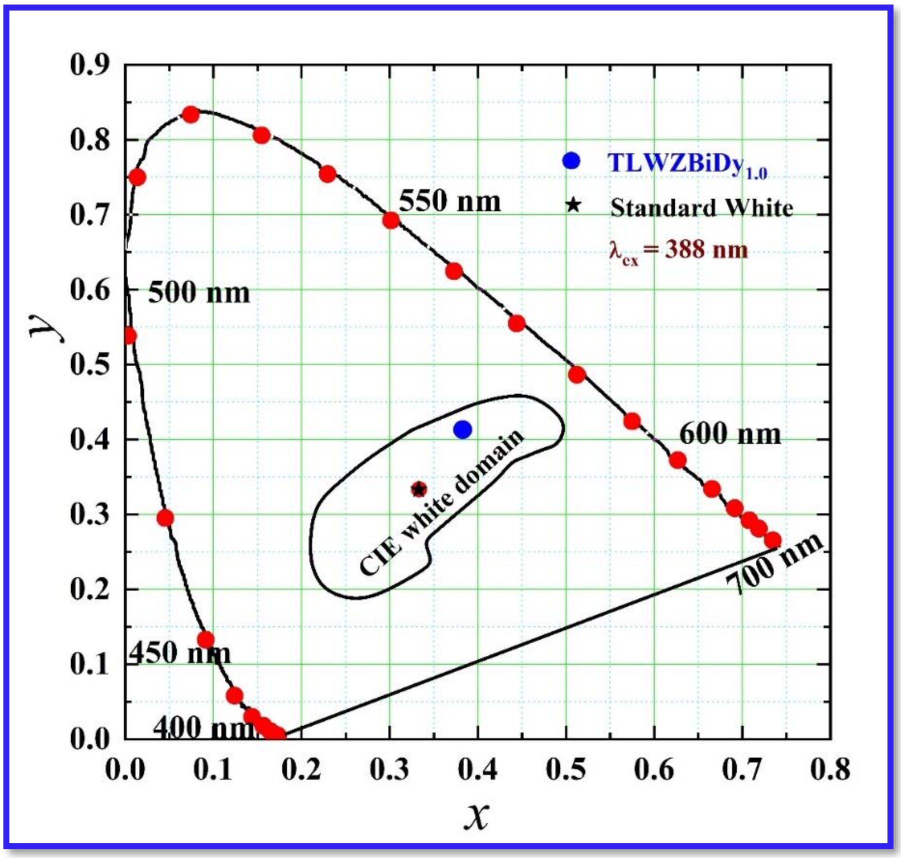

Fig. 3.07. *CIE diagram of TLWZBiDy$_{1.0}$ glass at λ_{ex} = 388 nm.*

As shown in Fig. 3.07, CIE coordinates (0.357, 0.435) for the optimized TLWZBiDy$_{1.0}$ glass sample lie within the white light domain of the CIE plot. The correlated color temperature (CCT) is a vital factor that explains the individual color of light given out through the luminous constituents and evaluated in kelvin (K). CCT values of TLWZBiDy glass samples were calculated using the McCamy empirical relation as expressed *in equation (1.10).* Based on the literature, white light is categorized into cool, natural, and warm light [125]. The CCT value for optimized TLWZBiDy glasses was found to be 4905 K, which is less than 5000 K. Hence, the calorimetric properties specified that the prepared TLWZBiDy glasses emitted the warm white light under n-UV excitation (388 nm). The results designate the direct utility of prepared glasses for solid-state lighting applications without any organic binder.

3.3.6. PL Decay Profiles

The decay profiles of TLWZBiDy$_{0.1}$, TLWZBiDy$_{1.0}$, and TLWZBiDy$_{2.0}$ glasses have been recorded emission at 575 nm ($^4F_{9/2}\rightarrow{}^6H_{13/2}$) wavelength under excitation of 388 nm as presented in Fig. 3.08. Decay curves were determined to find the lifetime values of TLWZBiDy glasses. The recorded decay curves demonstrate the exponential nature and best fitting obtained for the bi-exponential equation as expressed in *equation (2.9)*. The average lifetime (τ_{avg}) values were calculated using the *equation (2.10)*. The average lifetime values of TLWZBiDy$_{0.1}$, TLWZBiDy$_{1.0}$, and TLWZBiDy$_{2.0}$ glasses were found to be 290.7, 261.7, and 136.1 μs, respectively. The average lifetime values diminish with an increment in Dy^{3+} ions content owing to energy transfer amid the nearest Dy^{3+}- Dy^{3+} ions in the glass matrix [124]. Furthermore, the energy transfer mechanism was analyzed via employing the Inokuti-Hirayama (I-H) model for lifetime curves of optimized (TLWZBiDy$_{1.0}$) glass under n-UV (388 nm) excitation wavelength.

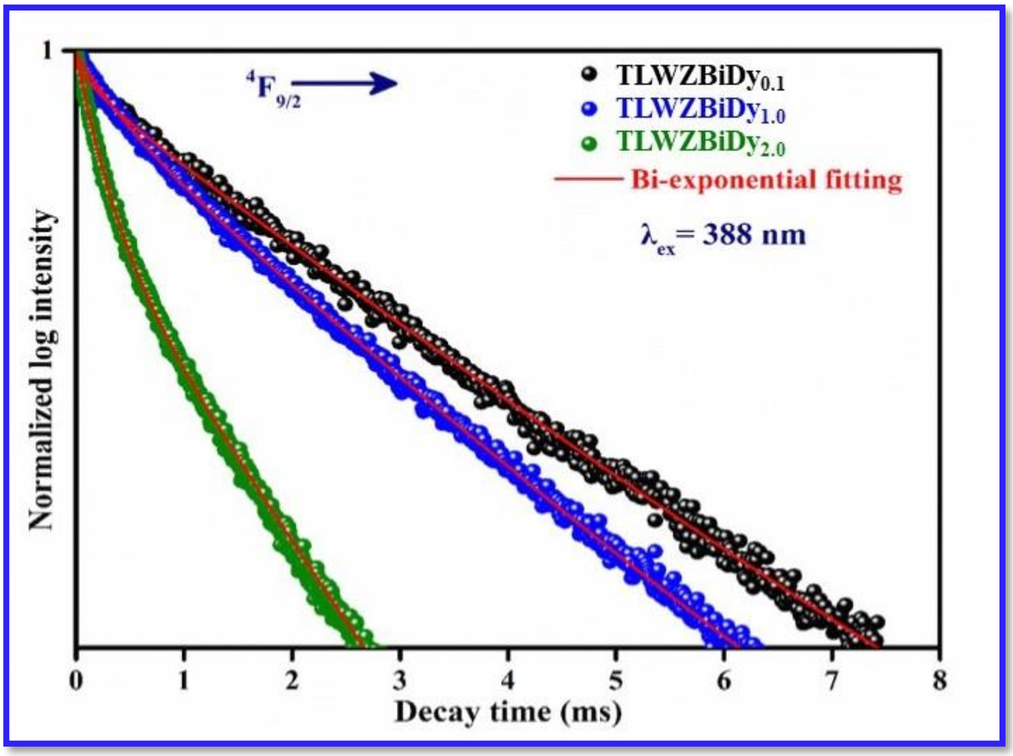

Fig. 3.08. *Luminescence decay profiles of TLWZBiDy$_{0.1}$, TLWZBiDy$_{1.0}$, and TLWZBiDy$_{2.0}$ glasses at wavelength λ_{ex}= 388 nm and λ_{em} = 575 nm.*

According to the I-H model, the luminescence lifetime intensity may be expressed as given below equation [124]:

$$I(t) = I_0 exp\left\{-\frac{t}{\tau_0} - Q\left(\frac{t}{\tau_0}\right)^{3/S}\right\} \quad (3.4)$$

where I(t) represents the PL intensity at a specified time (t). τ_0 signifies the intrinsic decay time of donors without acceptor ions. *Q* denotes the energy transfer parameter. The parameter *S* has values of 6 for dipole-dipole (d-d), 8 for dipole-quadrupole (d-q), and 10 for quadrupole-quadrupole (q-q), respectively. The lifetime curve for an optimized (TLWZBiDy$_{1.0}$) glass has been fitted with various values of the *S* parameter as shown in Fig. 3.09. It is evident that the best fitting has been obtained for *S* = 6, which validates the d-d interaction among Dy^{3+} ions in the prepared TLWZBiDy glasses.

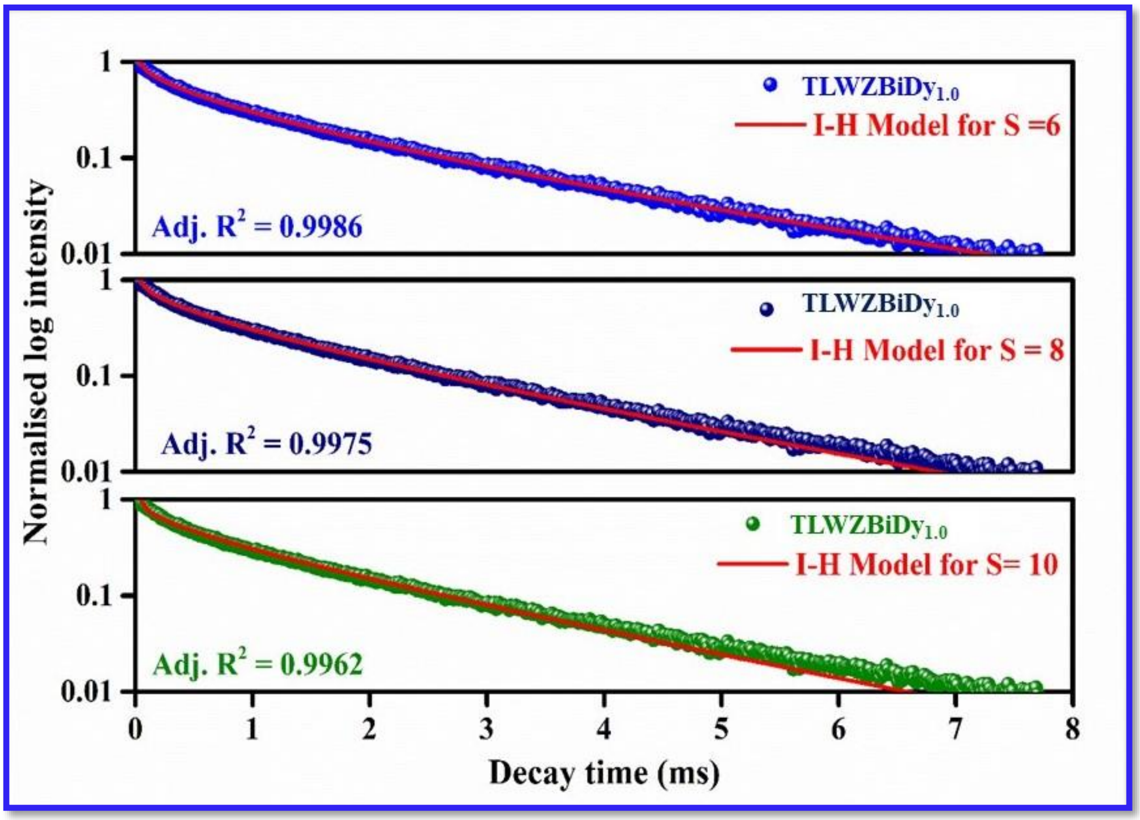

Fig. 3.09. *Decay profile fitted by I-H model (S = 6, 8 & 10) for optimized TLWZBiDy$_{1.0}$ glass under 388 nm excitation.*

3.3.7. Temperature Dependent PL Analysis

To examine the practicability of the synthesized TLWZBiDy glass samples for w-LEDs appliances, temperature-dependent PL spectra of TLWZBiDy$_{1.0}$ glass were recorded with rising temperature from room temperature (RT) to 200 ºC under excitation 388 nm wavelength. As shown in Fig. 3.10, the PL intensity has been reduced with rising temperature from RT to 200 ºC owing to the thermal quenching effect. The PL intensity of TLWZBiDy$_{1.0}$ glass has retained up to 69.86% at 150 ^{0}C from its initial intensity at RT, which reveals that the TLWZBiDy glasses have good thermal stability. Activation energy is an important parameter for the prepared glasses and is calculated using the Arrhenius equation as expressed in *equation (2.11)*.

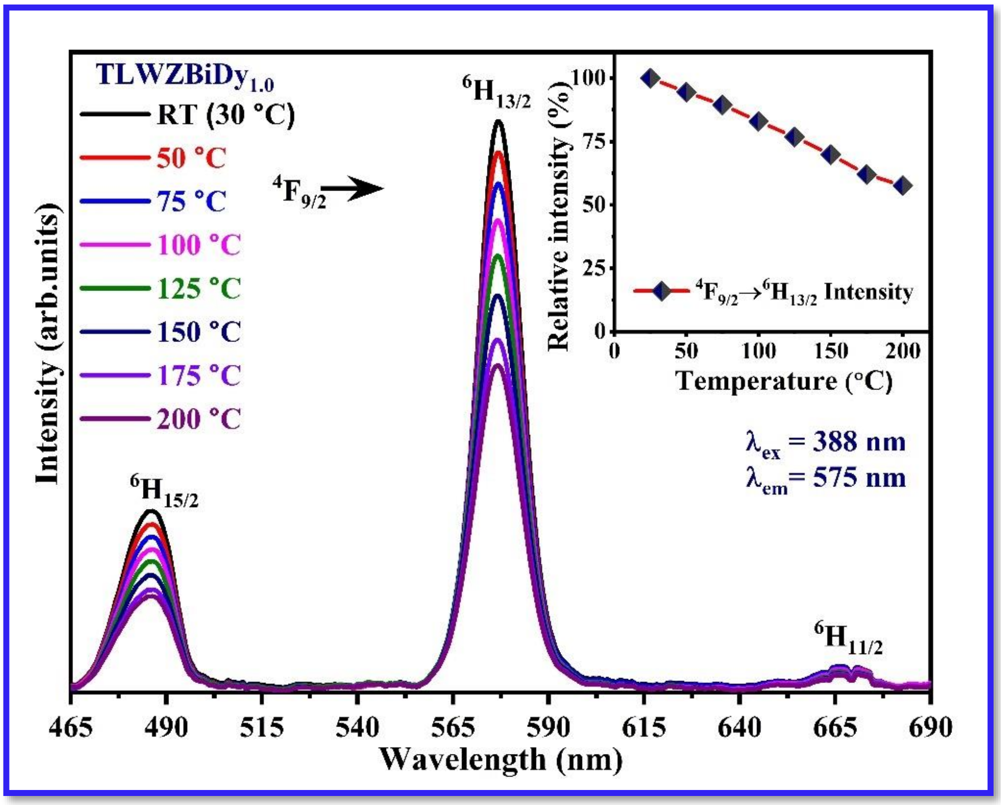

Fig. 3.10. *Temperature dependent emission spectra of TLWZBiDy$_{1.0}$ glass with rise in temperature from room temperature to 200 °C.*

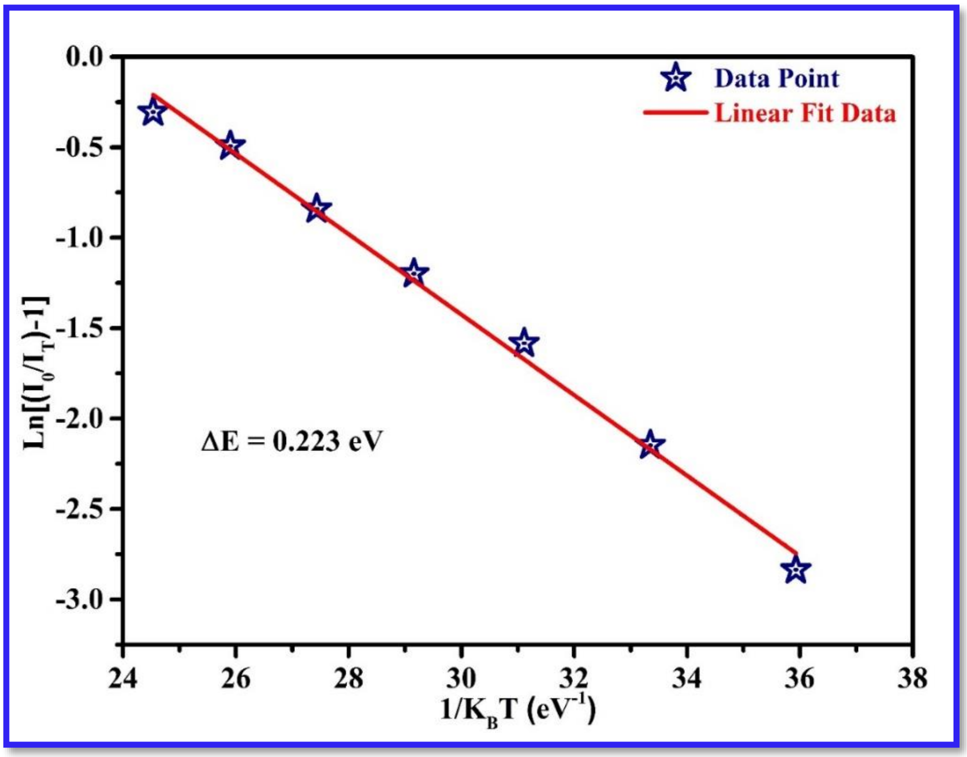

Fig. 3.11. *Linear fitted plot between ln [(I_0/I_T) – 1] against 1/K_BT.*

According to the Arrhenius *equation (2.11)*, the slope can be calculated from the graph $ln\ [(I_0/I_t) - 1]$ against $1/K_BT$ gives the value of activation energy (straight line slope equals ΔE) as shown in Fig. 3.11. Therefore, activation energy has been found to be 0.223 eV, which is quite higher than the value reported in the published papers [125-127]. The high ΔE value recommended that the prepared TLWZBiDy glass has excellent thermal stability and is applicable in SSL devices.

3.4. Conclusions

Dy^{3+} doped TLWZBi glasses were synthesized via the melt quenching procedure. The structural, physical, and luminescent characteristics have been explored via XRD, density, refractive index, absorption, PLE, PL, and decay profile measurements. The density values decreased with an increase in the Dy^{3+} ions content in TLWZBi glasses owing to structural variations such as the formation of NBOs. A board hump in the XRD profiles affirms the amorphous or non-crystalline behaviour of the as-prepared glasses. The band gap (E_{opt}) energy of TLWZBiDy glasses reveals a gradual decrement with increment in the Dy^{3+} ions contents. Under 388 nm excitation, Dy^{3+} doped TLWZBi glasses exhibit emission peaks attributed to transition starting from ($^4F_{9/2}$) level to distinct lower energy states ($^6H_{15/2}$) blue, ($^6H_{13/2}$) yellow and ($^6H_{11/2}$) red, respectively. The concentration quenching was observed at 1.0 mol% of Dy^{3+} content owing to the energy transfer through CR channels. The chromaticity coordinates(x, y) of TLWZBiDy$_{1.0}$ glass (0.357, 0.435) lie in the white region, which is nearest to the standard white region (0.33, 0.33) under 388 nm excitation. Further, the CCT values for the optimized (TLWZBiDy$_{1.0}$) glass were found to be 4905 K, which shows that the glass can radiate warm white light. The experimental decay profiles exhibit a bi-exponential nature and temperature-dependent PL spectra specify that the prepared TLWZBiDy glasses have good thermal stability pertaining to the high value of activation energy. The results affirm that the warm white light emitting Dy^{3+} doped TLWZBi glass has great potential for SSL and other device applications.

Chapter – 04

Optical and Luminescent Characteristics of Eu^{3+} Doped Potassium Tungstate-Tellurite Glasses for Epoxy Free Luminescent Devices

Transparent, Eu^{3+} doped potassium tungstate-tellurite (TKWZBiEu) glass matrices were successfully synthesized via employing the traditional melt quenching method and their thermal, structural and photoluminescent characteristics were thoroughly investigated. To estimate the aggregate weight loss, glass transition temperature (T_g) *and thermal stability factor* (ΔT) *of the prepared host glass matrix, thermogravimetric analysis-differential scanning calorimetry (TGA-DSC) were utilized. The non-crystalline character of the prepared TKWZBiEu glass was studied via XRD profile. Various vibrational functional groups were revealed via employing Fourier transform infrared (FT-IR) spectroscopy. The optical bandgap* (E_{opt}) *values for all prepared TKWZBiEu glasses have been evaluated by employing the absorption spectra. Under n-UV and blue excitations, all the prepared TKWZBiEu glasses are demonstrating reddish emission at 614 nm ascribed to the* $^5D_0 \rightarrow {}^7F_2$ *transition, in which the intensity is increasing continuously with* Eu^{3+} *ion content up to 5.0 mol%. The experimental lifetime* (τ) *profiles demonstrate the single-exponential nature of prepared TKWZBiEu glasses under n-UV excitation. Furthermore, temperature dependent photoluminescence (TDPL) spectra indicate excellent thermal stability of the TKWZBiEu glass matrix with the highest value of activation energy* (ΔE)*. The prototype organic epoxy resin/binder-free device has been developed using the 5.0 mol%* Eu^{3+} *doped with TKWZBi glass matrix and n-UV LED chip. All the aforementioned findings validate that the optimized*

TKWZBiEu glass is an auspicious candidate for the red component to fabricate organic epoxy-free w-LEDs.

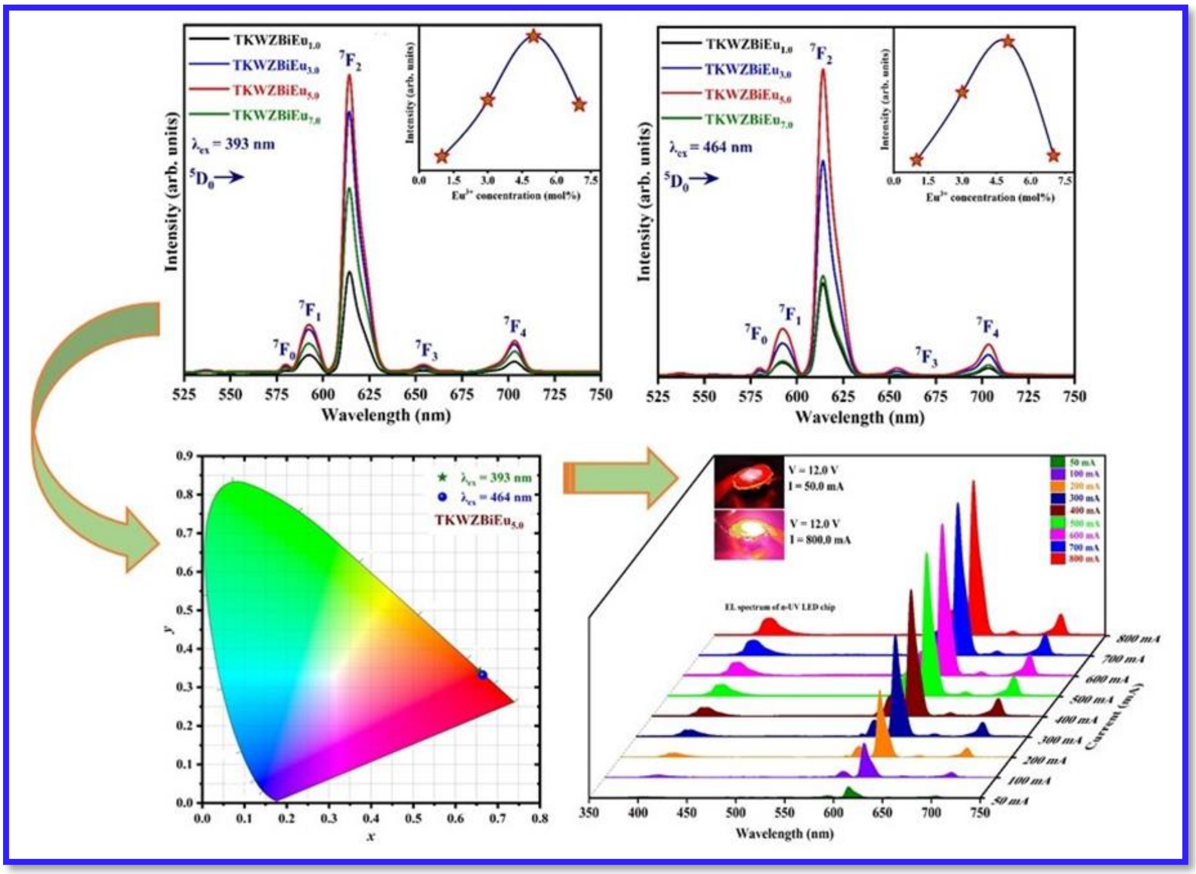

Part of this work has been published in

Current Applied Physics 58 (2024) 11-20 (I.F.: 2.40)

4.1. Introduction

In *Chapter 3*, trivalent dysprosium (Dy^{3+}) activated lithium tungstate-tellurite glasses have been synthesized, which presented the prominent potential for white LED applications. However, lithium oxide (Li_2O) has a decent ability to diminish the melting temperature, and viscosity as well as enhance the stability. To optimize the enhanced luminescent characteristics and thermal stability factor, another glass composition of tungstate-tellurite glasses has been synthesized. Introducing alkali metal oxides (Li_2O, Na_2O, and K_2O) in the tungstate-tellurite glass host helps to decrease the non-radiative loss and enhances the strength of the glass host matrix. Also, alkali metal oxides eliminate the air bubbles from the molten glass and improve the glass transition temperature (T_g) [63]. By utilizing the above-mentioned chemicals, a new glass matrix has been prepared named alkali tungstate tellurite glass to explore the luminescence properties for visible photonic applications.

Over recent years, with the growth of human civilization, the necessity for advanced and cost-effective lighting, high-resolution display devices along eco-friendly, reliable, and energy-saving white light emitting diodes (w-LEDs) has increased precipitously. Thus, researchers have been looking for high quality light emitting materials such as crystalline or amorphous with enhanced illumination and excellent color purity [128-130]. The essential physical characteristics of the light emitting materials accelerate their use in diverse applications like solid state lasers, optical sensors, display devices, and white light-emitting diodes (w-LEDs) [93, 128, 131-134]. Recently, w-LEDs have been reckoned as the next-era illumination source owing to their virtues like less energy consumption, eco-friendliness, longer lifespan, and high efficiency in comparison to the traditional fluorescent and incandescent light bulbs [36, 135]. However, the commercially available white LEDs suffer from a low colour rendering index (CRI), which is due to the absence of the red component. Amidst all rare-earth (RE^{3+}) ions, the trivalent europium (Eu^{3+}) with $4f^6$ electronic configuration is the foremost activator and has attracted widely due to their strong emission in the red region that occurs from the $^5D_0 \rightarrow {}^7F_2$ transition upon excitation via n-UV/blue excitation. Eu^{3+} is the perfect selection for red emission in the visible spectrum owing to its simple energy level arrangement and the site-selective behaviour of intensities among the $^5D_0$ and ^7F_J energy states [136].

In this chapter, Eu^{3+} doped alkali tungstate-tellurite glass matrices were synthesized using the traditional melt quenching procedure for the first time. The host glass was used to investigate the thermal and structural features by employing various characterization techniques, including TGA-DSC, XRD, and FT-IR. The photoluminescent, decay measurement and temperature dependent PL studies of the alkali tungstate-tellurite glass samples have shown to explore the applicability of these glasses in the realm of w-LEDs and other photonic devices.

4.2. Experimental Procedure and Characterization Tools

In the current work, a set of transparent alkali tungstate-tellurite glasses with various doping concentrations of Eu^{3+} ions has been synthesized by applying the conventional melt quenching procedure as described in *section 2.2.1*. The molar composition of the alkali tungstate tellurite glasses 49.0 TeO_2 – 20.0 M_2O – 15.0 WO_3 – 10.0 ZnO – 5.0 Bi_2O_3 – 1.0 Eu_2O_3, (M = Li, Na and K) and labelled as $TLWZBiEu_{1.0}$, $TNWZBiEu_{1.0}$ and $TKWZBiEu_{1.0}$, respectively. Further, the molar composition of TKWZBiEu glass is (50.0 – x) TeO_2 – 20.0 K_2O – 15.0 WO_3 – 10.0 ZnO – 5.0 Bi_2O_3 – x Eu_2O_3, where x has values of dopant ion concentration as 0.0, 1.0, 3.0, 5.0 and 7.0 mol%, respectively. The prepared transparent glasses are coded as TKWZBi, $TKWZBiEu_{1.0}$, $TKWZBiEu_{3.0}$, $TKWZBiEu_{5.0}$, and $TKWZBiEu_{7.0}$ represented for the 0.0, 1.0, 3.0, 5.0 and 7.0 mol% of Eu^{3+} ions doping in the bare glass, respectively. Finally, transparent TKWZBiEu glasses have been obtained for further characterizations such as XRD, FT-IR, photoluminescence (PLE and PL), PL decay measurements and temperature dependent PL studies.

4.3. Results and Discussion

4.3.1. Optimization of Alkali Ions in the Tungstate-Tellurite Glasses

Fig. 4.01 (a & b) depicts the measured excitation and emission spectral profiles for the 1.0 mol% Eu^{3+} doped tungstate-tellurite glasses containing different alkali ions, including lithium (Li), sodium (Na), and potassium (K). When monitoring the intense red (614 nm) emission wavelength, the excitation spectral profiles reveal multiple peaks in the 325 to 550 nm range, which are related to the *4f-4f* electronic transitions as presented in Fig 4.01 (a). Further, the emission profiles for each glass sample consist of five peaks observed at 579, 592, 614, 654, and 703 nm pertaining to the $^5D_0 \rightarrow {}^7F_J$ (where J = 0 to 4) transitions as illustrated in Fig. 4.01 (b). From Fig. 4.01 (a & b), it is conspicuous that the TKWKZBiEu$_{1.0}$ glass demonstrates relatively higher luminescent characteristics than the remaining two alkali ions based tungstate-tellurite glasses (TLWKZBiEu$_{1.0}$ and TNWKZBiEu$_{1.0}$), which suggest the superior quality of the potassium tungstate-tellurite glass for further studies.

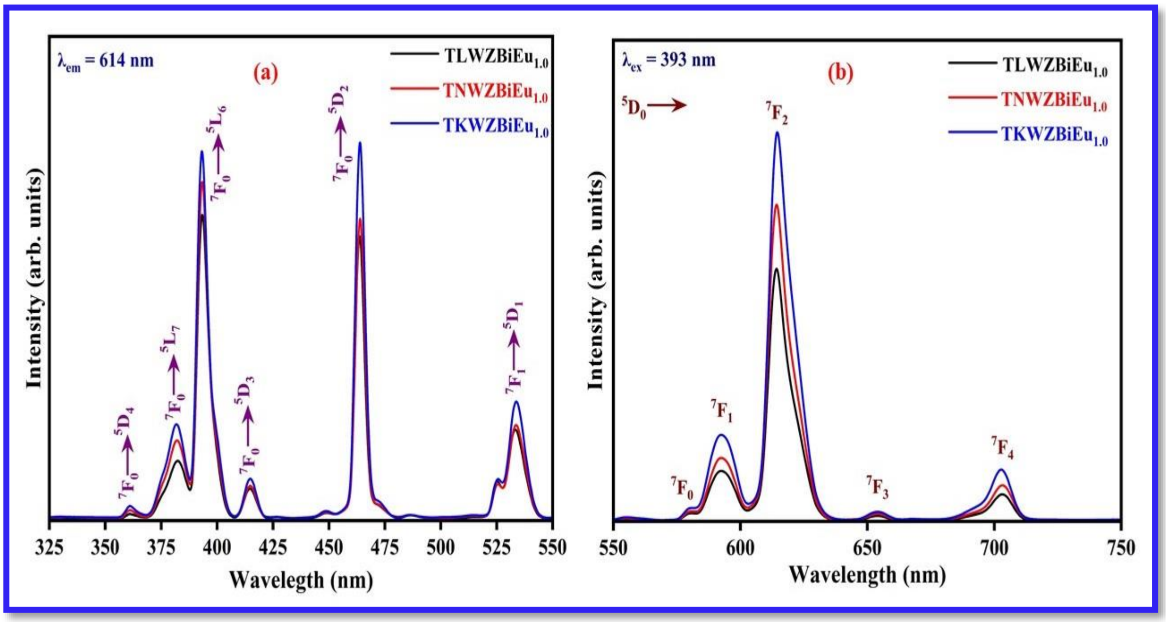

Fig. 4.01 (a & b). *Optimization of alkali ions in the tungstate-tellurite glass.*

4.3.2. TGA-DSC Analysis

In the thermo-analytical technique known as differential scanning calorimetry (DSC), a variable quantity of heat is required to raise the temperature of a sample while determining the reference as a function temperature. DSC profiles are made up of two diverse kinds of transitions such as endothermic and exothermic. Peaks in the endothermic transition have been produced by heat capacity (i.e., heating), glass transition (T_g), melting, and vaporization. Exothermic peaks originated from the heat capacity (i.e., cooling), crystallization and oxidation peaks [137]. DSC profile of the glass host matrix (TKWZBi) was measured in the temperature range from 200 to 900 ºC along with a heating rate of 10 ºC/min as indicated in Fig. 4.02 (a). Several temperature characteristics such as melting temperature (T_m), peak crystallization temperature (T_c), onset crystallization temperature (T_x) and glass transition temperature (T_g), have been observed at 860, 425, 399 and 352 ºC, respectively.

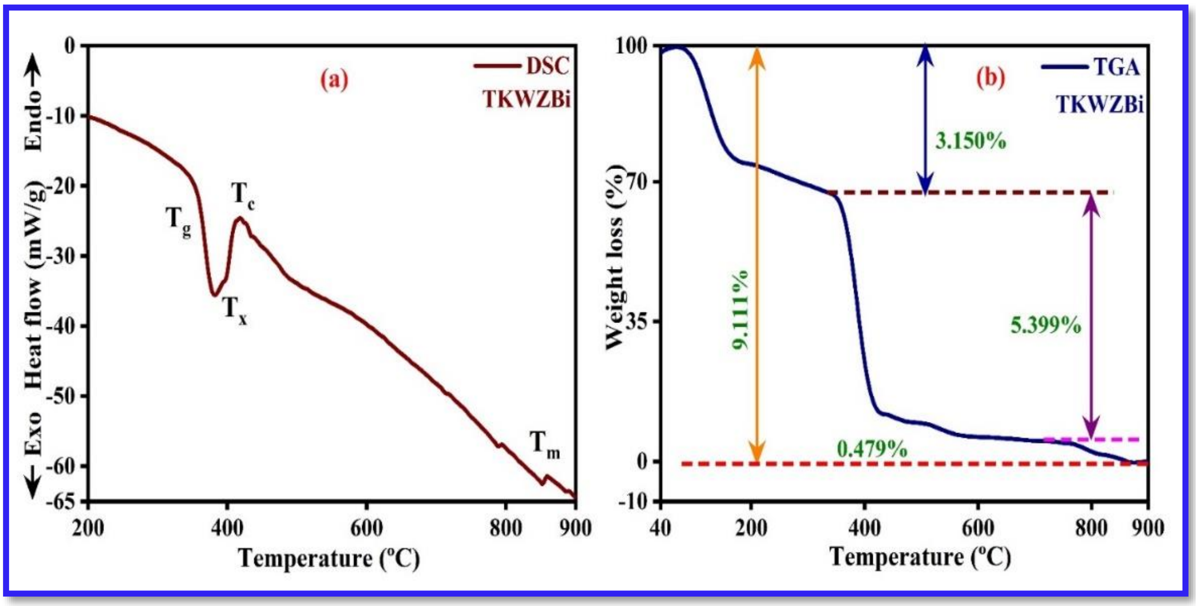

Fig. 4.02. (a & b). *Differential scanning calorimetry (DSC) and thermogravimetric analysis (TGA) of the TKWZBi glass host matrix.*

The thermal stability of the glass host matrix (TKWZBi) has been estimated by employing the following expression [137, 138]:

$$\Delta T = T_X - T_g \tag{4.1}$$

The higher ΔT value prefers the glass formation through controlling the crystallization process and hence signifies the enhanced temperature stability of the glass host matrix. In the current studies, the estimated ΔT value has been found to be 47 ºC, which is greater than the value reported earlier [138]. Hence, the aforementioned result validates the prepared (TKWZBi) glass host matrix has good thermal stability and may be evident as a promising choice for photonic device applications. Fig. 4.02 (b) illustrates the thermogravimetric analysis (TGA) profile of the glass host matrix (TKWZBi) was determined in the temperature range from 40 to 900 ºC. Three different temperature ranges have been observed during which the glass host matrix loses its aggregate weight and the total weight loss is found to be 9.111% as shown in Fig. 4.02 (b). Initially, the weight loss is about 3.150% in the range of 40 to 325 ºC because of the dehydration of adsorbed water molecules from the surface of a sample [139]. The second weight loss is approximately 5.399% happens beyond 325 to 650 ºC owing to the chemisorbed water, and loss of solvent in the glass host sample [137]. Finally, a nominal weight loss of about 0.479% occurs in a range of 650 to 900 ºC owing to the presence of combustibles in the glass host [137-140]. The aggregate weight loss in the glass host matrix was observed to be 9.111% and the remaining weight is approximately 90.889%. Thus, the as-prepared TKWZBi glass matrix has more heat resistant capability with smaller weight reduction at higher temperatures.

4.3.3. Structural Analysis

4.3.3.1. XRD Profile

To explore the non-crystalline behavior of undoped TKWZBi glass, XRD has been carried out and displayed in Fig. 4.03. There is absolutely no sharp peak and the appearance of a broad hump in the XRD profile in the 2θ range from 22º to 34º, as depicted in Fig. 4.03. The non-appearance of sharp Bragg's peak validated the non-crystalline behavior of the prepared undoped TKWZBi glass.

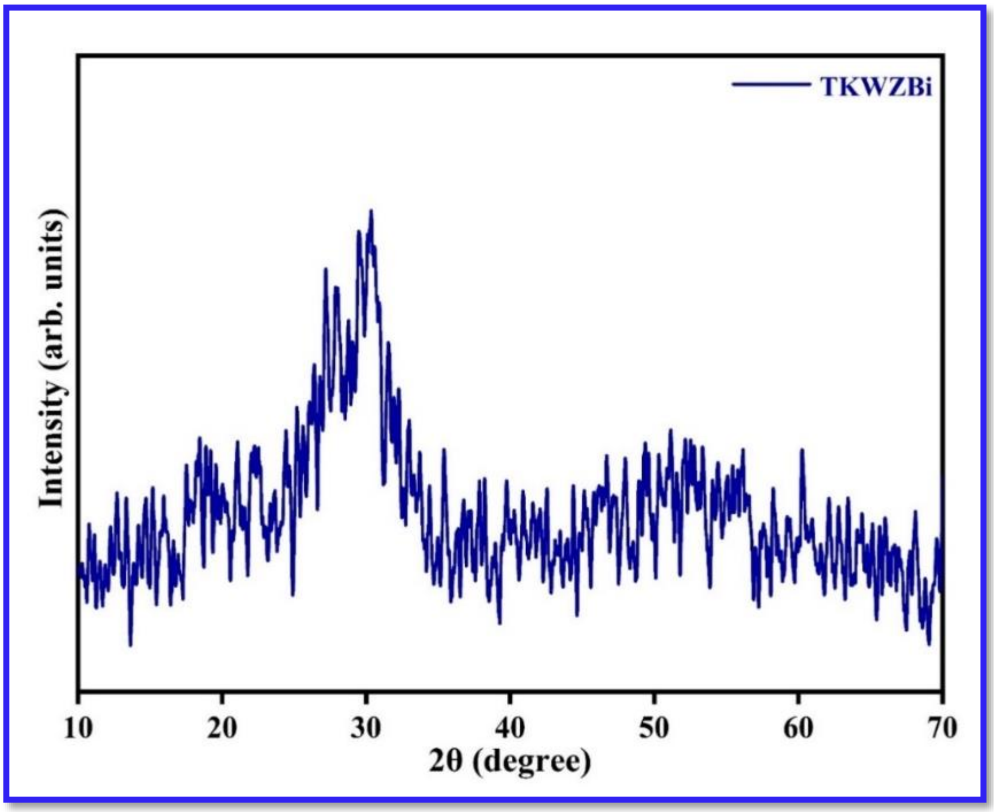

Fig. 4.03. *X-ray diffraction (XRD) pattern of the undoped (TKWZBi) glass.*

4.3.3.2. FT-IR Analysis

In order to explore the presence of several vibrational functional units in the prepared 1.0 mol% Eu^{3+} activated TKWZBi ($TKWZBiEu_{1.0}$) glass sample, the FT-IR spectrum has been carried out in the spectral interval from 400 to 4000 cm^{-1} as shown in Fig. 4.04. Moreover, $TKWZBiEu_{1.0}$ glass has many vibrational functional groups assigned at 438, 618, 827, 906, 1053, 2985 and 3673 cm^{-1}, respectively. Table 4.01 summarizes the functional bands and their band assignments of the prepared 1.0 mol% Eu^{3+} doped TKWZBi glass. The existence of tetrahedral bending vibration of the ZnO_4 unit and the bending vibration of O-Te-O or Te-O-Te bonds is attributed to the band at 438 cm^{-1} [63, 102].

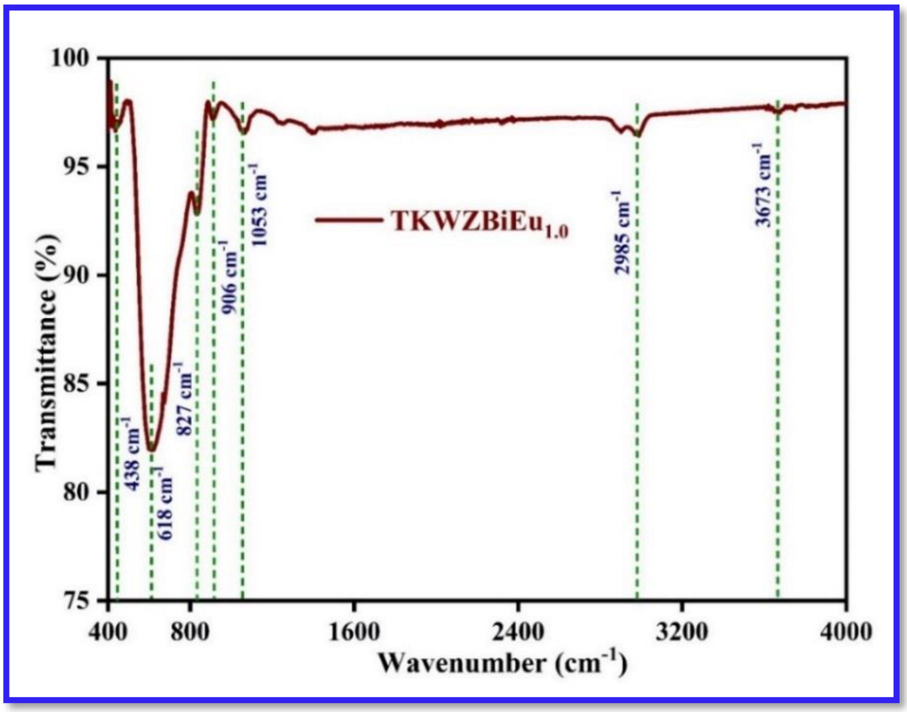

Fig. 4.04. *FT-IR spectrum of 1.0 mol% Eu^{3+} doped TKWZBi glass.*

Table 4.01. The functional bands and their band assignments of the prepared 1.0 mol% Eu^{3+} doped TKWZBi glass.

Wavenumber (in cm^{-1})	**Bands assignments**
438	Presence of tetrahedral bending vibration of ZnO_4 or bending vibration of Te-O-Te or O-Te-O linkages.
618	Stretching vibrational of Te-O-Te linkages in trigonal bipyramid units.
827	Stretching vibration of W-O-W linkages.
906 & 1053	Stretching vibration of W-O$^-$ and W=O linkages in WO_4 and WO_6 units.
2985	Presence of hydrogen bonding.
3673	Stretching vibration of the hydroxyl group.

The Te-O-Te bonds stretching vibration in the TeO_4 trigonal bipyramid units is attributed to the band position at 618 cm^{-1} [141]. The band centered at 827 cm^{-1} was ascribed to the stretching vibration of W-O-W bonds, whereas the peak at 906 and 1053 cm^{-1} have been assigned to the stretching vibration of W=O linkages in tetrahedral (WO_4) and octahedral (WO_6) units [141, 142]. Furthermore, the band located at 2985 cm^{-1} is assigned to the hydrogen bonding in the prepared TKWZBiEu$_{1.0}$ glass. The weak band around 3673 cm^{-1} is allocated at the stretching vibration of the hydroxyl group [63, 143].

4.3.4. Optical Absorption Spectral Analysis

The absorption spectra for all TKWZBiEu glass samples were measured at ambient temperature in the UV to NIR spectral range and presented in Fig. 4.05. The spectra consist of two absorption peaks in the visible range centered around 464 and 534 nm attributed to $^7F_0 \rightarrow {}^5D_2$ and $^7F_1 \rightarrow {}^5D_1$ and two absorption peaks are in the NIR range centered around 2084 and 2207 nm ascribed to $^7F_0 \rightarrow {}^7F_6$ and $^7F_1 \rightarrow {}^7F_6$, respectively [144]. The peaks arising from ^7F_J to ^5D_J are weak in comparison to the other transitions owing to the parity allowed and spin forbidden owing to the J mixing through the crystal field [145].

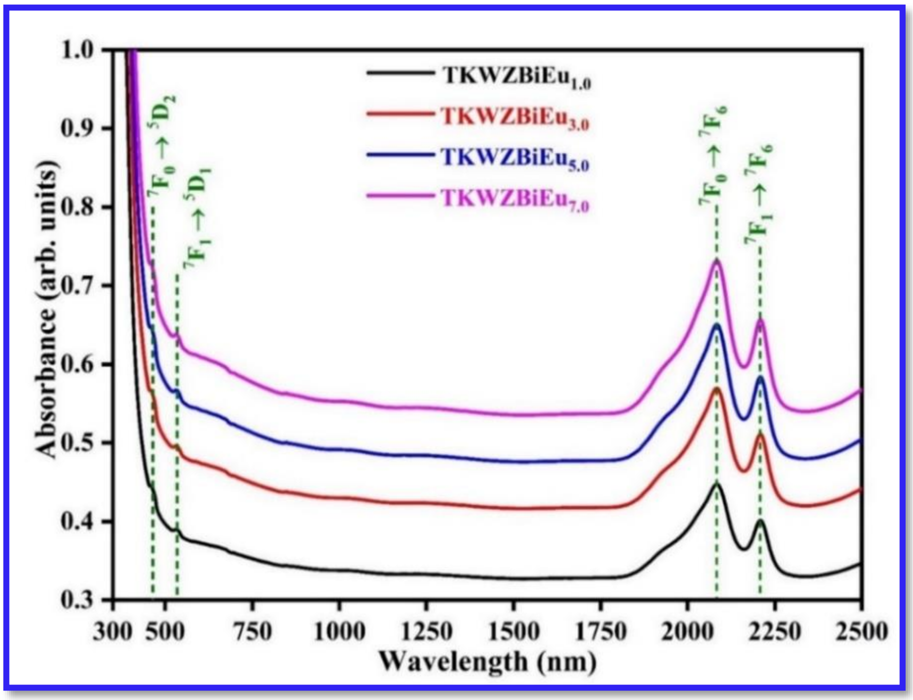

Fig. 4.05. *The optical absorption spectra for all prepared TKWZBiEu glasses in the UV-VIS-NIR region.*

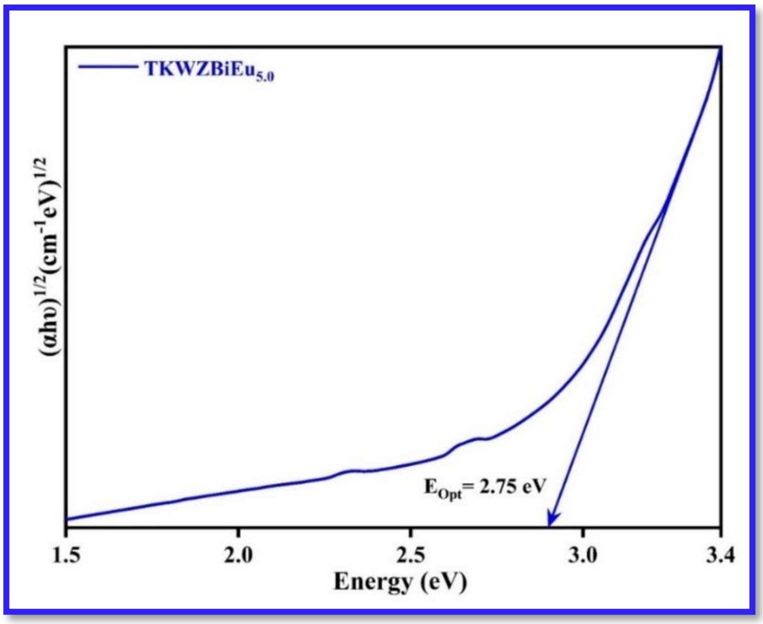

Fig. 4.06. *The band gap energy for an indirect allowed transition of the optimized TKWZBiEu$_{5.0}$ glass sample using Tauc's plot.*

With enhancing the dopant ions concentration of Eu^{3+} in the prepared TKWZBi glasses, there is no peak shifting detected in the absorption spectra apart from variation in the absorption peak intensities. From absorption spectra, the optical band gap (E_{opt}) energies for all TKWZBiEu glasses have been evaluated via employing Davis and Mott's method as expressed in *equation (3.3)*. The E_{opt} value of optimized TKWZBiEu$_{5.0}$ glass can be graphically obtained from the Tauc's plot via an extrapolating straight-line portion of the graph $(\alpha h\vartheta)^{1/2}$ versus energy as presented in Fig. 4.06. The estimated E_{opt} for the indirect allowed transition of the prepared TKWZBiEu glasses are in the range from 2.66 to 2.94 with decreasing dopant concentration. It was noticed that indirect allowed E_{opt} values systematically diminish along with increases in Eu^{3+} concentration because of structural changes in the prepared glass matrix [146]. Furthermore, using the indirect allowed E_{opt} values, the refractive index (n) of all prepared TKWZBiEu glasses has been estimated using the following Dimitrov et al. relation as presented in *equation (3.2)*. The estimated refractive index (n) for TKWZBiEu glasses is around 2.45.

4.3.5. Luminescent Properties of **TKWZBiEu** *Glasses*

The PLE spectrum of the TKWZBiEu$_{1.0}$ glass matrix has been scanned at ambient temperature in the spectral wavelength range from 325 to 550 nm by fixing the 614 nm emission wavelength as demonstrated in Fig. 4.07. The PLE reveals the six excitation peaks, which are located at 361, 381, 393, 414, 464 and 534 nm attributed to $^7F_0 \rightarrow {}^5D_4$, $^7F_0 \rightarrow {}^5L_7$, $^7F_0 \rightarrow {}^5L_6$, $^7F_0 \rightarrow {}^5D_3$, $^7F_0 \rightarrow {}^5D_2$ and $^7F_1 \rightarrow {}^5D_1$ transitions of the Eu^{3+} ions [63, 93, 131]. Amongst all the detected excitation peaks, the transitions ascribed to $^7F_0 \rightarrow {}^5L_6$ and $^7F_0 \rightarrow {}^5D_2$ positioned at 393 nm (n-UV region) and 464 nm (blue region) are highly intense transitions, which can be utilized to measure the PL spectra for all the prepared TKWZBiEu glasses.

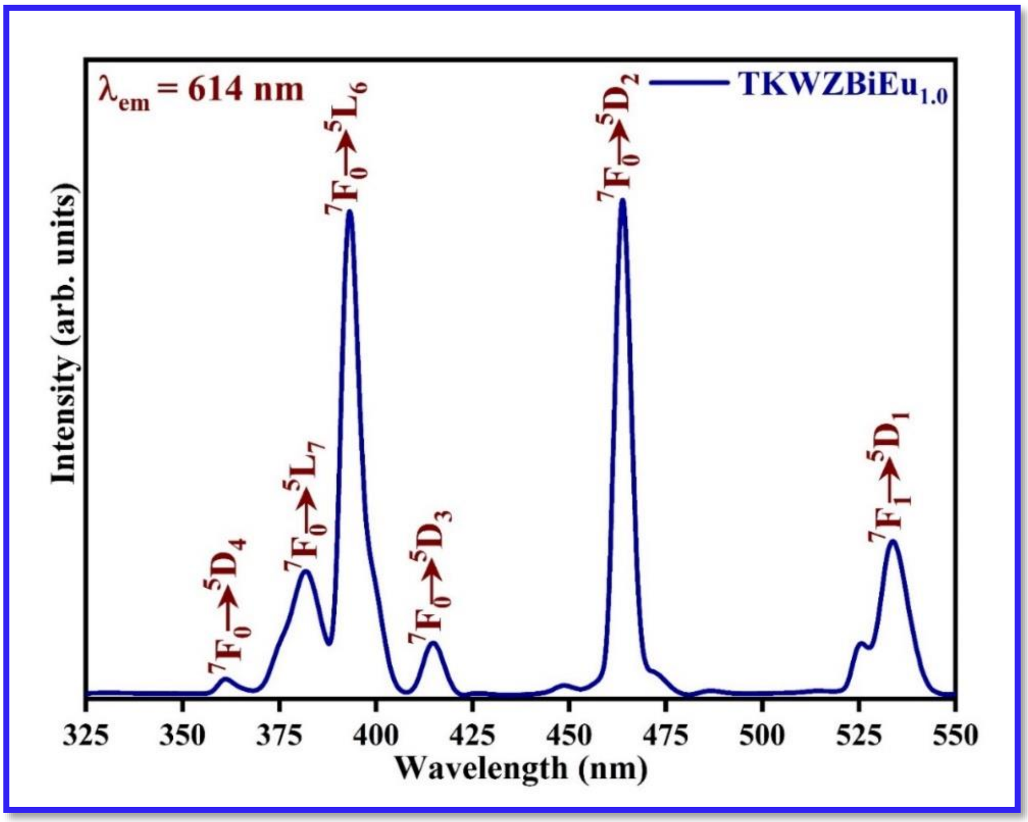

Fig. 4.07. *PLE spectrum of TKWZBiEu$_{1.0}$ glass by monitoring emission at* λ_{em} = *614 nm.*

The PL spectra of TKWZBiEu glasses have been scanned in the spectral range from 525 to 750 nm at ambient temperature by pumping with n-UV and blue excitations are illustrated in Fig. 4.08 (a & b). Under n-UV and blue excitations, the PL spectra show five intense emission peaks at 579, 592, 614, 654 and 703 nm attributed to the excited state ($^5D_0$) and various ground states such as $^7F_0$, $^7F_1$, $^7F_2$, $^7F_3$ and $^7F_4$ transitions of Eu^{3+} ions [93, 131, 147]. The emission peak centered at 592 nm ($^5D_0 \rightarrow {}^7F_1$) is an MD transition, which is recognized as an orange emission and follows a selection rule ($\Delta J = 1$), whereas the emission peak positioned at 614 nm ($^5D_0 \rightarrow {}^7F_2$) is ascribed to the forced ED transition and obeying the selection rule such as $\Delta J = 2$ [131].

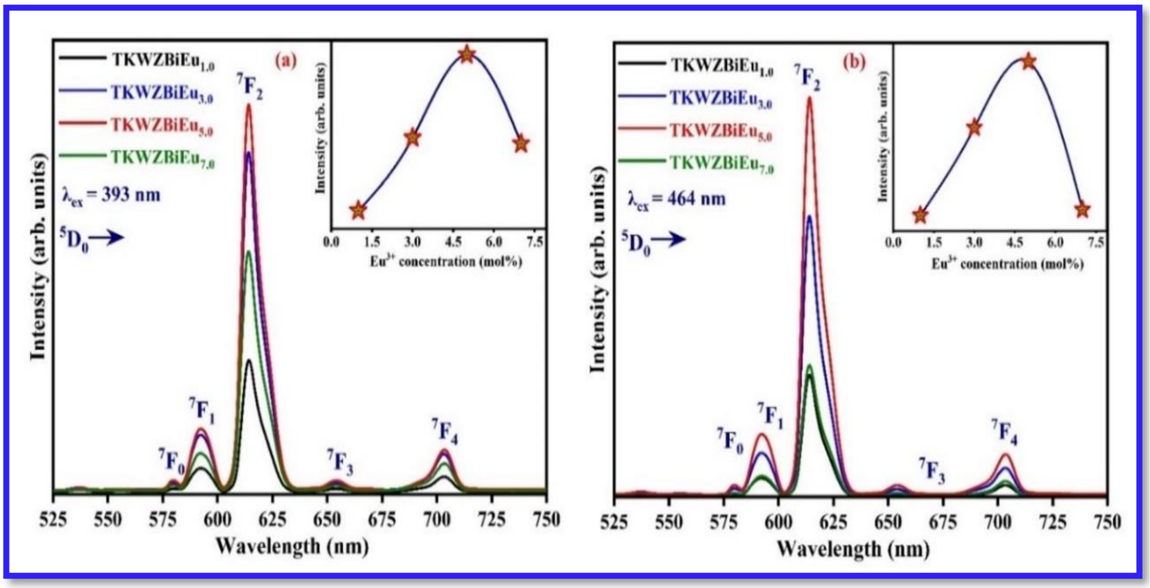

Fig. 4.08 (a and b). *PL spectra of all prepared Eu^{3+} doped TKWZBi glasses at n-UV (λ_{ex}= 393 nm) and blue (λ_{ex}= 464 nm) excitations. The inset plot shows the variation of PL intensity with Eu^{3+} concentrations.*

The forced ED ($^5D_0 \rightarrow {}^7F_2$) transition is a hyper-sensitive transition in behavior and the PL intensity of this transition is effectively influenced via the crystal field of ligand atoms [93]. Conversely, the MD transition is independent of local symmetry around Eu^{3+} ions as well as their surroundings [147]. The transition assigned to the $^5D_0 \rightarrow {}^7F_4$ transition is also recognized as an electric dipole transition in behavior [147]. The PL intensity ratio of red (614 nm) to orange (592 nm) (I_{614}/I_{592}) is defined as the asymmetric ratio that gives the behavior of the chemical environment around Eu^{3+} ions in the glass host matrix and their values specify the covalency and local symmetry [93, 147]. The asymmetric ratio values have been evaluated via integrating the area below the curves of ($^5D_0 \rightarrow {}^7F_2$) to the ($^5D_0 \rightarrow {}^7F_1$) transitions. The values of asymmetric ratio for TKWZBiEu$_{1.0}$, TKWZBiEu$_{3.0}$, TKWZBiEu$_{5.0}$ and TKWZBiEu$_{7.0}$ glass samples under n-UV and blue excitations have been found to be 5.56, 6.11, 6.38 & 6.30 and 6.40, 6.55, 6.70 & 6.67, respectively. The ratio under n-UV/blue excitation is greater than one, thus the ED transition dominates over the MD transition, which specifies the presence of dopant (Eu^{3+}) ions at sites without the inversion center. The higher value of the (I_{614}/I_{592}) ratio demonstrates higher covalency among the Eu^{3+} ions and their ligands atoms (i.e., Eu^{3+} and O^{2-}) [147]. Thus, it may be determined that the prepared TKWZBiEu glass sample can be beneficial for display and lighting applications [93, 147]. The inset of Fig. 4.08 (a & b) illustrates the variation of PL intensity with a doping concentration of Eu^{3+} ions under n-UV and blue excitations, respectively.

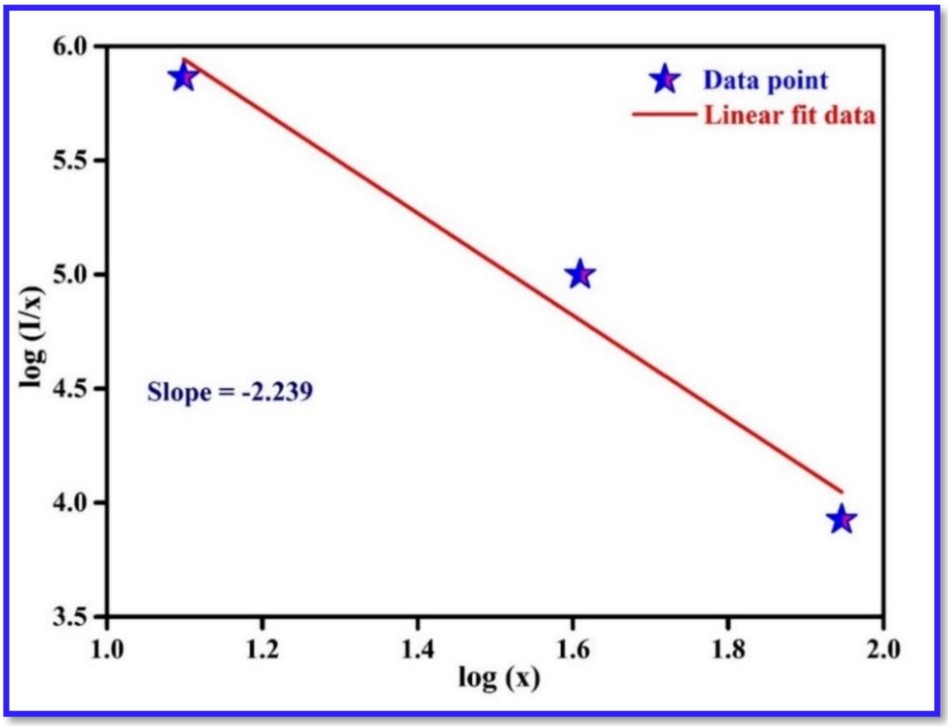

Fig. 4.09. *Relation between* $log\left({}^{I}/_{x}\right)$ *and* $log(x)$ *for the varying concentration of* Eu^{3+} *ions.*

As demonstrated in the inset, the PL intensity of the prepared TKWZBiEu glasses increases with increasing the concentration of Eu^{3+} ions up to 5.0 mol%, and beyond that, the emission intensity diminishes with enhancing the Eu^{3+} ions concentrations. This phenomenon is due to concentration quenching phenomena. The separation between the dopant (Eu^{3+}) ions is reduced with an increment in Eu^{3+} concentrations that promotes the non-radiative energy transfer (NRET) between Eu^{3+} - Eu^{3+} ions and thus, the quenching phenomena occur. The cause for quenching phenomena might be due to the non-radiative energy transfer among the dopant (Eu^{3+}) ion concentrations. The type of interaction can be evaluated via employing Dexter's theoretical model. As per Dexter's model, if the dopant (Eu^{3+}) concentration is sufficiently large, the correlation among PL intensity (I) along with dopant concentration (x) is given as [148]:

$$\frac{I}{x} = \frac{1}{K(1+\beta x^{S/3})} \tag{4.2}$$

in the above expression, K and β are related to the constant parameters. The x value denotes the doping concentration of Eu^{3+} ions in mol%. The parameter S suggests the kind of interaction amidst the adjacent Eu^{3+} ions and takes the values as 10 for quadrupole-quadrupole (q-q), 8 for dipole-quadrupole (d-q), & 6 for dipole-dipole (d-d) interaction [148].

In the above equation, the assumption is that $(\beta X^{S/3}) \gg 1$, the expression may be reduced as follows:

$$\log\left(\frac{I}{X}\right) = K' - \frac{S log(X)}{3}; \quad (K' = logK - log\beta) \tag{4.3}$$

The parameter S has been evaluated through the slope of the graph between $\log\left(\frac{I}{X}\right)$ and $log(X)$ are presented in Fig. 4.09. The evaluated slope (-2.239) value of a straight-line fit is equivalent to the S/3, which yields the value of S is equal to -6.717 that is nearby 6. Therefore, the S value suggests that the multipolar interaction among the Eu^{3+} ions is d-d in nature. Fig. 4.10 signifies the partial energy level illustration for the PL excitation and emission along with other kinds of possible transitions such as cross-relaxation channels. The Eu^{3+} ions at lower energy levels are initially excited to higher energy levels under n-UV and blue excitations, and then quickly relax to the lower energy level ($^5D_0$) via the non-radiative transition (NRT) process [147].

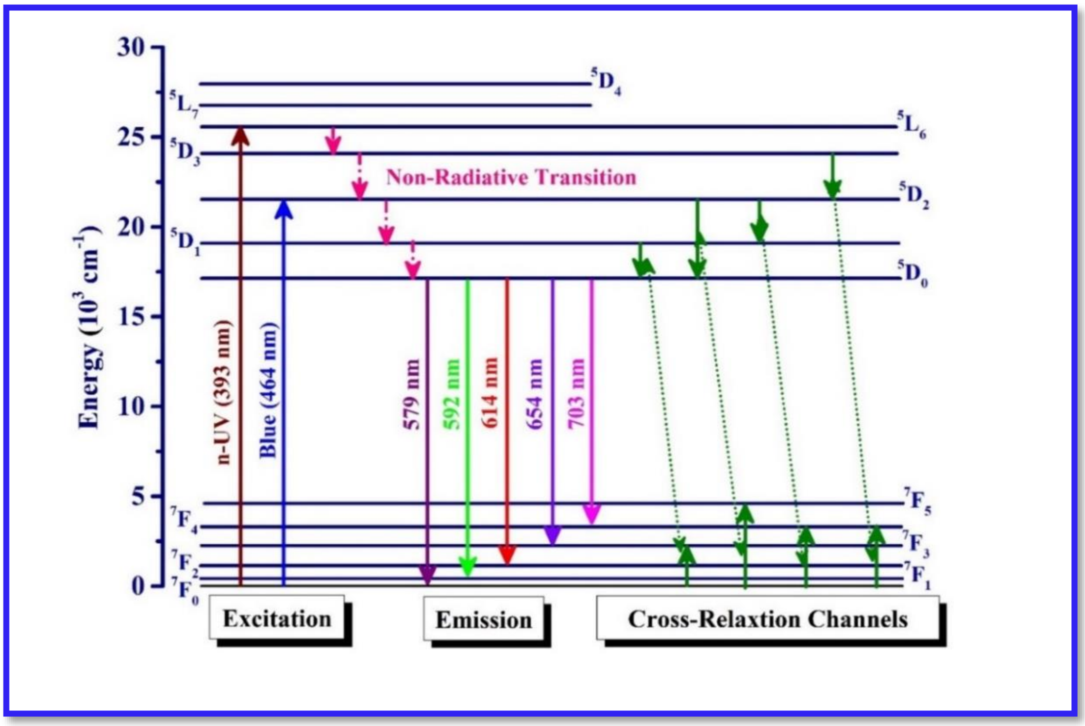

Fig. 4.10. *Partial energy level scheme of the Eu^{3+} doped TKWZBi glasses.*

Owing to the appropriate energy gap among the $^5D_0$ and lower energy level ($^7F_5$), radiative transition (RT) takes place from the $^5D_0$ level to $^7F_0$, $^7F_1$, $^7F_2$, $^7F_3$ and $^7F_4$ levels and indicates different emission peaks at 579, 592, 614, 654 and 703, respectively. Moreover, NRT is depicted with dotted arrows, whereas vertical up and down solid lines illustrate excitation and radiative emission, respectively. The NRT may occur due to the possible resonant energy transfer (RET) or cross-relaxation channels (CRCs). For the studied TKWZBiEu glasses, the possible CRCs are provided below [147]:

CRC 01: $^5D_1 + {}^7F_0 \rightarrow {}^5D_0 + {}^7F_3$

CRC 02: $^5D_2 + {}^7F_0 \rightarrow {}^5D_0 + {}^7F_5$

CRC 03: $^5D_2 + {}^7F_0 \rightarrow {}^5D_1 + {}^7F_4$

CRC 04: $^5D_3 + {}^7F_0 \rightarrow {}^5D_2 + {}^7F_4$

4.3.6. Estimation of CIE Chromaticity Coordinates, CCT and Color Purity

To realize the final emission color of the prepared TKWZBiEu glass samples, CIE chromaticity coordinates have been estimated. The CIE (x, y) coordinates of the prepared TKWZBiEu glass matrix have been evaluated via employing the emission spectra measured under n-UV and blue excitations. The CIE coordinates are found to be (0.658, 0.340) and (0.658, 0.341) for the optimized TKWZBiEu$_{5.0}$ under n-UV and blue excitations, respectively, and situated in the reddish zone of the CIE plot as displayed in Fig. 4.11. The coordinates for the optimized TKWZBiEu$_{5.0}$ glass matrix are near to the color coordinates of National Television Standard Committee (NTSC) (0.670, 0.330) and Y_2O_2S: Eu^{3+} commercial red phosphor (0.647, 0.343) [93]. Furthermore, correlated color temperature (CCT) was assessed via utilizing a given expression presented in *equation (1.10)*, to evaluate the quality of the light.

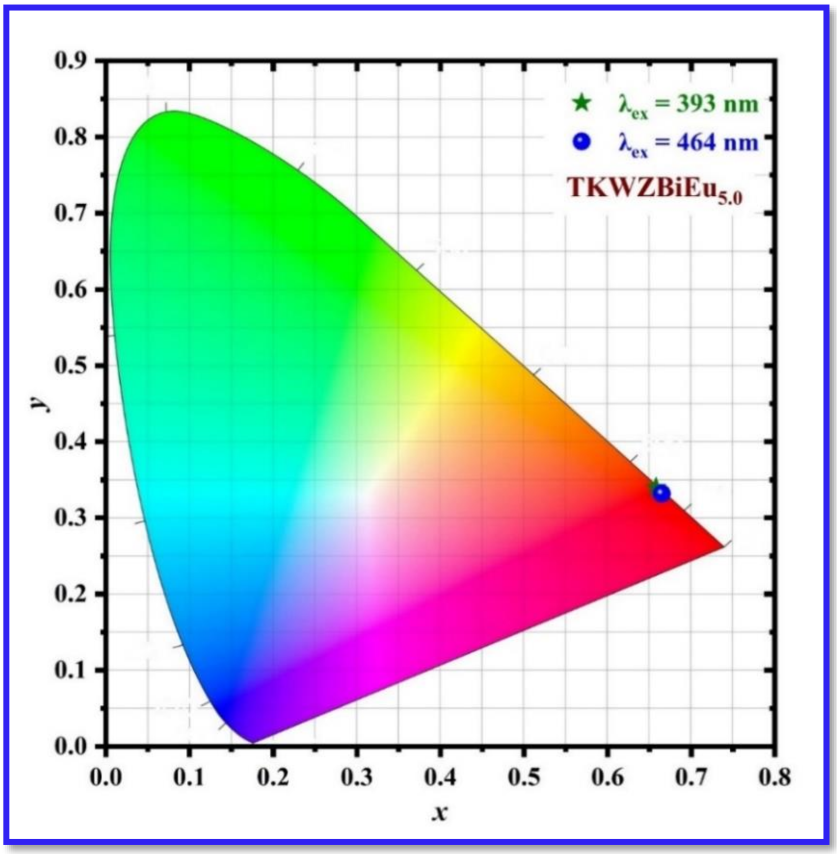

Fig. 4.11. *CIE chromaticity diagram of the optimized TKWZBiEu$_{5.0}$ glass under n-UV and blue excitations.*

The CCT value for the optimized $TKWZBiEu_{5.0}$ glass matrix has been found to be 2970 and 2939 K under n-UV and blue excitations, respectively, which are less than 5000 K. Furthermore, the color purity (CP) (or) color saturation (CS) of prepared TKWZBiEu glasses have been estimated employing the following relation [149]:

$$CP = \sqrt{\frac{(x-x_{ee})^2+(y-y_{ee})^2}{(x_d-x_{ee})^2+(y_d-y_{ee})^2}} \times 100 \tag{4.4}$$

here, (x, y) represents the color coordinates of TKWZBiEu glass samples, (x_{ee}, y_{ee}) illustrates equal energy points and (x_d, y_d) implies the dominant wavelength points, respectively. Under n-UV and blue excitations, the CP for optimized $TKWZBiEu_{5.0}$ glass was observed to be 99.01 and 99.10%. Henceforth, the aforementioned parameters like CIE coordinates, CCT, and CP values validate that the prepared TKWZBiEu glasses may be useful candidates to include as a red luminescent component in the realm of photonic device applications.

4.3.7. Decay Profile Analysis

The decay profiles of the prepared TKWZBiEu glasses have been assessed at ambient temperature by keeping the emission wavelength at 614 nm under n-UV excitation, as demonstrated in Fig. 4.12. The decay profiles of the prepared TKWZBiEu glass samples reveal the single-exponential behavior and follow (*equation 2.8)*. The lifetime values for TKWZBiEu glasses under n-UV excitation have been tabulated in Table 4.02. It was evident from Table 4.02 that the lifetime value decreases with an increment in the concentration of Eu^{3+} ions owing to existing non-radiative processes (CRCs) between the dopant (Eu^{3+}-Eu^{3+}) ions [147].

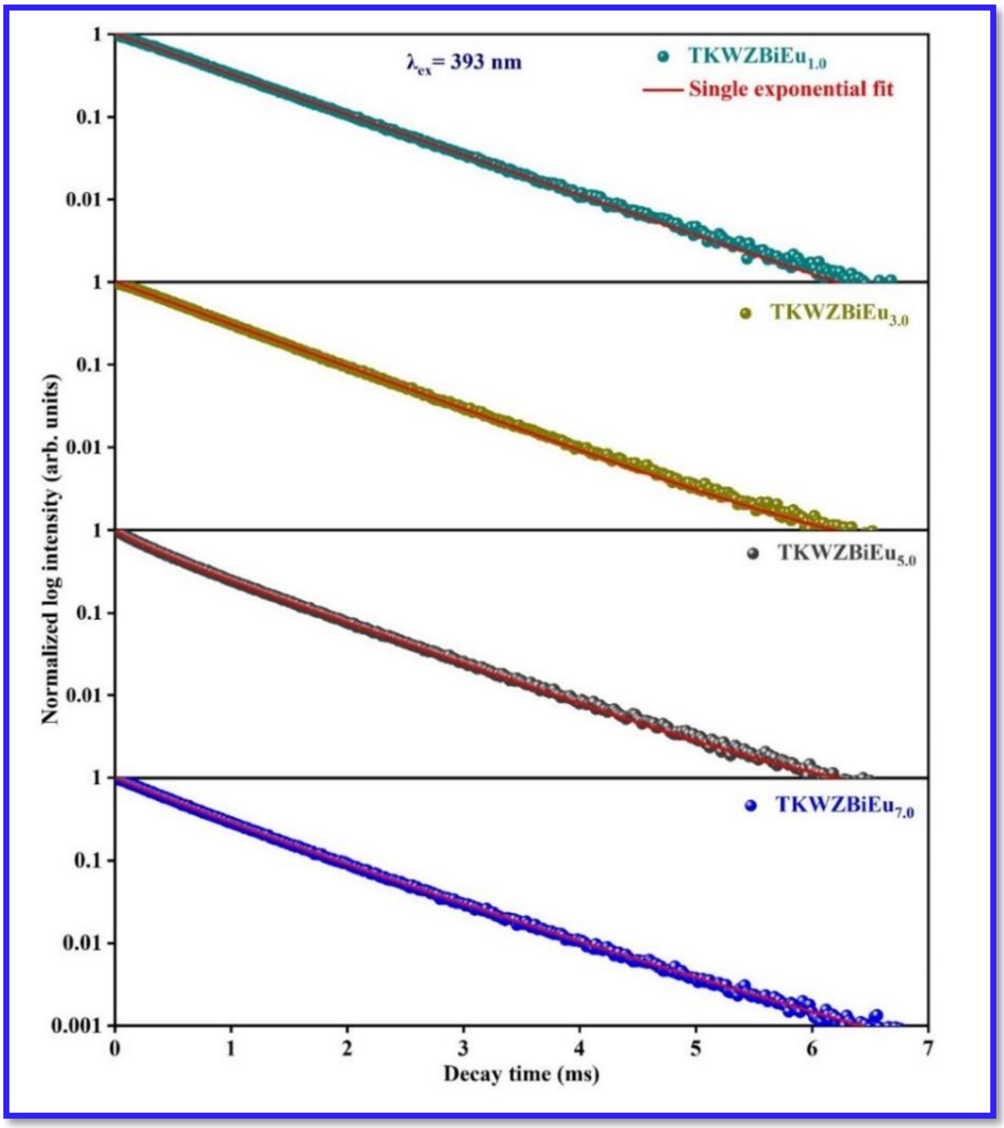

Fig. 4.12. *Decay profiles for prepared TKWZBiEu glasses under n-UV excitation.*

Table 4.02. Experimental decay time (τ) for $^5D_0$ level ($\lambda_{em} = 614\, nm$) of the prepared TKWZBi glasses under n-UV excitation.

Glass sample	τ (n-UV excitation) (ms)
TKWZBiEu$_{1.0}$	0.885
TKWZBiEu$_{3.0}$	0.813
TKWZBiEu$_{5.0}$	0.701
TKWZBiEu$_{7.0}$	0.635

4.3.8. Thermal Quenching Behaviour and Fabrication of Organic Resin/Binder Free Prototype Device

Temperature dependent photoluminescence (TDPL) is the most powerful characterization tool for materials to investigate thermal stability from the practical point of view for photonic device applications. This characterization allows us to understand better the thermal quenching behavior of the prepared luminescent materials (crystalline or non-crystalline). The relation between emission spectra with varying temperatures from RT (298 K) to 448 K of $TKWZBiEu_{5.0}$ glass sample under n-UV excitation is presented in Fig. 4.13. The PL intensity is reduced with the rise in temperature in a range from room temperature to 448 K.

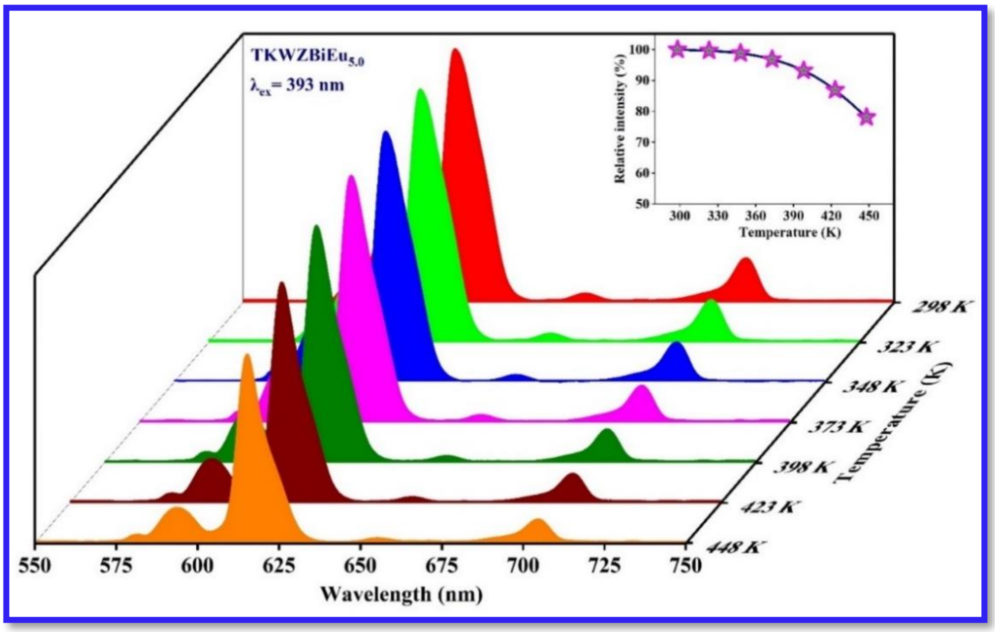

Fig. 4.13. *Temperature dependent photoluminescence spectra of $TKWZBiEu_{5.0}$ glass with the rise in temperature from room temperature to 448 K. Inset plot shows the intensity variation with temperature.*

The inset of Fig. 4.13 indicates the relationship between relative intensity (%) with respect to temperature (Kelvin). The emission peak position of the $TKWZBiEu_{5.0}$ glass sample remains unchanged with varying temperatures while the emission intensity decreases with an increment in temperature. The emission intensity of the TKWZBiEu$_{5.0}$ glass sample sustained up to 95.85% at 373 K and 86.87% at 448 K, which indicates that the prepared TKWZBiEu$_{5.0}$ glass has excellent thermal stability. Furthermore, the thermal stability of TKWZBiEu$_{5.0}$ glass has been analyzed by estimating activation energy (ΔE) with the following Arrhenius *equation (2.11)*. The slope of the straight-line fitted graph among $ln\left[\left({}^{I_0}/_{I_T}\right) - 1\right]$ and ${}^{1}/_{K_B T}$ provides the value of ΔE, which is illustrated in Fig. 4.14. The estimated ΔE value (0.447 eV) is much higher than the value reported earlier [63, 150]. Furthermore, the prototype device has been fabricated to reveal the practical application of Eu^{3+} doped TKWZBi glass via attaching the prepared glass on n-UV LED chip with the 395 nm excitation wavelength. Fig. 4.15. depicts the electroluminescent (EL) profile of optimized TKWZBiEu$_{5.0}$ glass after applying a voltage of 12.0 V and current (I) in a range from 50 mA to 800 mA. The photographs of the device under voltage (V = 12.0 V) and current (I = 50 mA & I = 800 mA), which clearly demonstrate that the sample emits red luminescence using an n-UV LED chip. Hence, the aforementioned results validate that the optimized TKWZBiEu$_{5.0}$ glass sample is a potential candidate for the fabrication of epoxy resin free red emitting luminescent devices.

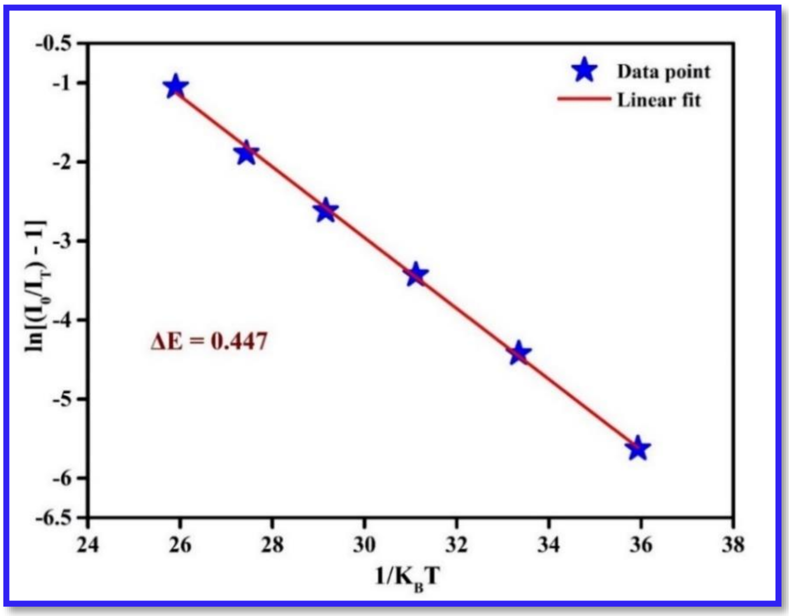

Fig. 4.14. *Linear fitted plot between ln [(I_0/I_T) – 1] against 1/K_BT for TKWZBiEu$_{5.0}$ glass.*

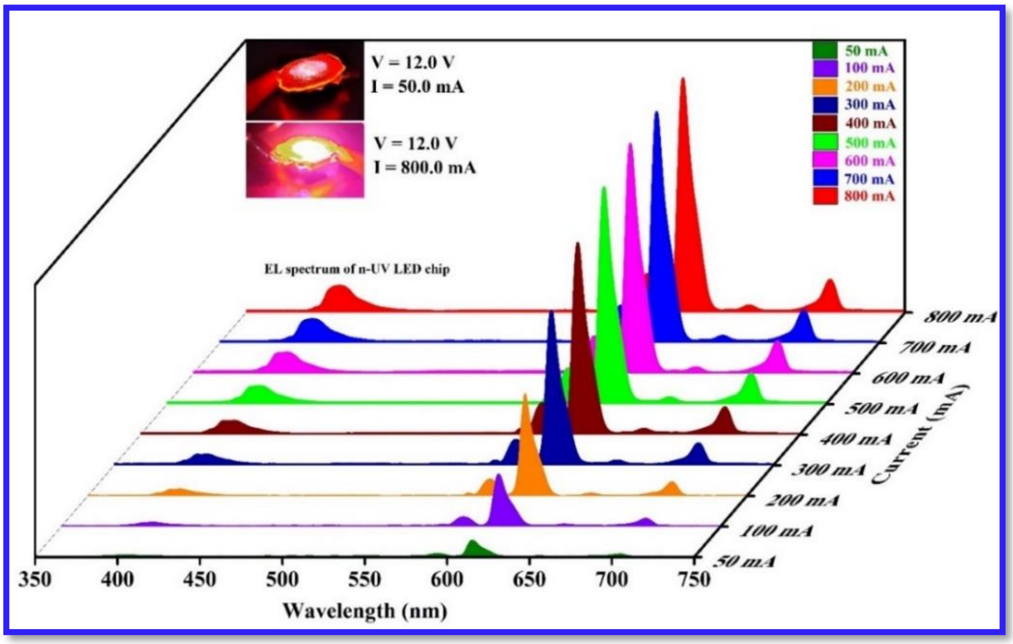

Fig. 4.15. *Emission spectra of 5.0 mol% Eu^{3+} doped TKWZBi glass under 395 nm n-UV LED chip driven at 12.0 volt. (The inset shows the photographs with V = 12.0 V & I = 50 mA and V = 12.0 V & I = 800 mA).*

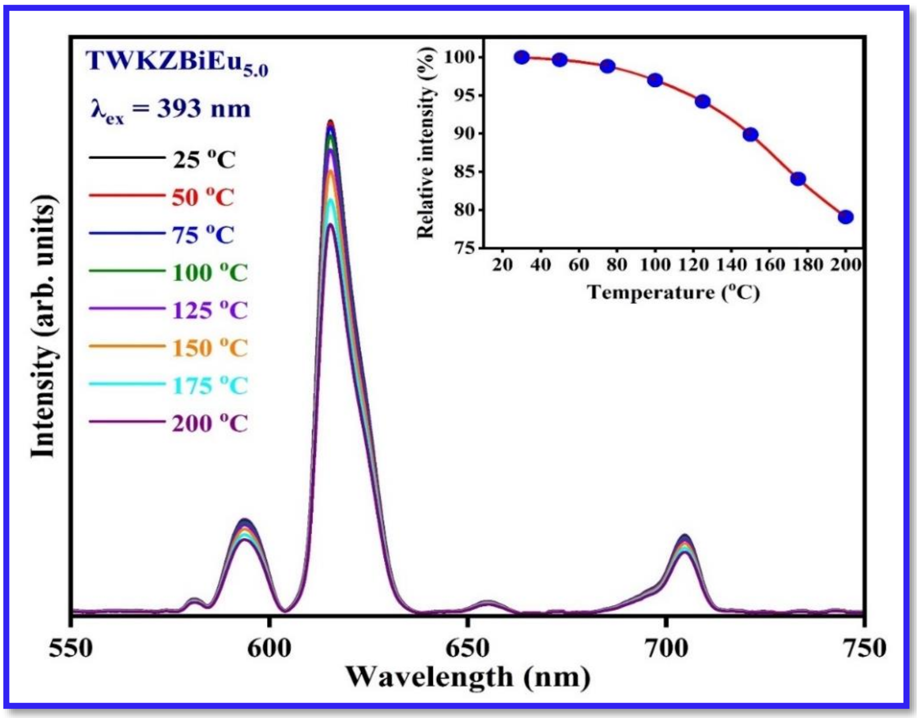

Fig. 4.16. *Temperature dependent photoluminescence spectra of TWKZBiEu$_{5.0}$ glass with the rise in temperature from room temperature (25 ºC) to 200 ºC. The inset plot shows the intensity variation with temperature.*

Furthermore, the temperature dependent emission profiles of the $TWKZBiEu_{5.0}$ glass have been measured under n-UV excitation wavelength along with varying temperatures from room temperature to 200 ºC, as represented in Fig. 4.16. It has been noted that the emission intensity of the $TWKZBiEu_{5.0}$ glass declines with an upsurge in the temperature profiles from room temperature to 175 ºC. The emission intensity of the $TWKZBiEu_{5.0}$ glass retained up to 96.990% at 100 ºC and 89.875% at 150 ºC, suggesting that the prepared $TWKZBiEu_{5.0}$ glass has excellent thermal stability. Based on the data presented in Fig. 4.13 and 4. 16, it is obvious that the $TWKZBiEu_{5.0}$ glass exhibits greater thermal stability in comparison to the $TKWZBiEu_{5.0}$ glasses. This suggests that the TWKZBi glasses are of higher thermal stability and used for further investigation in the upcoming chapters.

4.4. Conclusions

Transparent and thermally stable glass series of potassium tungstate-tellurite (TKWZBi) with varying Eu^{3+} ion concentrations have been synthesized via traditional melt quenching procedure. The TGA-DSC analysis performed on the TKWZBi glass host matrix affirms the thermal stability and aggregated weight loss at higher temperatures. A wide band in the XRD validated the non-crystalline/amorphous behaviour of the TKWZBiEu glass. Various functional linkages that exist in the prepared TKWZBiEu glass matrix were scrutinized through FT-IR spectroscopy. Using absorption spectra, the optical band gap energy (E_{opt}) of the prepared TKWZBiEu glasses have been assessed with the help of Tauc's plot. PLE spectrum exhibited numerous excitation peaks originating from the *4f-4f* electronic transition of Eu^{3+} ions in the range from 325 to 550 nm with intense peaks at 393 (n-UV) and 464 nm (blue). Among all five emission peaks in the PL spectra, an intense peak has been detected at 614 nm wavelength ascribed to $^5D_0 \rightarrow {}^7F_2$ transition for all prepared TKWZBiEu glasses under n-UV and blue excitations. The optimal concentration of the Eu^{3+} ions in the TKWZBiEu glasses was observed to be 5.0 mol%. The chromaticity coordinates of all TKWZBiEu glasses have been located in the red zone of the CIE diagram under n-UV and blue excitations. The decay profiles of the prepared TKWZBiEu glasses reveal the single-exponential behaviour under n-UV excitation. Temperature-dependent PL analysis has been conducted for an optimized $TKWZBiEu_{5.0}$ (5.0 mol% Eu^{3+} doped) glass and demonstrates its thermal stability along with high activation energy. An organic resin-free prototype device has been fabricated using the combination of optimized $TKWZBiEu_{5.0}$ glass and n-UV LED chip. Hence, the TWKZBi glasses are of higher thermal stability and used as a better encapsulant as well as a luminescent converter for fabricating binder-free light-emitting diodes.

Chapter – 05

Colour Tunable and Warm White Light Emitting Thermally Stable (Dy^{3+}/Sm^{3+}) and (Dy^{3+}/Eu^{3+}) Co-activated Tungstate-Tellurite Glasses for Solid State Lighting Applications

Transparent single Sm^{3+} and Dy^{3+}/Sm^{3+} co-activated tungstate-tellurite (TWKZBi) glass matrices were synthesized via a melt quenching process. The optical features of the prepared glass matrices were examined with the aid of the absorption spectra. Sm^{3+} doped TWKZBi (TWKZBiSm) glass matrices reveal a strong intense emission peak at ~600 nm related to the orange red ($^4G_{5/2} \rightarrow {}^6H_{7/2}$) transition. In Dy^{3+}/Sm^{3+} co-doped glasses, the emission intensity progressively surges with an increment in Sm^{3+} ion content (up to 1.5 mol%), confirming the ET mechanism between Dy^{3+} and Sm^{3+} ions. Likewise, Dy^{3+}/Eu^{3+} dual doped glasses demonstrate intense emission peaks in the blue, yellow and red regions of the electromagnetic spectrum. Application of Dexter's ET formulation with Reisfeld's approximation revealed that the ET mechanism involves a non-radiative dipole-dipole (d-d) interaction between (Dy^{3+} to Sm^{3+}) and (Dy^{3+} to Eu^{3+}) ions. The average lifetime (τ_{avg}) values for the $^4F_{9/2}$ state of Dy^{3+} ions in the TWKZBiDySm and TWKZBi: Dy^{3+}/Eu^{3+} glass samples were measured and found that these values decreased with increasing Sm^{3+} and Eu^{3+}ion contents. In addition, the ET efficiencies $(\eta_{Dy \rightarrow Sm})$ of the TWKZBiDySm and TWKZBi: Dy^{3+}/Eu^{3+}glass matrices were evaluated using the lifetime curves. The color coordinates (x, y) and the correlated color temperature (CCT) values of the co-activated glass samples were estimated. Based on the chromaticity coordinates and CCT values, it was found that the desired color of the TWKZBiDySm glass samples can be modulated from warm white

light to orange-red light and warm white to red light by precisely adjusting the concentration of Sm^{3+} and Eu^{3+} ions and at specified n-UV/blue excitations, respectively. Furthermore, the emission intensity observed at 373 K was 83.83% for TWKZBiDySm and 85.92% at 373 K for TWKZBi: Dy^{3+}/Eu^{3+} glasses compared to the emission intensity at the initial temperature, indicating the excellent thermal stability of the prepared glasses. The above results confirm that the prepared (Dy^{3+}/Sm^{3+}) and (Dy^{3+}/Eu^{3+}) co-activated TWKZBi glass matrix can be a promising candidate for white light and other photonic devices.

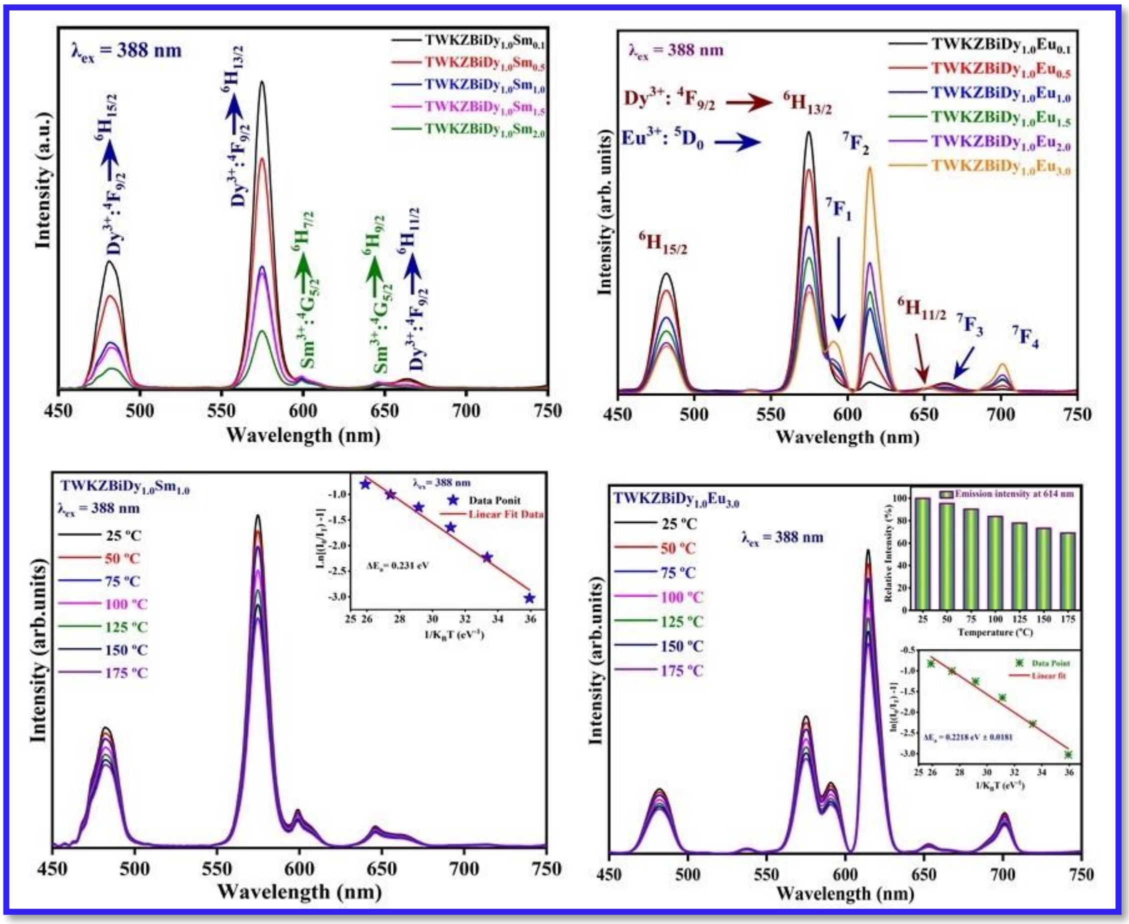

Part of this work has been published in
Journal of Luminescence 266 (2024) 120276 (I.F.: 3.60)
&
Communicated in
Journal of Molecular Structure (I.F.: 4.00)

5.1. Introduction

In Chapter 4, Eu^{3+} activated alkali (Li, Na and K) tungstate-tellurite glasses have been synthesized with the help of the melt melt-quenching approach. The potassium tungstate-tellurite glass demonstrates relatively higher luminescent properties than the remaining alkali-based tungstate tellurite glasses. However, REIs-activated glasses exhibit many remarkable properties as they offer low manufacturing cost, high thermal stability, excellent solubility of REIs, easy formability and uniform luminescence. These glasses are mainly used in optical applications including optical amplifiers, optical detectors, optical fibers, and display devices. Moreover, REIs have significant dopant character due to their *4f* valance shell and distinct energy level distribution [151-153]. The sensitizer can also be utilized along with the activator to improve the emission profiles of activator ions. Among various sensitizers, dysprosium (Dy^{3+}) has been found to be the most suitable sensitizer. Dy^{3+}-activated glass matrices are interesting to study as they can produce isolated white light due to their characteristic yellow and blue emission peaks. Nevertheless, w-LED consists of a Dy^{3+}-activated glass matrix, which has a low CRI and high CCT due to the absence of red color, hinders their practical applications [71, 154]. In the current research, co-doping with trivalent samarium (Sm^{3+}) and europium (Eu^{3+}) ions is used to overcome the mentioned shortcomings, since it produces a strong emission intensity in the orange-red and red regions [154, 155]. Then there is the probability of achieving both white light and multi-coloured emission by appropriately changing the content of Sm^{3+} and Eu^{3+} ions in the glass matrix.

Tellurite based glasses have been considered the most admirable glass formers among the various glass forming oxides owing to their numerous unique features, including low melting temperature (≈ 850 ºC), wide transmission ranges from 0.4 to 5.0 μm, minimum phonon energy (≈ 800 cm^{-1}), maximum refractive index (≈ 1.9-2.5) and better solubility of REIs [25, 71]. As tellurite glasses possess low phonon energy, the light output shall be enhanced by reducing the non-radiative transition (NRT) between the higher and lower energy states of REIs. Tellurium oxide (TeO_2) not only acts as a conditional glass former but also ensures a durable glass due to the existence of certain glass modifiers such as tungsten trioxide (WO_3). The addition of WO_3 in tellurite glasses can act as an excellent modifier helping to increase chemical stability and quantum efficiency and reduce non-radiative losses [71, 108]. Furthermore, the inclusion of K_2O, ZnO, and Bi_2O_3 has been used to synthesize glass for several scientific patronages [71].

In the current research, the melt quenching approach was used to synthesize the single Sm^{3+}, (Dy^{3+}/Sm^{3+}) and (Dy^{3+}/Eu^{3+}) co-activated TWKZBi glasses. The optical, luminescent characteristics and the ET mechanism among (Dy^{3+} to Sm^{3+}) and (Dy^{3+} to Eu^{3+}) as well as lifetime measurements were studied in detail. In addition, the CIE coordinates and TDPL studies of these glasses were examined to investigate the suitability of these glasses for solid state lighting applications.

5.2. Experimental Procedure and Characterization Tools

TWKZBi glasses activated with single Dy^{3+}, Sm^{3+}, double (Dy^{3+}/Sm^{3+}) and (Dy^{3+}/Eu^{3+}) ions were synthesized via a melt-quenching approach as described in *section 2.2.1*. The molar composition (in mol%) of the titled TWKZBi glasses is mentioned as given below:

1) $49.0\ TeO_2 – 20.0\ WO_3 – 15.0\ K_2O – 10.0\ ZnO – 5.0\ Bi_2O_3 – 1.0\ Dy_2O_3$, sample named as $TWKZBiDy_{1.0}$.
2) $(50.0 – x)\ TeO_2 – 20.0\ WO_3 – 15.0\ K_2O – 10.0\ ZnO – 5.0\ Bi_2O_3 – x\ Sm_2O_3$.

The Sm_2O_3 ion concentration (x) varies from 0.1 to 2.0 mol% (i.e., 0.1, 0.5, 1.0, 1.5, and 2.0 mol% and are given as $TWKZBiSm_{0.1}$, $TWKZBiSm_{0.5}$, $TWKZBiSm_{1.0}$, $TWKZBiSm_{1.5}$ and $TWKZBiSm_{2.0}$, respectively). (Dy^{3+}/Sm^{3+}) and (Dy^{3+}/Eu^{3+}) co-activated TWKZBi glasses were synthesized with a fixed Dy^{3+} concentration of 1.0 mol% along with varying Sm^{3+} and

Eu^{3+} ion concentrations. The transparent TWKZBi glasses co-activated with (Dy^{3+}/Sm^{3+}) and (Dy^{3+}/Eu^{3+}) have the molar compositions (in mol%) are given below:

3) (49.0-y) TeO_2 – 20.0 WO_3 – 15.0 K_2O – 10.0 ZnO – 5.0 Bi_2O_3 – 1.0 Dy_2O_3 – y Sm_2O_3

4) (49.0-z) TeO_2 – 20.0 WO_3 – 15.0 K_2O – 10.0 ZnO – 5.0 Bi_2O_3 – 1.0 Dy_2O_3 – z Eu_2O_3

The Sm_2O_3 (y) ion concentrations were assumed to be 0.1, 0.5, 1.0, 1.5 and 2.0 mol% and the samples were designated $TWKZBiDy_{1.0}Sm_{0.1}$, $TWKZBiDy_{1.0}Sm_{0.5}$, $TWKZBiDy_{1.0}Sm_{1.0}$, $TWKZBiDy_{1.0}Sm_{1.5}$ and $TWKZBiDy_{1.0}Sm_{2.0}$, respectively. Further, the Eu_2O_3 (z) ion concentrations were assumed to be 0.1, 0.5, 1.0, 1.5, 2.0 and 3.0 mol% and the sample's name was designated as $TWKZBiDy_{1.0}Eu_{0.1}$, $TWKZBiDy_{1.0}Eu_{0.5}$, $TWKZBiDy_{1.0}Eu_{1.0}$, $TWKZBiDy_{1.0}Eu_{1.5}$, $TWKZBiDy_{1.0}Eu_{2.0}$, and $TWKZBiDy_{1.0}Eu_{3.0}$, respectively. Finally, transparent glasses were obtained for further characterization.

5.3. Results and Discussion

5.3.1. Optical Absorption Studies of Dy^{3+}/Sm^{3+} Co-activated **TWKZBi** *Glasses*

The optical absorption spectra for $TWKZBiDy_{1.0}$, $TWKZBiSm_{1.0}$ and $TWKZBiDy_{1.0}Sm_{1.0}$ glass matrices were measured in the spectral range from n-UV to NIR (350 – 2000 nm) at ambient temperature as displayed in Fig. 5.01 (a-c). The spectrum shows seven absorption peaks assigned to Dy^{3+} ions centred at 454, 758, 804, 909, 1104, 1284 and 1696 nm observed in the prepared $TWKZBiDy_{1.0}$ and $TWKZBiDy_{1.0}Sm_{1.0}$ glasses. These transitions were initiated from the lower energy level ($^6H_{15/2}$) to the numerous upper energy levels including $^4I_{15/2}$, $^4F_{3/2}$, $^6F_{5/2}$, $^6F_{7/2}$, $^6F_{9/2}$, $^6F_{11/2}$ + $^6H_{9/2}$ and $^6H_{11/2}$ respectively [71, 154]. For Sm^{3+} ions, the spectrum consists of seven absorption peaks initiating from the ground energy level ($^6H_{5/2}$) and located at 476, 956, 1091, 1241, 1390, 1495 and 1555 nm found in $TWKZBiSm_{1.0}$ and $TWKZBiDy_{1.0}Sm_{1.0}$ glasses. These absorption peaks were excited from the $^6H_{5/2}$ energy state to several upper energy states including ($^{4}I_{13/2} + {}^{4}I_{11/2} + {}^{4}M_{15/2}$), $^{6}F_{11/2}$, $^{6}F_{9/2}$, $^{6}F_{7/2}$, $^{6}F_{5/2}$, $^{6}F_{3/2}$ and $^{6}H_{15/2}$, respectively [3, 156].

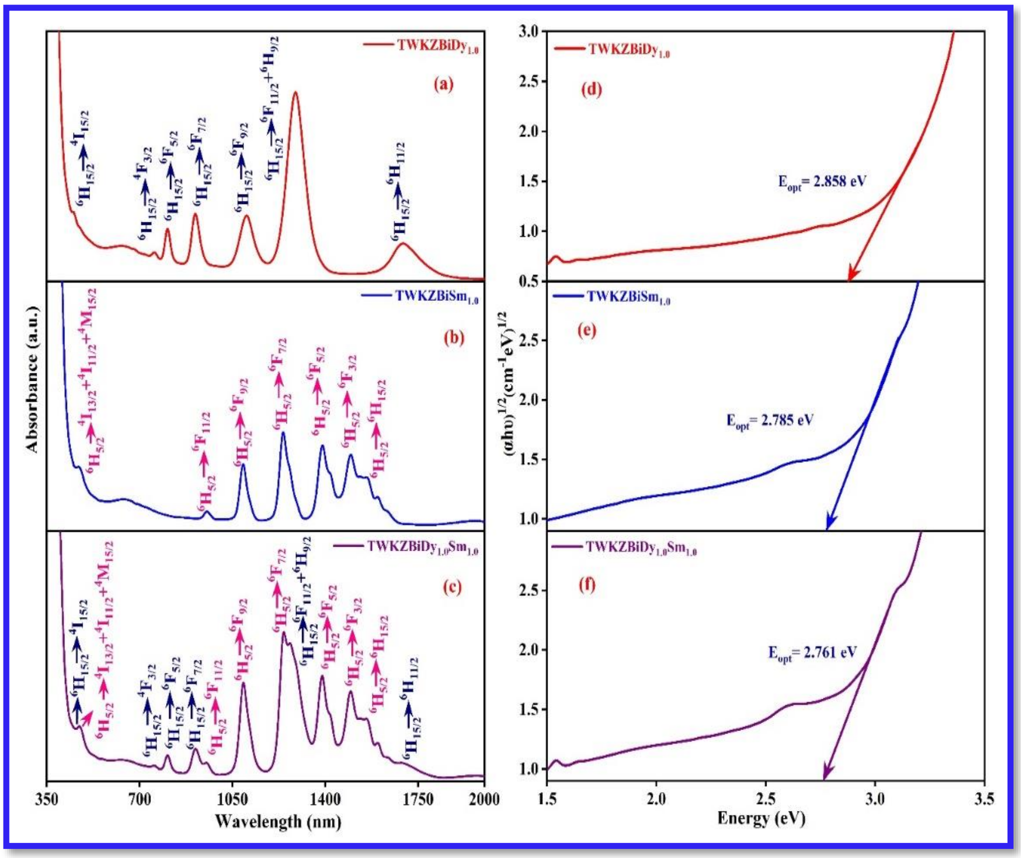

Fig. 5.01. **(a)** *The absorption spectrum of the TWKZBiDy$_{1.0}$,* **(b)** *TWKZBiSm1.0 and* **(c)** *TWKZBiDy$_{1.0}$Sm$_{1.0}$ glass sample,* **(d)** *The band gap energy for an indirect allowed transition of the TWKZBiDy$_{1.0}$,* **(e)** *TWKZBiSm$_{1.0}$ and* **(f)** *TWKZBiDy$_{1.0}$Sm$_{1.0}$ glass sample using Tauc's plot.*

The absorption peaks observed in the n-UV and visible regions were less intense whereas in the NIR region, the strong absorption peaks are due to the following selection criteria, such as spin allowed ($\Delta S = 0$) and orbital angular momentum rule ($\Delta L = 2$) [3, 157]. Among all the absorption peaks, the strong absorption peak at 1284 nm (Dy^{3+}) related to the $^{6}H_{15/2} \rightarrow {}^{6}F_{11/2} + {}^{6}H_{9/2}$ transition and at 1241 nm (Sm^{3+}) attributed to the $^{6}H_{5/2} \rightarrow {}^{6}F_{7/2}$ transition was observed to be hypersensitive and meets with the selection criteria, including $|\Delta S| = 0$, $|\Delta L| \leq 2$, and $|\Delta J| \leq 2$ [3, 154].

5.3.1.1. Optical Bandgap, Urbach Energy and Refractive Index Analysis

The optical band gap energy $\left(E_{opt}\right)$ for the prepared glass samples of TWKZBiDy$_{1.0}$, TWKZBiSm$_{1.0}$ and TWKZBiDy$_{1.0}$Sm$_{1.0}$ was evaluated with the optical absorption spectra via the following Davis and Mott relationship as expressed in *equation (3.3)*. The allowed indirect E_{opt} for prepared glasses were estimated using Tauc's diagram via extrapolating the straight line to the plot $(\alpha h\nu)^{1/2}$ versus energy (eV), as demonstrated in Fig. 5.01 (d-f). The observed indirectly allowed E_{opt} values for TWKZBiDy$_{1.0}$, TWKZBiSm$_{1.0}$ and TWKZBiDy$_{1.0}$Sm$_{1.0}$ glasses are 2.858, 2.785 and 2.761 eV, respectively. In addition, most non-crystalline or amorphous materials possess fundamental edges that confirm the presence of inter-band transition tails and are a crucial factor in predicting the level of disorder in the host matrix, termed as the Urbach energy [36]. The Urbach empirical formula has been proposed in *equation (2.7)*. The ΔE values were analyzed by plotting the graph of $ln\left(\alpha(\nu)\right)$ versus energy (eV) and then evaluating the inverse of the slope. Estimated ΔE values for the prepared TWKZBiDy$_{1.0}$, TWKZBiSm$_{1.0}$, and TWKZBiDy$_{1.0}$Sm$_{1.0}$ glasses were observed to be 0.181, 0.258, and 0.262, respectively. The lower values of Urbach energy designate the lower defect concentration in the prepared glasses [36]. Also, using the correlation proposed by Dimitrov *et al.*, the refractive index (n) of titled glasses was calculated using *equation (3.2)*. The observed values of n for the prepared TWKZBiDy$_{1.0}$, TWKZBiSm$_{1.0}$ and TWKZBiDy$_{1.0}$Sm$_{1.0}$ glasses are 2.425, 2.457 and 2.464, respectively.

5.3.2. PL Studies of Dy^{3+}/Sm^{3+} Co-activated TWKZBi *Glasses*

5.3.2.1. Luminescent Properties of TWKZBiSm *Glasses*

Fig. 5.02 (a) shows the PLE spectra for the TWKZBiSm glass matrices analyzed at ambient temperature (RT) in the spectral range from 325 to 500 nm with a fixed orange red emission wavelength (λ_{em} = 600 nm). The PLE spectra reveal multiple *4f-4f* transitions from the lowest energy state ($^6H_{5/2}$) to numerous higher energy states including $^4D_{3/2}$, $^4D_{1/2}$, $^4F_{7/2}$, $^4M_{19/2}$, $^4G_{9/2}$ and ($^4I_{13/2} + {}^4I_{11/2} + {}^4M_{15/2}$) are assigned to the excitation peaks of Sm^{3+} ions at 363, 376, 405, 418, 439 and 476 nm, respectively [3, 156].

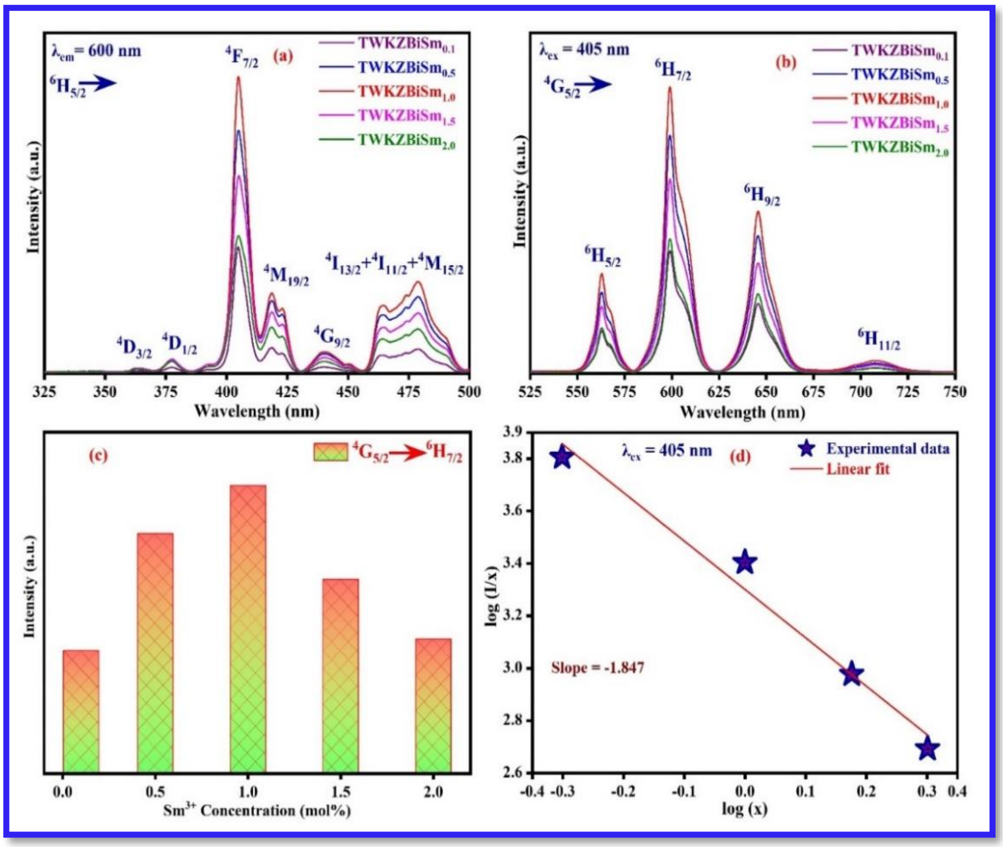

Fig. 5.02. **(a)** *Excitation spectra of Sm^{3+} doped TWKZBi (TWKZBiSm) glasses under 600 nm emission wavelength,* **(b)** *Emission spectra of TWKZBiSm glasses monitoring under 405 nm excitation wavelength,* **(c)** *The emission intensity variation with the dopant (Sm^{3+}) ion concentration in the prepared TWKZBiSm glasses and* **(d)** *The plot of log(I/x) versus log(x) for TWKZBiSm glasses.*

The PLE peak related to the $^6H_{5/2} \rightarrow {}^4F_{7/2}$ transition at 405 nm is utilized as the highest prominent peak among all these excitation peaks and was further used to examine the emission profiles of the prepared TWKZBiSm glass matrices. Fig. 5.02 (b) shows the emission spectral profiles of the TWKZBiSm glass matrices scanned in the wavelength range 525 to 750 nm at ambient temperature with monitored excitation at 405 nm. The four intense emission peaks in the emission spectra, located at 563, 600, 645 and 708 nm, are linked to the Sm^{3+} ions *4f-4f* transitions, including $^4G_{5/2} \rightarrow {}^6H_{5/2}$, $^4G_{5/2} \rightarrow {}^6H_{7/2}$, $^4G_{5/2} \rightarrow {}^6H_{9/2}$ and $^4G_{5/2} \rightarrow {}^6H_{11/2}$, respectively [3, 158]. Prominent and narrow emission bands were observed owing to the shielding influence of the $4f^6$ electrons with the external ligands. Both magnetic and electric dipole (MD) behavior is allowed for the emission peak at 600 nm assigned to the $^4G_{5/2} \rightarrow {}^6H_{7/2}$ transition [158].

Furthermore, the $^4G_{5/2} \rightarrow {}^6H_{5/2}$ (563 nm) transition reveals forbidden MD in behavior and satisfies the selection criteria $\Delta J = 0$, $J \neq 0 \leftrightarrow 0$ values. However, the transition ($^4G_{5/2} \rightarrow {}^6H_{9/2}$) at 645 nm has purely an ED character with the selection rule $\Delta J = \pm 2$ and the transition $^4G_{5/2} \rightarrow {}^6H_{11/2}$ (708 nm) is forbidden with the weak intensity by selection rule $\Delta J = \pm 3$ [158, 159]. In general, the ratio of the $^4G_{5/2} \rightarrow {}^6H_{9/2}$ (ED) to $^4G_{5/2} \rightarrow {}^6H_{5/2}$ (MD) is owing to the analysis of the degree of symmetry in the vicinity of the REIs. In the current research, the strength of the ED transition is significantly higher than the MD transition, indicating the asymmetric character of the TWKZBiSm glasses. With increasing Sm^{3+} ion concentrations, the ED to MD for the prepared TWKZBiSm glass samples ranges from 2.346 to 2.411. The observed ED to MD values were found to be greater than unity, indicating greater distortion from the inversion symmetry or asymmetric character of the neighbouring Sm^{3+} ions. Fig. 5.02 (c) shows a graphical representation of the correlation between the emission intensity of $^4G_{5/2} \rightarrow {}^6H_{7/2}$ transition and Sm^{3+} ion concentration. The emission intensity of the prepared TWKZBiSm glasses gradually surges up to 1.0 mol% Sm^{3+} ion content and thereafter gently declines with an increment in Sm^{3+} ion content due to concentration quenching phenomena. This phenomenon may be owing to non-radiative energy transfer (NRET) or multipolar-multipolar interaction among Sm^{3+}-Sm^{3+} ions. To comprehend the mechanism of concentration quenching, Dexter provided a theoretical explanation for the correlation between emission intensity and REI content. According to Dexter's theoretical model, the correlation between the variation in emission intensity (I) and the doping ion concentrations (x) is presented in *equation*

(4.3). In Fig. 5.02 (d) the parameter Q was analyzed via the slope of the diagram among log $\left(\frac{I}{x}\right)$ and $\log(x)$. The measured slope value (-1.847) of the straight line fit corresponds to Q/3, giving a Q value of -5.541, close to 6. Thus, the Q value designates that the multipolar interaction between the Sm^{3+} ions is related to the d-d interaction.

5.3.2.2. Luminescent Properties of TWKZBiDy *Glasses*

The PLE and emission spectra for the prepared $TWKZBiDy_{1.0}$ glass sample are depicted in Fig. 5.03 (a and b). The PLE spectrum shows several excitation peaks ascribed to the electronic transitions of the Dy^{3+} ions scanned at the yellow emission (575 nm).

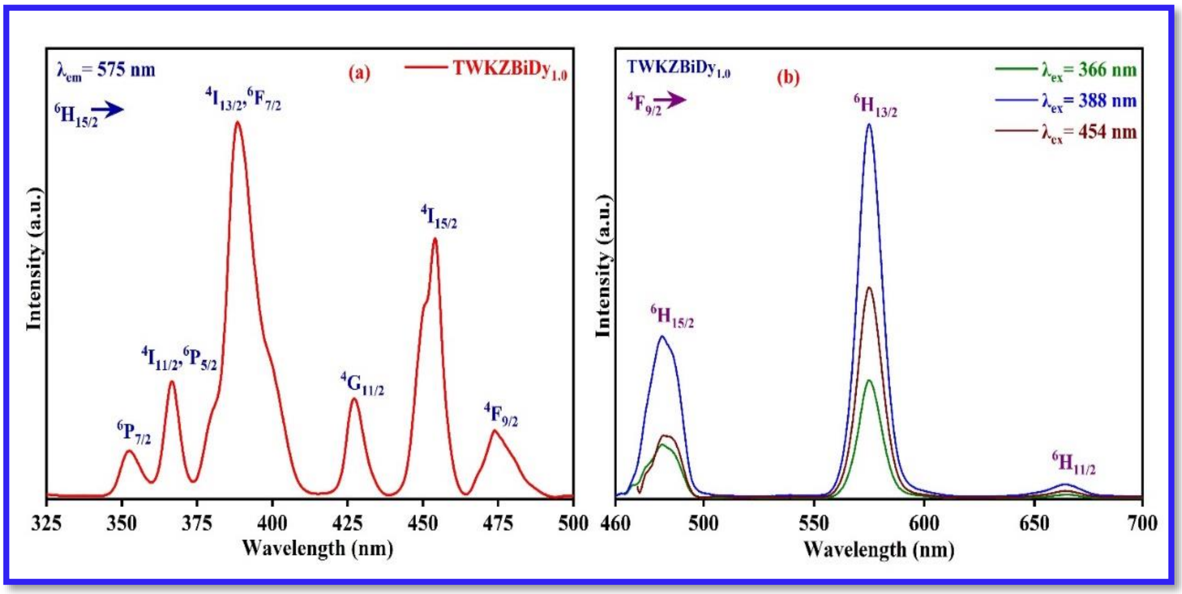

Fig. 5.03. (a) *Excitation spectrum of $TWKZBiDy_{1.0}$ glass under 575 nm emission wavelength and* **(b)** *Emission spectra for $TWKZBiDy_{1.0}$ glass sample under different excitation wavelengths 366, 388 and 454 nm.*

The detected excitation peaks were transformed from the lower lying energy state ($^6H_{15/2}$) to numerous higher lying energy states, including $^6P_{7/2}$, ($^4I_{11/2}$, $^6P_{5/2}$), ($^4I_{13/2}$, $^6F_{7/2}$), $^4G_{11/2}$, $^4I_{15/2}$ and $^4F_{9/2}$, respectively [36, 160]. As seen in Fig 5.03 (a), the peaks at 366 nm ($^4I_{11/2}$, $^6P_{5/2}$), 388 nm ($^4I_{13/2}$, $^6F_{7/2}$) and 454 nm ($^4I_{15/2}$) were further used to carry out the emission profiles of the prepared TWKZBiDy$_{1.0}$ glass sample. Under different excitations, the emission spectra of the TWKZBiDy$_{1.0}$ glass matrix were scanned in the spectral range from 460 to 700 nm and presented in Fig. 5.03 (b). The *4f-4f* transitions of Dy^{3+} ions such as $^4F_{9/2} \rightarrow {}^6H_J$ (where J= 11/2, 13/2 and 15/2) have been associated with three emission peaks located at 664 (red), 575 (yellow) and 481 nm (blue), respectively [161]. The emission peak at 575 nm ($^4F_{9/2} \rightarrow {}^6H_{13/2}$ transition) is associated with the forced ED behaviour, while the emission peak located at 481 nm ($^4F_{9/2} \rightarrow {}^6H_{15/2}$ transition) is associated with MD behaviour. In addition, the feeble emission peak at 664 nm is attributed to the $^4F_{9/2} \rightarrow {}^6H_{11/2}$ transition [160, 161]. The emission intensity corresponding to the $^4F_{9/2} \rightarrow {}^6H_{13/2}$ transition was higher than that of the $^4F_{9/2} \rightarrow {}^6H_{15/2}$ transition, indicating the presence of Dy^{3+} ions at low symmetry sites lacking an inversion center [160, 161].

5.3.2.3. Luminescent Properties of TWKZBiDySm *Glasses*

The PLE spectra of the TWKZBiDy$_{1.0}$Sm$_{1.0}$ glass sample were measured while monitoring emission peaks of Dy^{3+} at 575 nm and Sm^{3+} at 600 nm, as depicted in Fig. 5.04 (a). Several excitation peaks have been assigned to the characteristic Dy^{3+} and Sm^{3+} transitions. An intense absorption peak at 405 nm of Sm^{3+} has been observed as presented in Fig. 5.04 (a). Based on the excitation spectra of TWKZBiDy$_{1.0}$Sm$_{1.0}$, various excitation peaks, including 388 and 405 nm were considered as applicable excitation wavelengths for the series of prepared TWKZBiDySm glass samples. The energy transfer (ET) approach between REIs involves that an ion with a higher fluorescent energy level transferring energy to an ion with a lower fluorescent energy level [162]. According to the energy level diagram, the possible ET mechanism may occur from the Dy^{3+} to the Sm^{3+} ions (i.e., the fluorescent or excited energy level of Dy^{3+} has a higher fluorescence energy level than that of Sm^{3+} ions). One of the crucial criteria for the emergence of the ET mechanism is the agreement of the PL spectrum of the sensitizer/donor (Dy^{3+}) and the PLE spectrum of the acceptor/activator (Sm^{3+}). According to

Fig. 5.04 (b), the observed emission peak of Dy^{3+} ions at 481 nm ($^4F_{9/2} \rightarrow {}^6H_{15/2}$ transition) coincides with the PLE peak of Sm^{3+} ions around 476 nm, corresponding to $^6H_{5/2} \rightarrow {}^4I_{13/2} + {}^4I_{11/2} + {}^4M_{15/2}$ transition affirms the probability of the ET mechanism from Dy^{3+} to Sm^{3+} ions.

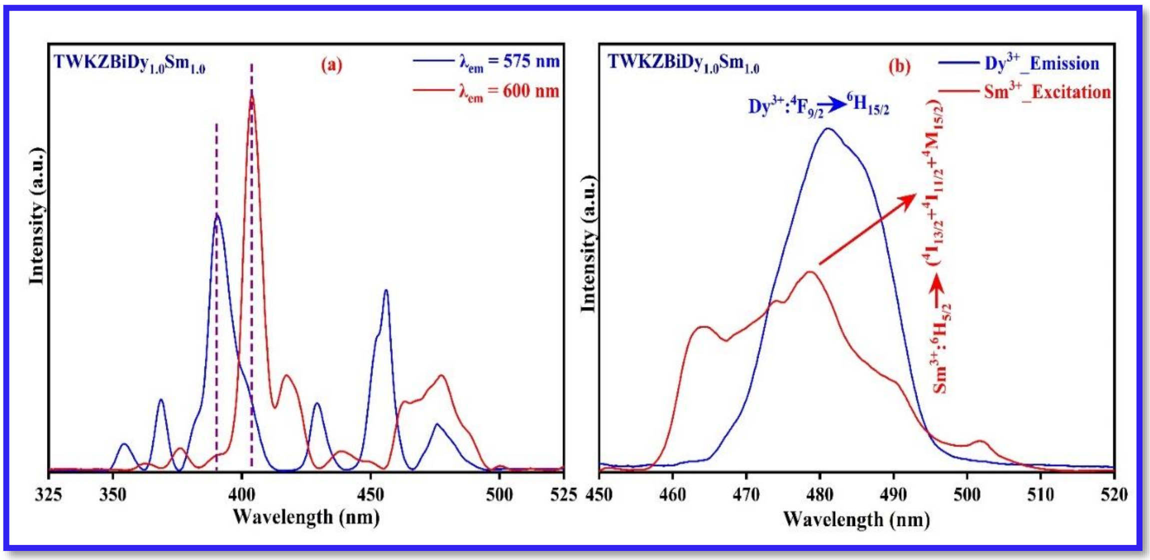

Fig. 5.04. **(a)** *PLE spectrum for 1.0 mol% Dy^{3+}/1.0 mol% Sm^{3+} co-doped TWKZBi (TWKZBiDy$_{1.0}$Sm$_{1.0}$) glass under 575 and 600 nm emission wavelength and* **(b)** *Spectral overlap of the sensitizer (Dy^{3+}) emission and activator (Sm^{3+}) excitation.*

Fig. 5.05 (a and b) illustrates the PL spectra of the TWKZBiDySm glass matrices, which were scanned in the 450 to 750 nm spectral range at RT via monitoring numerous excitation wavelengths including 388 and 405 nm. It was noticed that when the TWKZBiDySm glass matrices were excited with different Dy^{3+} ion wavelengths, three intense emission peaks located at 481, 575 and 664 nm associated with the $^4F_{9/2} \rightarrow {}^6H_J$ transitions (where J = 15/2, 13/2 and 11/2) and two less intense emission peaks from Sm^{3+} ions at 600 nm and 645 nm associated with the $^4G_{5/2} \rightarrow {}^6H_J$ transitions (where J = 7/2 and 9/2), were observed as illustrated in Fig. 5.05 (a). However, the PL spectra scanned under the excitation wavelength of Sm^{3+} ions give rise to six different emission peaks at 481, 563, 575, 600, 645, and 708 nm as depicted in Fig. 5.05 (b). Among them, the *4f-4f* transitions at 481 and 575 nm are corresponding to the

Dy^{3+} ions, and the remaining peaks at 563, 600, 645, and 708 nm were attributed to the Sm^{3+} ions [3, 163]. Fig. 5.05 (c and d) illustrates the variation of emission intensity of Dy^{3+} and Sm^{3+} with the Sm^{3+} ion concentrations. It was evident that the emission intensity of the Dy^{3+} peaks declines with an increment in Sm^{3+} ion concentrations up to 1.5 mol% and thereafter the intensity of the Sm^{3+} emission peaks diminishes owing to the concentration quenching mechanism.

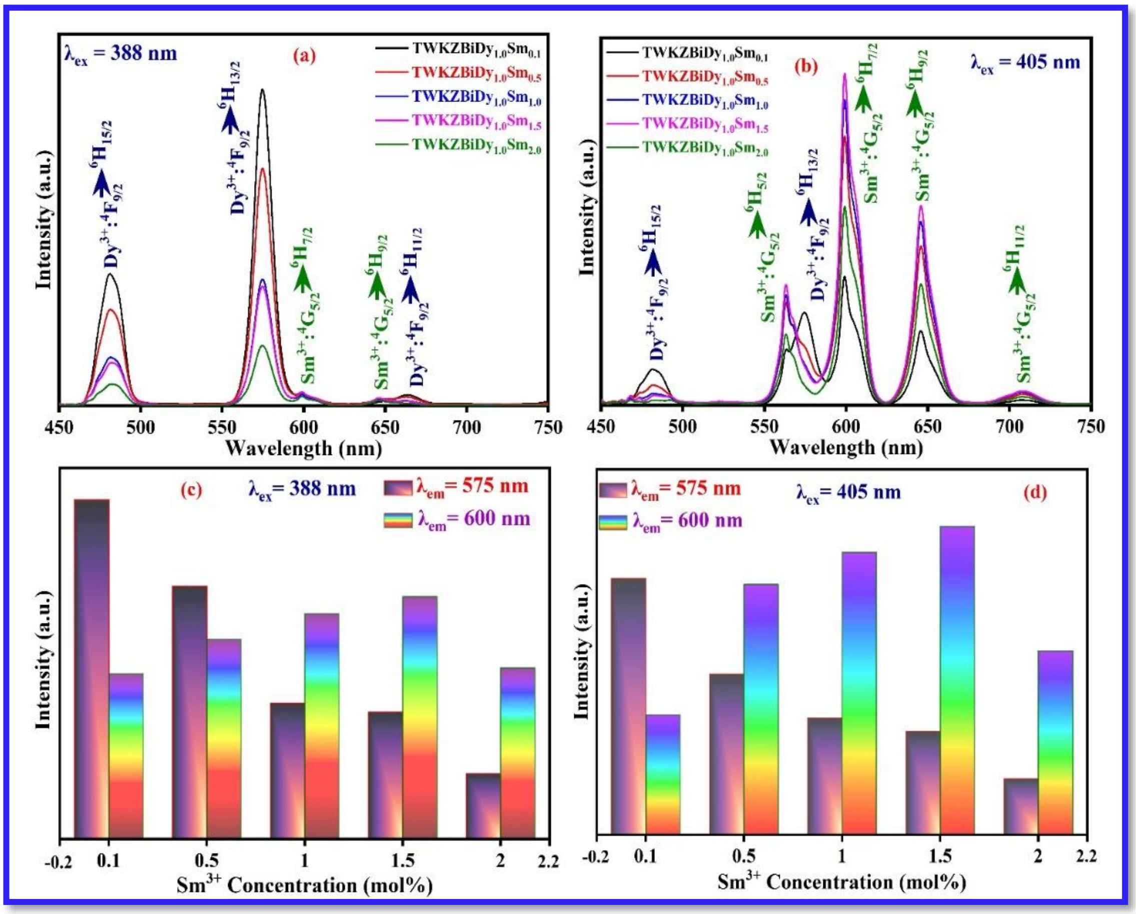

Fig. 5.05. (a) *Emission spectra for Dy^{3+}/Sm^{3+} co-doped TWKZBi (TWKZBiDySm) glasses under 388 nm excitation,* **(b)** *405 nm excitation,* **(c)** *The variation of Dy^{3+} and Sm^{3+} emission intensity along with varying the concentration of Sm^{3+} ions under 388 nm and* ***(d)*** *405 nm excitation wavelengths.*

The self-quenching phenomenon that occurs when energy is transferred from one Sm^{3+} ion to another Sm^{3+} ion reduces the probability of a radiative transition, which in turn can cause quenching. The decrease in emission intensity of Dy^{3+} is due to the ET mechanism from Dy^{3+} to Sm^{3+} ions.

The partial energy level scheme of the TWKZBiDySm glasses is demonstrated in Fig. 5.06 along with the estimated cross-relaxation channels (CRCs) for Dy^{3+} and Sm^{3+} ions and possible ET processes. For TWKZBiDy1.0 glasses, the Dy^{3+} ions in the lower energy state ($^6H_{15/2}$) are excited to higher energy states including ($^4I_{11/2}$, $^6P_{5/2}$), ($^4I_{13/2}$, $^4F_{7/2}$) and $^4I_{15/2}$, after absorbing the radiation at 366, 388 and 454 nm, respectively.

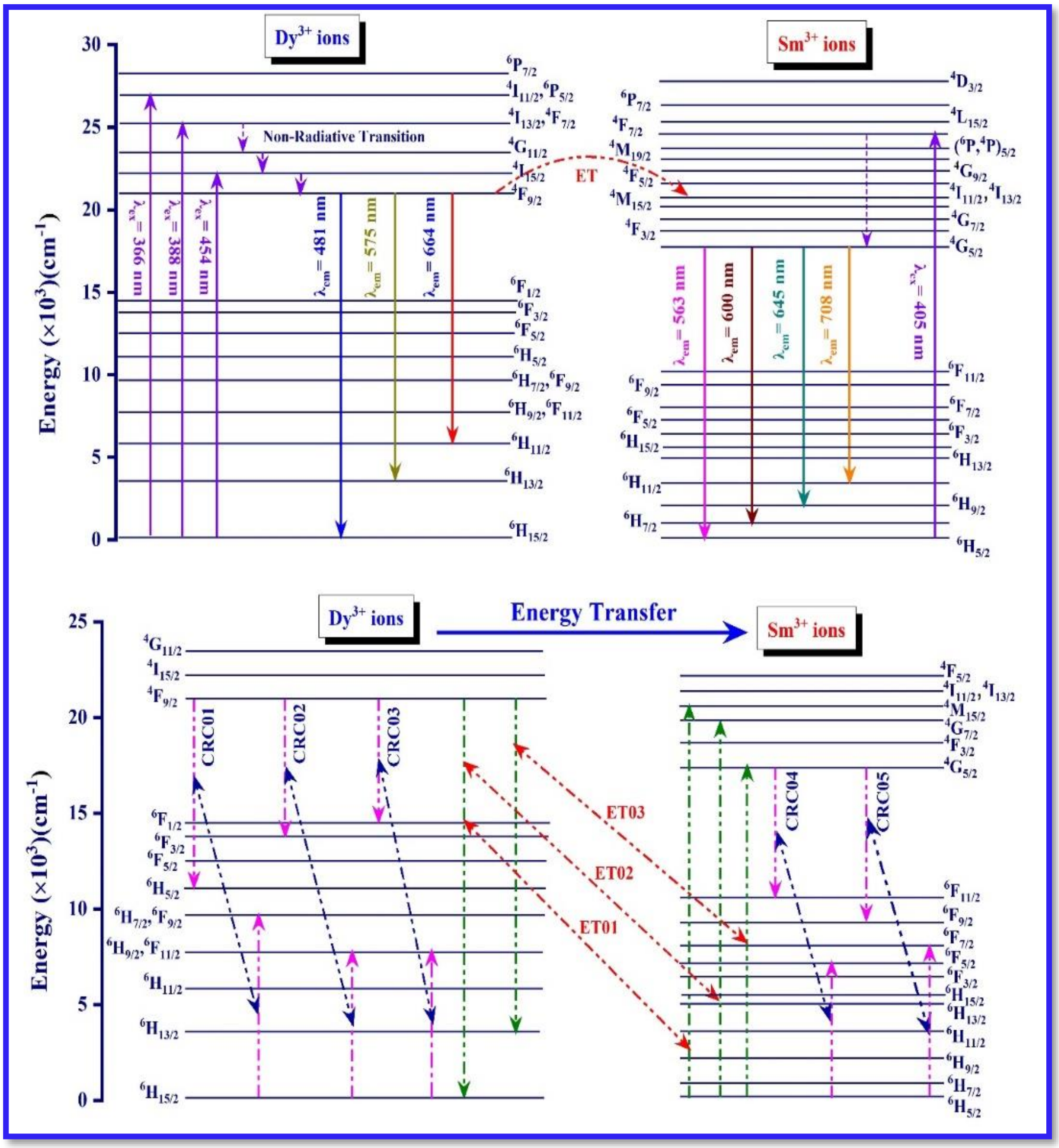

Fig. 5.06. *Partial energy level diagram of Dy^{3+}/Sm^{3+} co-activated TWKZBi glass samples.*

After reaching the excited energy levels, Dy^{3+} ions decay non-radiatively from the $^4F_{9/2}$ energy state to the lower-lying energy states, including $^6H_{15/2}$ (481 nm; blue band), $^6H_{13/2}$ (575 nm; yellow band) and $^6H_{11/2}$ (664 nm; red band), respectively. In the present work, NRT and concentration quenching mechanisms can occur due to potential CRCs. The possible CRCs of Dy^{3+} ions are denoted as follows [164, 165]:

CRC01: - $^4F_{9/2} + {}^6H_{15/2} \rightarrow {}^6H_{5/2} + {}^6H_{7/2}, {}^6F_{9/2}$

CRC02: - $^4F_{9/2} + {}^6H_{15/2} \rightarrow {}^6F_{3/2} + {}^6H_{9/2}, {}^6F_{11/2}$

CRC03: - $^4F_{9/2} + {}^6H_{15/2} \rightarrow {}^6F_{1/2} + {}^6H_{9/2}, {}^6F_{11/2}$

In TWKZBiSm glasses, the Sm^{3+} ions absorbed the excitation energy (405 nm), which in turn excites the Sm^{3+} ions from the $^6H_{5/2}$ energy state to the higher energy state ($^4F_{7/2}$). The excited Sm^{3+} ions then rapidly relax from higher energy levels ($^4G_{5/2}$) to lower energy levels non-radiatively, respectively. The possible CRCs of Sm^{3+} ions are identified as [164]:

CRC04: - $^4G_{5/2} + {}^6H_{5/2} \rightarrow {}^6F_{11/2} + {}^6F_{5/2}$

CRC05: - $^4G_{5/2} + {}^6H_{5/2} \rightarrow {}^6F_{9/2} + {}^6F_{7/2}$

The Dy^{3+} ions in TWKZBiDySm glasses get excited from their lower lying energy level to their higher lying energy level and then decay to the $^4F_{9/2}$ energy state. The small energy difference between the $^4F_{9/2}$ energy state of Dy^{3+} ions and the $^4I_{13/2}$ energy state of Sm^{3+} ions enables ET by phonon-assisted NRT. This indicates that the Dy^{3+} ion functions as a sensitizer/donor and the Sm^{3+} ion functions as an activator/acceptor. The following possible channels were responsible for the ET mechanism from sensitizer/donor (Dy^{3+}) to activator/acceptor ions (Sm^{3+}) [164, 165]:

ET01: - Dy^{3+} ($^4F_{9/2}$) + Sm^{3+} ($^6H_{5/2}$) → Dy^{3+} ($^6H_{15/2}$) + Sm^{3+} ($^4M_{15/2}$)

ET02: - Dy^{3+} ($^4F_{9/2}$) + Sm^{3+} ($^6H_{5/2}$) → Dy^{3+} ($^6H_{15/2}$) + Sm^{3+} ($^4G_{7/2}$)

ET03: - Dy^{3+} ($^4F_{9/2}$) + Sm^{3+} ($^6H_{5/2}$) → Dy^{3+} ($^6H_{13/2}$) + Sm^{3+} ($^4G_{5/2}$)

Further, the ET mechanism from the donor (Dy^{3+}) to the acceptor (Sm^{3+}) is further classified into d-d, d-q, and q-q interactions. According to Dexter's ET relation alongside Reisfeld's approximation, the character of the interaction was determined by [158, 166]:

$$\frac{\eta_0}{\eta} \propto C^{n/3} \tag{5.1}$$

here, the luminescent quantum efficiencies of sensitizer (Dy^{3+}) with and without activator (Sm^{3+}) are represented as η and η_0, respectively. *C* indicates the total mole percentage of the donor (Dy^{3+}) and acceptor (Sm^{3+}) ions. The kind of multipolar interaction is denoted as *n*, which has a value of 10 for q-q, 8 for d-q, and 6 for d-d interactions, respectively.

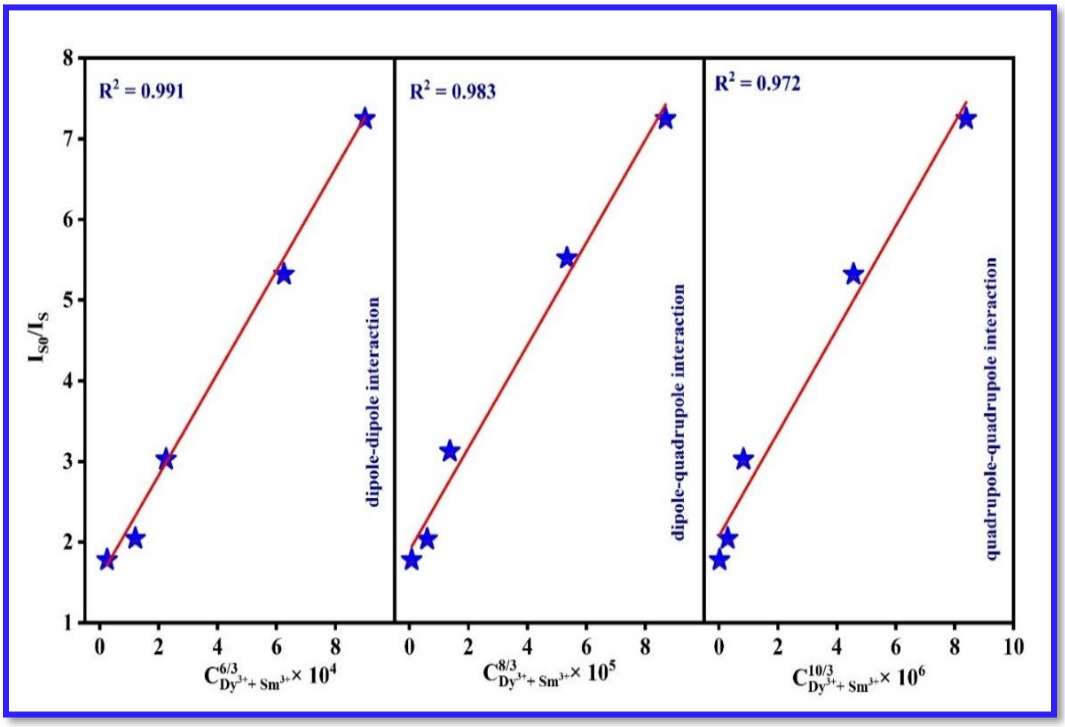

Fig. 5.07. *The dependence of* $\frac{I_{S0}}{I_S}$ *versus* $C^{6/3}_{Dy^{3+}+Sm^{3+}} \times 10^4$, $C^{8/3}_{Dy^{3+}+Sm^{3+}} \times 10^5$ *and* $C^{10/3}_{Dy^{3+}+Sm^{3+}} \times 10^6$ *for* Dy^{3+}/Sm^{3+} *co-doped TWKZBi glasses under 388 nm excitation.*

The proportion of the $\frac{\eta_0}{\eta}$ is approximately evaluated using the equation as shown below [158]:

$$\frac{I_{S0}}{I_s} \propto C^{n/3} \tag{5.2}$$

here, the emission intensities of the donor (Dy^{3+}) with and without the acceptor (Sm^{3+}) are signified as I_s and I_{S0}, respectively. The graph for the $\frac{I_{S0}}{I_s}$ versus $C^{n/3}$ for the value of n = 6, 8, and 10, as depicted in Fig. 5.07. The most accurate fit was achieved for n = 6 proving the character of the Dy^{3+} to Sm^{3+} interaction as a result of the non radiative d-d interaction.

5.3.2.4. Lifetime Analysis of TWKZBiDySm *Glasses*

In order to analyze the ET process that prevails between the Dy^{3+} and Sm^{3+} luminescent centers, the PL lifetime curves of TWKZBiDySm glass matrices have been measured at an excitation wavelength of 388 nm (Dy^{3+}) as depicted in Fig. 5.08.

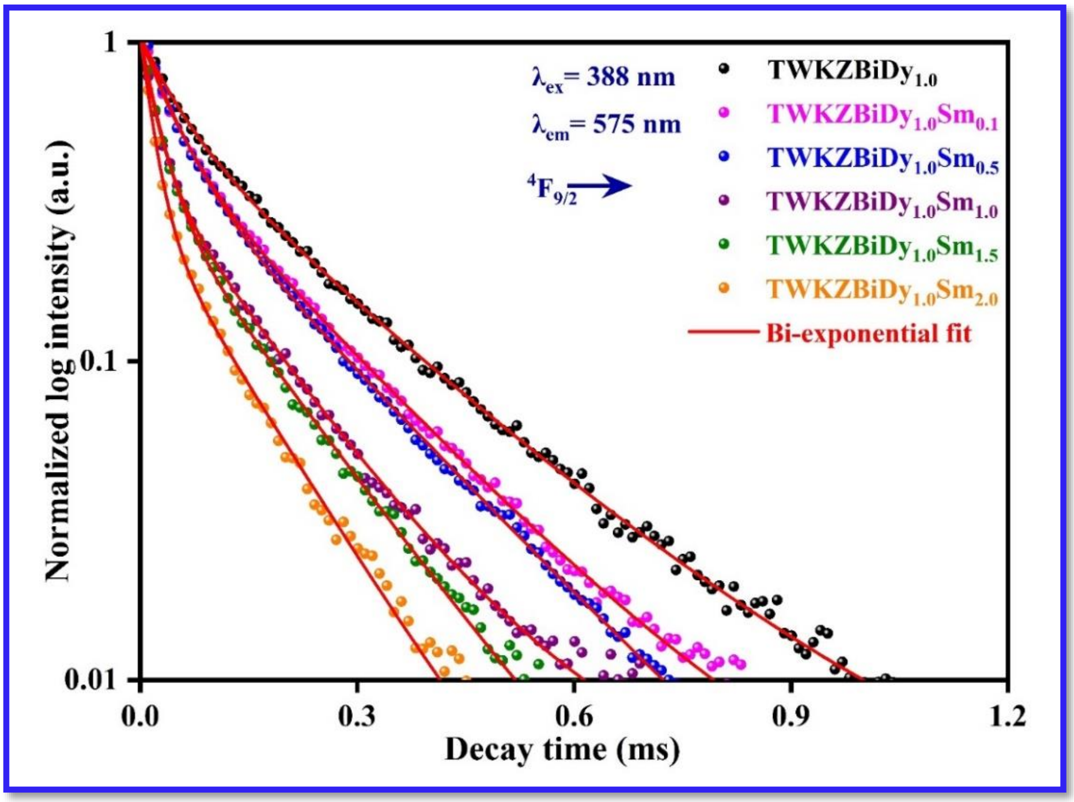

Fig. 5.08. *Lifetime profiles of the TWKZBiDySm glass samples under 388 nm excitation wavelength with the bi-exponential fitting curve.*

The observed lifetime curves of the prepared glasses were most accurately fitted with the double exponential expression as shown in *equation (2.9)*. The average lifetime $\left(\tau_{Avg}\right)$ for the prepared TWKZBiDySm glasses was estimated by utilizing the following relationship as given in *equation (2.10)*. The observed τ_{Avg} values for the prepared TWKZBiDySm glass samples are illustrated in Table 5.01.

Table 5.01. The average lifetimes (μs) for the $^4F_{9/2}$ level (λ_{em} = 575 nm) of Dy^{3+}/Sm^{3+} co-activated TWKZBi glasses under 388 nm excitation wavelength.

Sample code	Average lifetime (μs)
TWKZBiDy$_{1.0}$	207.81
TWKZBiDy$_{1.0}$Sm$_{0.1}$	190.85
TWKZBiDy$_{1.0}$Sm$_{0.5}$	178.19
TWKZBiDy$_{1.0}$Sm$_{1.0}$	164.37
TWKZBiDy$_{1.0}$Sm$_{1.5}$	144.87
TWKZBiDy$_{1.0}$Sm$_{2.0}$	130.93

It has been identified that the τ_{Avg} values of Dy^{3+} ions for the $^4F_{9/2}$ level (λ_{em} = 575 nm) was found to be progressively decreased with increasing content of Sm^{3+} ions. Aside from that, it was also obtained that the τ_{Avg} values of Dy^{3+} ions in the TWKZBiDySm glasses are shorter than that of the single TWKZBiDy$_{1.0}$ glass matrix. Therefore, the above results provide additional validation for the non-radiative ET process from Dy^{3+} to Sm^{3+} ions. In addition, the ET parameters such as energy transfer efficiency (η) for the prepared TWKZBiDySm glass matrices were estimated using the following equation [167]:

$$\eta_{Dy\rightarrow Sm} = 1 - \frac{\tau_{Dy-Sm}}{\tau_{Dy}} \tag{5.3}$$

here, the lifetime values of TWKZBiDySm glasses without and with Sm^{3+} ion concentrations are represented as τ_{Dy} and τ_{Dy-Sm}, respectively.

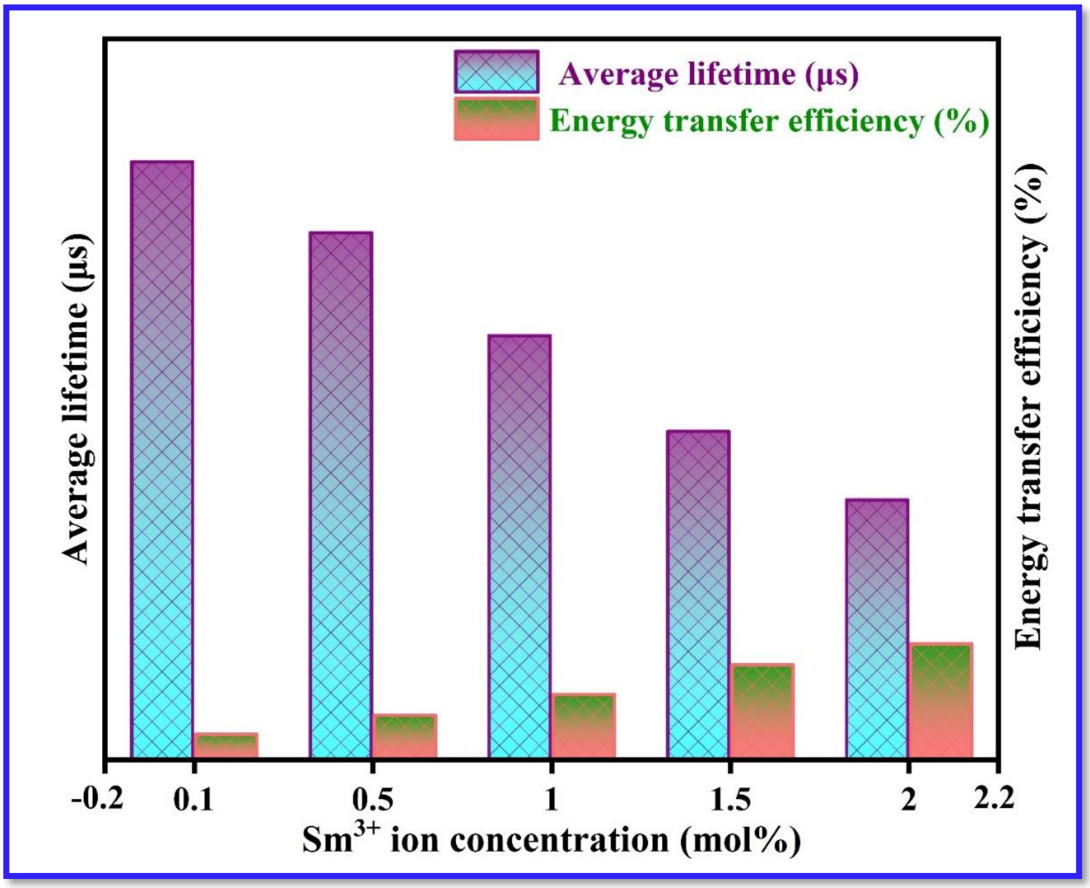

Fig. 5.09. *The average lifetime and energy transfer efficiency along with varying the Sm^{3+} ion concentrations in the Dy^{3+}/Sm^{3+} co-activated TWKZBi glasses under 388 nm excitation wavelength.*

The changes in average lifetime and ET efficiency by changing Sm^{3+} ion concentrations in the TWKZBiDySm glasses are revealed in Fig. 5.09. It was found that the $\eta_{Dy\rightarrow Sm}$ values enhanced from 8.16 to 36.99% with a surge in Sm^{3+} ion content from 0.1 to 2.0 mol% in the TWKZBiDySm glasses.

5.3.2.5. Colorimetric Properties of TWKZBiDySm Glasses

To analyze the luminescent color characteristics, the CIE color coordinates were evaluated via employing the Commission Internationale de I'Eclairage (CIE) 1931 chart. Fig. 5.10 (a) shows the predicted CIE (*x*, *y*) color coordinates for the prepared TWKZBiDy$_{1.0}$ and TWKZBiSm$_{1.0}$ glass samples stimulated at different wavelengths, especially 388 and 405 nm, respectively. The color coordinates (0.393, 0.410) for the prepared TWKZBiDy$_{1.0}$ glass matrix are situated in the white light zone of the CIE graph over the excitation wavelength of Dy^{3+} ions (388 nm).

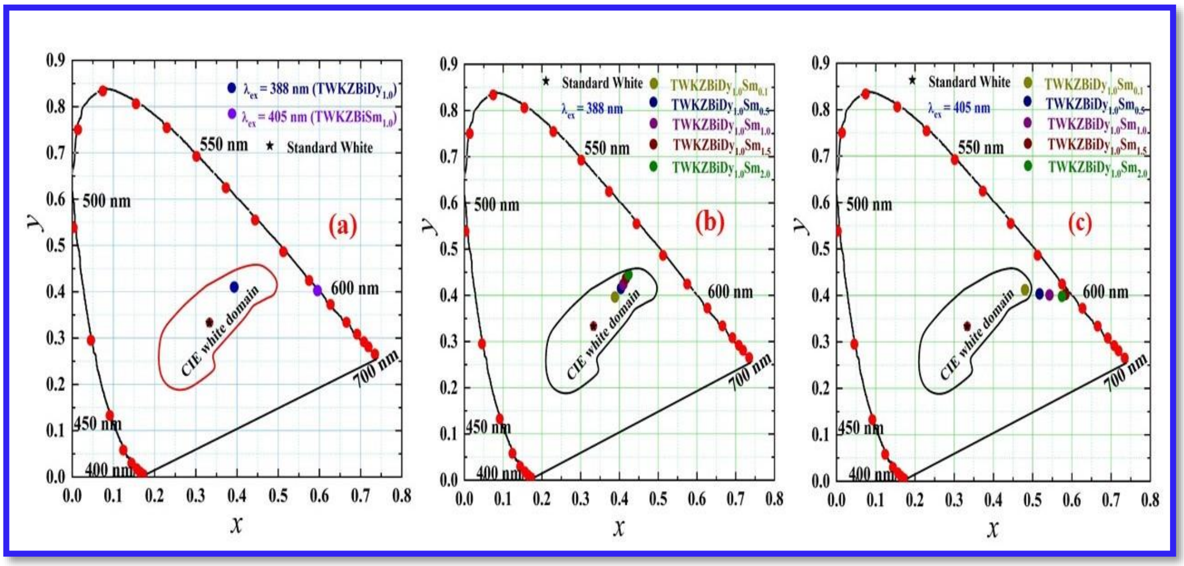

Fig. 5.10. (a) *CIE chromaticity coordinates of TWKZBiDy$_{1.0}$ and TWKZBiSm$_{1.0}$ glasses under Dy^{3+} and Sm^{3+} excitation wavelengths,* **(b)** *CIE chromaticity coordinates of TWKZBiDySm glasses under 388 nm and* **(c)** *405 nm excitation wavelengths.*

In addition, the (*x*, *y*) coordinates (0.595, 0.403) of the TWKZBiSm$_{1.0}$ glass matrix correlate with the orange-red zone of the CIE graph under 405 nm excitation of Sm^{3+} ions. In addition, the CCT is a measure of the different colors of white light. The CCT has been used in the lighting industry to study the standard of light emitted by a lighting source. McCamy's empirical relation can be utilized to assess CCT values, which can be expressed in *equation (1.10)*. At the Dy^{3+} excitation wavelength, the CCT value of 4032 K was observed for the prepared $TWKZBiDy_{1.0}$ glass. When monitoring a Sm^{3+} excitation wavelength, the CCT value of the $TWKZBiSm_{1.0}$ glass sample is 1720 K.

Table 5.02. CIE (*x*, *y*) coordinates, correlated color temperature (CCT) and color purity (CP) of Dy^{3+}/Sm^{3+} co-activated TWKZBi glasses under different excitation wavelengths.

Sample code	Excitation (nm)	Color coordinates (*x*, *y*)	CCT values (K)	Color purity (%)
$TWKZBiDy_{1.0}Sm_{0.1}$	**388**	(0.388, 0.396)	4120	33.78
	405	(0.480, 0.412)	2138	67.06
$TWKZBiDy_{1.0}Sm_{0.5}$	**388**	(0.403, 0.414)	3870	44.28
	405	(0.517, 0.403)	1794	77.20
$TWKZBiDy_{1.0}Sm_{1.0}$	**388**	(0.410, 0.424)	3703	49.30
	405	(0.543, 0.401)	1743	81.52
$TWKZBiDy_{1.0}Sm_{1.5}$	**388**	(0.416, 0.436)	3601	54.71
	405	(0.584, 0.402)	1734	88.06
$TWKZBiDy_{1.0}Sm_{2.0}$	**388**	(0.423, 0.445)	3108	59.43
	405	(0.575, 0.398)	1689	91.39

Another crucial characteristic, color purity (CP) in percentage has been estimated via employing the following expression as given in *equation (4.4)*. The estimated CP for the prepared $TWKZBiDy_{1.0}$ and $TWKZBiSm_{1.0}$ glasses are found to be 39.37 and 97.81%, respectively. In addition, Fig. 5.10 (b and c) also shows the CIE (*x*, *y*) coordinates of Dy^{3+}/Sm^{3+} co-activated TWKZBi (TWKZBiDySm) glasses excited at different excitation wavelengths including 388, and 405 nm. Table 5.02 summarizes the CIE chromaticity coordinates and CCT (in kelvin) values of the TWKZBiDySm glass samples for different excitation wavelengths. It was found that changing the proportion of Dy^{3+} and Sm^{3+} ions can change the luminescent hue characteristics from white light to an orange-red region of the CIE graph. The white light region contains the (x, y) coordinates of TWKZBiDySm glasses excited at Dy^{3+} wavelength. The (x, y) coordinates shifted from white to an orange-red region via varying the Sm^{3+} ion content at an excitation wavelength of 405 nm. Furthermore, the CCT values of the co-activated $TWKZBiDy_{1.0}Sm_y$ glasses at an excitation wavelength of 388 nm were perceived in the range of 4120 to 3108 K, which is less than 5000 K. Thus, the CIE chromaticity properties suggest that the TWKZBiDySm glasses could radiate the warm white light under the excitation of Dy^{3+} ions. Therefore, the TWKZBiDySm glass samples can produce warm white luminescent features and could be suitable for solid-state lighting applications.

5.3.2.6. Effect of Temperature on PL Analysis of TWKZBiDySm *Glasses*

To investigate the suitability of the prepared TWKZBiDySm glass matrices for lighting applications, temperature dependent PL (TDPL) spectra have been recorded for the prepared $TWKZBiDy_{1.0}Sm_{1.0}$ glass sample with increasing temperature from ambient temperature (25 ºC) to 175 ºC by monitoring the excitation wavelengths at 388 and 405 nm, as described in Fig. 5.11 (a and b). The emission intensity of the $TWKZBiDy_{1.0}Sm_{1.0}$ glass sample decreases with increasing temperature from ambient temperature to 175 ºC. The variation in relative emission intensity in percentage along with the increasing temperature is illustrated in the inset of Fig. 5.11 (a and b). The persisted emission intensity for the prepared $TWKZBiDy_{1.0}Sm_{1.5}$ glass sample was ~83.83% at 100 ºC and 73.20% at 150 ºC under 388 nm excitation and 85.35% at 100 ºC and 74.95% at 150 ºC under 405 nm excitation in comparison to the initial emission intensity at 25 ºC, which confirm good thermal stability of the prepared TWKZBiDySm glasses [137, 167].

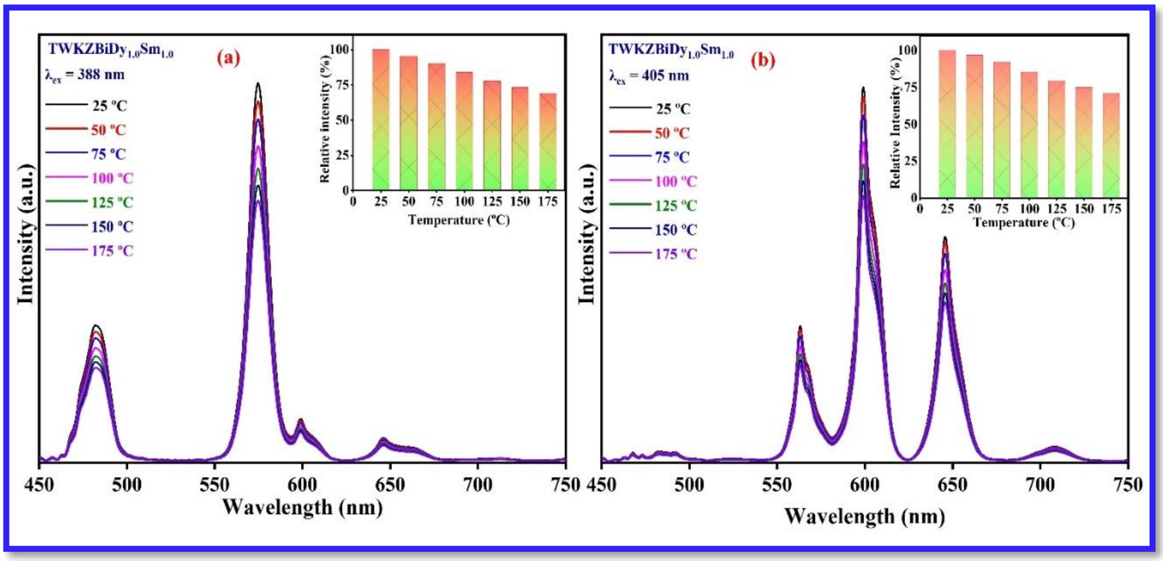

Fig. 5.11. *Temperature dependent PL spectra of TWKZBiDy$_{1.0}$Sm$_{1.0}$ glass sample under* **(a)** *388 nm and* **(b)** *405 nm excitation wavelengths. [Inset represents the relative emission intensity variation in the temperature range from 25 ºC to 175 ºC.]*

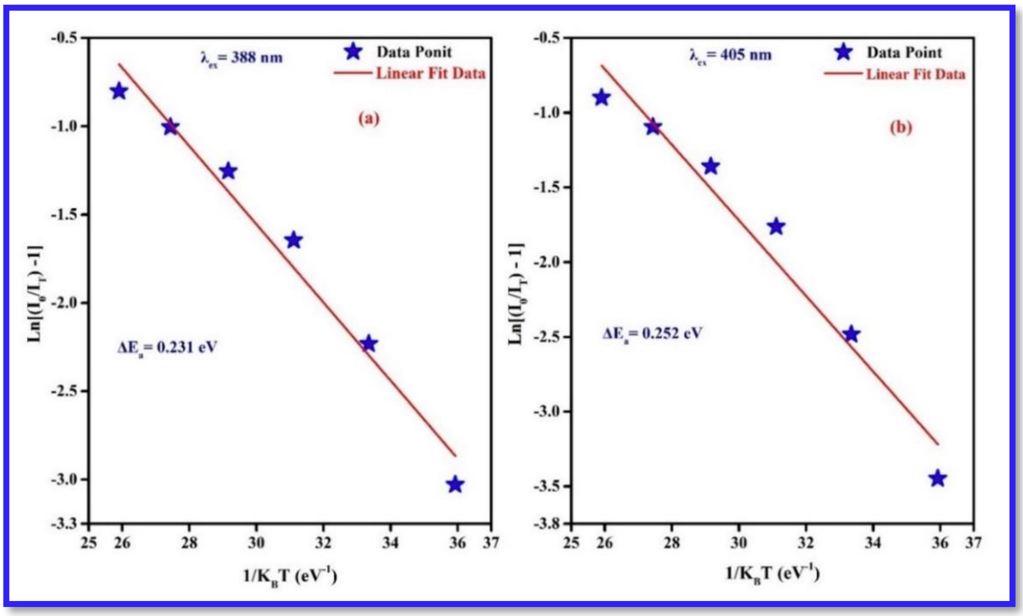

Fig. 5.12. *Linear fitted plot between ln[(I$_0$/I$_T$) – 1] against 1/K$_B$T under* **(a)** *388 nm and* **(b)** *405 nm excitation wavelengths.*

Furthermore, the activation energy is another important constraint on the thermal stability behaviour of the prepared TWKZBiDySm glass matrices and was evaluated via employing the Arrhenius equation as given in *equation (2.10)*. The slope can be found using the Arrhenius equation by the plot of Ln[(I_0/I_T) -1] versus 1/K_BT, which assigns the value of ΔE_a as shown in Fig. 5.12 (a and b). The estimated values of ΔE_a are 0.231 and 0.252 eV at excitation wavelengths of 388 and 405 nm. The observed ΔE_a values are relatively greater than the reported values [137, 150, 168]. The high value of ΔE_a henceforth recommends that the prepared TWKZBiDySm glasses have excellent thermal stability and are suitable for lighting applications.

5.4. Luminescent Features of the Dy^{3+}/Eu^{3+} Co-doped TWKZBi Glasses

Furthermore, the energy transfer dynamics and luminescent characteristics for the Dy^{3+}/Eu^{3+} co-doped TWKZBi glasses for solid state lighting applications, especially for white LED applications. In the above section, *5.3.2.2* and *Chapter 4* explain the luminescent features of single Dy^{3+} and Eu^{3+} doped glasses in detail. Based on the results mentioned above, the prepared TWKZBi: 1.0 mol% Dy^{3+} glass matrix has been co-activated with varying content of Eu^{3+} ions to boost the red color constituent, a prerequisite for white LED applications.

Fig. 5.13 illustrates the PL excitation spectral profiles for the TWKZBi$Dy_{1.0}Eu_{1.0}$ glass sample was captured in the 325 to 550 nm range via monitoring the noteworthy yellow (575 nm) and red (614 nm) emission wavelength of each dopant. It has been observed that the characteristic excitation peaks of the dopant ions (Dy^{3+} and Eu^{3+}) demonstrate in the n-UV to the blue area, as discussed earlier. From Fig. 5.13, it has been noted that four distinct n-UV/blue excitations (i.e., 388, 393, 454 and 464 nm indicated as dotted lines) were further used to capture the emission profiles of the TWKZBiDyEu glasses. Moreover, the ET route from Dy^{3+} to Eu^{3+} ion necessitates that the excitation of the acceptor/activator (Eu^{3+}) overlaps with the emission of donor/sensitizer (Dy^{3+}), which is fulfilled in this report and depicted in Fig. 5.14. To demonstrate the ET process and colour tunable behaviour of the prepared TWKZBiDyEu glasses, the titled glasses were stimulated with the above mentioned n-UV/blue excitations.

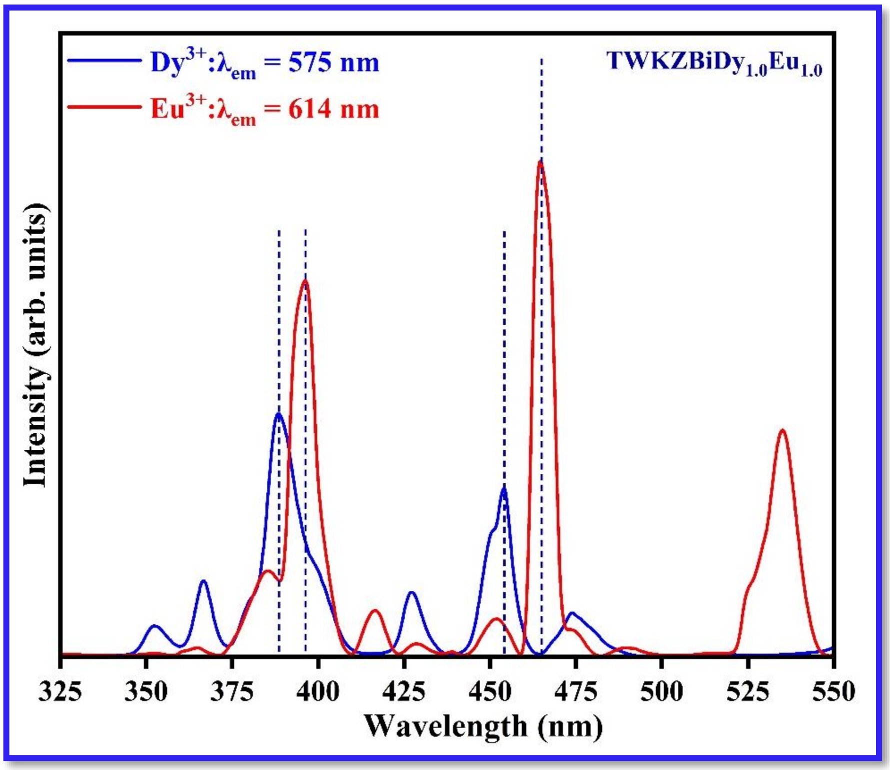

Fig. 5.13. *Excitation spectra for the prepared TWKZBiDy$_{1.0}$Eu$_{1.0}$ glass under emission wavelengths of Dy^{3+} (575 nm) and Eu^{3+} (614 nm).*

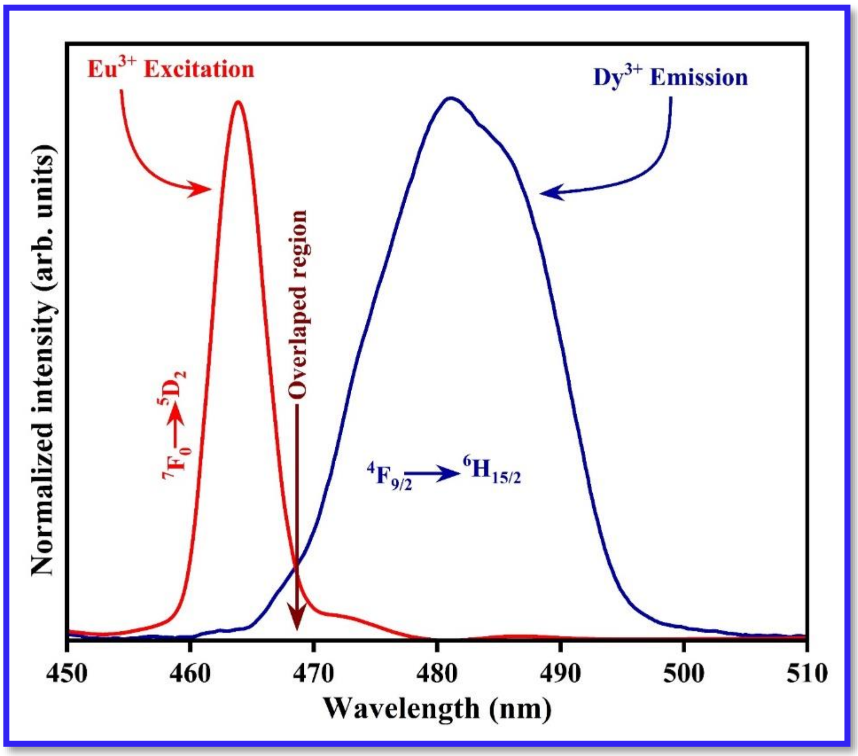

Fig. 5.14. S*pectral overlap of the sensitizer (Dy^{3+}) emission and activator (Eu^{3+}) excitation.*

Furthermore, the emission spectral profiles of the TWKZBiDy$_{1.0}$Eu$_y$ (where y = 0.1, 0.5, 1.0, 1.5, 2.0 and 3.0 mol%) glasses were captured under 388, 393, 454 and 464 nm excitation wavelengths and are depicted in Fig. 5.15 (a, b, c and d).

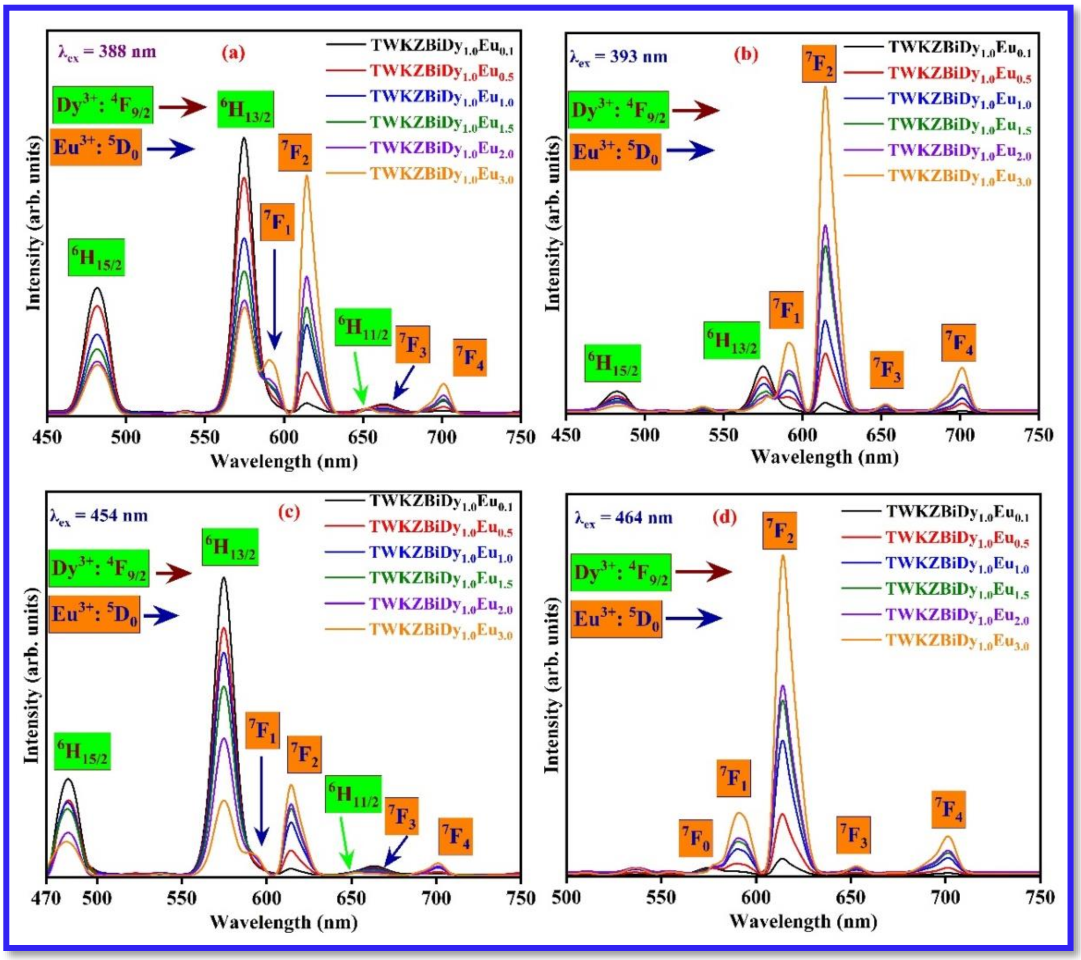

Fig. 5.15. *Emission spectra for the prepared TWKZBi: Dy^{3+}/Eu^{3+} glass samples under* ***(a)*** *388 nm excitation,* ***(b)*** *393 nm excitation****,*** ***(c)*** *454 nm excitation and* ***(d)*** *464 nm excitation.*

It has been noted that the emission peaks are seen in the blue, yellow, and red regions. These peaks occur due to the energy transitions between the ground and excited energy levels of Dy^{3+} ions ($^4F_{9/2} \rightarrow {}^6H_J$, where J = 15/2, 13/2, and 11/2) and Eu^{3+} ions ($^5D_0 \rightarrow {}^7F_J$, where J = 0 to 4). Furthermore, it has been evident that the excitations and the activator ion concentrations can strongly impact the emission peaks of the Dy^{3+} and Eu^{3+} ions and their intensities. The emission peak attributed to the Dy^{3+} ions under 388, and 454 nm excitation reveals a decrement in the emission intensities, while an increase in the emission intensity was detected for the peaks related to the activator (Eu^{3+}) ions. Therefore, the increase in the concentration dependent Eu^{3+} emission intensity is caused by an upsurge in the absorption probability of Eu^{3+} ions and the process of ET from Dy^{3+} to Eu^{3+} ions is confirmed [169]. The ET process from the Dy^{3+} to Eu^{3+} ions is more noticeable and apparent under the Dy^{3+} excitation wavelengths. Further, the emission peaks arising from the Eu^{3+} ions were prominent under 393 nm excitation, along with weak peaks associated with the Dy^{3+} ions. The foremost emission peaks under the 464 nm excitation wavelength have been confirmed as associated with the Eu^{3+} ions since their absorption intensity is higher than that of the Dy^{3+} ions. Thus, it has been noted that energy is not transferred back from Eu^{3+} to Dy^{3+} ions. Moreover, color tunability can be accomplished by adjusting the excitation wavelength and altering the activator ion concentrations through ET between the sensitizer and activator ions, which will be discussed in the following *section 5.4.2*.

The partial energy level scheme with different energy levels and energy transitions (both non-radiative & radiative), are illustrated in Fig. 5.16. When the incident light falls on the TWKZBiDyEu glasses, the incident energy may be absorbed by the Dy^{3+} ions at the lowest energy level ($^6H_{15/2}$) and then get excited to the distinct higher levels of energy ($^4I_{11/2}$, $^6P_{5/2}$), ($^4I_{13/2}$, $^4F_{7/2}$) and $^4I_{15/2}$. After that, some non-radiative (NR) transitions occur to the $^4F_{9/2}$ level, leading to the emission of blue, yellow and red light from the same intermediate energy level of Dy^{3+} ions. Additionally, some energy has been simultaneously transferred to the nearest energy levels ($^5D_0$ & $^5D_1$) of the activator (Eu^{3+}) ions along with their radiative emission in the visible region. Thus, the ET in the TWKZBiDyEu glasses may occur through the higher excited state of Dy^{3+} to Eu^{3+} ions via phonon-assisted NRET in the prepared glasses.

The process of ET occurs by either exchange or multipolar interaction between donor ions (Dy^{3+}) and acceptor (Eu^{3+}) ions. The multipolar interaction may be categorized into three types:

quadrupole-quadrupole, dipole-quadrupole and dipole-dipole interactions. The Dexter ET formula and Reisfeld's approximation were employed to ascertain the character of the interaction based on the equation given in the literature [170-172].

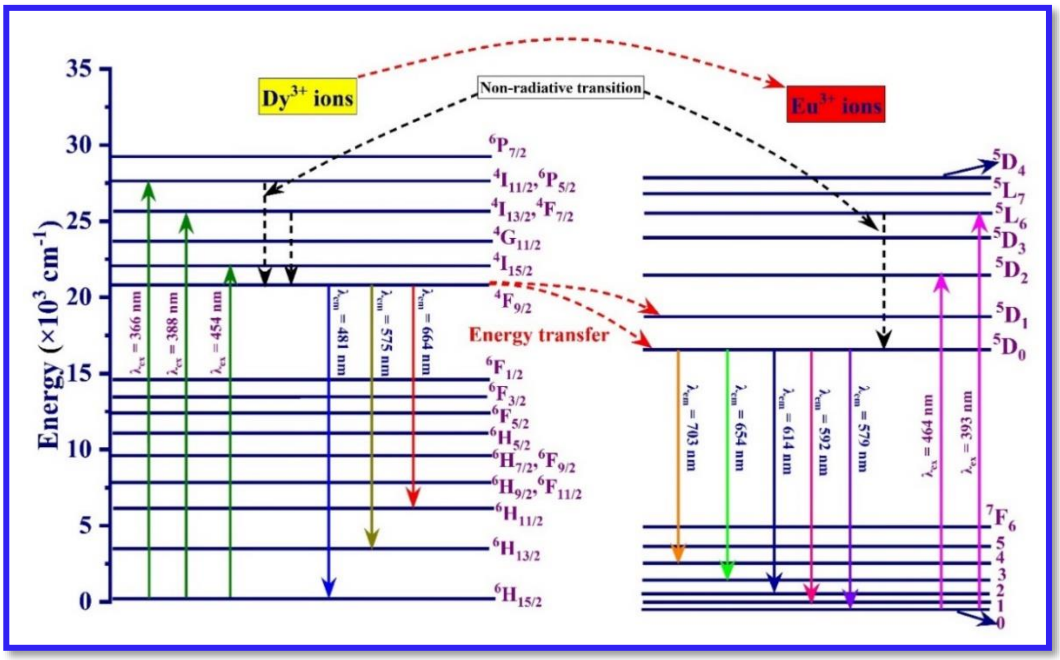

Fig. 5.16. *Partial energy level diagram for the prepared TWKZBiDyEu glass samples.*

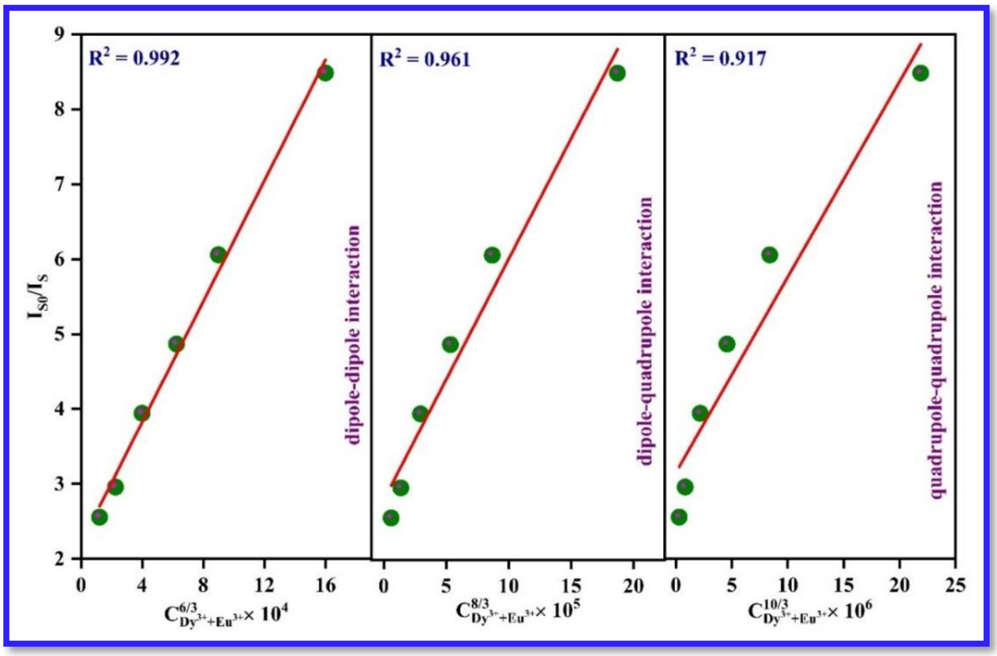

Fig. 5.17. The dependence of $\frac{I_{S0}}{I_S}$ versus $C^{6/3}_{Dy^{3+}+Eu^{3+}} \times 10^4$, $C^{8/3}_{Dy^{3+}+Eu^{3+}} \times 10^5$ and $C^{10/3}_{Dy^{3+}+Eu^{3+}} \times 10^6$ for the prepared TWKZBiDyEu glasses under 388 nm excitation.

Fig. 5.17 depicts the relationship between $\frac{I_{S0}}{I_S}$ and $C^{n/3}$ for the values of n equal to 6, 8 and 10. The most precise fitting was accomplished for n = 6 determines the kind of interaction amidst the donor and acceptor ions is the non-radiative dipole-dipole interaction. Moreover, the efficiency of energy transfer (η_{ET}) between the donor (Dy^{3+}) and acceptor (Eu^{3+}) may be assessed via utilizing an expression as follows [173, 174]:

$$\eta_{ET} = 1 - \frac{I_S}{I_{S0}} \tag{5.4}$$

in the above expression, I_S and I_{S0} denote the intensity of emission of the Dy^{3+} ions with and without Eu^{3+} ions, respectively. Table 5.03 summarises the estimated values of η_{ET} for the titled TWKZBiDy$_{1.0}$Eu$_y$ glasses. The highest η_{ET} value for the TWKZBiDy$_{1.0}$Eu$_{3.0}$ glass sample has been obtained to be 84.57%.

Table 5.03. The energy transfer efficiency (η_{ET} in %), energy transfer probability (P) and average lifetimes (µs) of TWKZBiDyEu glasses under 388 nm excitation.

Sample codes (in mol%)	Energy transfer efficiency (η_{ET} in %)	Energy transfer probability (P)	Average lifetime (µs)
TWKZBi: 1.0 Dy^{3+}	-	-	209.974
TWKZBiDy$_{1.0}$Eu$_{0.1}$	60.903	1.109	189.203
TWKZBiDy$_{1.0}$Eu$_{0.5}$	66.204	1.214	172.851
TWKZBiDy$_{1.0}$Eu$_{1.0}$	74.638	1.286	163.189
TWKZBiDy$_{1.0}$Eu$_{1.5}$	79.457	1.553	135.175
TWKZBiDy$_{1.0}$Eu$_{2.0}$	83.490	1.827	144.87
TWKZBiDy$_{1.0}$Eu$_{3.0}$	84.578	2.174	96.545

5.4.1. Decay Measurements of TWKZBi Glasses Embedded with Dual Dy^{3+}/Eu^{3+} Ions

To examine the mechanism of ET among the Dy^{3+} and Eu^{3+} luminescent centers, the decay measurement profiles of TWKZBiDyEu glasses were measured for the energy level of the Dy^{3+} ion at $^4F_{9/2}$ with an excitation wavelength of 388 nm. The observed decay patterns were the best precise match using the bi-exponential function as shown in Fig. 5.18.

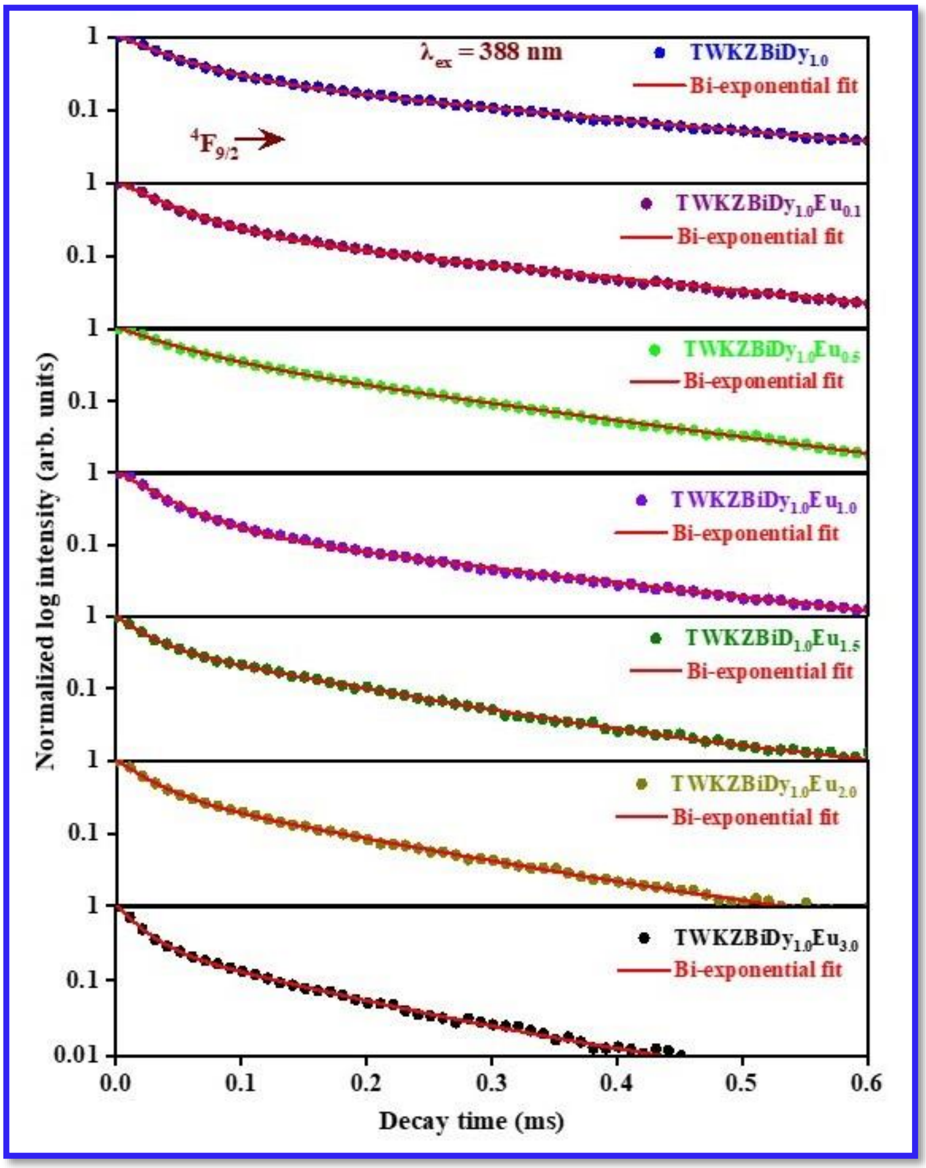

Fig. 5.18. *Decay profiles for the prepared TWKZBiDyEu glasses under 388 nm excitation.*

The relation given in *equation (2.10)* has been applied to estimate the average decay time (τ_{avg}). The estimated values of τ_{avg} for the $^4F_{9/2}$ energy level of Dy^{3+} ions were reported in

Table 5.03. When stimulated with 388 nm light, it was noticed that the τ_{avg} values decrease as the amount of Eu^{3+} ions upsurges in the $TWKZBiDy_{1.0}Eu_y$ glasses. This result gives additional confirmation for the NRET amid Dy^{3+} and Eu^{3+} ions. With the help of the estimated values of average decay time, the probability rate (P) of dipole-dipole ET for the titled glasses can be computed by the following expression [175]:

$$P = \frac{1}{\tau} - \frac{1}{\tau_0} \tag{5.5}$$

The observed ET probability rates with varying amounts of Eu^{3+} ions in the $TWKZBiDy_{1.0}Eu$ glasses are reported in Table 5.03. It was detected that the ET probability rate upsurges with increasing the Eu^{3+} ion concentrations in the titled glasses.

5.4.2. Colorimetric Characteristics of TWKZBi Glass Samples Embedded with Dual Dy^{3+}/Eu^{3+} Ions

To demonstrate the ability of the white light and color tunability character of the TWKZBiDyEu glasses, the chromaticity coordinates were determined using the PL spectral data and manifest on the CIE diagram, as revealed in Fig. 5.19 (a, b, c and d). It has been noticed that the color coordinates of the prepared TWKZBiDyEu glasses located in the white light and near white domain of the CIE chart under 388 and 454 nm, respectively (see Fig. 5.19 (a and c)), while the color reflects in the red zone under the excitation of 464 nm (see Fig. 5.19 (d)). Further, the (x, y) coordinates from the $TWKZBiDy_{1.0}Eu_{0.1}$ to $TWKZBiDy_{1.0}Eu_{3.0}$ glasses indicate the color tunability from the white light to the red zone along with varying activator ion concentrations under 393 nm excitation, respectively, as portrayed in Fig. 5.19 (b). The lack of back energy transfer from the Eu^{3+} to Dy^{3+} ions in the TWKZBiDyEu glasses can be observed by the pure red hue under 464 nm excitation, as depicted in Fig. 5.19 (d). Furthermore, the correlated colour temperature (CCT) for the prepared TWKZBiDyEu glasses was computed using the McCamy relation, as followed by the literature [18, 65].

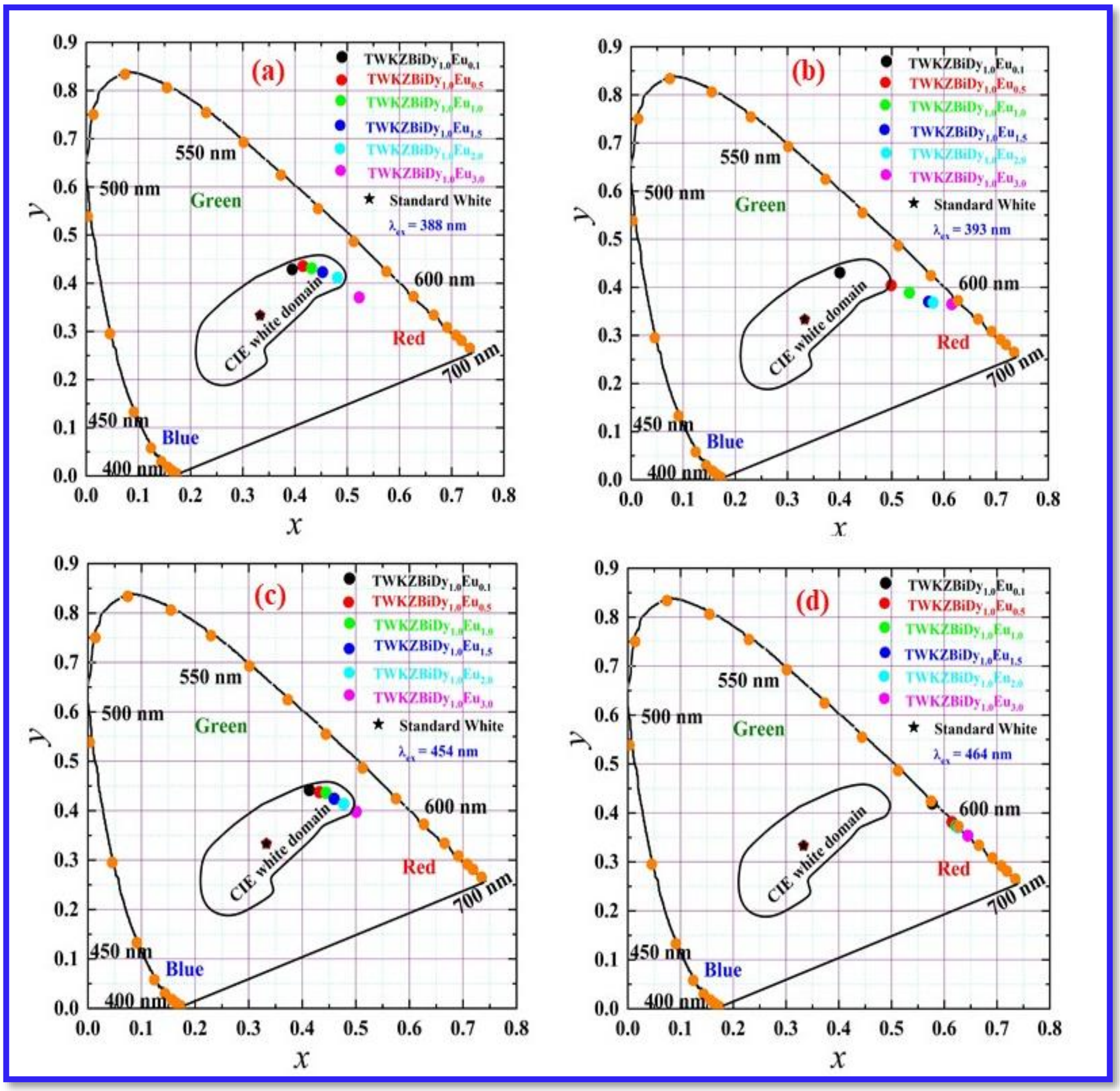

Fig. 5.19. *Chromaticity coordinates for the prepared TWKZBiDyEu glasses under* ***(a)*** *388 nm excitation,* ***(b)*** *393 nm excitation,* ***(c)*** *454 nm excitation and* ***(d)*** *464 nm excitation.*

The CIE coordinates and CCT values for all the TWKZBiDyEu glass samples under selected excitations are reported in Table 5.04. It was observed that the estimated CCT values are lower than that of 5000 K, which suggests that the prepared glasses colour lies in the warm white light domain via introducing the activator ions under n-UV/blue excitations. The result related to the colorimetric characteristics under selected n-UV/blue LED excitation sources of the prepared TWKZBiDyEu glasses has shown versatility for applications in the white LED and colour tunability for optoelectronic applications.

Table 5.04. CIE (*x*, *y*) coordinates and correlated color temperature (CCT) of Dy^{3+}/Eu^{3+} co-activated TWKZBi glasses under selected excitation wavelengths.

Sample codes	Excitations (nm)	Color coordinates (*x*, *y*)	CCT values (K)
TWKZBiDy$_{1.0}$Eu$_{0.1}$	**388**	(0.374, 0.448)	4505
	393	(0.400, 0.440)	3933
	454	(0.423, 0.463)	3641
	464	(0.577, 0.491)	1783
TWKZBiDy$_{1.0}$Eu$_{0.5}$	**388**	(0.395, 0.441))	4442
	393	(0.498, 0.404)	2188
	454	(0.432, 0.456)	3458
	464	(0.614, 0.381)	1810
TWKZBiDy$_{1.0}$Eu$_{1.0}$	**388**	(0.432, 0.431)	4398
	393	(0.533, 0.388)	1831
	454	(0.450, 0.449)	3128
	464	(0.622, 0.373)	1908
TWKZBiDy$_{1.0}$Eu$_{1.5}$	**388**	(0.452, 0.423)	4316
	393	(0.570, 0.370)	1734
	454	(0.458, 0.440)	2947
	464	(0.624, 0.371)	1954
TWKZBiDy$_{1.0}$Eu$_{2.0}$	**388**	(0.481, 0.411)	4267
	393	(0.579, 0.368)	1752
	454	(0.477, 0.443)	2659
	464	(0.625, 0.370)	1966
TWKZBiDy$_{1.0}$Eu$_{0.0}$	**388**	(0.522, 0.370)	4219
	393	(0.615, 0.364)	1951
	454	(0.500, 0.397)	2125
	464	(0.644, 0.353)	2418

5.4.3. Temperature Dependent PL Analysis of TWKZBi Glass Samples Embedded with Dual Dy^{3+}/Eu^{3+} Ions

To examine the thermal stability of the TWKZBiDyEu glass samples for practical usage in the white LED applications, the TDPL spectra were captured for the TWKZBiDy$_{1.0}$Eu$_{3.0}$ glass sample along with rising temperature from 25 °C to 175 °C under 388 nm excitation wavelength as depicted in Fig. 5.20.

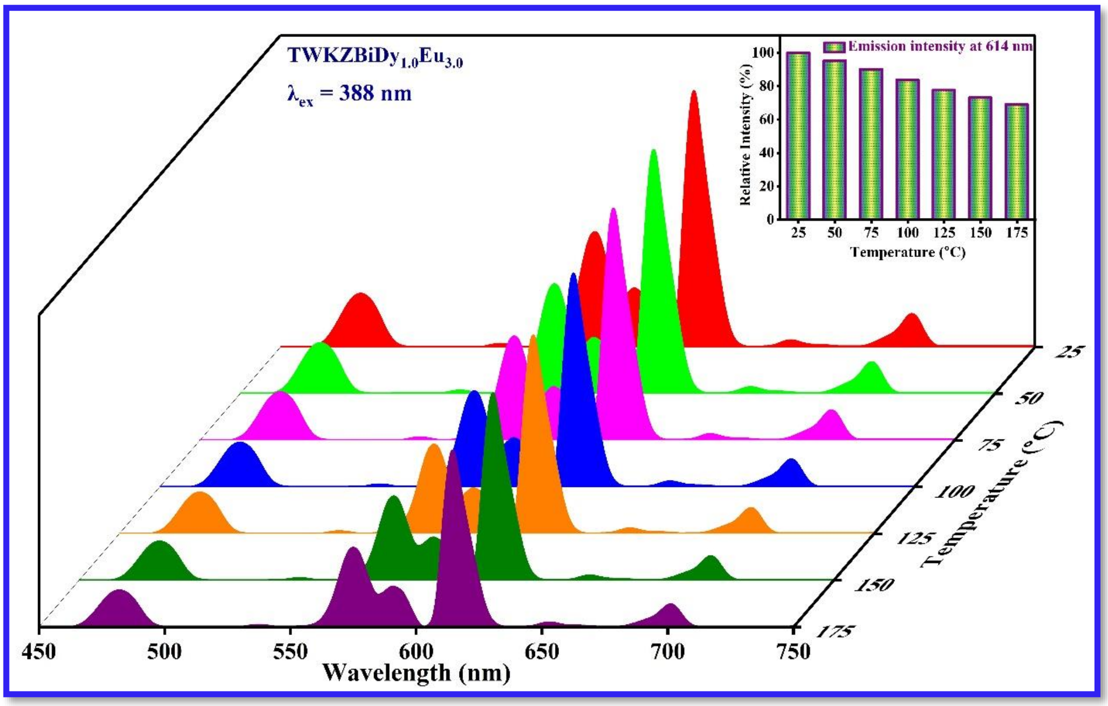

Fig. 5.20. *Temperature dependent emission spectra for the prepared TWKZBiDy$_{1.0}$Eu$_{3.0}$ glass sample with various temperatures from 25 to 175 °C under 388 nm excitation wavelength. [Inset shows the relative emission intensity of the peak at 614 nm by varying temperature.]*

When the temperature profile rises from 25 °C to 175 °C, the intensity of emission peaks of the TWKZBiDy$_{1.0}$Eu$_{3.0}$ glass decreases. Inset of Fig. 5.20 illustrates the relative emission intensity of the peak at 614 nm changes (in %) and temperature variation (in °C). Whereas the intensity of the emission decreased with an upsurge in temperature, the position of the emission peaks remained unaffected irrespective of the temperatures. The emission intensity of the prepared TWKZBiDy$_{1.0}$Eu$_{3.0}$ glass matrix retained up to 85.92% at 100 ºC and 75.12% at 150 ºC as compared to the initial emission intensity at 388 nm excitation, suggesting that the titled glass samples have outstanding thermal stability [125]. Furthermore, another essential parameter for the thermal stability of the titled glass matrices is the activation energy (ΔE_a) and has been computed using the Arrhenius relation as described in the literature [97, 172].

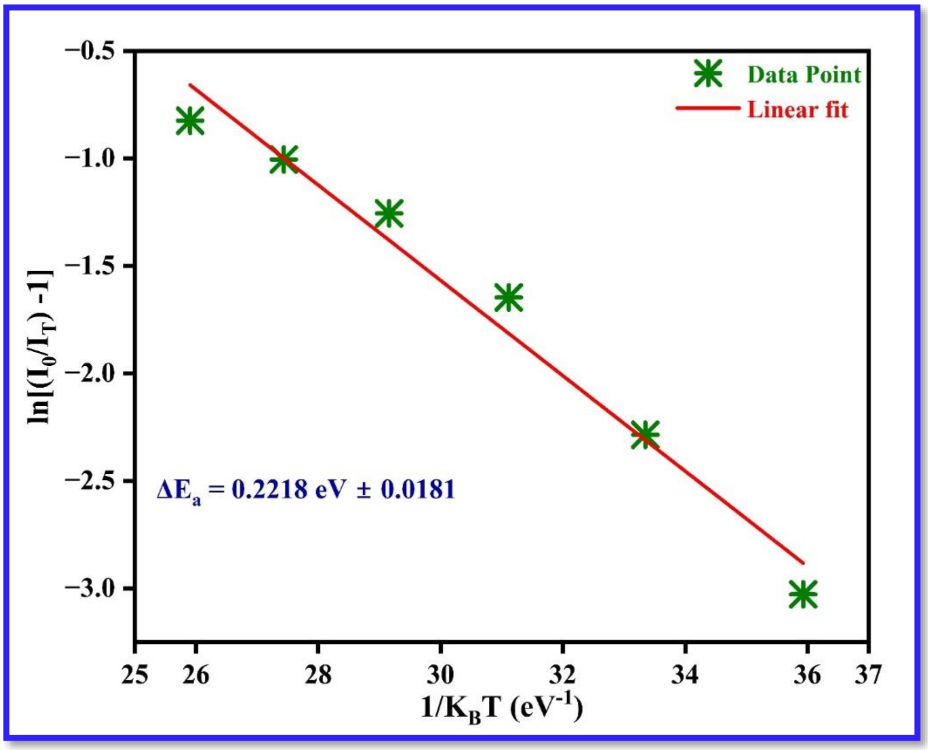

Fig. 5.21. *Linear fitted graph between* $ln[(I_0/I_T) - 1]$ *against* $1/K_BT$ *under 388 nm excitation.*

Fig. 5.21 depicts the slope of the straight fitted line between the $ln\left[\left(\frac{I_0}{I_T}\right) - 1\right]$ and $\frac{1}{K_BT}$ provides the value of activation energy. The observed activation energy value turned out to be 0.2218 ± 0.0181 eV, which was greater than the value described in the literature [97, 125]. Hence, the results mentioned above recommend that the glasses have outstanding thermal stability and are beneficial for white LED and other optoelectronic applications.

5.5. Conclusions

Transparent single ion Sm^{3+} activated, (Dy^{3+}/Sm^{3+}), and (Dy^{3+}/Eu^{3+}) co-activated TWKZBi glasses were successfully prepared via the melt-quench approach. Using optical absorption spectra, several optical features were estimated, including indirect band gap, Urbach energy, and refractive index for the prepared TWKZBiDySm glass matrices. TWKZBiSm glasses exhibit an intense emission peak associated with the $^4G_{5/2} \rightarrow {}^4H_{7/2}$ (600 nm) transition at an excitation wavelength of 405 nm. The (x, y) coordinates (0.595, 0.403) for the TWKZBiSm$_{1.0}$ glass correlate with the orange-red region at an excitation wavelength of 405 nm corresponding to Sm^{3+} ions. In TWKZBiDySm glasses, the emission spectral profiles reveal a self-quenching behavior for Sm^{3+} ions and 1.5 mol% was found to be the optimal concentration. The emission color for co-activated TWKZBiDySm glasses was tuned from warm white light to the orange-red zone of the CIE chart by varying the excitation wavelengths and the concentration of Sm^{3+} ions. In addition, TWKZBi glasses doped with both Dy^{3+} and Eu^{3+} ions demonstrate the emission peaks in the blue (B), yellow (Y) and red (R) zones of the electromagnetic spectrum. Moreover, by regulating the activator (Eu^{3+}) ions and selected excitations, the TWKZBi: Dy^{3+}/Eu^{3+} glass samples were able to tune the emission colour from the white to red zone of the chromaticity diagram. By applying Dexter's ET relationship with Reisfeld's approximation based on the PL spectra, the ET processes involving a non-radiative d-d interaction between (Dy^{3+} to Sm^{3+}) and (Dy^{3+} to Eu^{3+}) ions were validated. The average lifetime (τ_{avg}) values of prepared TWKZBiDySm and TWKZBiDyEu glasses were measured and it was found that the average lifetime values of the $^4F_{9/2}$ energy state of Dy^{3+} ions diminished with a surge in the content of Sm^{3+} and Eu^{3+} ions. In addition, the ET efficiencies $(\eta_{Dy\rightarrow Sm})$ of the TWKZBiDySm glass matrices were estimated by the lifetime curves. The emission profiles alongside the varying temperatures from RT to 448 K indicate the good thermal stability of the prepared TWKZBiDySm and TWKZBiDyEu glasses. Therefore, the prominent results confirm that the prepared TWKZBiDySm and TWKZBiDyEu glasses will be beneficial for white light and other colour tunable photonic device applications.

Chapter – 06

Multicolour emitting Tb^{3+}/Eu^{3+} Co-doped Tungstate-Tellurite Glasses for Photonic Applications

The melt quenching procedure has been followed to synthesize transparent Tb^{3+} singly activated and Tb^{3+}/Eu^{3+} co-activated $TeO_2 - WO_3 - K_2O - ZnO - Bi_2O_3$ (TWKZBi) glasses. The existence of functional units corresponding to the different vibrations has been examined via Raman spectroscopy. The photoluminescent (PL) characteristics and energy transfer (ET) analysis in the Tb^{3+}/Eu^{3+} co-activated TWKZBi glasses were investigated in depth. Several emission peaks have been observed in Tb^{3+} doped TWKZBi glasses under n-UV and blue excitations and the maximum luminescent intensity has been detected for 2.0 mol% of Tb^{3+} doped TWKZBi glass sample. The emission spectra of co-doped Tb^{3+} and Eu^{3+} ions in the TWKZBi glasses have been studied, and the maximum energy transfer efficiency is found to be 32.82% under n-UV excitation. The ET from sensitizer (Tb^{3+}) to activator (Eu^{3+}) ion happens through dipole-dipole (d-d) interaction, as confirmed by Dexter's and Reisfeld's approximation. The color tunable emission in the prepared glass samples can be achieved by varying the content of activator ions. The decay profiles for the $^5D_4$ level of Tb^{3+} ions diminish with varying the concentration of Eu^{3+} ions, confirming the energy transfer from Tb^{3+} to Eu^{3+} ions. Furthermore, temperature-dependent photoluminescence (TDPL) studies show that the Tb^{3+}/Eu^{3+} co-doped TWKZBi glasses have good thermal stability. All the aforementioned results reveal the suitability of the Tb^{3+}/Eu^{3+} co-activated TWKZBi glass samples for photonic applications.

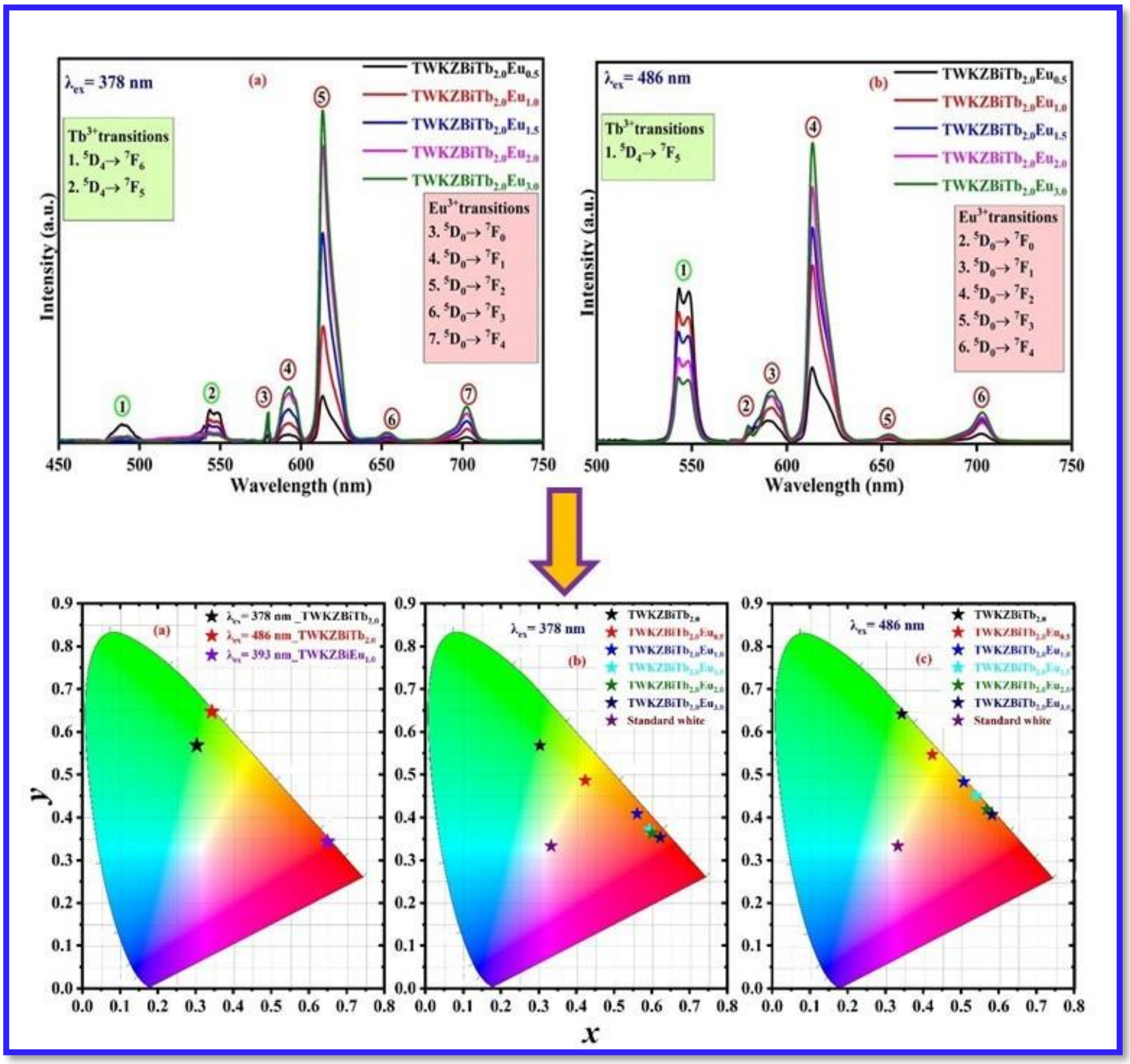

Part of this work has been Published in

Journal of Physics D: Applied Physics 57 (2024) 195301 (I.F.: 3.40)

6.1. Introduction

In *Chapter 5*, (Dy^{3+}/Sm^{3+}) and (Dy^{3+}/Eu^{3+}) co-activated tungstate-tellurite glasses were synthesized and their importance for solid state lighting applications, especially for white LEDs have been thoroughly examined. This chapter aims to achieve multicolour and energy transfer analysis via doping/co-doping suitable rare earth ions (REIs) in the tungstate-tellurite glasses under n-UV/blue excitation wavelengths. Among all the several REIs, trivalent europium (Eu^{3+}) is an excellent activator ion for producing red light with proper CIE color coordinates [176]. Further, the conventional red phosphors with the doping of Eu^{3+} ions, including Y_2O_3: Eu^{3+} and Y_2O_3S: Eu^{3+}, display weak absorption in n-UV and blue regions [177]. All of the noticed *4f-4f* transitions of Eu^{3+} ions originating from the lowest energy state $^7F_0$ to the various higher energy states are parity forbidden. Therefore, it is required to sensitize Eu^{3+} ions with other suitable ions [176-178]. One of the suitable ions for sensitization of Eu^{3+} is terbium (Tb^{3+}) ion with the electronic configuration of $4f^8$, which enables efficient energy transfer from Tb^{3+} to Eu^{3+}. Many investigations are carried out to analyze the ET mechanism and sensitization of green emission demonstrated via Tb^{3+} ions with Eu^{3+} ions in various host matrices [179-181]. Moreover, by adjusting the concentrations of Eu^{3+} and Tb^{3+} ions in a single glass host composition, it is possible to achieve multicolour emission for practical applications.

In this chapter, transparent Tb^{3+} activated and Tb^{3+}/Eu^{3+} co-activated tungstate-tellurite (TWKZBi) glasses have been prepared. The vibrational, luminescent characteristics, PL decay measurements and ET mechanism between Tb^{3+} and Eu^{3+} ions were investigated in depth. Furthermore, the chromaticity coordinates, ET probability and efficiency have been analyzed to explore the prospective usage of these glasses in photonic devices.

6.2. Experimental Procedure and Characterization Tools

The TWKZBi glass samples have been prepared via melt quenching procedure as discussed in *section 2.1*. The molar composition (in mol%) is listed below:

(1) 49.0 TeO_2 – 20.0 WO_3 – 15.0 K_2O – 10.0 ZnO – 5.0 Bi_2O_3 – 1.0 Eu_2O_3 (Sample named as TWKZBiEu$_{1.0}$).

(2) (50.0 –x) TeO_2 – 20.0 WO_3 – 15.0 K_2O – 10.0 ZnO – 5.0 Bi_2O_3 – x Tb_4O_7

The Tb_4O_7 ion concertation ranges from 0.5 to 3.0 mol% (i.e., x = 0.5, 1.0, 2.0 & 3.0 mol%) and are named as TWKZBiTb$_{0.5}$, TWKZBiTb$_{1.0}$, TWKZBiTb$_{2.0}$ & TWKZBiTb$_{3.0}$, respectively. Further, Tb^{3+} and Eu^{3+} co-doped glasses have been prepared with the fixed Tb^{3+} concentration (2.0 mol%) and varying Eu^{3+} concentration (in mol%). The content of Tb^{3+} ions has been set at 2.0 mol% for the co-doped glasses owing to the optimal Tb^{3+} ion content in the titled glasses based on the photoluminescence properties as established in the current research work. The composition of the transparent Tb^{3+}/Eu^{3+} co-doped TWKZBi glasses is shown as follows:

(3) (48.0 – y) TeO_2 – 20.0 WO_3 – 15.0 K_2O – 10.0 ZnO – 5.0 Bi_2O_3 – 2.0 Tb_4O_7 – y Eu_2O_3

The different concentrations of Eu_2O_3 (y) have been co-doped in the above glass matrix with mol% of 0.5, 1.0, 1.5, 2.0 & 3.0, and the prepared glass samples were named as TWKZBiTb$_{2.0}$Eu$_{0.5}$, TWKZBiTb$_{2.0}$Eu$_{1.0}$, TWKZBiTb$_{2.0}$Eu$_{1.5}$, TWKZBiTb$_{2.0}$Eu$_{2.0}$ & TWKZBiTb$_{2.0}$Eu$_{3.0}$, respectively. Finally, transparent TWKZBi glasses have been prepared along with proper thickness for further characterization.

6.3. Results and Discussion

6.3.1. Vibrational Spectroscopy

To determine the existence of different molecular/chemical groups and characterize the structure around the dopant ions, Raman spectroscopy analysis was performed on the prepared glass samples. The Raman spectrum of the undoped and Tb^{3+}/Eu^{3+} co-activated TWKZBi glasses was scanned at ambient temperature in the spectral range from 100 to 1600 cm^{-1} as depicted in Fig 6.01 (a and b). The Raman spectrum of the prepared TWKZBiTbEu glass samples exhibits broad shoulder peaks that are being assigned to the disorderliness of the glass network. To identify the precise molecular vibrations in the prepared glasses, the Raman spectrum is deconvoluted into the symmetrical Gaussian function. The deconvoluted Raman spectrum of the TWKZBiTb$_{2.0}$Eu$_{1.0}$ glass sample is depicted in Fig. 6.01 (b).

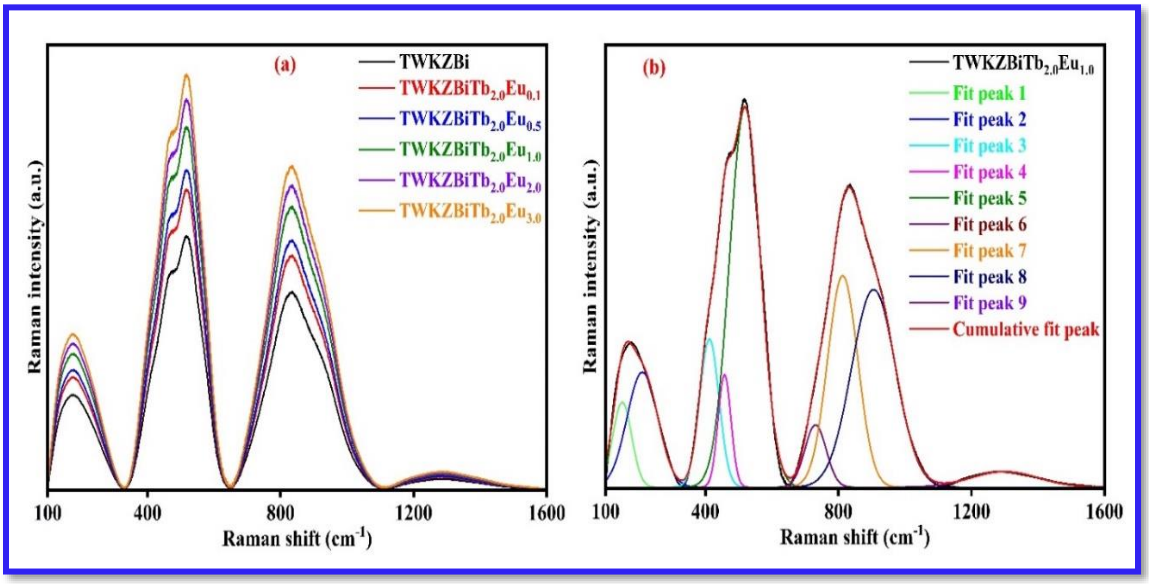

Fig. 6.01 (a). *Raman spectra for the undoped and Tb^{3+}/Eu^{3+} co-activated TWKZBi glass samples, and* ***(b)*** *The deconvoluted Raman spectrum for the TWKZBiTb$_{2.0}$Eu$_{1.0}$ glass sample.*

The Raman spectrum reveals different shoulder peaks located at 140, 214, 409, 523, 732, 812, 908, and 1250 cm^{-1}, respectively. The peak at 140 cm^{-1} could be related to the symmetric stretching vibration of Bi-O-Bi linkages in BiO_3 pyramidal and BiO_6 octahedron units [182]. The bending vibration of Zn-O linkages from the ZnO_4 units in the prepared glasses can be responsible for the shoulder peak noted at 214 cm^{-1} [182, 183]. The shoulder peak around 409 cm^{-1} may be ascribed to the bending vibration of the W-O-W linkages in WO_6 units. Further, the continuous network comprised of TeO_4 trigonal bipyramids may have undergone antisymmetric stretching, which is caused by the shoulder peak position at 523 cm^{-1} [184, 185]. The peak positioned at 732 cm^{-1} may be ascribed to the stretching vibration of TeO_3 trigonal bipyramids units [185]. On the other hand, both peaks allocated at 812 and 908 cm^{-1} may be related to the stretching variations of W-O-W and W=O linkages in the WO_4 or WO_6 unis [186]. The stretching vibrations of Bi-O linkages in the BiO_3 units may be related to the shoulder peak around 1250 cm^{-1} [182]. Furthermore, the phonon energy of the prepared glasses has been revealed from the Raman analyses. According to the literature, the phonon energy is equivalent to the energy matching of the maximum intensity Raman shoulder peak [187]. Thus, the phonon energy of the existing glass host composition has been estimated to be 523 cm^{-1}. Such a low phonon energy yields to a significant enhancement in the luminescent potential of the host matrix as a consequence of the suppression of the non-radiative losses.

6.3.2. Photoluminescence Studies

6.3.2.1. *Luminescent Characteristics of Tb^{3+} Doped* TWKZBi *Glasses*

By keeping fixed green (545 nm) emission wavelength, the photoluminescence excitation (PLE) spectrum of 2.0 mol% Tb^{3+} doped TWKZBi ($TWKZBiTb_{2.0}$) glass sample has been scanned in the 300 to 500 nm spectral region at ambient temperature as depicted in Fig. 6.02. Two excitation peaks in the PLE spectrum at a wavelength of n-UV (378 nm) and blue (486 nm) are linked with the transitions initiating from the ground energy level ($^7F_6$) to excited energy levels of $^5G_6$ and $^5D_4$, respectively [188, 189]. The emission spectra have been recorded for the prepared Tb^{3+} doped TWKZBi glass samples under 378 and 486 nm excitation wavelengths, as demonstrated in Fig. 6.03 (a and b). A minute difference in the emission intensity profile has been observed under the 378 and 486 nm excitations. It was obvious from Fig. 6.03 (a) that the emission spectra of the prepared TWKZBiTb glasses consist of several prominent emission peaks around 490, 545, 585 and 621 nm associated with the $^5D_4 \rightarrow {}^7F_6$, $^5D_4 \rightarrow {}^7F_5$, $^5D_4 \rightarrow {}^7F_4$ and $^5D_4 \rightarrow {}^7F_3$ *4f-4f* electronic transitions of Tb^{3+} ions, respectively [188-191]. Whereas the emission spectra consist of three emission peaks in Fig. 6.03 (b) located at 545, 585, and 621 nm ascribed to the $^5D_4 \rightarrow {}^7F_5$, $^5D_4 \rightarrow {}^7F_4$ and $^5D_4 \rightarrow {}^7F_3$ electronic transitions of Tb^{3+} ions, respectively under 486 nm excitation [189, 190].

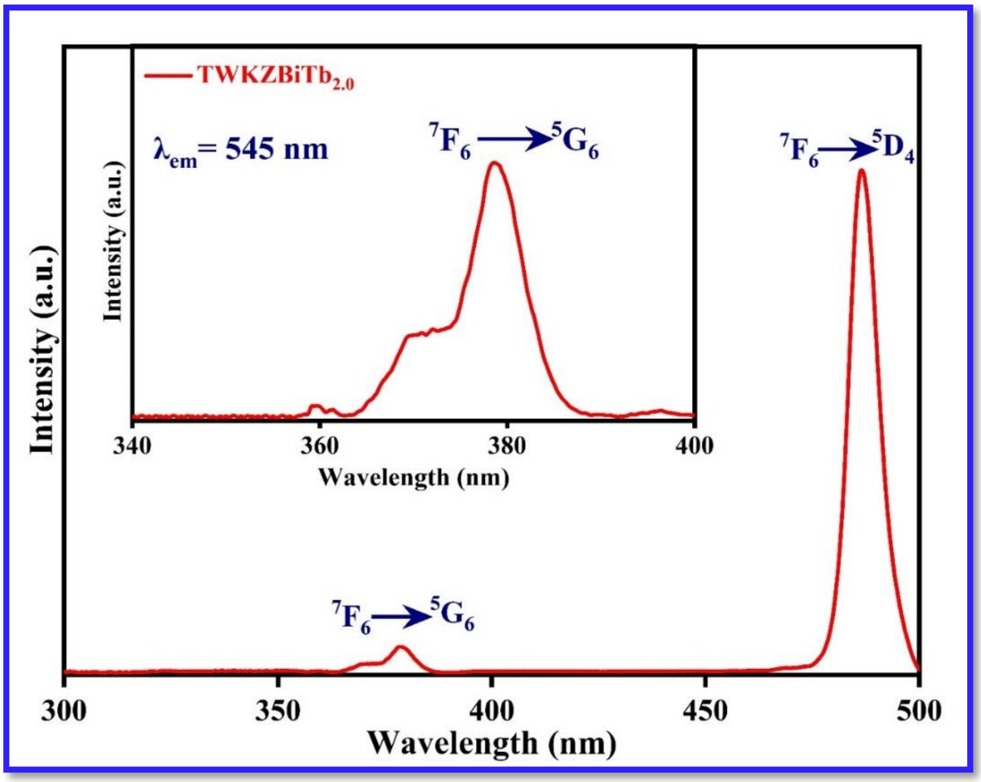

Fig. 6.02. *Excitation spectrum of 2.0 mol% Tb^{3+} doped TWKZBi glass under 545 nm emission wavelength. (Inset: Represents magnified excitation spectrum in the wavelength range 340-400 nm.)*

Amongst all the emission peaks under n-UV and blue excitations, the most intense green emission peak is situated at 545 nm ($^5D_4 \rightarrow {}^7F_5$) transition and is considered as a magnetic dipole (MD) via the selection rule, i.e., $\Delta J = \pm 1$, and the emission peak positioned at 490 nm ($^5D_4 \rightarrow {}^7F_6$) is ascribed to the forced electric dipole (ED) transition obeys via the selection criteria, i.e., $\Delta J = 2$ [189]. The emission peak in the green region at 545 nm splits into two peaks due to the crystal field splitting [188, 192]. The emission intensity variation with Tb^{3+} ion concentration in the TWKZBi glass samples is displayed in the inset Fig. 6.03 (a & b). It has been noted that the emission intensity of the TWKZBiTb glasses progressively raises with an increment in the content of Tb^{3+} ions up to 2.0 mol% and gradually drops after this concentration with a surge in the content of Tb^{3+} ions up to 3.0 mol%. This declining behaviour in emission intensity occurs owing to the content quenching phenomenon. The explanation for quenching phenomena by increasing the Tb^{3+} content ions may correspond to the non-radiative multipole interaction between Tb^{3+} ions and cross-relaxation channels (CRCs) via energy transfer (ET) mechanism between the dopant ions [192].

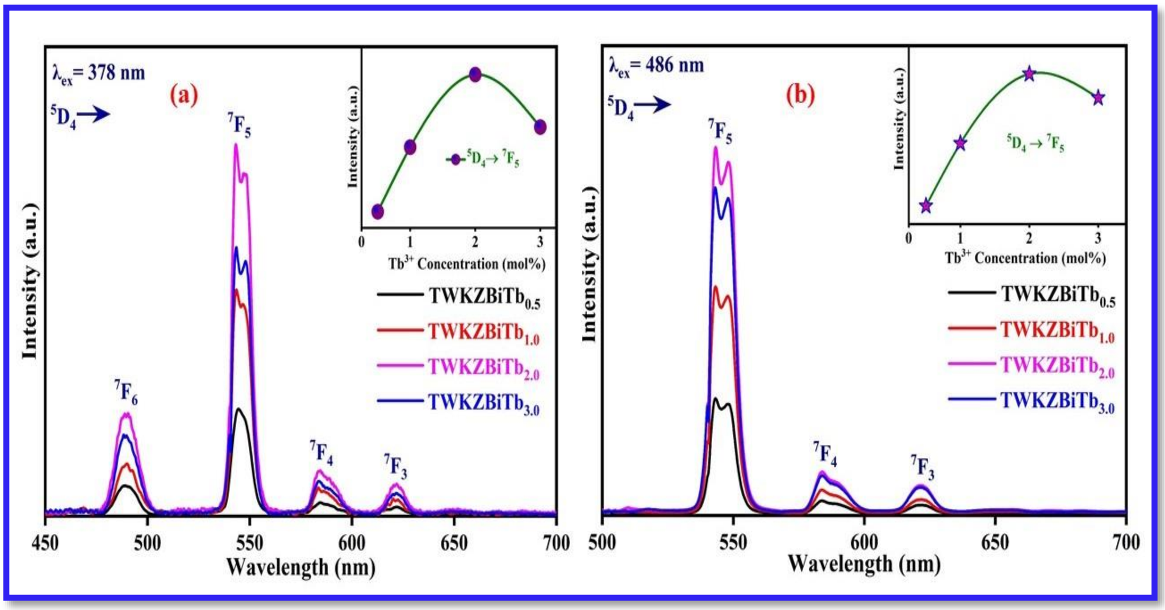

Fig. 6.03. *Emission spectra of Tb^{3+} doped TWKZBi glasses under* ***(a)*** *378 and* ***(b)*** *486 nm excitation wavelengths. (Inset: Represents the variation in emission intensity of 545 nm peak with varying the Tb^{3+} ion concentration in TWKZBi glasses).*

6.3.2.2. Luminescent Characteristics of Eu^{3+} Doped TWKZBi *Glasses*

Fig. 6.04 depicts the PLE and emission spectrum of 1.0 mol% Eu^{3+} activated TWKZBi (TWKZBiEu$_{1.0}$) glass sample. With monitoring the red (614 nm) emission wavelength, the PLE spectrum for TWKZBiEu$_{1.0}$ glass was measured at ambient temperature in the 300 to 550 nm spectral region. The PLE spectrum involves several excitation peaks observed at 360, 381, 393, 413, 465 and 534 nm attributed to the *4f-4f* electronic transitions $^7F_0 \rightarrow {}^5D_4$, $^7F_0 \rightarrow {}^5L_7$, $^7F_0 \rightarrow {}^5L_6$, $^7F_0 \rightarrow {}^5D_3$, $^7F_0 \rightarrow {}^5D_2$ and $^7F_1 \rightarrow {}^5D_1$ of the Eu^{3+}, respectively [191, 193]. Fig. 6.04 demonstrates the emission spectrum of the TWKZBiEu$_{1.0}$ glass sample was measured at n-UV (393 nm) excitation. The emission spectrum of the prepared TWKZBiEu$_{1.0}$ glass revealed various emission peaks observed at 579, 591, 614, 653 and 703 nm attributes to $^5D_0 \rightarrow {}^7F_0$,

$^5D_0 \rightarrow {}^7F_1$, $^5D_0 \rightarrow {}^7F_2$, $^5D_0 \rightarrow {}^7F_3$ and $^5D_0 \rightarrow {}^7F_4$ electronic transitions of Eu^{3+} ions, respectively [14, 35, 194].

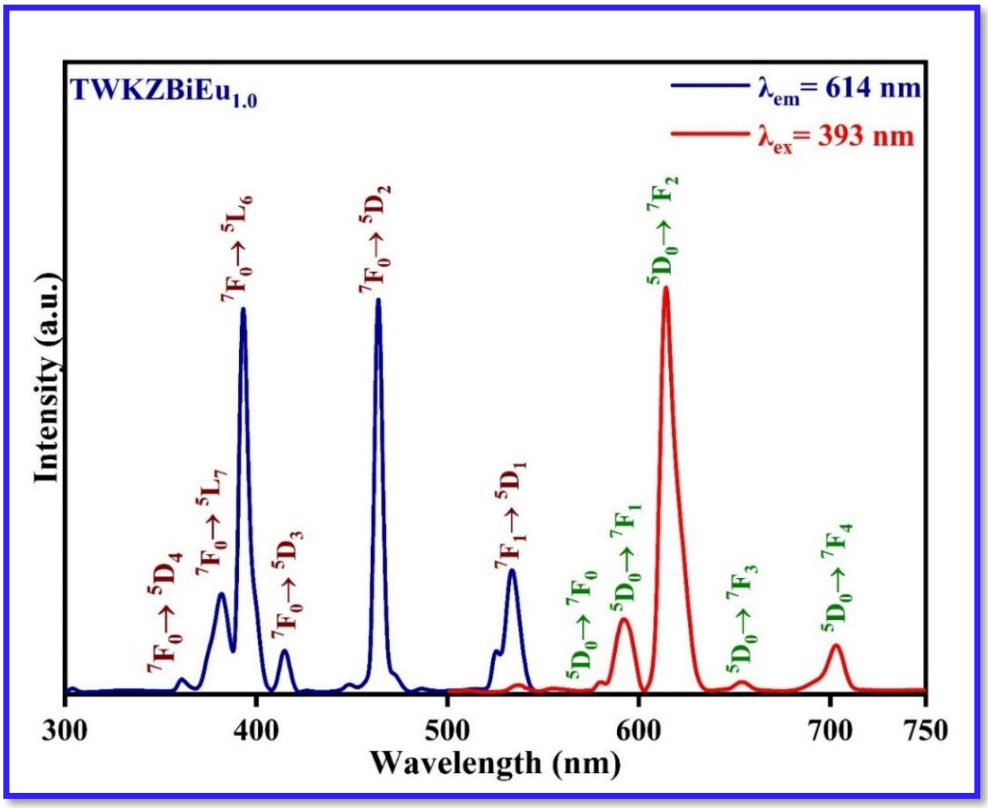

Fig. 6.04. *Excitation spectrum of TWKZBiEu$_{1.0}$ glass under 614 nm emission wavelength and emission spectrum of TWKZBiEu$_{1.0}$ glass under 393 nm excitation wavelength.*

Following the similar selection rules mentioned in *section 6.3.2.1*, the emission peak spotted around 614 nm (red region) corresponds to the forced ED in behaviour, whereas the emission peak seen in the orange region (591 nm) corresponds to the $^5D_0 \rightarrow {}^7F_1$ transition is MD in behaviour [38]. In the current study, the forced ED transition is more intense than the MD transition, which indicates that the dopant (Eu^{3+}) ions exist at low symmetry locations without an inversion center [14, 193]. Furthermore, the fraction of red-to-orange emission transition ($^5D_0 \rightarrow {}^7F_2/{}^5D_0 \rightarrow {}^7F_1$) is described as the asymmetric ratio and suggests estimating the site symmetry of Eu^{3+} ions. This ratio has been estimated to be 6.20 in the current scenario, implying that the red emission is 6.20 times higher than the orange emission. The greater asymmetric proportion values refer to the low symmetry of the dopant ions and higher covalency of dopant and ligand (Eu^{3+}-O^{2-}) atoms [14, 195].

6.3.2.3. Luminescence Characteristics of Tb^{3+}/Eu^{3+} Co-doped TWKZBi *Glasses*

Dieke's energy level scheme can be utilized to predict the probability of ET across two rare-earth (RE^{3+}) ions. The ET occurs from a higher energy level of one RE^{3+} ion to the lower energy level of another RE^{3+} ion [192, 196, 197]. In the case of Tb^{3+} and Eu^{3+} ions, the transition levels of Tb^{3+} are higher in the present investigation than that of Eu^{3+}, suggesting the probability of ET may take place from Tb^{3+} to Eu^{3+} ions. The spectrum overlap between the donor (Tb^{3+}) emission and acceptor (Eu^{3+}) excitation is one of the most crucial conditions for ET [197].

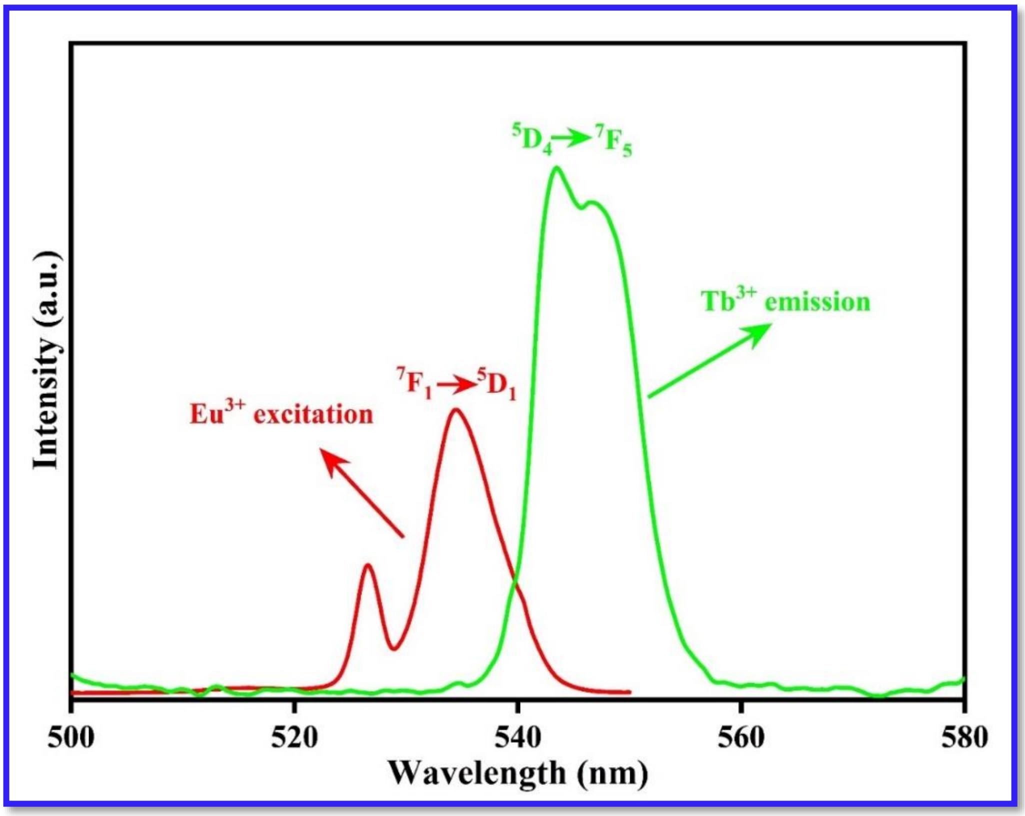

Fig. 6.05. *The spectral overlap of emission of Tb^{3+} (sensitizer) and excitation of Eu^{3+} (activator) in the $TWKZBiTb_{2.0}Eu_{2.0}$ glass sample.*

The excitation peak around 534 nm corresponds to the $^7F_1 \rightarrow {}^5D_1$ electronic transition of Eu^{3+} ions overlapping with the emission peak around 545 nm is attributed to the $^5D_4 \rightarrow {}^7F_5$ transition of Tb^{3+} ions as depicted in Fig. 6.05. This overlapping region demonstrates that the Eu^{3+} ion works as an activator/acceptor, whereas the Tb^{3+} serves as a sensitizer/donor. The PLE and emission spectral features of the prepared Tb^{3+}/Eu^{3+} co-activated TWKZBi glasses were measured to determine their luminous characteristics at adequate wavelength regions. As reported in the previous section, the optimum doping concentration of Tb^{3+} ions has been 2.0 mol% in TWKZBi glasses. The PLE spectrum of 2.0 mol% Tb^{3+}/2.0 mol% Eu^{3+} co-doped TWKZBi (TWKZBiTb$_{2.0}$Eu$_{2.0}$) glass has been observed at ambient temperature by monitoring the red (614 nm) emission wavelength, at ambient temperature in the 325 to 500 nm spectral wavelength range, as shown in Fig. 6.06 (a).

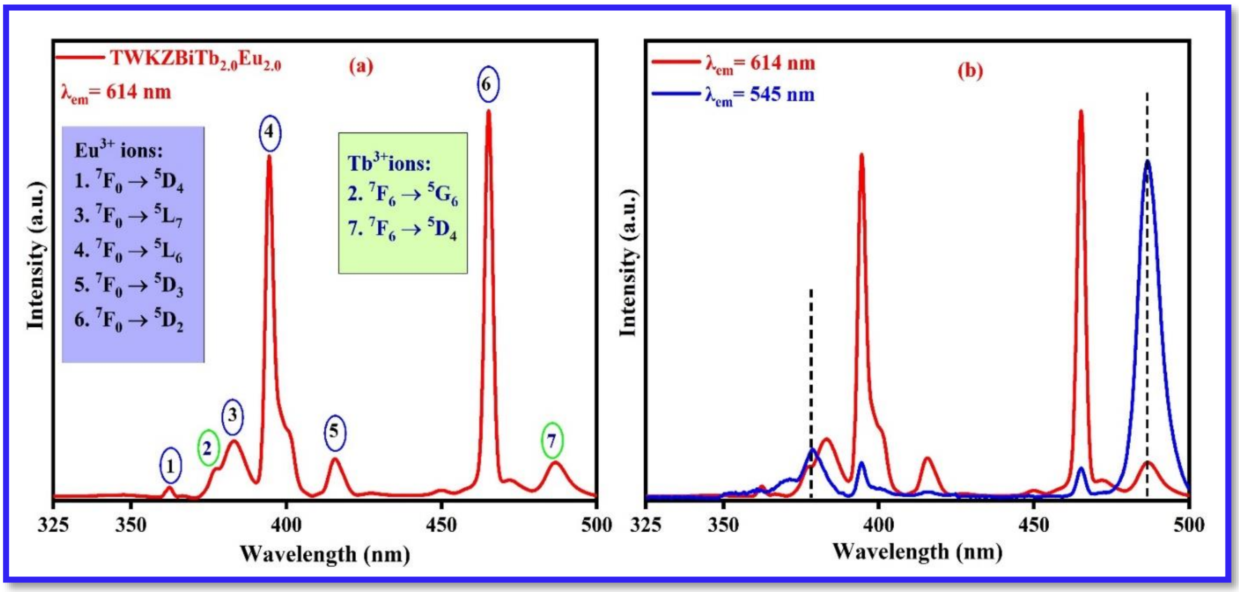

Fig. 6.06. (a) *Excitation spectrum of the TWKZBiTb$_{2.0}$Eu$_{2.0}$ glass under red (614 nm) emission wavelength.* ***(b)*** *Excitation spectra of TWKZBiTb$_{2.0}$Eu$_{2.0}$ glass under green (545 nm) and red (614 nm) emission wavelengths.*

In this PLE spectrum, few observed excitation peaks are due to the Eu^{3+} ions, and certain other excitation peaks owing to Tb^{3+} ions. The detected excitation peaks around 378 and 486 nm correspond to the transitions from the lower lying energy state ($^7F_6$) to different higher energy states such as $^5G_6$ and $^5D_4$ of Tb^{3+} ions, respectively. The PLE spectra of the prepared TWKZBiTb$_{2.0}$Eu$_{2.0}$ glass were recorded under fixed intense green (545 nm) and red (614 nm) emission wavelengths, as displayed in Fig 6.06 (b). Based on the PLE spectra of the TWKZBiTb$_{2.0}$Eu$_{2.0}$ glass sample, the n-UV (378 nm) and blue (486 nm) were determined to be appropriate excitation wavelengths for the series of Tb^{3+}/Eu^{3+} co-doped TWKZBi glasses.

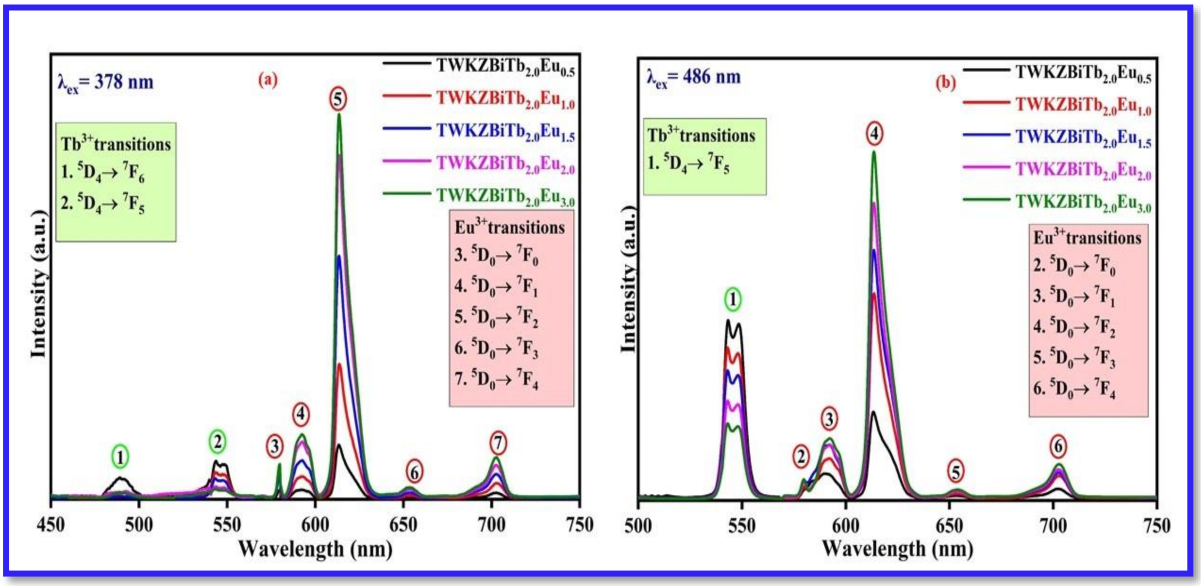

Fig. 6.07. *Emission spectra of Tb^{3+}/Eu^{3+} co-doped TWKZBi glasses under* ***(a)*** *n-UV and* ***(b)****blue excitation wavelengths.*

The PL spectra for the Tb^{3+}/Eu^{3+} co-activated TWKZBi glasses have been recorded at n-UV and blue excitations are demonstrated in Fig. 6.07 (a and b). Under n-UV excitation, the PL spectra have shown several different emission peaks observed at 490, 545, 579, 591, 614, 653 and 703 nm, whereas PL spectra reveal distinct emission peaks in the green to red regions such as 545, 579, 591, 614, 653 and 703 nm under the blue excitation. The PL peaks were observed around 490 and 545 nm associated with the transitions $^5D_4 \rightarrow {}^7F_6$ and $^5D_4 \rightarrow {}^7F_5$ of Tb^{3+} ions, as described in the preceding section [181]. Moreover, the emission peaks were observed at 579, 591, 614, 653 and 703 nm associated with the $^5D_0 \rightarrow {}^7F_0$, $^5D_0 \rightarrow {}^7F_1$, $^5D_0 \rightarrow {}^7F_2$, $^5D_0 \rightarrow$

$^7F_3$ and $^5D_0 \rightarrow {}^7F_4$ transitions as a result of the co-doping Eu^{3+} ions. Under n-UV and blue excitations, the PL intensity of Tb^{3+} ions decline with an increment in the Eu^{3+} ion concentrations as illustrated in Fig. 6.08 (a and b). The PL intensity variation in both Tb^{3+} and Eu^{3+} ions is due to the interaction and ET between the RE^{3+} ions.

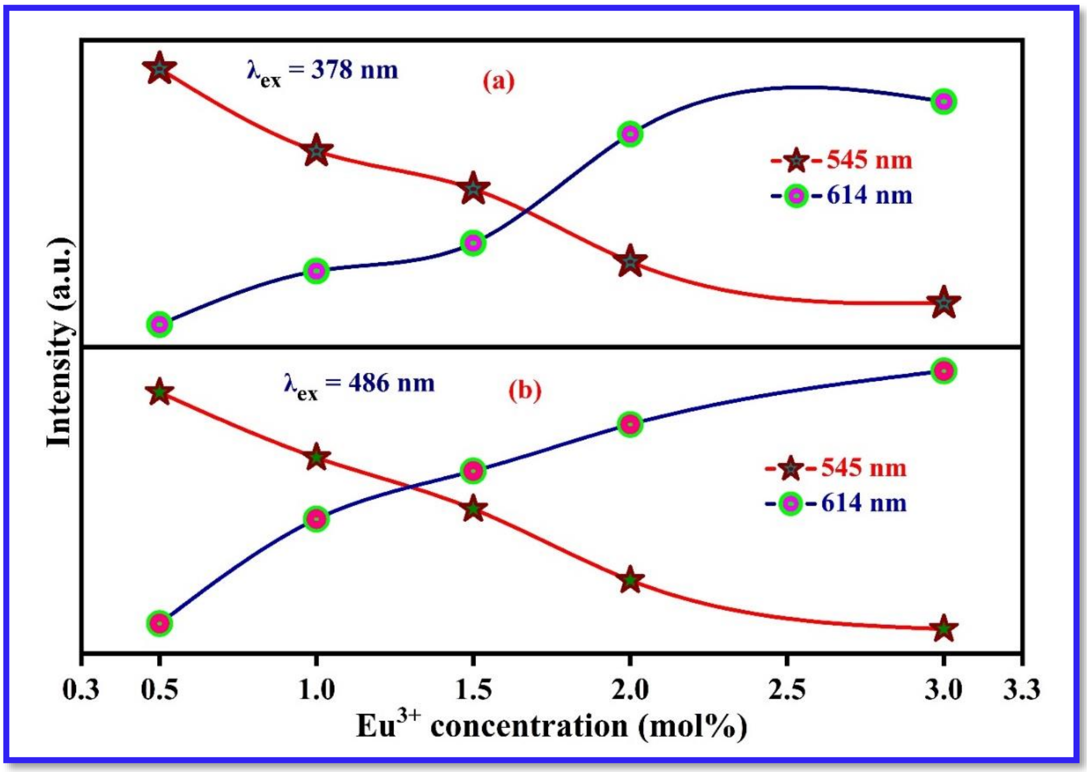

Fig. 6.08. *The variation in emission intensity of emission peaks of 545 nm and 614 nm under **(a)** n-UV and **(b)** blue excitation wavelengths.*

The partial energy scheme for the Tb^{3+}, Eu^{3+} activated TWKZBi glass clarifies the ET mechanism, as depicted in Fig. 6.09. The Tb^{3+} ions absorb specific n-UV and blue radiation, which in turn excites the electrons from the ground energy level to higher excited energy levels. As mentioned by black-dotted lines, the excited electrons decline in their energy via non-radiative transition and fall to the $^5D_4$ energy state of the Tb^{3+} ions and give radiative emission in the visible spectral region as explained in earlier PL properties. The $^5D_0$ energy level of Eu^{3+} ions is lesser than that of the $^5D_4$ energy level of Tb^{3+} ions. Hence, it is probable that the energy from Tb^{3+} ions was partially transferred non-radiatively to Eu^{3+} ions leading to a decrease in the emission of Tb^{3+} ions. The energy gap between the $^5D_4$ level and $^5D_0$ level is smaller than that of making the ET possible through phonon-assisted NRT [181, 197]. This suggests that the Tb^{3+} ion is an efficient sensitizer for the Eu^{3+} ions. The exchange and multipolar interaction may be used to carry out the ET from a sensitizer/donor (Tb^{3+}) ion to an activator/acceptor (Eu^{3+}) ion.

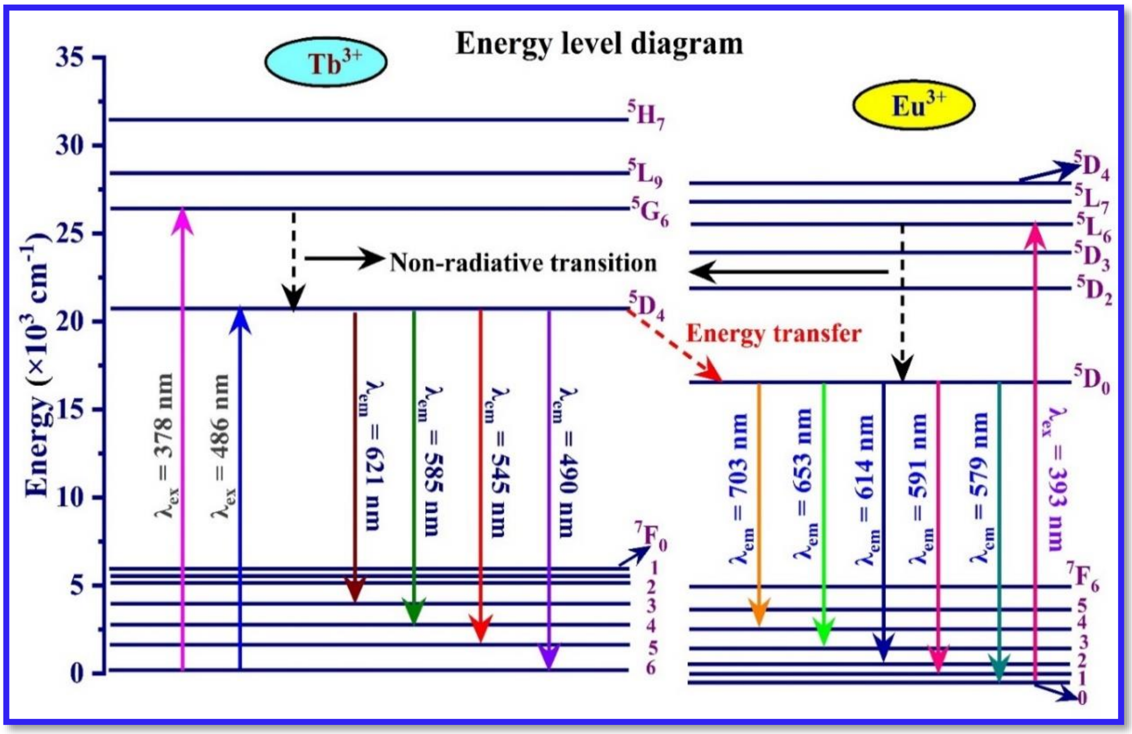

Fig. 6.09. *Energy level diagram indicating the energy transfer involved in Tb^{3+}/Eu^{3+} co-doped TWKZBi glasses.*

Depending on Reisfeld's approximation and Dexter's ET formula for multipolar interaction, a correlation may be written in *equation (5.1)*. The value of the parameter $^{\eta_0}/_{\eta}$ may be estimated via the proportion of relative emission intensities as expressed in *equation (5.2)*. As demonstrated in Fig. 6.10 (a and b), the relationship among the $^{I_{SO}}/_{I_S}$ against $C^{n/3}$ has been plotted and the finest match has been retrieved for n = 6, under the n-UV and blue excitations. It was evident from Fig. 6.10 (a and b) that the ET from the donor (Tb^{3+}) to the acceptor (Eu^{3+}) owing to the non-radiative d-d interaction in the prepared glasses.

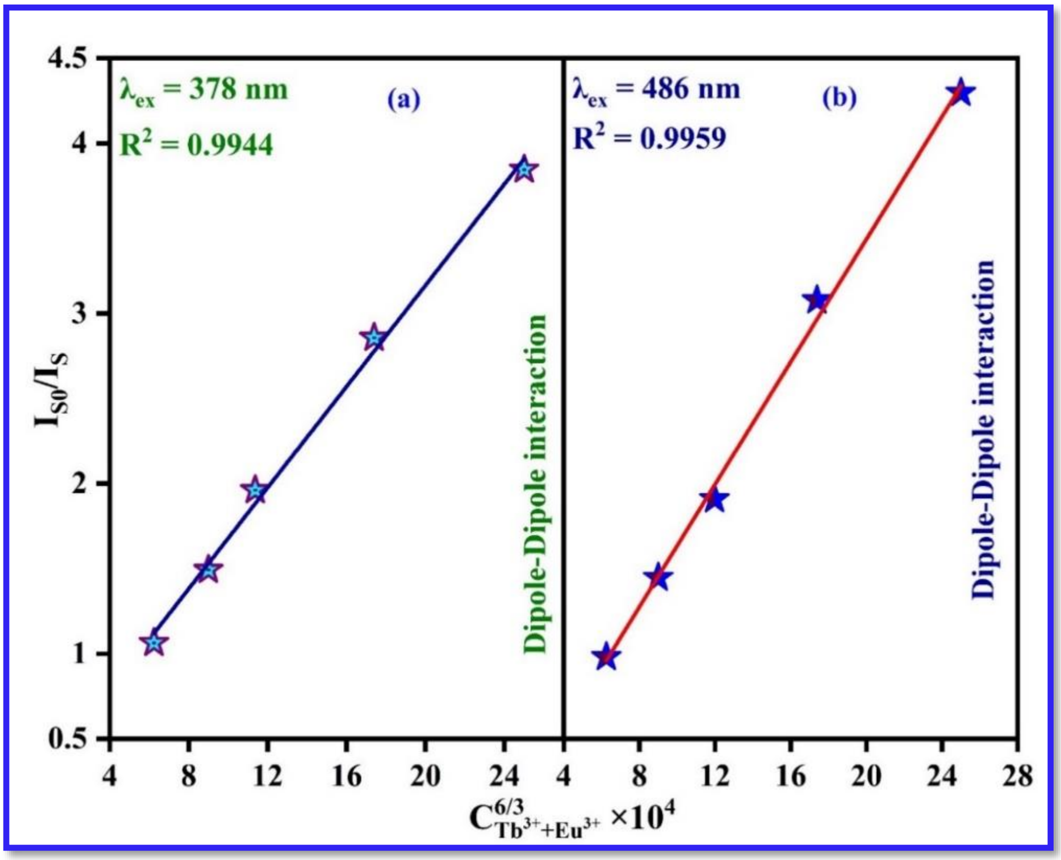

Fig. 6.10. *The dependence of* $^{I_{S0}}/_{I_S}$ *versus* $C^{6/3}_{Tb+Eu} \times 10^4$ *in co-doped glasses for* ***(a)*** *n-UV and* ***(b)*** *blue excitation wavelengths.*

6.3.3. PL Decay Measurement and Energy Transfer Efficiency

Fig. 6.11 illustrates that the PL lifetime has been measured via fixed green emission (545 nm) wavelength excited by 378 nm excitation wavelength to explore the lifetime of Tb^{3+}/Eu^{3+} co-activated TWKZBi glasses. The lifetime profiles have been most exceptionally fitted with the bi-exponential equation as presented in the literature [172, 197-199]. The average lifetime (τ_{Avg}) for Tb^{3+}/Eu^{3+} co-doped TWKZBi glasses have been calculated via applying *equation (2.10)*. The calculated τ_{Avg} values for Tb^{3+} doped and Tb^{3+}/Eu^{3+} co-doped TWKZBi glasses under 378 nm excitation have been presented in Table 6.1. It has been noticed that the τ_{Avg} values for Tb^{3+}/Eu^{3+} co-doped TWKZBi glass samples decline with the surge in the Eu^{3+} ion concentrations, which is convincing that the ET happens from sensitizer (Tb^{3+}) to activator (Eu^{3+}) ions. The ET efficiency (η_T) from the sensitizer to activator ions was estimated as per *equation (5.3)*. Using the average lifetime values, the ET probability (P_T) may be estimated using *equation (5.5)*. The estimated values of η_T and P_T were shown in Table 6.01. The change in τ_{Avg} and η_T via varying the Eu^{3+} ion concentrations in the prepared TWKZBiTbEu glasses under 378 nm excitation are depicted in Fig. 6.12. With an increase in the Eu^{3+} ion concentrations, it has been noticed that the τ_{Avg} values decrease and increase in η_T values, suggesting that the energy has been transferred from Tb^{3+} to Eu^{3+} ions.

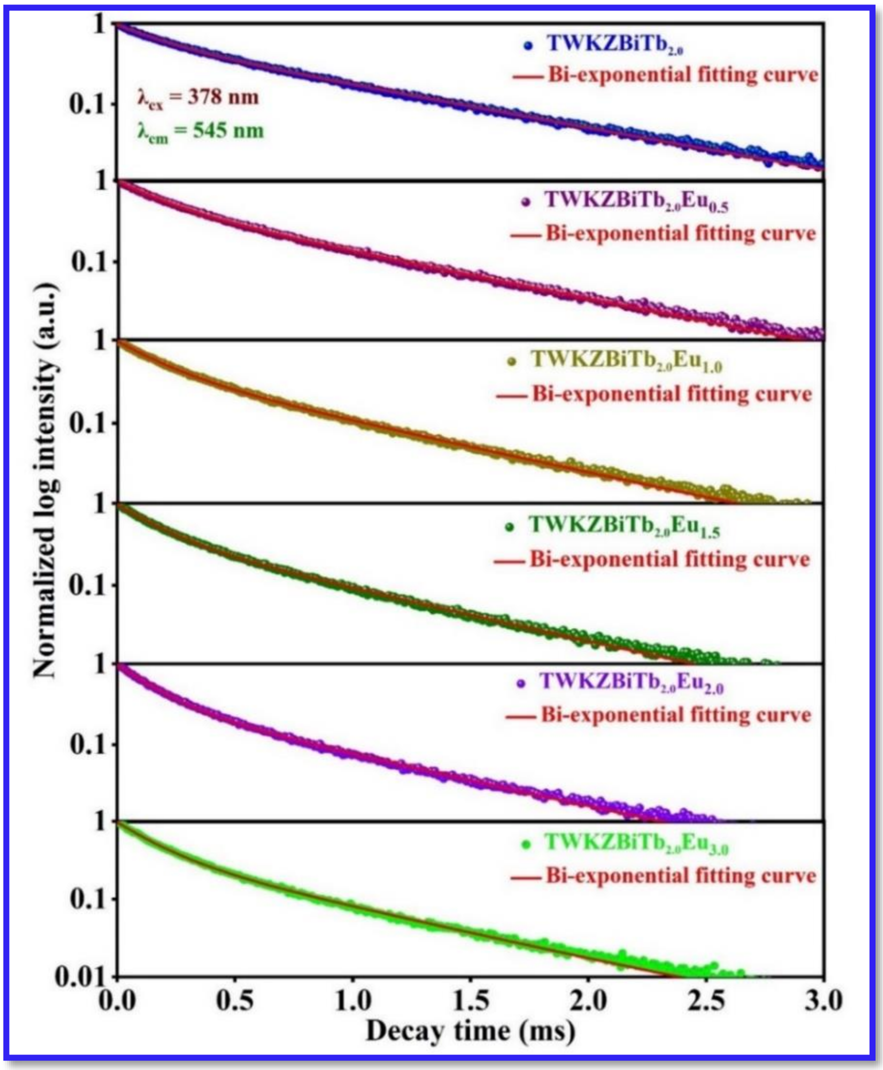

Fig. 6.11. *Decay profiles for TWKZBiTb2.0, TWKZBiTb2.0Eu0.5, TWKZBiTb2.0Eu1.0, TWKZBiTb2.0Eu1.5, TWKZBiTb2.0Eu2.0 and TWKZBiTb2.0Eu3.0 glass samples under 378 nm excitation.*

Table 6.01. The average lifetime (μs), energy transfer efficiency (η_T) and energy transfer probability (P_T) for Tb^{3+}/Eu^{3+} co-doped TWKZBi glasses under n-UV excitation.

Sample code	**Average lifetime (μs)**	**Energy transfer efficiency (η_T, %)**	**Energy transfer probability (P_T)**
TWKZBiTb2.0	722.302	-	-
TWKZBiTb2.0Eu0.5	637.448	11.747	1.133
TWKZBiTb2.0Eu1.0	572.419	20.750	1.261
TWKZBiTb2.0Eu1.5	531.017	26.482	1.360
TWKZBiTb2.0Eu2.0	501.535	30.564	1.440
TWKZBiTb2.0Eu3.0	485.195	32.826	1.448

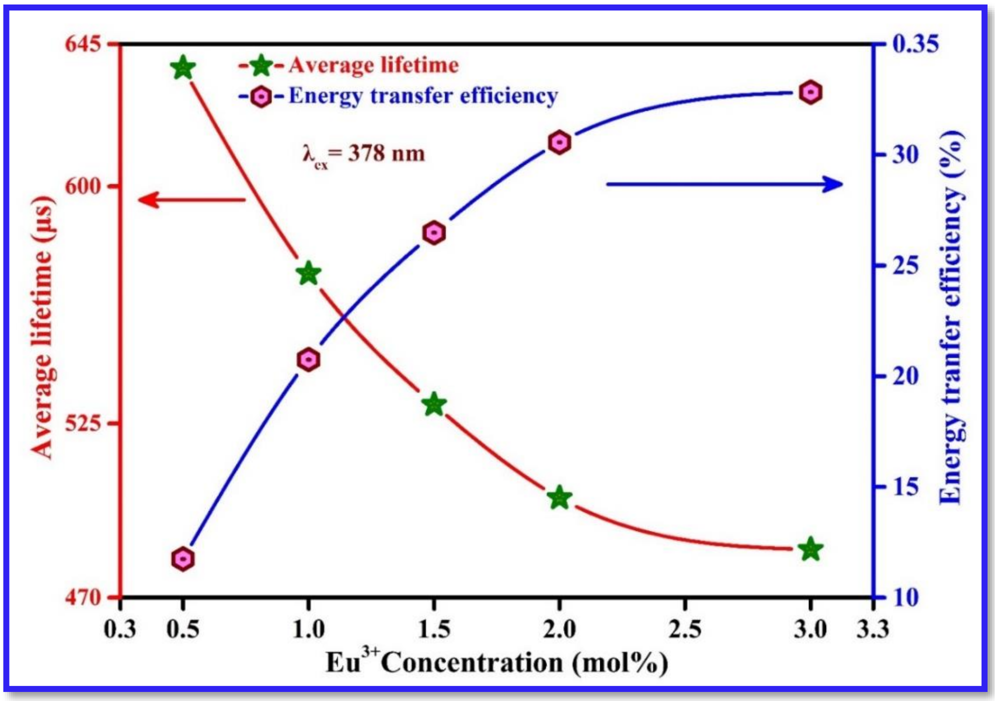

Fig. 6.12. *The average lifetime and energy transfer efficiency along with varying the Eu^{3+} ion concentration in the Tb^{3+}/Eu^{3+} co-doped TWKZBi glasses under 378 nm excitation.*

6.3.4. Colorimetric Properties

The Commission International de l'Eclarirage (CIE) chromaticity coordinates of the optimized TWKZBiTb$_{2.0}$ and TWKZBiEu$_{1.0}$ glasses have been evaluated using the PL spectra and shown in Fig. 6.13 (a). Under n-UV and blue excitations, the chromaticity coordinates (x, y) for TWKZBiTb$_{2.0}$ glass have been found to be (0.303, 0.568) and (0.343, 0.646), respectively, which lie within the green region of the CIE graph. These coordinates are in excellent agreement with the widely recognized green phosphors such as ZnS: Au$_{0.05}$, Cu$_{0.01}$ (0.267, 0.582) and (Zn, Cd) S: Ag (0.260, 0.600) [188, 192]. Moreover, the (x, y) coordinates for the TWKZBiEu$_{1.0}$ glass sample were observed to be (0.650, 0.348) under 393 nm excitation, lying in the reddish emission zone of the CIE graph and match closely to the color coordinates of Y_2O_2S: Eu^{3+} commercial red phosphor (0.647, 0.343) [196].

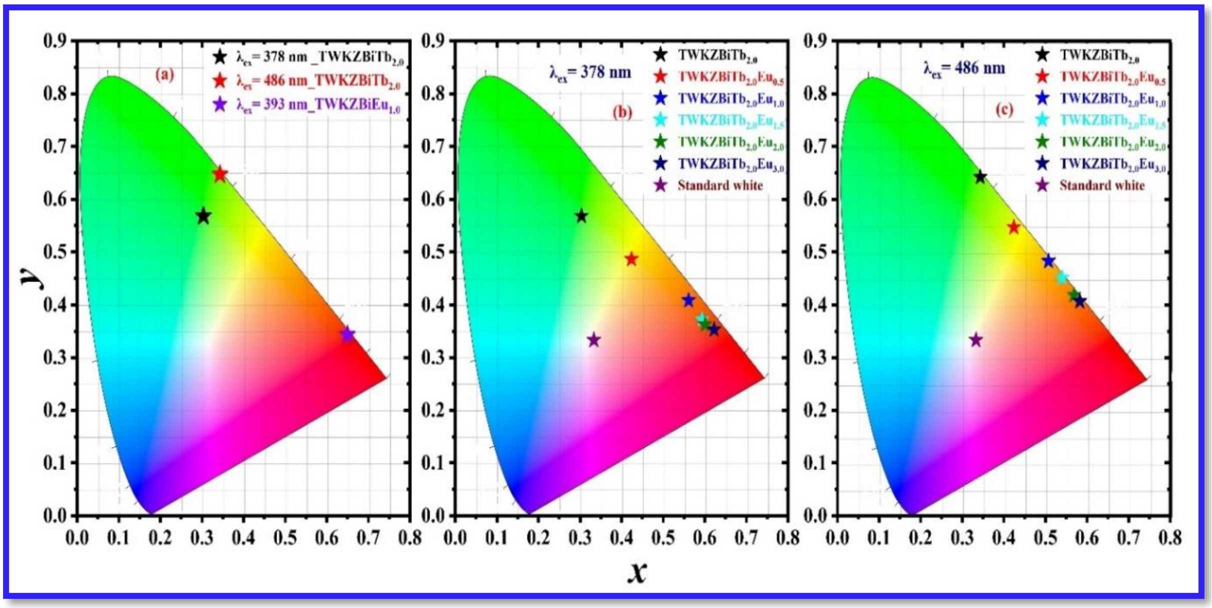

Fig. 6.13. (a) *CIE diagram demonstrating the chromaticity coordinates for the prepared TWKZBiTb$_{2.0}$ under 378, 486 nm and TWKZBiEu$_{1.0}$ under 393 nm excitation wavelengths,* ***(b** and **c)*** *CIE diagram representing the chromaticity coordinates for Tb^{3+}/Eu^{3+} co-doped TWKZBi glasses under 378 nm and 486 nm excitation wavelengths, respectively.*

Furthermore, the emission profile can also be employed to evaluate the correlated color temperature (CCT) in the form of McCamy's expression as presented in the previous reports [14, 18, 71].

Table 6.02. CIE color coordinates (*x*, *y*) for Tb^{3+}/Eu^{3+} co-doped TWKZBi glasses under n-UV and blue excitations.

Sample codes	Excitations	Color coordinates (*x*, *y*)
$TWKZBiTb_{2.0}Eu_{0.5}$	n-UV	(0.423, 0.486)
	Blue	(0.424, 0.546)
$TWKZBiTb_{2.0}Eu_{1.0}$	n-UV	(0.561, 0.408)
	Blue	(0.507, 0.482)
$TWKZBiTb_{2.0}Eu_{1.5}$	n-UV	(0.593, 0.371)
	Blue	(0.540, 0.456)
$TWKZBiTb_{2.0}Eu_{2.0}$	n-UV	(0.601, 0.362)
	Blue	(0.568, 0.428)
$TWKZBiTb_{2.0}Eu_{3.0}$	n-UV	(0.622, 0.353)
	Blue	(0.582, 0.416)

The CCT values for the optimized $TWKZBiTb_{2.0}$ glass are 6055 and 5356 K under n-UV (378 nm) and blue (486 nm) excitations, respectively. Also, the CCT value for the prepared $TWKZBiEu_{1.0}$ glass is 2601 K under 393 nm excitation. Hence, the results mentioned above validate the aptness of Tb^{3+} and Eu^{3+} activated TWKZBi glass samples for appliances in the domain of display and lighting devices. Moreover, the CIE coordinates have been estimated for Tb^{3+}/Eu^{3+} co-doped TWKZBi glasses under 378 nm and 486 nm excitations are exhibited in Fig. 6.13 (b and c), respectively. Under 378 nm and 486 nm excitations, the estimated (x, y) coordinates for Tb^{3+}/Eu^{3+} co-doped TWKZBi glass samples have been tabulated in Table 6.02. The (x, y) coordinates estimated under n-UV and blue excitations for all Tb^{3+}/Eu^{3+} co-doped TWKZBi glass samples suggest that color tone varies from green to red with the activator (Eu^{3+}) ion concentrations. The estimated (x, y) coordinates in both cases validated that the tunable color emission is achieved by varying the activator (Eu^{3+}) concentrations in the Tb^{3+}/Eu^{3+} co-doped TWKZBi glasses. Moreover, the evaluated CCT values for the prepared $TWKZBiTb_{2.0}Eu_{3.0}$ glass have been found to be 2116 and 1721 K under 378 and 486 nm excitations, which are below 5000 K. Hence, the results mentioned above endorse that the Tb^{3+}/Eu^{3+} co-doped TWKZBi glasses have promising properties for the usage in photonic applications.

6.3.5. Thermal Stability of Tb^{3+}/Eu^{3+} Co-doped TWKZBi Glasses

In general, thermal stability is an effective characteristic of luminescent materials and has practical in photonic applications. To observe the thermal stability of $TWKZBiTb_{2.0}Eu_{2.0}$ glass, the variation of emission intensity under the n-UV excitation has been registered with changing temperature from room temperature to 175 ºC as depicted in Fig. 6.14 and the inset of Fig. 6.14 represents the variation of relative emission intensity in percentage with varying temperatures. The PL intensity diminishes with an increment in the temperature and the preserved emission intensity of $TWKZBiTb_{2.0}Eu_{2.0}$ glass was around 85.80% at 100 ºC and 75.46% at 150 ºC when compared to the emission intensity at room temperature under 378 nm excitation. Therefore, the Tb^{3+}/Eu^{3+} co-doped TWKZBi glass shows excellent thermal stability.

Moreover, the activation energy (ΔE_a) has been estimated to reveal the thermal stability via employing the Arrhenius *equation (2.11)*.

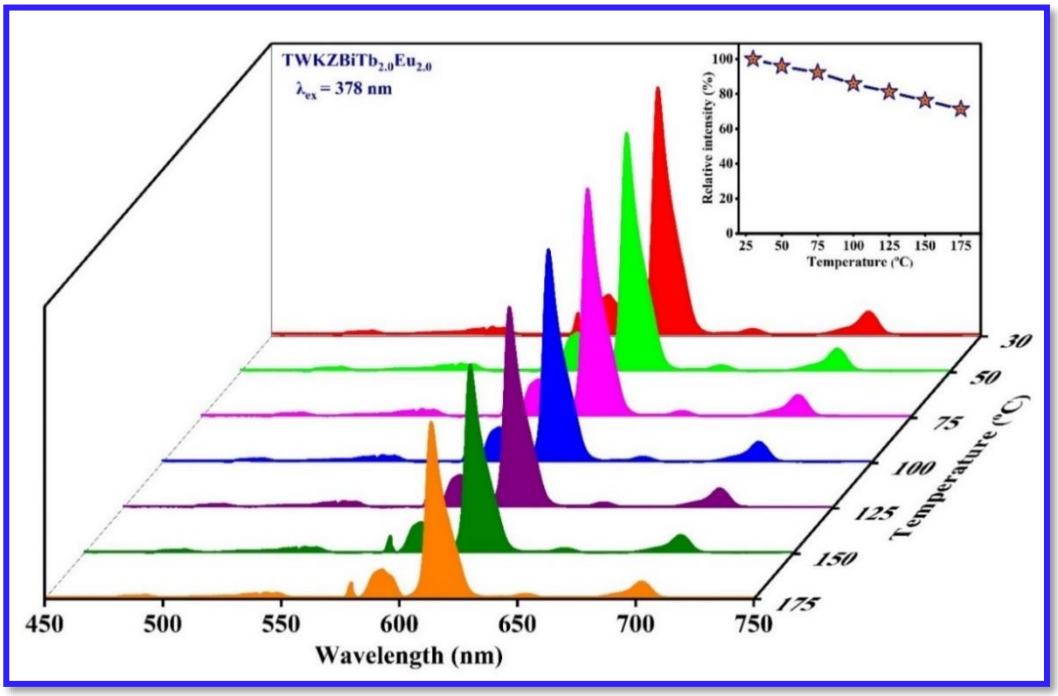

Fig. 6.14. *Temperature dependent PL spectra of the prepared TWKZBiTb*$_{2.0}$*Eu*$_{2.0}$ *glass sample with the temperature range from room temperature (30 ºC) to 175 ºC under 378 nm excitation. [Inset: represents the variation of emission intensity with temperature.]*

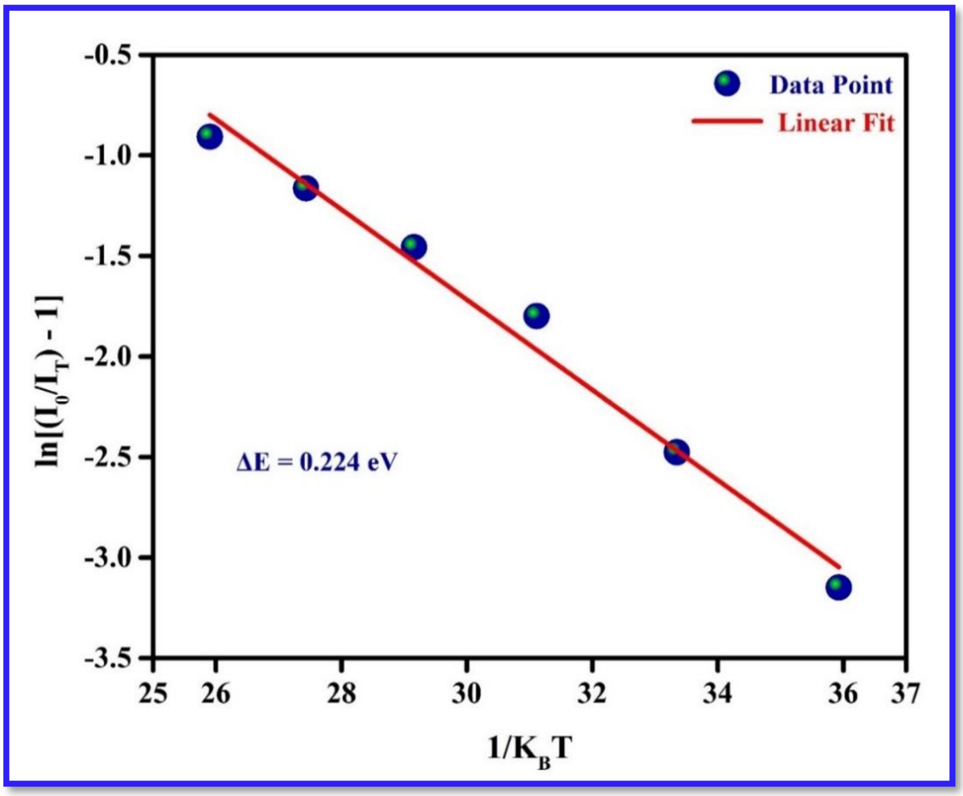

Fig. 6.15. *Plot between* $\ln[(I_0/I_T) - 1]$ *against* $1/K_BT$.

The slope of the linearly fitted diagram among the $\ln[(I_0/I_T) - 1]$ and $1/K_BT$ aids in calculating the activation energy (ΔE) as represented in Fig. 6.15. The estimated ΔE is 0.224 eV for $TWKZBiTb_{2.0}Eu_{2.0}$ glass under n-UV excitation, which is relatively higher than the other glasses reported elsewhere [125, 127].

6.4. Conclusions

In summary, the traditional melt quenching procedure was successfully used to prepare the transparent Tb^{3+} activated and Tb^{3+}/Eu^{3+} co-activated TWKZBi glass samples. The non-crystalline or amorphous behavior was confirmed via the XRD profiles of the prepared glasses. The PL results indicate that Tb^{3+}-activated TWKZBi glasses demonstrate a strong green emission (545 nm) band under n-UV and blue excitations, whereas Eu^{3+}-activated TWKZBi glasses exhibit prominent red emission (614 nm) under n-UV excitation. Tb^{3+}/Eu^{3+} co-activated TWKZBi glasses exhibit emission peaks in the blue, green, and red regions under n-UV excitation, while green and red emission bands under blue excitation. The (x, y) coordinates for Tb^{3+} singly activated TWKZBi glass have been (0.303, 0.568) and (0.343, 0.646) falling in the green region under the n-UV and blue excitations, whereas the (x, y) coordinates for Eu^{3+} singly activated TWKZBi glass has been (0.650, 0.348) falling in the reddish zone under n-UV excitation wavelength. The emission profiles from Tb^{3+}/Eu^{3+} co-doped TWKZBi glasses have been easily tunable from green to red regions in the CIE diagram through varying Eu^{3+} ion concentrations. The ET from sensitizer (Tb^{3+}) ions to activator (Eu^{3+}) ions appears d-d interaction that has been validated via employing Dexter's and Reisfeld's approximation on emission spectra. The PL lifetime values of the prepared TWKZBiTbEu glasses have been computed and it has been observed that the lifetime values of the $^5D_4$ level of Tb^{3+} ions decline with an increment in the Eu^{3+} ion concentration under n-UV excitation. Moreover, the temperature dependent PL spectra show that the prepared TWKZBiTbEu glass samples have admirable thermal stability. Hence, the aforementioned results corroborated that the Tb^{3+}/Eu^{3+} co-activated TWKZBi glasses accomplish their utility in the field of photonic applications.

Chapter – 07

Luminescent properties of Red emitting $Ca_3Bi(PO_4)_3$: Eu^{3+} Phosphor in Tungstate-Tellurite Glasses for Photonic Applications

The current research work includes the fabrication of transparent red emitting phosphor in glass (PiG) with different concentrations using a melt quenching process via inclusion of CBP: xEu^{3+} phosphor into the tungstate-tellurite (TWKZBi) glass. The structural and morphological characteristics of the fabricated PiG samples have been examined in detail with the help of X-ray diffraction (XRD) and field emission scanning electron microscopy (FE-SEM) with energy dispersive X-ray spectroscopy (EDS) analysis. CBP: xEu^{3+} phosphor and TWKZBi: CBPEu PiG samples revealed many individual emission peaks in the visible spectrum including a strong red emission band around 612 nm connected to the $^5D_0 \rightarrow {}^7F_2$ transition under 392 and 464 nm excitations. Further, the colorimetric characteristics of the synthesized phosphor and PiG sample were examined and found that the color coordinates lie in the red region with high colour purity. Under excitation at 392 nm, the decay profile of the TWKZBi: CBPEu08 PiG samples exhibit a bi-exponential with a lifetime value of 2.459 ms. Moreover, the emission intensity sustains up to 84.72% at 100 ^{0}C for the phosphor and 91.52% at 100 ^{0}C for the PiG sample. This assures that the PiG sample reveals better thermal stability than the phosphor. Based on all findings, the fabricated TWKZBi: CBPEu, PiG samples could potentially be utilized for photonic applications and also as a red-emitting component of white light-emitting diodes.

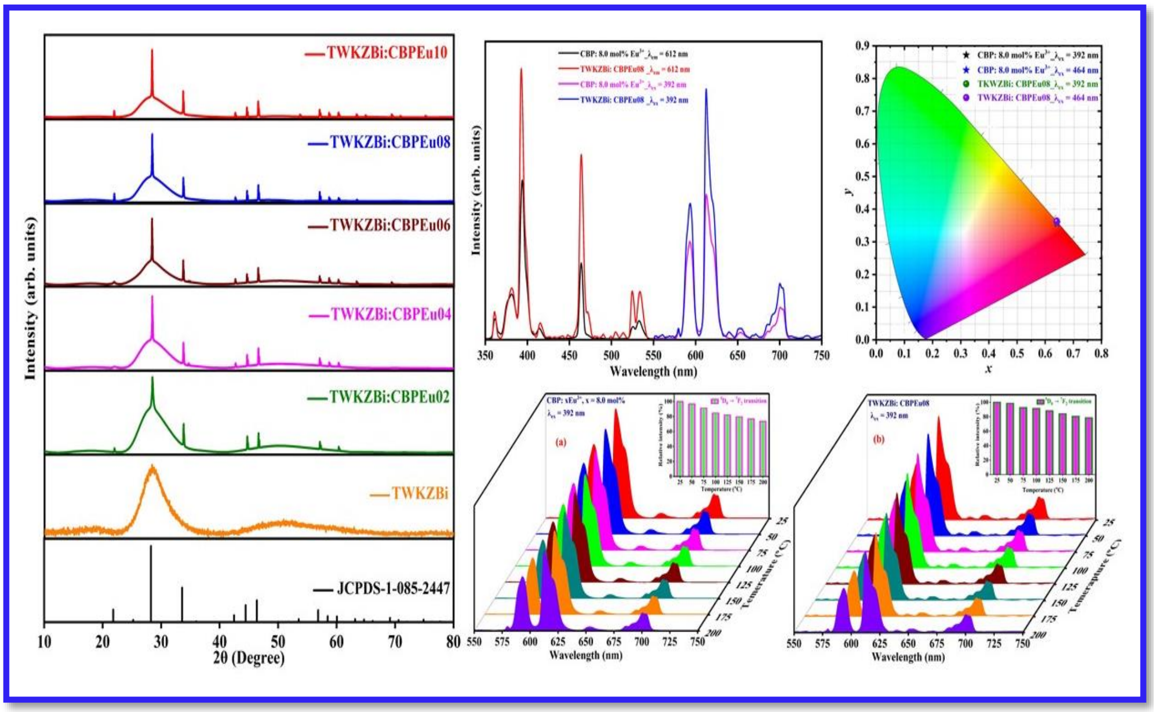

Part of this work has been Communicated in

Optical Materials (I.F.: 3.80)

7.1. Introduction

This chapter aims to attain enhanced luminescent characteristics of red emitting $Ca_3Bi(PO_4)_3$: Eu^{3+} phosphor in the tungstate-tellurite glasses under n-UV/blue excitation wavelengths for photonic applications, especially for white light-emitting diodes (w-LEDs). White LEDs have gained considerable devotion as auspicious solid-state lighting (SSL) technology that can replace conventional incandescent and fluorescent bulbs, owing to their exceptional benefits of energy saving, high luminous efficiency, eco-friendly, compact dimensions, long lifespan, and rapid response time [128, 199, 200]. Nowadays, the most common approach used to fabricate commercial w-LEDs involves the process of encapsulating a yellow phosphor (YAG: Ce^{3+}) on the top of a blue-emitting InGaN LED chip along with an organic epoxy resin. However, the encapsulating structures may turn yellow as a result of continuous usage and the heat generated by the package. This can cause a decline in luminous efficiency, a shift in chromaticity coordinates, and a deterioration of long-term reliability [93, 132]. The deterioration of LED performance hindered their future applications as a potential candidate for high-power SSL technology.

In order to strengthen the disadvantages of the organic epoxy resin, three distinct inorganic materials, notably single crystal, transparent ceramics and phosphor in glass (PiG) have evolved as realistic alternative possibilities [201, 202]. Nevertheless, single-crystal and transparent ceramics keep facing inherent challenges in commercial usage, such as complicated methods of preparation, high manufacturing costs and low reproducibility [201]. PiG has gained much attention because it has several advantages over single crystal and transparent ceramics. These advantages include the luminescence of PiG can be simply controlled via mixing diverse phosphor and glass host compositions as well as the method of preparation is straightforward and may be replicated consistently [203, 204]. Thus, PiG has been deemed as an appropriate luminescence converter for high-power w-LEDs as a result of its robustness, excellent thermal stability, minimal thermal expansion coefficient, and high temperature as well as humidity resistance [205-207]. Consequently, the phosphor in glass is anticipated to be a viable alternative to substitute the organic epoxy resin with glass based components for encapsulating the requisite phosphors [207]. The phosphor particles in PiGs can be strongly segregated via a thermally conductive glass matrix and the optical characteristics of the added phosphor remain intact even in adverse conditions, including intense UV light radiation and high temperature [207]. Furthermore, the luminous characteristics of PiGs might be easily modified by adjusting the fraction of mixed phosphor. Thus, the PiGs can be an appropriate candidate to replace the organic epoxy resin with a glass matrix to encapsulate the essential phosphor. Currently, a YAG: Ce^{3+} based PiG has been developed with the potential for being used in w-LEDs applications [208-211]. Fortunately, due to the absence of the red colour constituents, these w-LEDs cannot meet the criteria of the illumination and display devices. Therefore, high-performance red phosphors having excellent luminescence characteristics are suitable for providing the red constituents. Herein, the appropriate host lattice for phosphor has been considered to be eulytite type orthophosphate with a standard formula $A_3B(PO_4)_3$ [212]. Eulytite-type orthophosphate has a broad bandgap and excellent thermal as well as chemical stability with high REIs solubility [212-214]. Because of the stable crystal structure, low phonon energy, good optical properties and water resistant properties, researchers worldwide have become more interested in analyzing the optical characteristics of the eulytite-type orthophosphate [215, 216]. $Ca_3Bi(PO_4)_3$ activated with Eu^{3+} has emerged as a probable host in illumination, laser, and display technologies [215-217]. Several investigations have been carried out with red phosphors, which exhibit incredible colour purity and exceptional luminescent properties [161]. Using these effective phosphors to fabricate red-emitting PiGs has not been extensively investigated. Thus, it has become essential for researchers/scientists to explore highly efficient and effective procedures for developing red emitting PiG systems.

In this research work, a series of phosphors in glass (PiGs) along with different concentrations of phosphor was synthesized with the help of a low temperature melt quenching process by adopting Eu^{3+} activated $Ca_3Bi(PO_4)_3$ phosphor and tungstate-tellurite (TWKZBi) bare glass. The structural and morphological analysis of the fabricated TWKZBi: CBPEu samples were examined in detail. Furthermore, the spectroscopic characteristics of the synthesized samples have been examined and analyzed to validate their suitability in the field of photonic device applications.

7.2. Experimental and Characterization Techniques

7.2.1. $Ca_3Bi(PO_4)_3$: Eu^{3+} phosphor synthesis

The $Ca_3Bi(PO_4)_3$: xEu^{3+} (CBP: xEu^{3+}) phosphor samples have been synthesized via applying the solid-state reaction (SSR) process discussed in *section 2.2.1*. The doping (x) concentrations were varied in the 1.0, 2.0, 4.0, 6.0, 8.0, and 10.0 mol% and corresponding phosphors were labelled as CBP: 1.0 mol%Eu^{3+}, CBP: 2.0 mol%Eu^{3+}, CBP: 4.0 mol%Eu^{3+}, CBP: 6.0 mol%Eu^{3+}, CBP: 8.0 mol%Eu^{3+} and CBP: 10.0 mol%Eu^{3+}, respectively. Finally, the CBP: xEu^{3+} phosphor has been synthesized and used for further analysis.

7.2.2. Fabrication of phosphor in glass (PiG) samples

The 50 TeO_2 + 20 WO_3 + 15 K_2O + 10 ZnO + 5 Bi_2O_3 (TWKZBi) glass host composition was prepared using the melt quenching approach discussed in *section 2.1*. For the fabrication of PiG samples, the previously prepared TWKZBi glass host was crushed and mixed with different concertation of CBP: xEu^{3+} phosphor powder, as deliberated in *section 2.3*. 10 wt% of each CBP: xEu^{3+} (where, x = 2.0, 4.0, 6.0, 8.0, and 10.0 mol%) phosphors and previously prepared TWKZBi glass sample was physically ground in an agate mortar for an hour. The corresponding labels of PiG samples are TWKZBi: CBPEu02, TWKZBi: CBPEu04, TWKZBi:

CBPEu06, TWKZBi: CBPEu08 and TWKZBi: CBPEu10, respectively. Finally, the TWKZBi: CBPEu PiG samples were prepared and used for further analysis.

7.3. Results and discussion

7.3.1. Structural analysis

The diffraction profiles for the synthesized CBP host lattice, CBP: 8.0 mol% Eu^{3+} phosphor have been compared with standard JCPDS card no. 1-085-2447 as depicted in Fig. 7.01 (a). The synthesized CBP sample has been identified to be composed of a cubic structure with $I\bar{4}3d$ space group.

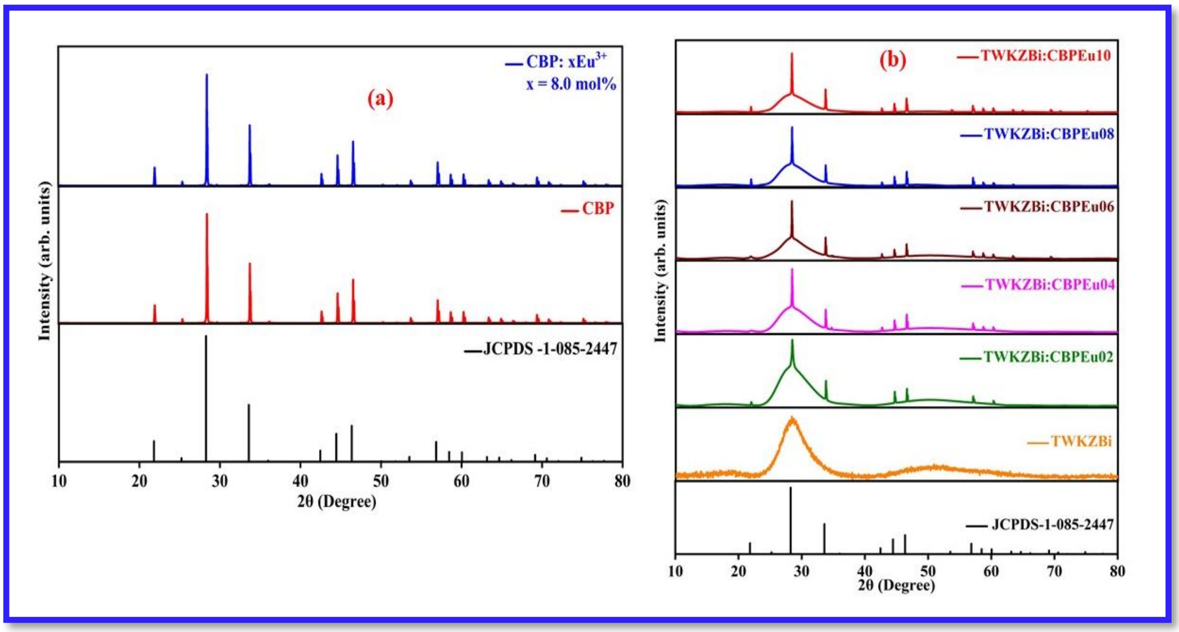

Fig. 7.01 (a) *The diffraction profiles of CBP host lattice, CBP: 8.0 mol%* Eu^{3+} *phosphor and standard JCPDS card no. 1-085-2447 and* ***(b)*** *The diffraction profiles of TWKZBi glass host and TWKZBi: CBPEu PiG samples along with standard JCPDS card no. 1-085-2447.*

Further, the diffraction patterns of the prepared CBP: 8.0 mol% Eu^{3+} phosphor are also in good agreement with standard data, with no additional diffraction peaks found. This demonstrates that the Eu^{3+} ions were successfully included in the CBP host matrix. The Eu^{3+}

ions occupied the Bi^{3+} site in the CBP host lattice due to their valence state being similar and the effective ionic radii of Bi^{3+} ions (r = 1.03 Ǻ) were slightly greater than that of the Eu^{3+} ions (r = 0.94 Ǻ) [218]. Moreover, the diffraction profiles of the synthesized TWKZBi glass and TWKZBi doped with varying concertation of CBP: xEu^{3+} (TWKZBi: CBPEu) PiG samples along with JCPDS data, as represented in Fig. 7.01 (b). It seems that the diffraction patterns of all the TWKZBi: CBPEu PiG systems exhibit a distinct broad peak in the 2θ range from 22 to 38 °, which is the characteristic of amorphous or glassy behaviour. The results indicate that all samples have retained their amorphous nature. While referring to the JCPDS data file no. 1-085-2447, it has been noted that all samples exhibit distinct diffraction peaks associated with the CBP crystal structure [218]. Interestingly, the intensity of the diffraction peaks slightly increases with an upsurge in the content of the Eu^{3+} ions, signifying that the increment of Eu^{3+} affects the crystallization of CBP within the glass matrix.

Further, to examine the phase and crystal structure of the synthesized CBP: 8.0 mol% Eu^{3+} phosphor, the Rietveld refinement was carried out using the Fullproof suite with the Pseudo-Voigt shape function and presented in Fig. 7.02 (a). The red solid line and the blue line with a dot represent the patterns of the calculated and observed data, respectively. The short purple vertical lines denote the Bragg angle (2θ) for the CBP: 8.0 mol% Eu^{3+} phosphor. The green line reveals the discrepancy between observed and calculated patterns. At last, the parameters of the crystal structure were refined and the parameters of the refined lattice have been determined to be $\alpha = \beta = \gamma = 90^{o}$ and a = b = c = 9.873 Ǻ, respectively. The refined lattice parameters were well-matched with the standard data [218]. Thus, the refinement profiles validate the pure single-phase formation of the cubic structure of CBP samples with no additional phase and the obtained goodness of fit (χ^2) is 1.96.

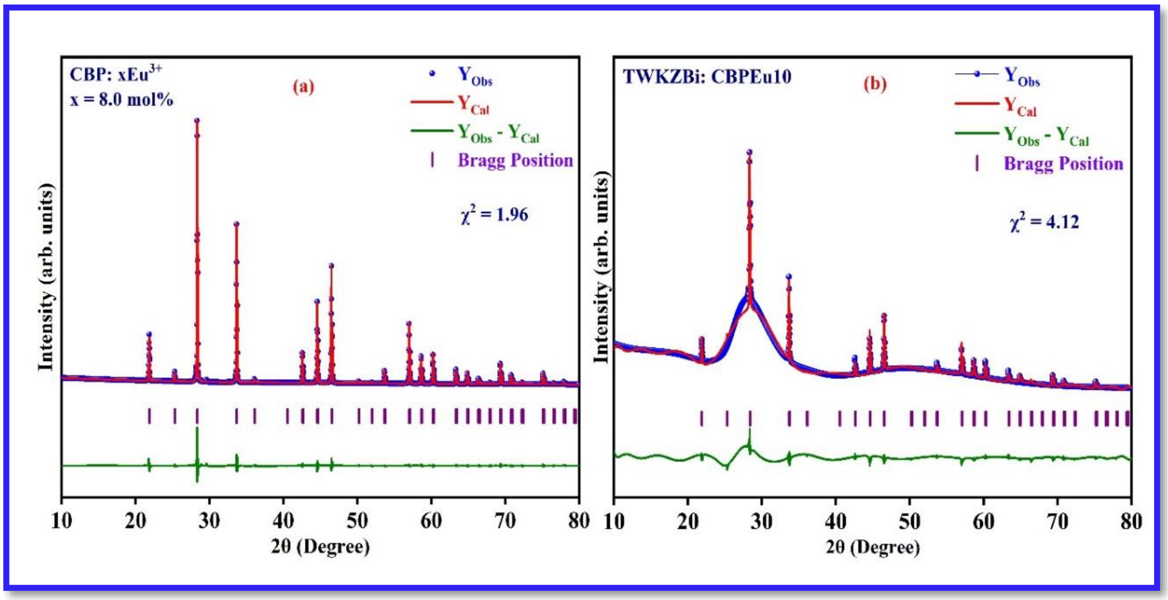

Fig. 7.02. *Rietveld refinement plot for the synthesized **(a)** CBP: 8.0 mol% Eu^{3+} phosphor and **(b)** TWKZBi: CBPEu08 PiG samples.*

Furthermore, the Rietveld refinement of the synthesized TWKZBi: CBPEu08 PiG sample has been performed with the same procedure described above and presented in Fig. 7.02 (b). The synthesized TWKZBi: CBPEu08 PiG sample was refined and it has been observed that the crystal peaks were verified to be of CBP host lattice. The observed parameters of the refined lattice were found to be as α = β = γ = 90 ° and a = b = c = 9.797 Å, respectively. The observed lattice parameters of CBP in the TWKZBi: CBPEu08 PiG sample are almost same as that of the CBP: 8.0 mol% Eu^{3+} phosphor. This suggests that the cubic crystal structure of the CBP host lattice was unaffected throughout the glass melting procedure and the obtained goodness of fit (χ^2) is 4.12.

7.3.2. Morphological studies

Fig. 7.03 (a) illustrates the FE-SEM photograph of the synthesized CBP: 8.0 mol% Eu^{3+} phosphor. The FE-SEM micrograph reveals the irregular, non-spherical and agglomerated morphology with 50 µm resolution of the synthesized phosphor sample. The size of particles was detected in the micron order. Fig. 7.03 (b) also depicts the EDS spectrum of the synthesized

CBP: 8.0 mol% Eu^{3+} phosphor. Calcium (Ca), bismuth (Bi), phosphorus (P), oxygen (O) and europium (Eu) are clearly visible in the EDS spectrum of the synthesized CBP: 8.0 mol% Eu^{3+} phosphor. Moreover, the elemental mapping for the synthesized CBP: 8.0 mol% Eu^{3+} phosphor verifies that all observed elements were recognized and homogenously distributed, as illustrated in Fig. 7.03 (c). The phosphor particles having micron size have been considered as more convenient for use in the w-LED applications.

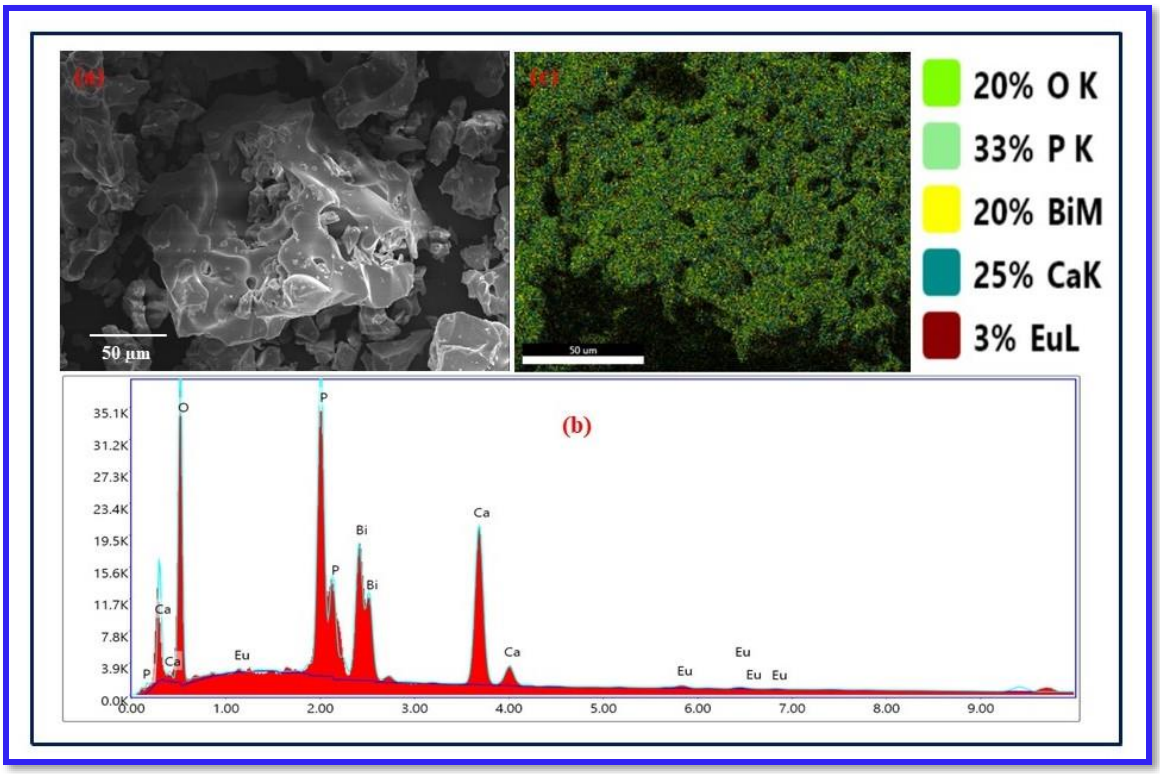

Fig. 7.03. (a) *FE-SEM micrograph of the CBP: 8.0 mol% Eu^{3+} phosphor,* **(b)** *EDS spectrum of the synthesized CBP: 8.0 mol% Eu^{3+} phosphor, and* **(c)** *Elemental mapping of the CBP: 8.0 mol%Eu^{3+} phosphor.*

Furthermore, the FE-SEM micrograph of the synthesized TWKZBi: CBPEu08 PiG sample is presented in Fig. 7.04 (a). It has been observed that the CBP: 8.0 mol% Eu^{3+} phosphor was well dispersed in the glassy network. The micrograph exhibits the irregular and agglomerated morphology with 2.0 µm resolution of the synthesized TWKZBi: CBPEu08 PiG sample. These characteristics show that the CBP: 8.0 mol% Eu^{3+} phosphor/glass PiG sample is homogenous and appropriate for photonic applications.

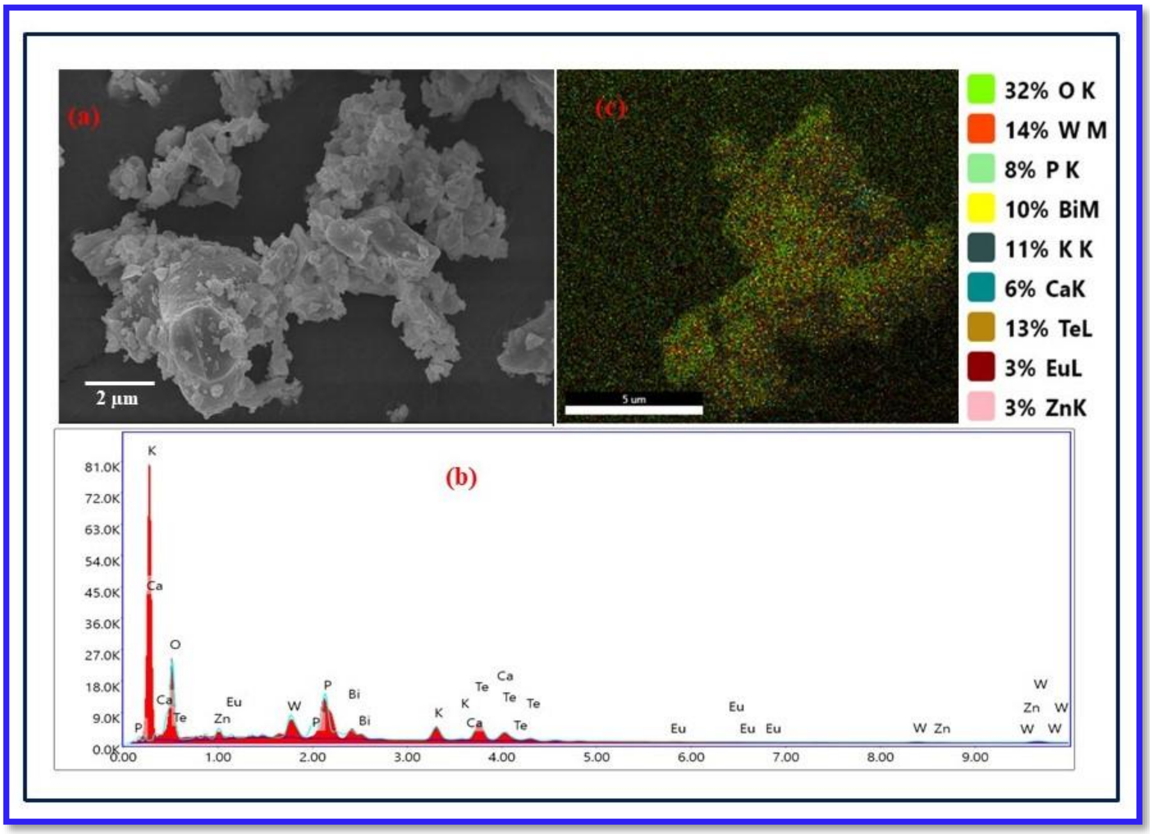

Fig. 7.04. (a) *FE-SEM micrograph of the TWKZBi: CBPEu08 PiG sample,* **(b)** *EDS spectrum of the fabricated TWKZBi: CBPEu08 PiG sample and* **(c)** *Elemental mapping of the TWKZBi: CBPEu08 PiG sample.*

Fig. 7.04 (b) illustrates the EDS spectrum of the synthesized TWKZBi: CBPEu08 PiG sample, which authenticates the existence of the fundamental elements. The EDS spectrum verified the presence of tellurium (Te), tungsten (W), potassium (Bi), zinc (Zn), bismuth (Bi), calcium (Ca), phosphorus (P), oxygen (O) and europium (Eu) in the synthesized sample. Further, the elemental mapping of the synthesized TWKZBi: CBPEu08 PiG sample confirms that all the elements were identified and distributed homogenously, as demonstrated in Fig. 7.04 (c).

7.3.3. Photoluminescence studies

Fig. 7.05 exemplifies the photoluminescent excitation (PLE) profile of the synthesized CBP: 8.0 mol% Eu^{3+} phosphor. The PLE spectrum has been captured in the 300 to 550 nm spectral range with a fixed intense red $(\lambda_{em} = 612\ nm)$ as the emission wavelength. In the PLE profile, there are distinct obvious peaks at the wavelengths of 317, 360, 381, 392, 415, 464, 524 and 533 nm that connected to the specific *4f-4f* electronic transitions, such as $^7F_0 \rightarrow {}^5H_6$, $^7F_0 \rightarrow {}^5D_4$, $^7F_0 \rightarrow {}^5L_7$, $^7F_0 \rightarrow {}^5L_6$, $^7F_0 \rightarrow {}^5D_3$, $^7F_0 \rightarrow {}^5D_2$, $^7F_0 \rightarrow {}^5D_1$ and $^7F_1 \rightarrow {}^5D_1$, respectively [93, 176, 219]. Amongst all the observed PLE peaks, the most prominent peaks were observed in the n-UV region (i.e., 392 nm) related to the $^7F_0 \rightarrow {}^5L_6$ transition and second intense peaks were found in the blue region (i.e., 464 nm) connected to the $^7F_0 \rightarrow {}^5D_2$ transition. Henceforth, these two intense peaks were opted to capture the emission profiles of the synthesized CBP: xEu^{3+} phosphor.

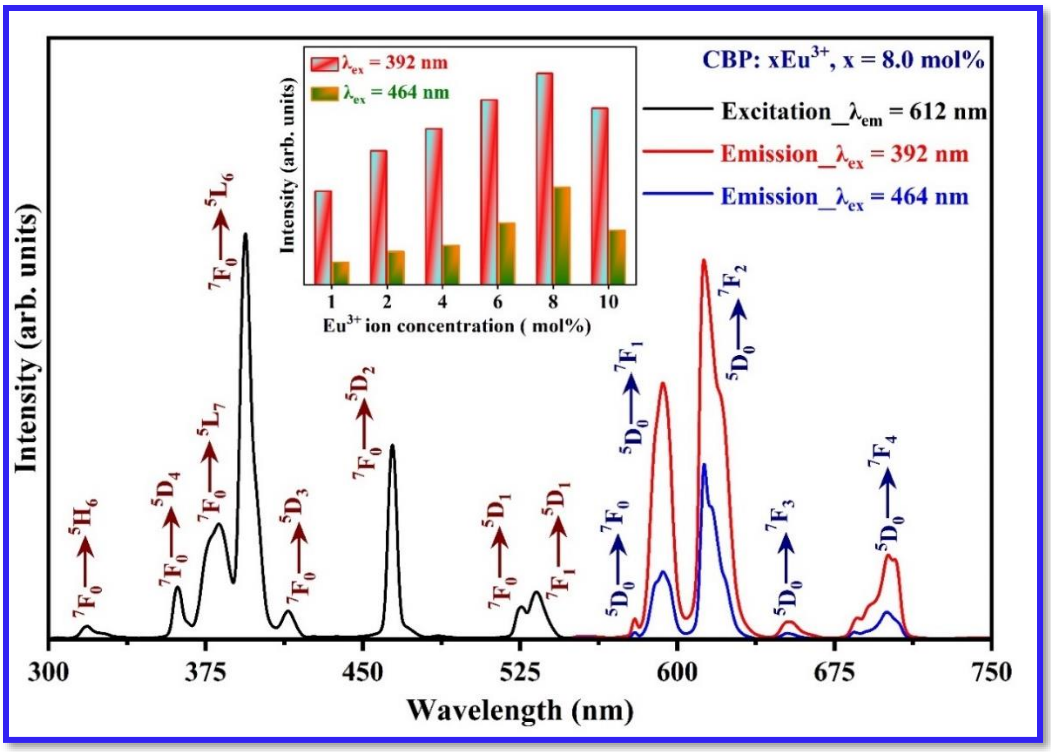

Fig. 7.05. *PLE spectrum and PL spectra of the optimized CBP: 8.0 mol% Eu^{3+} phosphor. [Inst represents the emission intensity of $^5D_0 \rightarrow {}^7F_2$ transition along with the varying concentration of Eu^{3+} in the CBP: xEu^{3+} phosphor under n-UV and blue excitations.]*

Further, the emission profile of the synthesized CBP: 8.0 mol% Eu^{3+} phosphor has been measured in the 550 to 750 nm spectral range under different (n-UV and blue) excitations, as presented in Fig. 7.05. It has been noticed that a small variation in the intensity of emission peaks of the synthesized phosphor when excited to different wavelengths, but there were no changes seen in the peak position. The emission profiles reveal five different characteristic peaks which have been detected around 579, 593, 612, 652 and 702 nm. These peaks are attributed to the $^5D_0 \rightarrow {}^7F_J$ (where J = 0 to 4) *4f-4f* electronic transitions, respectively [93, 176]. Among all the emission peaks, the intense emission peak has been obtained at 612 nm related to the $^5D_0 \rightarrow {}^7F_2$ transition. Further, a correlation between the emission intensity under different excitations with varying concentrations of the Eu^{3+} ions, as demonstrated in inset Fig. 7.05. It was observed that the content of Eu^{3+} ions upsurges to 8.0 mol%, and the intensity of emission peaks rises when stimulated via both n-UV/blue radiation. Furthermore, when the content of Eu^{3+} ion upsurges, the emission profiles diminish owing to the concentration quenching mechanism. This mechanism happens as a result of the non-radiative energy transfer amid the adjacent dopant (Eu^{3+}) ions. The optimal concertation of Eu^{3+} ions in the synthesized phosphor has been obtained to be 8.0 mol%.

Further, in order to examine the luminescent characteristics of the fabricated TWKZBi bare glass doped with a weight of 10% of each CBP: xEu^{3+} (where, x = 2.0 to 10.0 mol% with a fixed interval of 2.0 mol%) phosphors (i.e., TWKZBi: CBPEu PiG samples), the PLE and emission profiles of the fabricated TWKZBi: CBPEu PiG samples have been performed. Fig. 7.06 (a) displays the PLE spectrum of the fabricated TWKZBi: CBPEu10 PiG sample has been measured in the 350 to 550 nm spectral range under a fixed intense red emission wavelength of 612 nm. The PLE spectrum of the fabricated PiG sample has demonstrated several excitation peaks located around 360, 381, 392, 415, 464, 524 and 533 nm, respectively [176, 219]. All the observed excitation peaks were similar to the excitation peak positioned in the excitation spectrum of synthesized phosphor samples (see Fig. 7.05). From Fig. 7.06 (a), it has been noticed that the two intense excitation peaks have been observed in the n-UV and the blue region corresponding to the $^7F_0 \rightarrow {}^5L_6$ and $^7F_0 \rightarrow {}^5D_2$ transitions, respectively. Thus, these peaks were further utilized to analyze the emission spectral profiles of the series of fabricated TWKZBi: CBPEu PiG samples.

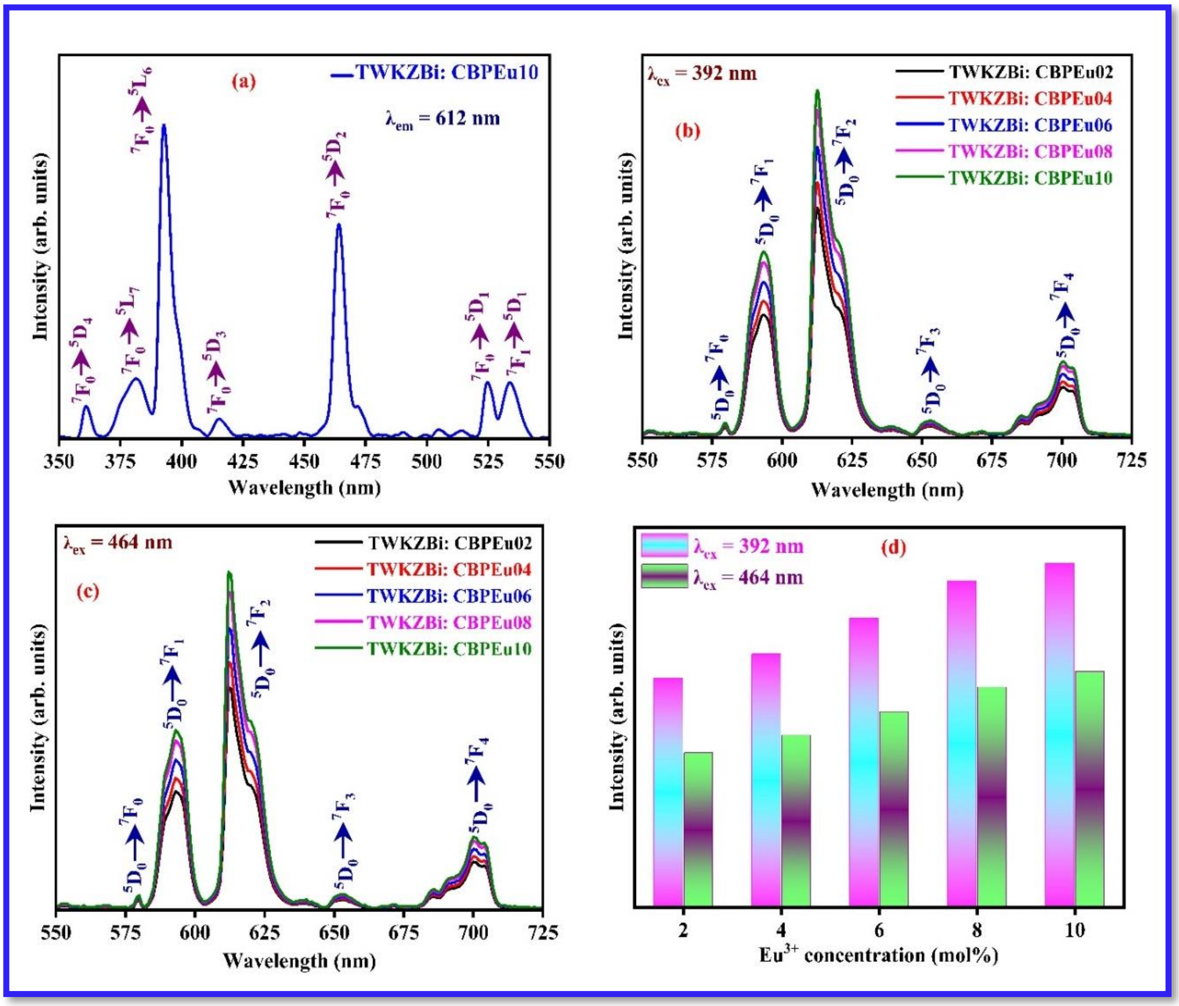

Fig. 7.06. (a) *PLE spectrum of the fabricated TWKZBi: CBPEu10 PiG sample under 612 nm excitation wavelength,* **(b)** *The emission spectral profiles of the fabricated TWKZBi: CBPEu PiG sample under n-UV (392 nm),* **(c)** *Blue (464 nm) excitation and* **(d)** *The emission intensity variation along with the varying concentration of* Eu^{3+} *ions in CBP:* xEu^{3+} *phosphor under n-UV and blue excitation of the fabricated TWKZBi: CBPEu PiG samples.*

Moreover, the emission spectral profiles of the fabricated series of TWKZBi: CBPEu PiG samples have been captured in the 550 to 725 nm spectral range with keeping different (392 and 464 nm) excitations and are demonstrated in Fig. 7.06 (b and c). The results revealed a slight distinction in the emission intensity, whereas the peak location remained the same for the fabricated TWKZBi: CBPEu PiG samples. Five distinct emission peaks have been seen at the wavelengths of about 579, 593, 612, 652 and 702 nm. These peaks are linked to the $^5D_0 \rightarrow {}^7F_0$, $^5D_0 \rightarrow {}^7F_1$, $^5D_0 \rightarrow {}^7F_2$, $^5D_0 \rightarrow {}^7F_3$ and $^5D_0 \rightarrow {}^7F_4$ *4f-4f* electronic transitions, respectively [93, 219]. The highest intensity of emission peak has been observed at 612 nm (red region) related to the $^5D_0 \rightarrow {}^7F_2$ transition, which is a forced electric dipole (ED) transition and complies with the following selection conditions, such as $\Delta J = 2$. Conversely, the emission peak centered at 593 nm (orange area) is caused by the $^5D_0 \rightarrow {}^7F_1$ transition, which is recognized as a magnetic dipole (MD) transition. The selection rule ($\Delta J = 1$) is followed by the MD transition [147]. The forced ED transition seems to be a hypersensitive transition and the emission intensity of the $^5D_0 \rightarrow {}^7F_2$ transition can be profoundly impacted through the crystal field of the ligand atoms [194]. In contrast, the MD ($^5D_0 \rightarrow {}^7F_1$) transition does not influence the local symmetry associated with the Eu^{3+} ions and the surrounding atmosphere [194]. Furthermore, the emission peak centered at 702 nm ($^5D_0 \rightarrow {}^7F_4$ transition) has also been classified as an electric dipole transition in nature.

Fig 7.06 (d) illustrates the emission intensity of TWKZBi: CBPEu PiG samples under n-UV and blue excitations along with increasing concentrations of the Eu^{3+} ions in the CBP: xEu^{3+} phosphor. It seems that the emission intensity of the fabricated TWKZBi: CBPEu PiG samples gradually increases with a surge in the Eu^{3+} ion contents in the CBP: xEu^{3+} phosphor from 2.0 to 10.0 mol%, which indicates that the concentration quenching does not occur. Moreover, it has been observed that the emission intensity of the fabricated PiG samples is higher when excited with n-UV light than that of the blue excitation. Therefore, the fabricated

TWKZBi: CBPEu PiG samples can effectively be excited with n-UV light for photonic applications, especially for w-LED applications. A comparison of the PLE and emission spectral profiles of the CBP: 8.0 mol% Eu^{3+} phosphor and TWKZBi: CBPEu08 PiG samples are demonstrated in Fig. 7.07 (a). Under the same condition and the same concertation of Eu^{3+} ions, both the PLE and emission intensity of the TWKZBi: CBPEu08 PiG sample were significantly greater than the CBP: 8.0 mol% Eu^{3+} phosphor. It seems that the emission intensity of the peak positioned at 612 nm ($^5D_0 \rightarrow {}^7F_2$) of the TWKZBi: CBPEu08 PiG sample is much greater than the CBP:8.0 mol% Eu^{3+} phosphor. This is due to the fact that the stable network structure and homogenous nature of Eu^{3+} ions promote electron transitions, resulting in reduced non-radiative loss. These characteristics greatly enhanced the luminescent characteristics of the Eu^{3+} ions and also increased the concertation quenching level [220].

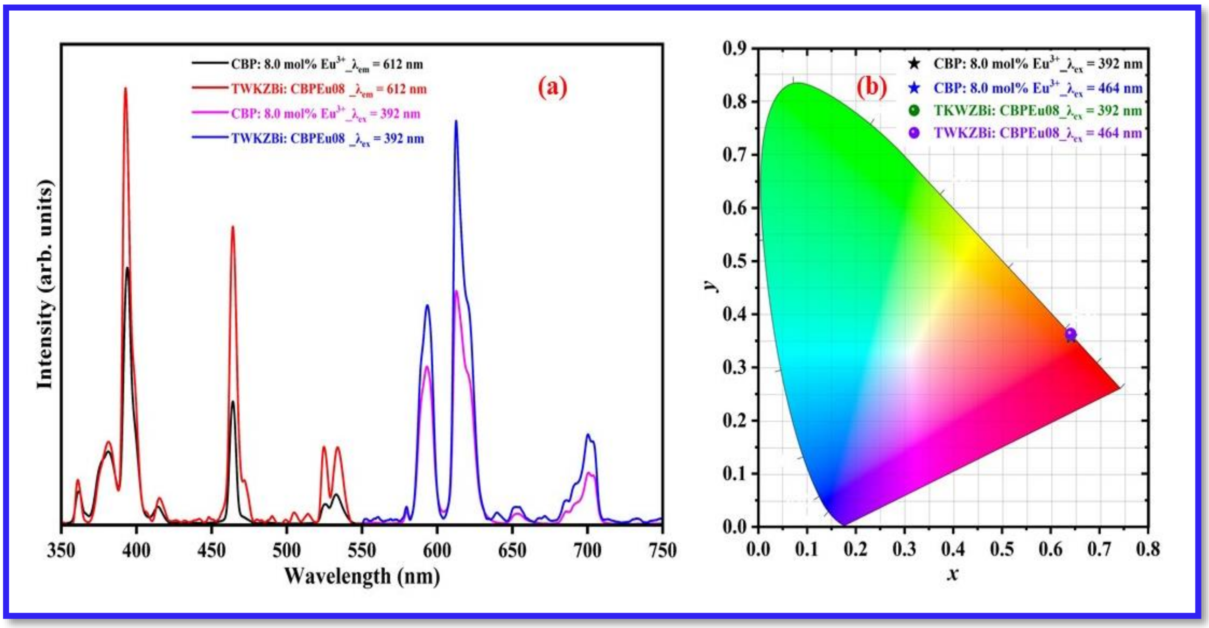

Fig. 7.07 (a) *A comparison of PLE and PL spectra of the CBP: 8.0 mol% Eu^{3+} phosphor and TWKZBi: CBPEu08 PiG sample and* **(b)** *Chromaticity coordinates for the synthesized CBP: 8.0 mol%Eu^{3+} phosphor and TWKZBi: CBPEu08 PiG sample under n-UV and blue excitations.*

7.3.4. Colorimetric analysis

On the basis of the emission data of the synthesized CBP: xEu^{3+} phosphor and TWKZBi: $CBPEu_x$ PiG samples, the chromaticity coordinates (x, y) could be governed via analyzing the colour function $\bar{x}(\lambda)$, $\bar{y}(\lambda)$ and $\bar{z}(\lambda)$ defined by the Commission International de I'Eclairage (CIE) 1931 diagram [93]. The identification of the colour of the light source can be achieved via utilizing colour (x, y) coordinates on the CIE 1931 graph. The computed colour (x, y) coordinates for the synthesized CBP: 8.0 mol% Eu^{3+} phosphor and TWKZBi: CBPEu08 PiG sample under 392 and 464 nm excitations, as displayed in Fig. 7.07 (b). The (x, y) coordinates were obtained to be (0.642, 0.359) and (0.642, 0.358) for the synthesized CBP: 8.0 mol% Eu^{3+} phosphor under the above-mentioned two excitations. Whereas, the color coordinates (0.641, 0.363) and (0.641, 0.361) for the TWKZBi: CBPEu08 PiG sample were observed under the same excitation wavelengths. The colour coordinates (x, y) for the synthesized CBP: 8.0 mol%Eu^{3+} phosphor and TWKZBi: CBPEu08 PiG samples were approximately comparable to the color coordinates of commercial Y_2O_2S: Eu^{3+} phosphor (0.647, 0.343) [93, 221]. Moreover, colour-correlated temperature (CCT) for the synthesized CBP: 8.0 mol% Eu^{3+} phosphor and TWKZBi: CBPEu08 PiG samples have been assessed with the help of McCamy expression, as reported in the literature [65, 222]. The observed CCT values for the synthesized CBP: 8.0 mol% Eu^{3+} phosphor are 2288 and 2320 K when stimulated via 392 and 464 nm excitations whereas, the CCT values for the fabricated TWKZBi: CBPEu08 PiG samples have been found to be 2412 and 2570 K under aforementioned excitations. Moreover, the colour purity (CP) of the red emission synthesized CBP: 8.0 mol% Eu^{3+} phosphor and TWKZBi: CBPEu08 PiG samples have been computed as described in *equation (4.4)*. The computed CP value for the synthesized CBP: 8.0 mol% Eu^{3+} phosphor is 99.09% and 99.01% under 392 and 464 nm excitation wavelengths. The CP value for the fabricated TWKZBi: CBPEu08 PiG sample has been obtained to be 99.32% and 99.26% under n-UV and blue excitations. Thus, the high CP of PiG samples makes them an appropriate candidate for red color emitting components in white-LED applications under an n-UV excitation source.

7.3.5. PL decay measurement studies

Fig, 7.08 signifies the decay curve profile of the fabricated TWKZBi: CBPEu08 PiG sample, which has been computed at ambient temperature for $^5D_0$ energy level under n-UV excitation (λ_{ex} = 392 nm) for intense red emission at a wavelength of 612 nm. The decay curve for the fabricated TWKZBi: CBPEu08 PiG sample shows the exponential character and was best fitted for the bi-exponential function as given in *equation (2.9).*

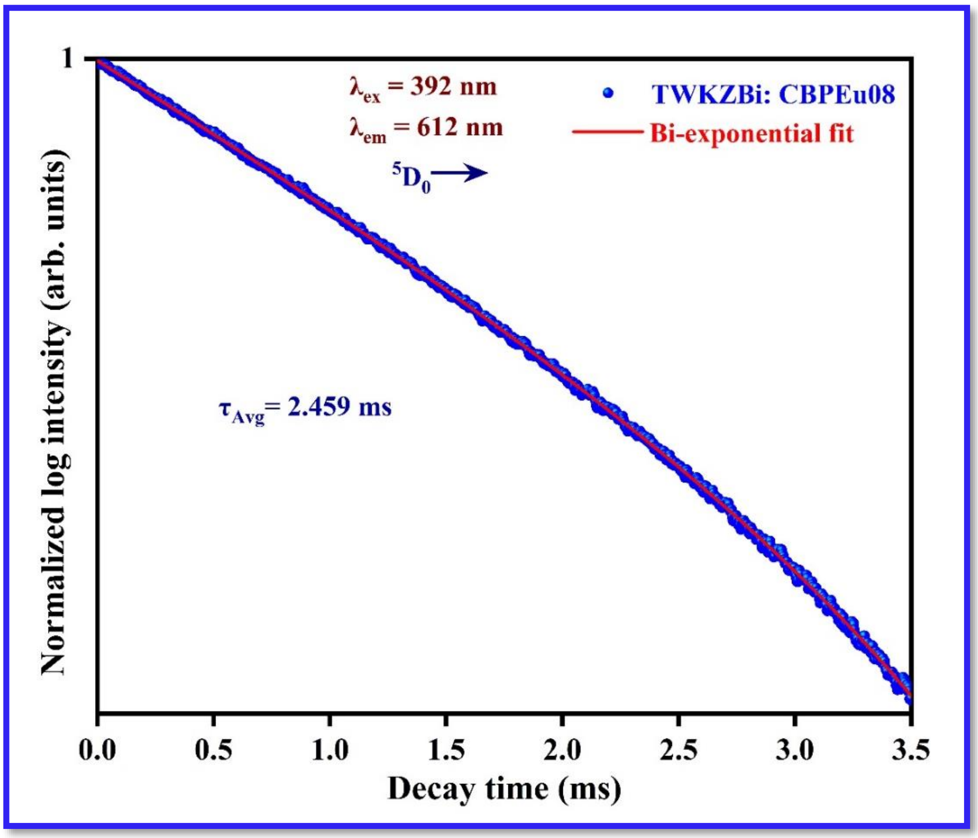

Fig. 7.08. *Decay profiles of the fabricated TWKZBi: CBPEu08 PiG sample under n-UV excitation.*

Further, the average lifetime (τ_{Avg}) values for the fabricated TWKZBi: CBPEu08 PiG sample has been assessed with the help of the following expression as given in *equation (2.10)*.

The assessed τ_{Avg} value for the $^5D_0$ energy level of the fabricated TWKZBi: CBPEu08 PiG sample is 2.459 ms under n-UV excitation.

7.3.6. *Thermal stability*

The most efficient technique for characterizing substances to examine thermal stability from the perspective of practicality usage for photonic devices is temperature dependent PL (TDPL). This analysis helps us to gain insight into the thermal quenching behaviour of the prepared luminescent substances. To examine the thermal quenching behaviour of prepared CBP: 8.0 mol% Eu^{3+} phosphor and TWKZBi: CBPEu08 PiG sample, the emission intensity variation with varying temperature profiles from room temperature (25 ºC) to 200 ºC via keeping 392 nm excitation are demonstrated in Fig. 7.09 (a and b).

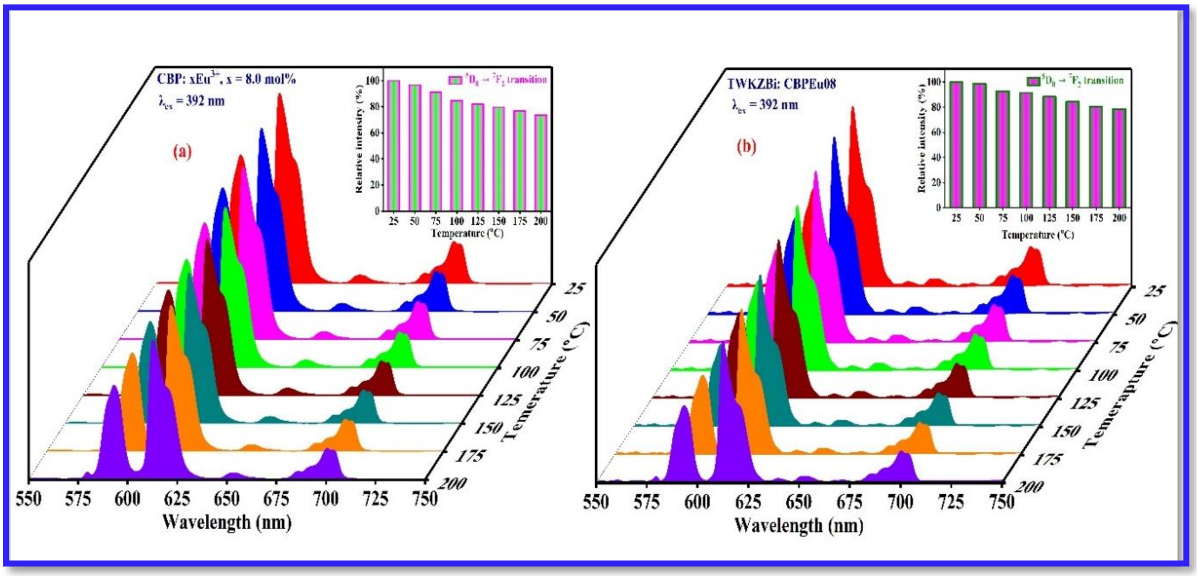

Fig. 7.09 (a) *Temperature dependent emission spectral profiles for the synthesized CBP: 8.0 mol% Eu^{3+} phosphor and* **(b)** *fabricated TWKZBi: CBPEu08 PiG sample along with the varying temperatures from room temperature to 200 ºC under n-UV excitation. [Inset represents the relative intensity of the 612 nm emission peak along with varying temperatures.]*

The emission intensity of both phosphor and PiG samples seems to decline as the temperature profiles upsurge from 25 ºC to 200 ºC. Furthermore, the percentage variation of emission intensity relative to initial temperature is depicted in inset Fig. 7.09 (a and b). The emission intensity of the synthesized CBP: 8.0 mol% Eu^{3+} phosphor and fabricated TWKZBi: CBPEu08 PiG sample were preserved up to 79.62 and 84.26% at 150 ºC, correlated to the initial temperature. Hence, the PiG sample reveals better performance than the phosphor sample, suggesting PiG sample has excellent thermal stability.

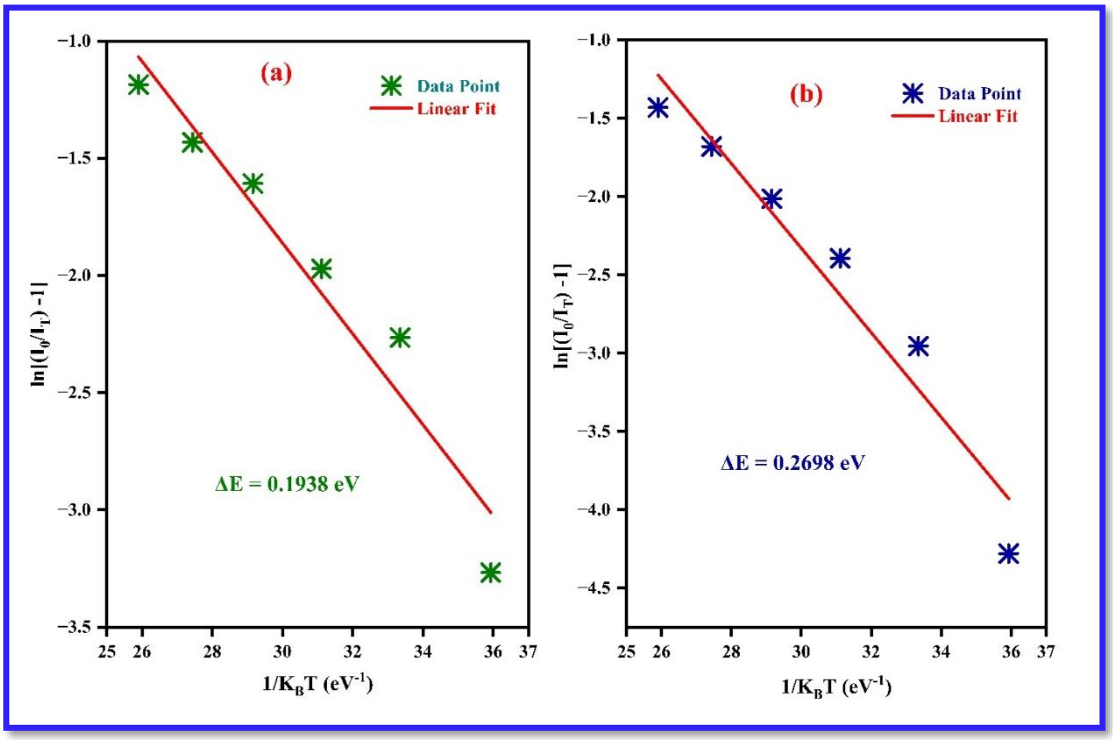

Fig. 7.10. *Linear fitted graph between* $ln[(I_0/I_T) – 1]$ *against* $1/K_BT$ *for* **(a)** *CBP: 8.0 mol%*Eu^{3+} *phosphor and* **(b)** *TWKZBi: CBPEu08 PiG sample.*

Moreover, activation energy is a crucial aspect of the thermal stability behaviour of synthesized luminescent materials. It has been computed using the Arrhenius formula as reported in the literature [161, 194, 199, 223]. The slope is to be determined via applying the Arrhenius formula by plotting $\ln[(I_0/I_T) – 1]$ against $1/K_BT$, which yields the value of activation energy, as illustrated in Fig. 7.10 (a and b). The computed value of activation energy is 0.1938 and

0.2698 eV for the prepared CBP: 8.0 mol% Eu^{3+} phosphor and TWKZBi: CBPEu08 PiG samples. The greater activation energy value suggests that the PiG sample is more stable than the phosphor at higher temperatures, which elucidates that the PiG sample has excellent thermal stability and is suitable for photonic applications.

7.4. Conclusions

In summary, the red emitting phosphor in glass (PiG) of varying concentrations of CBP: Eu^{3+} phosphor was successfully fabricated via employing a low temperature melt quenching method. Numerous analyses, such as XRD, FE-SEM, photoluminescence (excitation and emission), and temperature dependent PL studies have been utilized to explore the structural, morphological, and spectroscopic characteristics of the phosphor and PiG samples. The structural and morphological examination authorizes the successful inclusion of the synthesized CBP: xEu^{3+} phosphor within the tungstate-tellurite glasses. PLE spectral profiles of the phosphor and PiG sample revealed that several sharp peaks initiating from *4f-4f* electronic transitions of Eu^{3+} ions, with a strong peak at n-UV (392 nm) and blue (464 nm). Under 392 and 464 nm excitations, the emission spectra of the phosphor and PiG samples exhibit a hypersensitive transition at 612 nm ($^5D_0 \rightarrow {}^7F_2$), which was stronger than that of other observed transitions. Under the same condition and the same concertation of Eu^{3+} ions, both the PLE and emission intensity of the TWKZBi: CBPEu08 PiG sample were significantly greater than the CBP: 8.0 mol% Eu^{3+} phosphor. Further, the decay curve for the fabricated TWKZBi: CBPEu08 PiG sample displays the bi-exponential character under 392 nm excitation. The thermal quenching behaviour has been improved from 84.72% to 91.52% at 100 ºC and activation energy increased from 0.1938 and 0.2698 eV in the temperature range from 25 to 200 ºC owing to the homogenous nature and better glass network stability. Furthermore, the color coordinates of the fabricated TWKZBi: $CBPEu_x$ PiG samples under 392 and 464 nm excitations are located in the red emission range and exhibit excellent color purity.

The combination of the aforementioned findings endorses that the red-emitting TWKZBi: CBPEu$_x$ PiG samples have the potential candidates to utilize in various photonic applications.

Chapter – 08

Summary and Future Scope of the Research Work

This chapter presents the detailed outcomes of the present work and the scope of the future research work. The overall objective of this thesis was to develop thermally stable rare earth activated tungstate-tellurite glasses with enhanced multi-color emitting n-UV/blue pumped luminescent materials and also to fabricate Phosphor-in-Glass (PiG) for advanced photonic device applications. The as-prepared rare earth activated tungstate-tellurite glasses reveal PL characteristics in spectral range pre-requisite for white LED applications. The present chapter also discusses the important results of the present research work and the scope of future work.

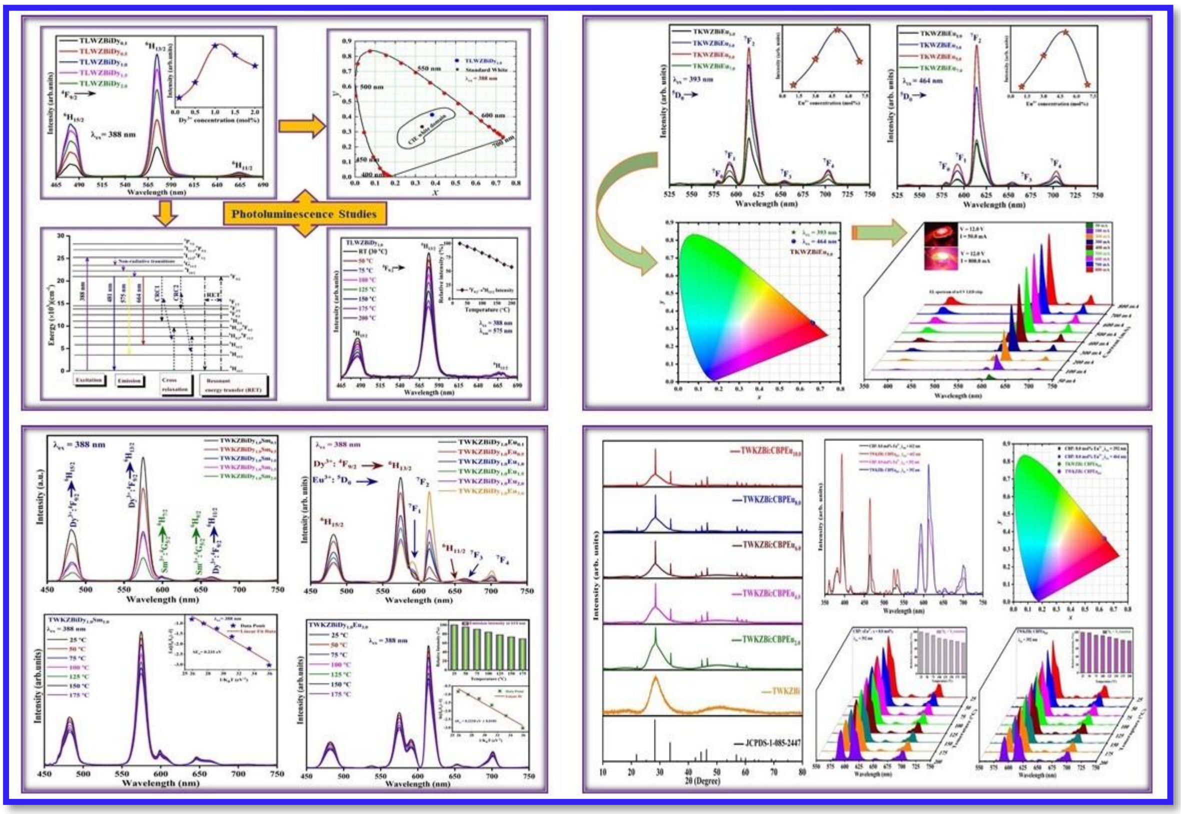

8.1. Summary of the Work

The main emphasis of the present thesis is to analyze the characteristics of rare earth activated tungstate-tellurite glasses for the deployment of photonic devices such as white LEDs. The focus is on their structural, morphological, optical, and luminescent characteristics. The findings were examined along with multiple rare earth ions and the combination of rare-earth ions (Dy^{3+}, Eu^{3+} and Tb^{3+}) activated in the tungstate-tellurite glasses prepared with the help of a conventional melt quenching approach. Also, a transparent series of phosphor in glass (PiG) along with different concentrations of appropriate phosphor has been synthesized with the help of low temperature melt quenching process adopting a Eu^{3+} activated $Ca_3Bi(PO_4)_3$ phosphor and tungstate-tellurite glass. The enhancement of luminescence was significantly improved by adjusting doping ion concentration and introducing co-dopants as activator ions. It has been discussed in the previous sections that white LEDs have recently received enormous interest because of their several distinct characteristics, including less energy consumption, eco-friendliness, longer lifespan and high efficiency in comparison to traditional fluorescent and incandescent lamps. Furthermore, rare earth activated inorganic glasses and PiG samples have been found in an extensive range of applications in our daily lives such as advanced optical displays, solid-state lighting, optical waveguides, lasers, white LEDs, and solar cells. Therefore, the present proposal aims to produce the most efficient inorganic glasses and PiG systems with enhanced luminescent properties by scaling up the processes for comfortable industrial acclimatization. The outcome of the research work for achieving the research objectives has been systematized into eight chapters. These chapters include the preparation of glass host and multicolor emission (blue, green, red, white light) emitting thermally stable tungstate-tellurite glasses activated (Dy^{3+}, Eu^{3+}, Dy^{3+} & Sm^{3+}, Dy^{3+}/Eu^{3+} and Tb^{3+}& Eu^{3+}) with the help of melt quenching approach. The current research demonstrates that the prepared glasses and PiG samples can meet the necessities for enhanced luminescent characteristics and thermal stability.

The prepared Dy^{3+} doped lithium tungstate tellurite (TLWZBiDy) glasses have been successfully prepared using the melt quenching approach. Under n-UV excitation (388 nm) excitation, TLWZBiDy glasses exhibit emission peaks attributed to the transition starting from ($^4F_{9/2}$) level to distinct lower energy states, such as $^6H_{15/2}$ (blue emission band), $^6H_{13/2}$ (yellow emission band) and $^6H_{11/2}$ (red emission band), respectively. The concentration quenching has been observed at 1.0 mol% of Dy^{3+} content owing to the energy transfer through CR channels. The chromaticity coordinates for the optimized glass under n-UV excitation were located in the white light domain of the CIE graph. The aforementioned findings indicate that the prepared glasses have great potential for usage in solid state lighting and other device applications.

A transparent glass series of alkali (Li, Na and K) tungstate-tellurite glass with a fixed doping concentration of (Eu^{3+}) ions has been synthesized via a melt quenching approach. The luminescent characteristics of the prepared alkali tungstate-tellurite glasses were examined to explore the optimization of the alkali ions in the prepared glasses. It has been observed from the luminescent characteristics that the potassium tungstate-tellurite glasses show relatively higher emission than the other two alkalis (Li and Na) based tungstate-tellurite glasses. This study suggests that potassium tungstate-tellurite glasses have superior quality for future research. Based on the above analysis, potassium tungstate-tellurite (TKWZBi) glasses with varying concentrations of Eu^{3+} ions have been prepared to determine the optimal concentration of the dopant ions. The TGA-DSC analysis performed on the TKWZBi glass host matrix affirms the thermal stability and aggregated weight loss at higher temperatures. PLE spectral profile showed several excitation peaks originating from the *4f-4f* electronic transition of Eu^{3+} ions in the range from 325 to 550 nm with intense peaks at 393 (n-UV) and 464 nm (blue). Among all five emission peaks in the PL spectra, an intense peak has been detected at 614 nm wavelength ascribed to $^5D_0 \rightarrow {}^7F_2$ transition for all prepared TKWZBiEu glasses under n-UV and blue excitations. The optimal concentration of the Eu^{3+} ions in the TKWZBiEu glasses was observed to be 5.0 mol%. The chromaticity coordinates of all prepared glasses under n-UV and blue excitations were located in the red region of the CIE diagram. Temperature dependent PL analysis has been conducted for an optimized glass and demonstrates its thermal stability along with high activation energy. An organic resin free prototype device has been fabricated using the combination of optimized glass and an n-UV LED chip. All the aforementioned results validate that the thermally stable prepared glass could be a better encapsulant as well as a luminescent converter for fabricating binder-free light emitting diodes.

The luminescent characteristics of the single Sm^{3+}, (Dy^{3+}/Sm^{3+}) and (Dy^{3+}/Eu^{3+}) co-doped potassium tungstate-tellurite glass samples prepared via melt quenching technique were examined for the first time. Sm^{3+} doped potassium tungstate tellurite glasses reveal a strong intense emission peak associated with the $^4G_{5/2} \rightarrow {}^6H_{7/2}$ (600 nm) transition at an excitation wavelength of 405 nm. In Dy^{3+}/Sm^{3+} co-doped glasses, the emission intensity progressively surges with an increase in the Sm^{3+} ion content (up to 1.5 mol%) confirming the energy transfer between Dy^{3+} and Sm^{3+} ions. The emission color for the prepared co-activated glasses was tuned from the warm white light to the orange-red region of the CIE diagram via varying the excitation wavelengths and the concentration of the Sm^{3+} ions. Further, Dy^{3+}/Eu^{3+} co-doped glasses demonstrate the emission peaks in blue, yellow, and red regions of the electromagnetic spectrum, and the combination of these emission peaks generates white light and orange-red light through properly controlling the activator (Eu^{3+}) ion concentrations and also selected excitations. By applying Dexter's energy transfer relationship with Reisfeld's approximation based on the emission spectral profiles, the energy transfer processes involving a non-radiative dipole-dipole interaction between the (Dy^{3+} to Sm^{3+}) and (Dy^{3+} to Eu^{3+}) ions were validated. The average lifetime $\left(\tau_{avg}\right)$ values of prepared co-activated glasses were measured and it was found that the average lifetime values of $^4F_{9/2}$ energy state of Dy^{3+} ions diminished with a surge in the content of Sm^{3+} and Eu^{3+} ions. Furthermore, the emission intensity observed at 373 K was 83.83% compared to the emission intensity at the initial temperature, indicating the excellent thermal stability of the prepared glasses Therefore, the prominent results confirm that the prepared (Dy^{3+}/Sm^{3+}) and (Dy^{3+}/Eu^{3+}) co-doped potassium tungstate-tellurite glass samples will be beneficial for white light and other fascinating photonic applications.

The successful incorporation of single Tb^{3+} and doubly Tb^{3+}/Eu^{3+} ions into the transparent tungstate-tellurite glasses was prepared using the melt quenching procedure. Multiple emission peaks have been observed in the Tb^{3+} doped tungstate-tellurite glasses under n-UV and blue excitations and the highest emission intensity has been found for 2.0 mol% of the Tb^{3+} doped glasses. The CIE coordinates of the prepared glass samples under n-UV and blue excitations were located in the pure green region. Further, the emission spectral profiles of the co-doped Tb^{3+} and Eu^{3+} ions in the tungstate-tellurite glasses were studied and the maximum energy transfer efficiency was found to be 32.82% under n-UV excitation. The emission color of the prepared Tb^{3+}/Eu^{3+} co-doped glasses has been easily tunable from green to reddish region in the CIE diagram via varying the Eu^{3+} ion concentrations under n-UV/blue excitations. Temperature-dependent emission profiles indicate that the Tb^{3+}/Eu^{3+} co-doped glasses have good thermal stability. All the aforementioned findings reveal the suitability of the Tb^{3+}/Eu^{3+} co-doped tungstate-tellurite glasses for photonic applications.

The red emitting phosphor in glass (PiG) of varying concentrations of CBP: Eu^{3+} phosphor has been fabricated by employing a melt quenching approach. The structural and morphological examination validates the successful inclusion of the CBP: Eu^{3+} phosphor within the tungstate-tellurite glasses. Also, the Rietveld refinement analysis of the PiG samples has confirmed that the crystal peaks indeed belong to the CBP: xEu^{3+} phosphor. PLE spectral profiles of the synthesized phosphor and PiG samples revealed multiple peaks initiating from

4f-4f electronic transitions of Eu^{3+} ions, with strong excitation peaks at n-UV (392 nm) and blue (464 nm). Further, emission profiles of the phosphor and PiG samples under n-UV and blue excitations reveal a hypersensitive transition at 612 nm ($^5D_0 \rightarrow {}^7F_2$), which was stronger than that of other observed transitions. Under the same condition and the same concertation of Eu^{3+} ions, both the PLE and emission intensity of the TWKZBi: CBPEu08 PiG sample were significantly greater than the CBP: 8.0 mol% Eu^{3+} phosphor. The thermal quenching behavior has been enhanced from 84.72% to 91.52% at 100 ºC and activation energy improved from 0.1938 to 0.2698 eV in the temperature range from room temperature to 200 ºC due to the homogenous behavior and better glass network stability. Furthermore, the color coordinates of the fabricated PiG samples under n-UV and blue excitations are located in the red emission range and exhibit excellent color purity. The combination of the above-mentioned results endorses that the red-emitting PiG samples have the potential to be utilized in photonic applications.

8.2. Important Findings of Research Work

The way to carry out research generally starts with self-motivation and identification of contemporary issues, which is then followed by the development and implementation of a systematic approach to address and resolve the problem. The motivation, literature survey, and origin of the research objectives for the development of efficient glasses and phosphor in glass (PiG) for diversified applications in the realm of photonic devices. It comprises the fundamentals of photoluminescence and comprehensive analyses of the inorganic amorphous (glassy) materials as well as their components. Moreover, this study delves into the significance of inorganic glassy materials in advanced photonic applications and emphasizes the importance of choosing the glass host composition and an appropriate phosphor for the development of phosphor in glass (PiG) samples.

All the necessary steps to complete the research work have been thoroughly examined. This includes selecting the activator/acceptor and sensitizer/donor, as well as optimizing the emission and thermal stability for various advanced photonic applications, especially w-LED applications.

Moving forward to synthesize trivalent RE ions doped tungstate-tellurite glasses and red-emitting PiG with varying Eu^{3+}*concentrations of the CBP:* Eu^{3+} *phosphors, the salient aspects/importance of the present thesis are summarized as follows:*

- Transparent Dy^{3+} doped TLWZBi glass can emit white light by combining blue and yellow peaks when effectively excited by n-UV LED chips. The color coordinates of the prepared glasses were situated in the white light region. The energy transfer mechanism between the Dy^{3+}-Dy^{3+} ions has been determined to be a dipole-dipole in nature using the Inokuti-Hirayama (I-H) model to the decay profiles of the prepared glasses. The above-mentioned findings suggest that the Dy^{3+} doped TLWZBi glass is a potential luminescent material to utilize in solid-state lighting applications, especially for white LEDs.
- Alkali (Li, Na, and K) based tungstate-tellurite glass system was successfully prepared and the best emission characteristics have been observed for potassium tungstate-tellurite glasses. Eu^{3+} doped potassium tungstate-tellurite glasses revealed red emission at 614 nm linked to the $^5D_0 \rightarrow {}^7F_2$ transition under n-UV and blue excitations, in which the intensity is increasing continuously with Eu^{3+} ions concentration up to 5.0 mol%. Temperature-dependent emission profiles indicate excellent thermal stability and a high activation energy value. Furthermore, a prototype organic epoxy-free device has been developed using the optimized glass and n-UV LED chip. The results validate that the prepared glass is an auspicious candidate for the red component to fabricate organic epoxy-free white LEDs.

- Sm^{3+} doped potassium tungstate-tellurite glass is properly excited by 405 nm and emitted in the orange-red region. For Dy^{3+}/Sm^{3+} co-activated glasses, the emission colour has been tuned from warm white light to the orange-red region via altering the excitation wavelengths and the Sm^{3+} ion concentrations. In Dy^{3+}/Eu^{3+} co-doped tungstate-tellurite glasses, the emission color tunability was observed from the white to the reddish region via regulating the activator (Eu^{3+}) ions and specified excitation wavelengths. Dexter ET relation and Reisfeld's approximation have been used to validate the process of ET that involves a non-radiative d-d interaction using the emission spectral profiles. The emission intensity of the prepared 1.0 mol% Dy^{3+}/3.0 mol% Eu^{3+} co-activated tungstate-tellurite glass retained up to 85.92% at 100 ºC and 75.12% at 150 ºC as compared to the initial emission intensity by monitoring at n-UV excitation. The aforementioned findings indicate that the (Dy^{3+}/Sm^{3+}) and (Dy^{3+}/Eu^{3+}) co-doped tungstate-tellurite glass has great potential for use in solid state lighting applications.
- Tb^{3+} doped tungstate-tellurite glass exhibits multiple emission peaks under n-UV and blue excitations. The color coordinates were obtained to be (0.303, 0.560) and (0.343, 0.646) under n-UV and blue excitations, which lie in the pure green region. The emission spectra of the co-doped Tb^{3+} and Eu^{3+} ions in the TWKZBi glasses have been studied and the maximum energy transfer efficiency is found to be 32.82% under n-UV excitation. The emission colour of the prepared Tb^{3+}/Eu^{3+} co-activated glasses has been easily tunable from green to reddish region by varying the Eu^{3+} ion concentrations. All the results mentioned above reveal the suitability of the Tb^{3+}/Eu^{3+} co-activated tungstate-tellurite glasses for multicolor photonic applications.
- Transparent series of red emitting PiG with different dopant concentrations were fabricated via the inclusion of CBP: Eu^{3+} phosphor into tungstate-tellurite glass. XRD, Rietveld refinement, and FE-SEM analysis confirm the successful inclusion of the CBP:

Eu^{3+} phosphor within the tungstate-tellurite glass. The phosphor and PiG systems exhibit a strong hypersensitive transition at 612 nm ($^5D_0 \rightarrow {}^7F_2$) under n-UV and blue excitations, which is stronger than other observed transitions. The emission intensity of the peak positioned at 612 nm of the TWKZBi: CBPEu8.0 PiG sample is much greater than the CBP: 8.0 mol% Eu^{3+} phosphor. This is because the stable network structure and homogenous nature of Eu^{3+} ions promote electron transitions, resulting in reduced non-radiative loss. The thermal quenching behavior has been improved from 84.72 to 91.52% at 100 ºC and activation energy increased from 0.1938 to 0.2698 eV in the temperature range from room temperature to 200 ºC owing to the homogenous behavior and better glass network stability. The combination of the aforementioned findings endorses that the red-emitting TWKZBi: CBPEu PiG samples have the potential to be utilized in various photonic applications.

All the significant findings mentioned above validate that the trivalent RE doped/co-activated tungstate-tellurite glasses and CBP: Eu^{3+} phosphor in tungstate-tellurite glass (i.e., development of PiG system) developed in the present thesis can be beneficial, especially for w-LEDs and advanced photonic applications.

8.3. Future Scope of the Work

- To enhance the luminescence properties in the above glasses via the tri-dopant method.
  - via combination of $Tm^{3+}/Er^{3+}/Sm^{3+}$
- To fabricate a prototype efficient white LED with the help of the optimized glass/PiG.
- To extend the utility of the prepared glasses/PiG for various applications, including lasers, temperature sensors, solar cells, etc.

References

[1] C. Shen, K. Zheng, C. Ruan, G. Lv, M. Eftekhari, Energy Built Environ 4 (2023) 270-280.

[2] R. A. Opoku, P. K. Adom, Clean. Responsible. Consum. 8 (2023) 100100.

[3] D. D. Ramteke, V. Kumar, H. C. Swart, J. Non-Cryst. Solids. 438 (2016) 49-58.

[4] A. Bergh, G. Craford, A. Duggal, R. Haitz, Phys. Today. 54 (2001) 42-47.

[5] H. Allcott, S. Mullainathan, Science (1979) 327 (2010) 1204-1205.

[6] W. Abrahamese, L. Steg, C. Vlek, T. Rothengatter, J. Environ. Psychol. 25 (2005) 273-291.

[7] D. Van der Voort, J.M.E. de Ruk, G. Blasse, Phys. Stat. Sol. A 135 (1993) 621-626.

[8] M. Sharif Hossain, Energy Policy 39 (2011) 6991-6999.

[9] A. Ozadowicz, J. Grela, Energy Effic. 10 (2017) 563-576.

[10] S. Ye, F. Xiao, Y. X. Pan, Y. Y. Ma, Q. Y. Zhang, Mater. Sci Eng. R Rep. 71 (2010) 1-34.

[11] J. McKittrick, L. E. Shea-Rohwer, J. Am. Ceram. Soc. 97 (2014) 1327-1352.

[12] X. Liang, Y. Yang, C. Zhu, S. Yuan, G. Chen, A. Pring, F. Xia, Phys. Lett. 91 (2007) 091104.

[13] F. Steudel, S. Loos, B. Ahrens, S. Schweizer, J. Lumin. 170 (2016) 770-777.

[14] K. Jha, M. Jayasimhadri, D. Haranath, K. Jang, J. Alloys Compd. 789 (2019) 622-629.

[15] A. Mohan Babu, B. C. Jamalaiah, T. Sasikala, S. A. Saleem, L. Rama Moorthy, J. Alloys Compd. 509 (2011) 4743–4747.

[16] M. Shang, C. Li, J. Lin, Chem. Soc. Rev. 43 (2014) 1372-1386.

[17] A. Bergh, G. Craford, A. Duggal, R. Haitz, Phys. Today. 54 (2001) 42-47.

[18] L. Mishra, A. Sharma, A. K. Vishwakarma, K. Jha, M. Jayasimhadri, B.V. Ratman, K. Jang, A. S. Rao, R. K. Sinha, J. Lumin. 169 (2016) 121-127.

[19] O. Ravi, K. Prasad, R. Jain, M. Venkataswamy, S. Chaurasia, B. Deva Prasad Raju, Luminescence 32 (2017) 688-694.

[20] D. Chen, Z. Wang, Y. Zhou, P. Huang, Z. Ji, J. Alloys Compd. 646 (2015) 339– 344.

[21] P. P. Pawar, S. R. Munishwar, R. S. Gedam, J. Alloys Compd. 660 (2016) 347-355.

[22] X. Zhang, L. Huang, F. Pan, M. Wu, J. Wang, Y. Chen, Q. Su, ACS Appl. Mater. Interfaces. 6 (2014) 2709–2717.

[23] V. K. Rai, S. B. Rai, D. K. Rai, Opt. Commun. 257 (2006) 112–119.

[24] G. Venkataiah, C. K. Jayasankar, J. Mol. Struct. 1084 (2015) 182-189.

[25] A. Kaur, A. Khanna, L. I. Aleksandrov, J. Non-Cryst. Solids, 476 (2017) 67-74.

[26] J. E. Shelby, Introduction to Glass Science and Technology, RSC, 2005.

[27] R. H. Doremus, Glass Science, Wiley, 1994.

[28] D. R. (Donald R. Uhlmann, N.J. Kreidl, Glass, Science and Technology. Volume 4, Academic Press, 1990.

[29] N. Deopa, A. S. Rao, J. Lumin. 192 (2017) 832–841.

[30] B. Valeur, M. Ario, N. Berberan-Santos, J. Chem. Educ 88 (2011) 731–738.

[31] C. R. Ronda, Luminescence - From Theory to Applications, Wiley-VCH, India, 2007.

[32] A. Kitai, Luminescent Materials and Applications, John Wiley & Sons Ltd, England, 2008.

[33] K. N. Shinde, S. J. Dhoble, H. C. Swart, K. Park, Phosphate Phosphors for Solid-State Lighting, Springer Series in Materials Science, vol 174. Springer, Berlin, Heidelberg. (2012).

[34] L. U. Khan, Z. U. Khan, Handbook of Material Characterization (2018) 345-404.

[35] S. Kaur, M. Jayasimhadri, A. S. Rao, J. Alloys Compd. 697 (2017) 367-373.

[36] K. Jha, M. Jayasimhadri, J. Alloys Compd. 688 (2016) 833-840.

[37] K. Jha, A. K. Vishwakarma, M. Jayasimhadri, D. Haranath, J. Alloys Compd. 719 (2017) 116–124.

[38] G. Blasse, B. C. Grabmaier, Luminescent Materials, Springer-Verlag, Germany, 1994.

[39] S. Gai, C. Li, P. Yang, J. Lin, Chem. Rev. 114 (2014) 2343–2389.

[40] G. Liu, B. Jacquier, Spectroscopic Properties of Rare Earths in Optical Materials, Springer, 2005.

[41] H. S. Nalwa, L. S. Rohwer, Handbook of Luminescence, Display Materials, and Devices, American Scientific Publishers, 2003.

[42] X. Chen, P. Dai, X. Zhang, C. Li, S. Lu, X. Wang, Y. Jia, Y. Liu, Inorg. Chem. 53 (2014) 3441–3448.

[43] Z. Zhang, W. Tang, J. Lumin. 169 (2016) 367–373.

[44] G. Blasse, Philips Res. Rep. 24 (1969) 131–144.

[45] A. Ruivo, V. S. F. Muralha, H. Águas, A. P. de Matos, C. A. T. Laia, J. Quant. Spectrosc. Radiat. Transf. 134 (2014) 29–38.

[46] W. H. Brock, The Norton History of Chemistry, 1st Americ, W.W. Norton, New York, 1993.

[47] S. Hüfner, Optical Spectra of Transparent Rare Earth Compounds, Academic Press, 1978.

[48] A. J. Freeman, R.E. Watson, Phys. Rev. 127 (1962) 2058–2075.

[49] G. Dieke, Spectra and Energy Levels of Rare Earth Ions in Crystals, Interscience, New York, 1968.

[50] W. T. Carnall, P. R. Fields, K. Rajnak, J. Chem. Phys. 49 (2003) 4424.

[51] W. M. Yen, S. Shionoya, H. Yamamoto, Fundamentals of Phosphors,1st ed. CRC Press, Boca Raton, 2007.

[52] V. B. Pawade, H. C. Swart, S. J. Dhoble, Renew. Sustain. Energy Rev. 52 (2015) 596–612.

[53] M. K. Sahu, M. Jayasimhadri, K. Jha, B. Sivaiah, A. S. Rao, D. Haranath, J. Lumin. 202 (2018) 475–483.

[54] B. V. Ratnam, M. K. Sahu, A. K. Vishwakarma, K. Jha, H. J. Woo, K. Jang, M. Jayasimhadri, J. Lumin. 185 (2017) 99–105.

[55] J. G. Sole, L. E. Bausa, D. Jaque, An Introduction to the Optical Spectroscopy of Inorganic Solids, John Wiley & Sons Ltd, England, 2005.

[56] J. Mckittrick, M.E. Hannah, A. Piquette, J. K. Han, J. I. Choi, M. Anc, M. Galvez, H. Lugauer, J.B. Talbot, K.C. Mishra, ECS J. Solid State Sci. Technol. 2 (2013) 3119– 3131.

[57] L. Yang, Y. Wan, Y. Huang, C. Chen, H. Jin, J. Alloys Compd. 684 (2016) 40–46.

[58] B. Tian, B. Chen, Y. Tian, X. Li, J. Zhang, J. Sun, H. Zhong, L. Cheng, S. Fu, H. Zhong, Y. Wang, X. Zhang, H. Xia, R. Hua, J. Mater. Chem. C 1 (2013) 2338–2344.

[59] J. C. G. Bünzli, C. Piguet, Chem. Soc. Rev. 34 (2005) 1048–1077.

[60] C. Madhukar Reddy, B. Deva Prasad Raju, N. John Sushma, N. S. Dhoble, and S. J. Dhoble, Renew. Sustain. Energy Rev. 51 (2015) 566–584.

[61] Joseph R. Lakowicz, Principles of Fluorescence Spectroscopy (2006).

[62] H. Y. William M. Yen Shigeo Shionoya, Handbook of Phosphors 2nd Ed. 23 (2003).

[63] Ravita, A. S. Rao, J. Lumin. 244 (2022) 118689.

[64] A. K. Vishwakarma, K. Jha, M. Jayasimhadri, B. Sivaiah, B. Gahtori, D. Haranath, Dalt. Trans. 44 (2015) 17166–17174.

[65] C. S. McCamy, Color Res. Appl. 17 (1992) 142–144.

[66] M. Venkateswarlu, M. V. V. K. S. Prasad, K. Swapna, S. Mahamuda, A. S. Rao, A. M. Babu, D. Haranath, Ceram. Int. 40 (2014) 6261.

[67] T. Kosuge, Y. Benino, V. Dimitrov, R. Sato, T. Komatsu, J. Non- Cryst. Solids. 242 (1998) 154.

[68] I. Shaltout, Y. Tang, R. Braunstein, E.E. Shaisha, J. Phys. Chem. Solids. 57 (1996) 1223.

[69] J. Yang, S.Dai., Y. Zhou., L. Wen, L. Hu, Z. H. Jiang, J. Appl. Phys. 93(2) (2003) 977.

[70] M. H. A. Mhareb, Appl. Phys. A 126 (2020) 71.

[71] Vikas, M. Jayasimhadri, D. Haranath, Int. J. Appl. Glass Sci. 13 (2022) 645-654.

[72] B. Oprea, T. Radu, S. Simon, J. Non-Cryst. Sol. 379 (2013) 35-39.

[73] J. Rose Jose, A. Gopinath, S. Anna Oommen, C. Joseph, P.R. Biju, Opt. Mater. 148 (2024) 114809.

[74] J. S. Zhong, H. B. Gao, Y. J. Yuan, L. F. Chen, D. Q. Chen, Z. G. Ji, J. Alloys Compd. 735 (2018) 2303-2310.

[75] Y. Chen, J. Wang, M. Gong, Q. Su, J. Solid State Chem. 180 (2007) 1165–1170.

[76] R. K. Tamrakar, D. P. Bisen, N. Bramhe, J. Radiat. Res. Appl. Sci. 7 (2014) 550–559.

[77] P. Godlewska, A. Matraszek, L. Macalik, K. Hermanowicz, M. Ptak, P.E. Tomaszewski, J. Hanuza, I. Szczygieł, J. Alloys Compd. 628 (2015) 199–207.

[78] D. Jugović, D. Uskoković, J. Power Sources. 190 (2009) 538–544.

[79] R. K. Tamrakar, D. P. Bisen, K. Upadhyay, I. P. Sahu, J. Phys. Chem. C 119 (2015) 21072–21086.

[80] B. D. Cullity, Elements of X-Ray Diffraction, Addison- Wesley Publishing Company, Inc, Philippines, 1978.

[81] M. Birkholz, C. Genzel, T. Jung, J. Appl. Phys. 96 (2004) 7202.

[82] L. R. B. Elton, D. F. Jackson, Am. J. Phys. 34 (1966) 1036–1038.

[83] I. H. Gul, A. Maqsood, J. Alloys Compd. 465 (2008) 227–231.

[84] P. R. Griffiths, J. A. De Haseth, Fourier Transform Infrared Spectrometry, Wiley-Interscience, 2007.

[85] W. H. Weber, R. Merlin, Raman Scattering in Materials Science, Springer Berlin Heidelberg, 2000.

[86] A. Agarwal, V. P. Seth, S. Sanghi, P. Gahlot, D.R. Goyal, Radiat. Eff. Defects Solids 158 (2003) 793–801.

[87] M. Altaf, M. A. Chaudhary, M. Zahid, J. Res. 14 (2003) 253–259.

[88] J. -C. G. Bünzli, S. V. Eliseeva Basics of Lanthanide Photophysics, Lanthanide Luminescence, Springer, Berlin, 2010.

[89] S. Shionoya, Photoluminescence, Luminescence of Solids, Springer New York, 1998, pp 95-133.

[90] K. Wakabayashi, Y. Yamaguchi, T. Sekiya, S. Kurita, J. Lumin. 112 (2005) 50–53.

[91] K. Suhling, D. M. David, D. Phillips, J. Fluoresc.12 (2002) 91-95.

[92] K. Li, X. Liu, Y. Zhang, X. Li, H. Lian, J. Lin, Inorg. Chem. 54 (2015) 323–333.

[93] K. Jha, M. Jayasimhadri, J. Am. Ceram. Soc. 100 (2017) 1402–1411.

[94] J. Sun, X. Zhang, Z. Xia, H. Du, Mater. Res. Bull. 46 (2011) 2179–2182.

[95] R. Bajaj, A. S. Rao, G. V. Prakash, J. Alloys Compd. 885 (2021) 160893.

[96] K. Li, M. Shang, H. Lian, J. Lin, Inorg. Chem. 54 (2015) 7992–8002.

[97] P. Li, M. Peng, X. Yin, Z. Ma, G. Dong, Q. Zhang, J. Qiu, Opt. Express. 21 (2013) 18943–18948.

[98] G. G. Li, D. L. Geng, M. M. Shang, C. Peng, Z. Y. Cheng, J. Lin, J. Mater. Chem. 21 (2011) 13334-13344.

[99] H. A. Hoppe, Angew. Chem. Int. Ed. Engl. 48 (2009) 3572-3582.

[100] R. L. Kohale, S. J. Dhoble, J. Lumin. 138 (2013) 153-156.

[101] A. K. Vishwakarma, M. Jayasimhadri, J. Lumin. 176 (2016) 112-117.

[102] P. Suthanthirakumar, K. Marimuthu, J. Mol. Struct. 1125 (2016) 443-452.

[103] X. Zhang, L. Huang, F. Pan, M. Wu, J. Wang, Y. Chen, Q. Su. ACS Appl. Mater. Interfaces 6 (2014) 2709-2717.

[104] V. K. Rai, S. B. Rai, D. K. Rai, Opt. Commun. 257 (2006) 112-119.

[105] A. M. Babu, B. C. Jamalaiah, J. S. Kumar, T. Sasikala, L. R. Moorthy, J. Alloys Compd. 509 (2011) 457-462.

[106] H. Masai, Y. Yamada, Y. Suzuki, K. Teamura, Y. Kanemitsu, T. Yoko, Sci Rep. 3 (2013) 351.

[107] C. M. Reddy, G. R. Dillip, B. D. P. Raju, J. Phys. Chem. Sol. 72 (2011) 1436-1441.

[108] M. Celikbilek, A.E. Ersundu, N. Solak, S. Aydin, J. Alloys Compd. 509 (2011) 5646-5654.

[109] W. Zhao, W. Zhou, M. Song, G. Wang, J. Du, H. Yu, J. Chen, J. Alloys Compd. 509 (2011) 3937-3942.

[110] K. Maheshvaran, K. Marimuthu, J. Alloys. Compd. 509 (2011) 7427-7433.

[111] Sd Z.A. Ahamed, C. M. Reddy, B. D. P. Raju, Opt. Mater. 35 (2013) 1385-1394.

[112] L. Jyothi, G. Upender, R. Kuladeep, D. N. Rao, Mater. Res. Bull. 50 (2014) 424-431.

[113] N. Elkhoshkhany, S. Maarzouk, M. El Sherbiny, H. Anwer, M.S. Alqahtani, H. Algarni, M. Rebwn, El S. Yousef, Results in Phy. 27 (2021) 104544.

[114] H. Lee, W.J. Chung, W.B. Im, J. Lumin. 236 (2021) 118064.

[115] L. Wang, M. Xu, H. Zhao, D. Jia, New J. Chem. 40 (2016) 3086-3093.

[116] K. Mariselvam, J. Liu, Opt. Mater. 114 (2021) 110997.

[117] M. Soltys, A. Gorny, L. Zur, M. Ferrari, G.C. Righini, W.A. Pisarski, J. Pisarska, Opt. Mater. 87 (2019) 63-69.

[118] K. Jha, A.K. Vishwakarma, M. Jayasimhadri, D. Haranath, K. Jang, J. Non-Cryst. Solids. 553 (2021) 120516.

[119] S. Badamasi, Y. A. Yamusa, N. N. Garba, M. Najamudden, J. Sci. 4 (2020) 190-199.

[120] V. Dimitrov, S. Sakka, J. Appl. Phys. 79 (1996) 1736.

[121] R. Sharma, A. S. Rao, J. Non-Cryst. Solids 495 (2018) 85-94.

[122] M. Gokce, D. Kocyigit, Opt. Mater. 89 (2019) 568-575.

[123] K. Liganna, Ch. Srinivasa Rao, C. K. Jayasankar, J. Quant. Spectro. Radiat. Transfer 118 (2013) 40-48.

[124] K. Damak, El S. Yousef, C. Ruseel, R. Maalej, J. Quant. Spectro. Radiat. Transfer 134 (2014) 55-63.

[125] X. Zhang, J. Wang, L. Hung, F. Pan, Y. Chan, B. Lei, M. Peng, M. Wu, ACS Appl. Matter. Interfaces 7 (2015) 10044-10054.

[126] P. Li, M. Peng, X. Yin, Z. Ma, G. Dong, Q. Zhang, et al. Opt. Express. 21(16) (2013) 18943-18943.

[127] Ravita, A. S. Rao, J. Lumin. 239 (2021) 118325.

[128] L. Vijayalakshmi, K.N. Kumar, J.D. Baek, Ceram. Int. 49 (2023) 5013-5021.

[129] E. F. Schubert, J. K. Kim, Science. 308 (2005) 1274-1278.

[130] V. Chandrappa, Ch. Basavapoornima, C. R. Kesavulu, A. Mohan Babu, Shobha Rani Depuru, C. K. Jayasankar, J. Non-Cryst. Solid. 583 (2022) 121466.

[131] X. Li, Y. Zhang, D. Geng, J. lian, G. Zhag, Z. Hou, J. Lin, J. Mater. Chem. C 2 (2014) 9924-9933.

[132] S. Damodaraiah, Y.C. Ratnakaram, J. Lumin. 207 (2019) 553-560.

[133] T. Mann, R. Mathieson, M. Murray, B. Richards, G. Jose, J. Appl. Phys. 124 (2018) 044903.

[134] T. Subrahmanyam, K. Rama Gopal, R. Padma Suvarna, B. C. Jamalaiah, M. V. Vijaya Kumar, Opt. Mater. 80 (2018) 154-159.

[135] S. Keenatampalle, N. Rama Devi, K. Vijayalakshmi, N.S. Abd EL-Gawaad, L.O. Mallasiy, B. Muni Sudhakar, N. Manohar Reddy, Phys. B: Condens. Mater 666 (2023) 415109.

[136] S. Ghosh, S. Jana, J. Lumin. 263 (2023) 119980.

[137] R. Bajaj, A.S. Rao, G. Vijaya Prakash, J. Non-Cryst. Solid. 575 (2022) 121184.

[138] N. Deopa, A.S. Rao, Sk. Mahamuda, M. Gupta, M. Jayasimhadri, D. Haranath, G.V. Prakash, J. Alloys Compd. 708 (2017) 911-921.

[139] Ravina, Naveen, Sheetal, V. Kumar, S. Dahiya, N. Deopa, R. Punia, A.S. Rao, J. Lumin. 229 (2021) 117651.

[140] N. Bansal, A. Arora, S. Singh Danewalia, K. Singh, Silicon 13 (2021) 1723-1730.

[141] O. Kibrish, A.E. Ersundu, M.C. Ersundu, J. Non-Cryst. Solids 513 (2019) 125-136.

[142] G.P. Singh, S. Kaur, P. Kaur, S. Kumar, D.P. Singh, Physica B 406 (2011) 1890-1893.

[143] Sanju, Ravina, Anu, A. Kumar, V. Kumar, M. K. Sahu, S. Dahiya, N. Deopa, R. Punia, A.S. Rao, Opt. Mater. 114 (2021) 110937.

[144] W.T. Carnall, P.R. Fields, K. Rajnak, J. Chem. Phys. 49 (1968) 4424-4442.

[145] S. Selvi, K. Marimuthu, N. S. Murthy, G. Muralidharan, J. Mol. Struct. 1119 (2016) 276-285.

[146] K. Mariselvam, J. Liu, Physica B. 614 (2021) 413024.

[147] S. Pravinraj, M. Vijaykumar, K. Marimuthu, Phys. B: Condens. 509 (2017) 84-93.

[148] M. K. Sahu, M. Jayasimhadri, J. Amer. Ceram. Soci. 102 (2019) 6089-6099.

[149] Poonam, Shivani, Anu, A. Kumar, M. K. Sahu, P. R. Rani, N. Deopa, R. Punia, A. S. Rao, J. Non-Cryst. Solids 544 (2020) 120187.

[150] X. Zhang, J. Wang, L, Hung, F. Pan, Y. Chan, B. Lei, et al. ACS Appl. Matter. Interfaces. 7 (2015) 10055-10054.

[151] V. K. Rai, B. C. Jamalaiah, J. S. Kumar, T. Sasikala, L. R. Moorthy, J. Alloys Compd. 509 (2011) 457-62.

[152] W. Yuan, R. Pang, S. Wang, T. Tan, C. Li, C. Wang, H. Zhang, Light Sci. Appl. 11 (2022) 184.

[153] I. Abdullahi, S. Hashim, S. K. Ghoshal, A. U. Ahmad, Mater. Chem. Phys. 240 (2020) 122862.

[154] K.A. Bashar, W.L. Fong, K.A. Haider, S.O. Baki, M.H.M. Zaid, M.A. Mahdi, J. Non-Cryst. Solids 534 (2020) 119943.

[155] D. D. Ramteke, V. Kumar, H. C. Swart, J. Non-Cryst. Solids 438 (2016) 49-58.

[156] S. Damodaraiah, V. Reddy Prasad, Y. C. Ratnakaram, Lumin. 33 (2018) 593-603.

[157] G. Vebkataiah, C. K. Jayasankar, J. Mol. Struct. 1084 (2015) 182-90.

[158] J. Biwas, S. Jana, Ceram. Int. 49 (2023) 24718-24729.

[159] J. C. Chang, C. T. Chen, M. Rudysh, M. G. Brik, M. Piasecki, W. R. Liu, J. Lumin. 206 (2019) 417-425.

[160] W. A. Pisarski, L. Zur, T. Goryczka, M. Soltys, J. Pisarska, J. Alloys Compd. 587 (2014) 90-98.

[161] M. K. Sahu, M. Jayasimhadri, J. Am. Ceram. Soc. 102 (10) (2019) 6087-6099.

[162] V. Naresh, N. Lee, Mater, Res. Bull. 142 (2021) 111381.

[163] A. Gorny, M. Soltys, J. Pisarska, W. A. Pisarski, J. Rare Earths 37 (2019) 1154-1151.

[164] V. Naresh, S. Buddhudu, J. Lumin. 147 (2014) 63-71.

[165] H. Pamuluri, M. Rathaiah, K. Linganna, C. K. Jayasankar, V. Lavin, V. Venkatramu, New J. Chem. 42 (2018) 1269-1270.

[166] O. Chatterjee, R. Rupam, A. Pramanik, T. Dutta, V. Sharma, P. Sarkar, Adv. Opt. Mater. 10 (2022) 2201187.

[167] G. Ye, L. Fang, X. Zhou, H. Xia, H. Song, B. Chen, J. Alloys Compd. 912 (2022) 165126.

[168] M. K. Sahu, H. Kaur, B.V. Ratnam, J.S. Kumar, M. Jayasimhadri, Ceram. Int. 46 (2020) 26410-26415.

[169] T. Leow, H. Liu, R. Hussin, Z. Ibrahim, K. Deraman, H. O. Lintang, W. N. W. Shamsuri, J. Rare Earths 34 (2016) 21-29.

[170] D.L Dexter, J. Chem. Phys. 21 (1953) 836-850.

[171] X. Wu, B. Yin, Q. Ren, J. Zheng, Y. Ren, O. Hai, J. Alloys Compd. 822 (2020) 153562.

[172] M. K. Sahu, M. Jayasimhadri, J. Mater Sci: Mater Electron 33 (2022) 5201-5213.

[173] K. Naveen Kumar, J. Su Kim, M. Cho, J. Shim, B. K. Gupta, M. Kang, J. Alloys Compd. 721 (2017) 554-562.

[174] M. Fhoula, T. Koubaa, M. Dammak, Opt. Laser Technol. 130 (2020) 106352.

[175] Y. Zhou, C. Zhu, M. Zhang, J. Liu, J. Alloys Compd. 688 (2016) 715-720.

[176] Vikas, M. Jayasimhadri, D. Haranath, Curr. Appl. Phys. 58 (2024) 11-20.

[177] W.U. Khan, J. Li, X. Li, Q. Wu, J. Yan, Y. Xu, F. Xie, J. Shi, M. Wu, Dalton Trans. 46(6) (2017) 1885-1891.

[178] D. Kang, H.S. Yoo, S.H. Jung, H. Kim, D.Y. Jeon, J. Phys. Chem. C. 115 (2011) 24334–2434.

[179] X. Zhang, F. Mo, Z-C. Wu, Y. Chen, J. Mater. Sci. 53 (5) (2018) 3613-3623.

[180] N. Hsouna, C. Bouzidi, Solid State Sci. 134 (2022) 107053.

[181] K. Rawat, A.K. Vishwakarma, K. Jha, Opt. Laser Technol. 145 (2022) 107455.

[182] F. He, Z. He, J. Xie, Y. Li, Am. J. Anal. Chem. 5 (2014) 1142-1150.

[183] V.O. Sokolov, V.G. Plotnichenko, E.M. Dianov, Inorg. Mater. 43 (2007) 194-213.

[184] H. Fares, I. Jlassi, H. Elhouichet, M. Ferid, J. Non-Cryst. Solids 396-397 (2014) 1-7.

[185] V. Sreenivasulu, G. Upender, Swapna, V. Priya, V.C. Mouli, M. Prasad, Raman, Phys. B 454 (2014) 60-66.

[186] G.S. Murugan, T. Suzuki, Y. Ohishi, J. Appl. Phys. Lett. 86 (2005) 131903.

[187] D. Munoz-Martin, M.A. Villegas, J. Gonzalo, J.M. Fernandez-Navarro, J. Eur. Ceram. Soc. 29 (2009) 2903-2913.

[188] M. Jayasimhadri, K. Jha, B.V. Ratnam, H. J. Woo, K. Jang, A.S. Rao, D. Haranath, J. Alloys Comp. 711 (2017) 395-399.

[189] K. Rawat, A.K. Vishwakarma, K. Jha, Mater. Res. Bull. 124 (2020) 110750.

[190] S.M. Hsu, S.W. Yung, Yi-C. Hsu, F.B. Wu, C. Fu, Y.S. Lai, Yi-Mu Lee, Ceram. Int.42 (2016) 4019-4025.

[191] S. Loos, F. Steudel, B. Ahrens, S. Schweizer, J. Lumin. 181 (2017) 31-35.

[192] K. Jha, A.K. Vishwakarma, M. Jayasimhadri, D. Haranath, J. Alloys Compd. 719 (2017) 116-124.

[193] K. Jha, M. Jayasimhadri, J. Lumin. 194 (2018) 102-107.

[194] Vikas, M. Jayasimhadri, Lumin.37(12) (2022) 2059-2066.

[195] G. Lakshminarayana, A. Wagh, S.D. Kamath, A. Dahshan, H.H. Hegazy, M. Marzec et. al., Opt. Mater. 99 (2020) 109555.

[196] J. Gou, J. Fan, S. Zuo, Y. Chen, X. Zhou, Y. Yang, B. Yu, S.F. Liu, J. Am. Ceram. Soc. 100 (2017) 4011-4020.

[197] L. He, D. Wang, M. Chen, R. Liu, Z. Su, C. Li, H. Lin, S. Li, Y. Zhou, L. Liu, F. Zeng, Opt. Mater. 122 (2021) 111754.

[198] D. Rajesh, K. Brahmachary, Y.C. Ratnakaram, N. Kiran, A.P. Baker, J. Alloys Compd. 646 (2015) 1096-1103.

[199] V. Sangwan, M. Jayasimhadri, D. Haranath, J. Lumin. 266 (2024) 120276.

[200] X.Y. Huang, Nat. Photonics 8 (2014) 748-749.

[201] X.J. Zhang, J.B. Yu, J. Wang, B.F. Lei, Y.L. Liu, Y.J. Cho, R.J. Xie, H.W. Zhang, Y.R. Li, Z.F. Tian, Y. Li, Q. Su, ACS Photonics 4 (2017) 986-995.

[202 Y. Peng, R.X. Li, S.M. Wang, Z. Chen, L. Nie, M.X. Chen, IEEE Trans. Electron. Dev. 64 (2017) 1114-1119.

[203] Q.Q. Zhu, X. Xu, L. Wang, Z.F. Tian, Y.Z. Xu, N. Hirosaki, R.J. Xie, J. Alloys Compd. 702 (2017) 193-198.

[204] R. Zhang, H. Lin, Y.L. Yu, D.Q. Chen, J. Xu, Y.S. Wang, Laser Photonics Rev. 8 (2014) 158-164.

[205] Y. Peng, R.X. Li, X. Guo, H. Zheng, M.X. Chen, Appl. Opt. 55 (2016) 8189-8195.

[206] Y. Gao, J.B. Qiu, D.C. Zhou, J. Am. Ceram. Soc. 100 (2017) 2901-2913.

[207] J.S. Zhong, W. Xu, Q.L. Chen, S. Yuan, Z.G. Ji, D.Q. Chen, Dalton Trans. 46 (2017) 9959-9968.

[208] X. Xu, H. Li, Y. Zhuo, R. Li, P. Tian, D. Xiong, M. Chen, J. Mater. Sci. 53 (2018) 1335–1345.

[209] X. Zhang, S. Si, J. Yu, Z. Wang, R. Zhang, B. Lei, Y. Liu, J. Zhuang, C. Hu, Y. Cho, R.-J. Xie, H.-W. Zhang, Z. Tian, J. Wang, J. Mater. Chem. C 7 (2019) 354–361.

[210] R. Wei, L. Wang, P. Zheng, H. Zeng, G. Pan, H. Zhang, P. Liang, T. Zhou, R. Xie, J. Eur. Ceram. Soc. 39 (2019) 1909-1917.

[211] H. Zhou, J. Zou, B. Yang, W. Wu, M. Shi, Z. Wang, Y. Liu, M. Li, G. Zhao, J. Non-Cryst. Solids 481 (2018) 537–542.

[212] X. Huang, S. Wang, B. Li, Q. Sun, H. Guo, Opt. Lett. 43 (2018) 1307.

[213] T. Krishnapriya, A. Jose, T.A. Jose, A.C. Saritha, C. Joseph, P.R. Biju, Mater. Res. Bull. 139 (2021) 111259.

[214] Z. Zhang, L. Sun, B. Devakumar, J. Liang, S. Wang, Q. Sun, S.J. Dhoble, X. Huang, J. Lumin. 221 (2020) 117105.

[215] X. Huang, H. Guo, B. Li, J. Alloys Compd. 720 (2017) 29–38.

[216] M. K. Sahu, M. Jayasimhadri, J. Lumin. 227 (2020) 117570.

[217] M. Jiao, N. Guo, W. Lü, Y. Jia, W. Lv, Q. Zhao, B. Shao, H. You, Dalton Trans. 42 (2013) 12395–12402.

[218] X. Zou, L. He, R. Li, Q. Zheng, Y. Liu, C. Xu, D. Lin, J. Mater. Sci. Mater. Electron. 28 (2017) 2826–2832.

[219] A. K. Vishwakarma, K. Jha, M. Jayasimhadri, A. S. Rao, K. Jang, B. Sivaiah, D. Haranath, J. Alloys Compd. 622 (2015) 97–101.

[220] S. Wang, Q. Chen, Ceram. Int. 49 (2023) 17212-17228.

[221] S. Qi, D. Wei, Y. Huang, S. Kim, Y.M. Yu, H.J. Seo, J. Am. Ceram. Soc. 97 (2014) 501-506.

[222] G. Annadurai, L. Sun, H. Guo, X. Huang, J. Lumin. 226 (2020) 117474.

[223] P. Li, M. Peng, X. Yin, Z. Ma, G. Dong, Q. Zhang, J. Qiu, Opt. Express 21 (2013) 18943–18948.